Extension of the Contour Integral Method for the Electrical Design of Planar Structures in Digital Systems

Dem Promotionsausschuss der
Technischen Universität Hamburg-Harburg
zur Erlangung des akademischen Grades
Doktor-Ingenieur (Dr.-Ing.)
genehmigte Dissertation

von
Xiaomin Duan

aus
Jiangsu, China

2012

1. Gutachter:

Prof. Dr. sc. techn. Christian Schuster

2. Gutachter:

Prof. Dr.-Ing. Stephan Dickmann

3. zusätzlicher Gutachter:

Prof. Dr.-Ing. Jan Luiken ter Haseborg

4. zusätzlicher Gutachter:

Prof. Dr.-Ing Arne Jacob

Vorsitzender des Promotionsverfahrens:

Prof. Dr. Ernst Brinkmeyer

Tag der mündlichen Prüfung: 03.04.2012

Summary

In response to the rapid advance of semiconductor technologies, the demand for dedicated electronic design automation tools has been continuously increasing. This thesis focuses on the efficient and accurate modeling of planar structures and power planes in digital systems by the extension of a fast two-dimensional (2D) numerical technique, the contour integral method (CIM).

The advantage of CIM rests on its capability to handle arbitrary shape planar structures and to generate field information efficiently. However, when dealing with power planes with a large number of cylindrical vias, its efficiency drops drastically due to the numerical modeling of via boundaries. To overcome this drawback, CIM is extended here using analytical solutions for circular ports to expedite the computation. Expressions are derived for isotropic modes as well as for anisotropic modes that concerns the accuracy of CIM when applying to dense via arrays at high frequencies.

Although CIM is restricted to 2D problems, the fact that it represents a closed planar region surrounded by microwave ports allows it to be easily networked with other models. Hence, CIM is further extended by combinations with efficient approaches including equivalent circuits, the method of moments, and the physics-based via model to account for the effects of decoupling capacitors, radiation losses, and multilayer substrates, respectively.

The validation and evaluation of the method and its extensions are thoroughly addressed by a variety of application examples. A selection of power/ground plane pair configurations is analyzed to assess the efficiency and applicability to complex shapes. Simulations of multiplayer printed circuit boards are then presented and the results concerning all respects of electrical designs are demonstrated, which cover the signal integrity, the power integrity, and radiated emissions. Application to dense via arrays will follow and the resolution of potential passivity problems is discussed. The overall efficiency and accuracy of the extended method are solid and the method can produce comparable results more than 100 times faster than general-purpose full-wave solvers.

Acknowledgment

My gratitude goes first to my thesis advisor, Prof. Christian Schuster, head of the institute of Electromagnetic Theory (TET) at the Hamburg University of Technology (TUHH), for the excellent guidance throughout this work. His commitment to research and academics has always motivated me.

I would also like to thank Prof. Stefan Dickmann for being the co-examiner and for the careful review of this work.

I would like to acknowledge the colleagues and staff of the TET institute. It has been a great experience working with them. I am grateful to Dr. Heinz Brüns for numerous ideas and suggestions to this work. I also thank Heike Herder, Angela Freiberg, Walter Burmester, and Stefan Conradi for the administrative and technical supports. I would like to express my gratitude to the team, especially Dr. Renato Rimolo-Donadio, Miroslav Kotzev, and Sebastian Müller for the contribution to this work. I also appreciate Prof. Frank Gronwald, Dr. Miguel Astner, Dr. Volker Vahrenholt, Arne Schröder, Andreas Hardock, Alexander Vogt, last but not least Fabian Happ and Dion Timmermann for various supports and productive discussions.

My gratitude goes also to Dr. Bruce Archambeault and Dr. Xiaoxiong (Kevin) Gu from IBM for mentoring and helping me understand deeper in related subjects. Thanks go also extensively to other colleagues whom I worked with at IBM T. J. Watson Research Center, New York, USA.

Finally, I am deeply indebted to my family, my parents Yihe and Meifang, my wife Muzi for their unconditional love and encouragements. This thesis is dedicated to them.

Contents

Notation, Symbols and Acronyms ix

1. Introduction 1

1.1. Motivation and Context of this Work 1

1.2. Organization of the Work 3

1.3. Conference and Journal Contributions 4

2. Modeling of Planar Structures in Digital Systems 5

2.1. Power Planes in Electronic Packages 5

2.1.1. Function for Power Delivery 5

2.1.2. Function for Signal Transmission and EMI Mitigation 7

2.1.3. Radial Wave Propagation in a Parallel-Plate Environment 10

2.1.4. Cavity Resonant Modes 12

2.2. State-of-the-Art Modeling Methods 14

2.3. Definition of Planar Circuits 16

2.4. Summary 17

3. CIM – the Contour Integral Method 19

3.1. Basic Formulation 19

3.2. Numerical Procedure and Line Ports 21

3.3. Modeling of Circular Ports 25

3.4. Cavity Field Distribution and Radiation 28

3.5. Limitations of the Method 28

3.6. Summary and Discussions 29

4. Extension using Analytical Solutions 31

4.1. Isotropic Circular Port Definition 31
4.2. Derivations for Isotropic Ports 33
  4.2.1. Infinite Planes 33
  4.2.2. Finite Planes 37
4.3. Identification of Non-uniform Currents 41
4.4. Generalized Circular Port Definition 44
4.5. Modeling of Anisotropic Modes 47
  4.5.1. Numerical Modeling of Modal Impedance 47
  4.5.2. Infinite Plane 49
  4.5.3. Finite Planes 56
  4.5.4. Port Array Analysis 59
4.6. Summary and Discussion 66

5. Extension using Hybridization 67

5.1. Inclusion of One-Port Circuits 69
  5.1.1. Decoupling Capacitor Model 69
  5.1.2. Inclusion of Decoupling Capacitors 69
  5.1.3. A Rectangular Board Example 71
5.2. Inclusion of Radiation Loss 78
  5.2.1. Domain Decomposition 78
  5.2.2. Modeling of the External Domain 79
  5.2.3. Merging of Sub-domains 81
  5.2.4. Validation and Examples 84
5.3. Hybridization with Via and Trace Model 89
  5.3.1. Physics-based Via Model 89
  5.3.2. Via and Trace Transition Model 92
  5.3.3. Connection to CIM Matrices 93
  5.3.4. Merging of Multiple Layers 97
  5.3.5. Validation and Examples 98

5.4. Summary and Discussion 106

6. Advanced Applications 107

6.1. Arbitrary Shaped Power Planes 107

6.1.1. L-Shape Board with Cut-Out Area 108

6.1.2. Board with Narrow Slot 112

6.1.3. Complex Shaped Board 116

6.1.4. Discussion on Applicability and Limitations 119

6.2. Stacked Power Planes 120

6.2.1. Dense Via Array and Passivity Issue 120

6.2.2. Analysis of Multilayer Printed Circuit Board 127

6.3. Summary and Discussion 132

7. Conclusions and Outlook 133

Appendix A: Mathematical Appendix 135

A.1. Bessel and Hankel Functions 135

A.2. Addition Theorems for Hankel Functions 138

A.3. Gaussian Quadrature 139

A.4 Derivation of Equation (4.11) 139

A.5. Derivation of Equation (4.12) 140

A.6. Derivation of Equations (4.19)-(4.22) 143

A.7. Derivation of Equations (4.44)-(4.45) 143

A.8. Derivation of Equations (4.48)-(4.51) 146

Appendix B: Extension of Cavity Resonator Model for Circular Ports 147

References 155

Curriculum Vitae 169

Notation, Symbols and Acronyms

Notation

V	Scalar
$\overline{V}$	Column vector
$\overline{\overline{V}}$	Matrix
V_{ij}^{pp}	Matrix entry, where indexes i and j denotes the matrix row and column, respectively, and the superscript the type of variable
x, y, z	Cartesian coordinates
$\boldsymbol{\rho}$, ϕ, z	Cylindrical coordinates
p	Superscript for circular ports
q	Superscript for boundary line ports
u	Superscript for upper/top side of a cavity
l	Superscript for lower/bottom side of a cavity
$\boldsymbol{r}$	Spatial vector with regard to coordinate origin
$\vec{\boldsymbol{\rho}}_{ab}$	Spatial vector from point $\boldsymbol{a}$ to $\boldsymbol{b}$.
$\hat{\boldsymbol{n}}$	Unit vector

Symbols

λ	Wavelength [m]
ω	Angular frequency [rad · s^{-1}]
j	Imaginary unit
∇	Nabla symbol
C	Capacitance [Farad] or plane boundary contour

C'	Internal via boundary contour
c_i, c_j	Contours on individual circular ports
ϕ	Azimuthal angle [rad]
$\Delta\phi$	Increment of azimuthal angle [rad]
d	Cavity thickness [m]
t_p	Metal plane thickness [m]
k	Wavenumber
η	Wave impedance [Ω]
κ	Conductivity [S · m^{-1}]
$\tan\delta$	Dielectric loss tangent
t_s	Skin depth [m]
I	Current [A]
V	Voltage [V]
t	Time [s]
f	Frequency [Hz]
f_c	Cutoff frequency [Hz]
f_r	Resonance frequency [Hz]
L	Inductance [H]
R	Resistance [Ω]
ρ_{ij}	Distance between ports
$\mathcal{E}$	Electric field phasor [V · m^{-1}]
$\mathcal{H}$	Magnetic field phasor [A · m^{-1}]
μ	Permeability (when subscripted, *d*: dielectric, *c*: conductor) [H · m^{-1}]
μ_0	Permeability of free space (~ $4\pi \cdot 10^{-7}$ H · m^{-1})
μ_r	Relative permeability
ε	Permittivity (when subscripted, *d* stands for dielectric) [F · m^{-1}]
ε_0	Permittivity of free space (~ $8.854 \cdot 10^{-12}$ F · m^{-1})
ε_r	Relative permittivity
J_n	Bessel function of first kind of the order n
J_n	Bessel function of second kind of the order n
$H_n^{(1)}$	Hankel function of first kind of the order n

$H_n^{(2)}$	Hankel function of second of the order n
Z^{pp}	Parallel-plate impedance
Y^{pp}	Parallel-plate admittance
$W_i,\ W_j$	Line port widths [m]
$a_i,\ a_j$	Circular port radii [m]
P_x, P_y	Lateral dimensions of rectangular plates [m]
h^l	Distance from trace to bottom reference plane
h^u	Distance from trace to top reference plane
S_{ij}	Scattering parameter
Z_{ij}	Impedance parameter [Ω]
Y_{ij}	Admittance parameter [S]
h_{ij}	h-parameter
l	Transmission line/trace length [m]
Z_0	Characteristic impedance [Ω]
t_r	Rise time [s]
P	Power [watt]
P_r	Radiated power [watt]
Q	Quality factor
S	Poynting vector [$\mathrm{W} \cdot \mathrm{m}^{-2}$] or total contour including C and C'
Y^c	Via-to-plane admittance [S]
C^v	Via-to-plane capacitance[F]
Z^c	Via-to-plane impedance [Ω]

Acronyms

2D	Two Dimensional
3D	Three Dimensional
ABC	Absorbing Boundary Condition
ABCD	Microwave Network Chain Parameters
AC	Alternating Current
ATC	Air Traffic Control

BER	Bit Error Rate
BGA	Ball Grid Array
C4	Controlled Collapse Chip Connection
CIM	Contour Integral Method
CISPR	International Special Committee on Radio Interference (in French)
CRM	Cavity Resonator Model
CM	Common-Mode
CPU	Central Processing Unit
DC	Direct Current
Decap	Decoupling Capacitor
DM	Differential Mode
DR	Data Rate
EDA	Electronic Design Automation
EFIE	Electric Field Integral Equation
EHF	Extremely High Frequency (30 GHz – 300 GHz)
EM	Electromagnetic
EMC	Electromagnetic Compatibility
EMI	Electromagnetic Interference
ESL	Equivalent Series Inductance
ESR	Equivalent Series Resistance
FCC	Federal Communications Commission
FDTD	Finite Difference Time Domain Method
FEM	Finite Element Method
FFT	Fast Fourier Transform
FIT	Finite Integration Technique
FMM	Fast Multipole Method
FR	Flame Resistant
GND	Ground
HF	High Frequency (3 MHz – 30 MHz)
HFSS	High Frequency Structure Simulator (FEM Solver)
IBM	International Business Machines Corp.
IC	Integrated Circuit (or chip)

LF	Low Frequency (30 kHz – 300 kHz)
IFFT	Inverse Fast Fourier Transform
LGA	Land Grid Array
I/O	Input/output
ITRS	International Technology Roadmap for Semiconductors
MCM	Multi-Chip Module
MF	Medium Frequency (300 kHz – 3 MHz)
M-FDM	Multilayered Finite Difference Method
MIC	Microwave Integrated Circuit
MoM	Method of Moments
MTL	Multiconductor Transmission Line
PC	Personal Computer
PCB	Printed Circuit Board
PDN	Power Distribution Network
PEC	Perfect Electric Conductor
PEEC	Partial Element Equivalent Circuit Method
PI	Power Integrity
PMC	Perfect Magnetic Conductor
PML	Perfectly Matched Layer
PWR	Power
RAM	Random Access Memory
RE	Radiated Emissions
RLC	Resistance-Inductance-Capacitance
RW	Radial Waveguide
RW-IT	Radial Waveguide – Image Theory
SDN	Signal Distribution Network
SHF	Super High Frequency (3 GHz – 30 GHz)
SI	Signal Integrity
SLF	Super Low Frequency (30 Hz – 300 Hz)
SMA	Sub-Miniature version A
SMT	Surface Mount Technology
SoC	System on Chip

SoP	System on Package
SPICE	Simulation Program with Integrated Circuit Emphasis
SSN	Simultaneous Switching Noise
TEM	Transverse Electromagnetic
TET	Institut für Theoretische Elektrotechnik, TUHH
TL	Transmission Line
TLM	Transmission Line Matrix Method
TM	Transverse Magnetic
TMM	Transmission Matrix Method
TSV	Through-Silicon-Via
TUHH	Technische Universität Hamburg-Harburg
TV	Test Vehicle
UHF	Ultra High Frequency (300 MHz – 3 GHz)
ULF	Ultra Low Frequency (300 Hz – 3 kHz)
VHF	Very High Frequency (30 MHz – 300 MHz)
VLF	Very Low Frequency (3 kHz – 30 kHz)
VRM	Voltage Regulator Module
Z_{pp}	Parallel-Plate Impedance

Throughout this work, board dimensions are given in inches and mils, which are the typical units used in the electronic industry. The conversions to SI units are as follows:

1 inch $\approx 2.54 \cdot 10^{-2}$ m

1 mil = 0.001 inch $\approx 25.4 \cdot 10^{-6}$ m

1. Introduction

1.1. Motivation and Context of this Work

According to the international technology roadmap of semiconductors (ITRS) [1], which summarizes the state of the art development of the semiconductor industry, the demands of compact high-speed electronic systems with higher bandwidth and lower power consumption have been continuously increasing in the past decades. The trend of digital and analog system convergence and miniaturization has led to evolutions of advanced packaging technologies such as system-on-chip (SoC), multichip modules (MCM), and system-on-packages (SoP) [2]-[4], which imposes new challenges in the electrical design and modeling methodologies due to the growing system complexity. A glance over the complexity of an exemplary IBM high-performance printed circuit board (PCB) is given in Fig. 1.1, where the board is populated with thousands of via pins, decoupling capacitors (decaps), and connector pins. On the other hand, the data rate and bandwidth requirement of off-chip interconnects continue to grow in order to meet the needs of advanced inter-module communications and multicore architectures [5]. For instance, 25 Gigabit per second (Gb/s) on-board signaling has been evaluated in [6]. As a consequence, the signal bandwidth of digital systems has been expanded to the multi-GHz microwave regime, as shown in Fig. 1.2, where the spectrum of digital system overlaps the frequency range of microwave circuits [7]. The electromagnetic phenomena become more complex at higher frequencies making many simplifications in conventional EDA tools invalid or inaccurate [8].

According to ITRS, the major challenges for simulation and modeling include rapid turn-around simulation and system-level electrical design associated with high frequency and low voltage switching. The ITRS also specifies an accuracy requirement for modeling and simulation technologies as such that the package delay accuracy should be lower than 1% of the inverse of off-chip clock frequency. This accuracy may be provided by general purpose full-wave methods. However, they usually suffer from extensive computation time and high resource demands. Conversely, static or quasi-static solutions are in general efficient but fail to account for high frequency electromagnetic effects. Development of advanced modeling techniques requires fulfilling both requirements of high efficiency and high accuracy over a broadband frequency

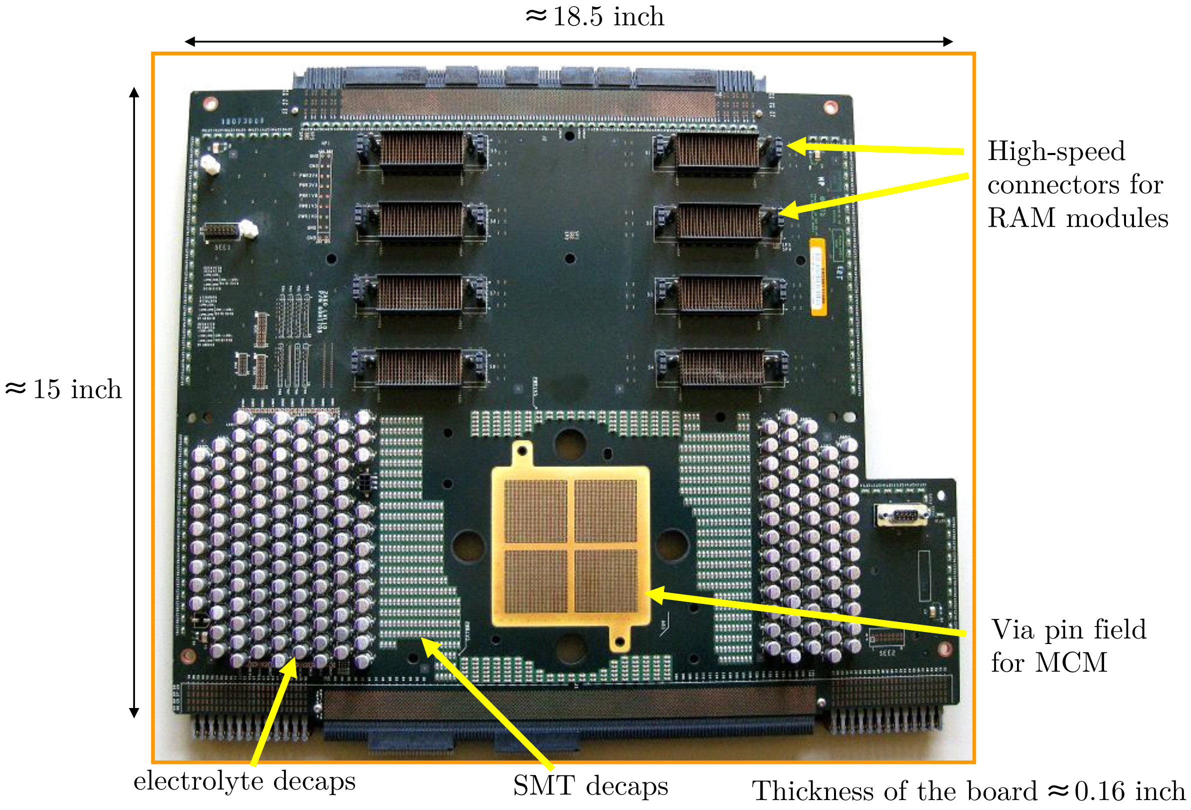

Figure 1.1 An exemplary IBM Power server board. (1 inch ≈ $2.54 \cdot 10^{-2}$ m) *Picture courtesy of IBM Germany Research and Development GmbH, Böblingen, Germany.*

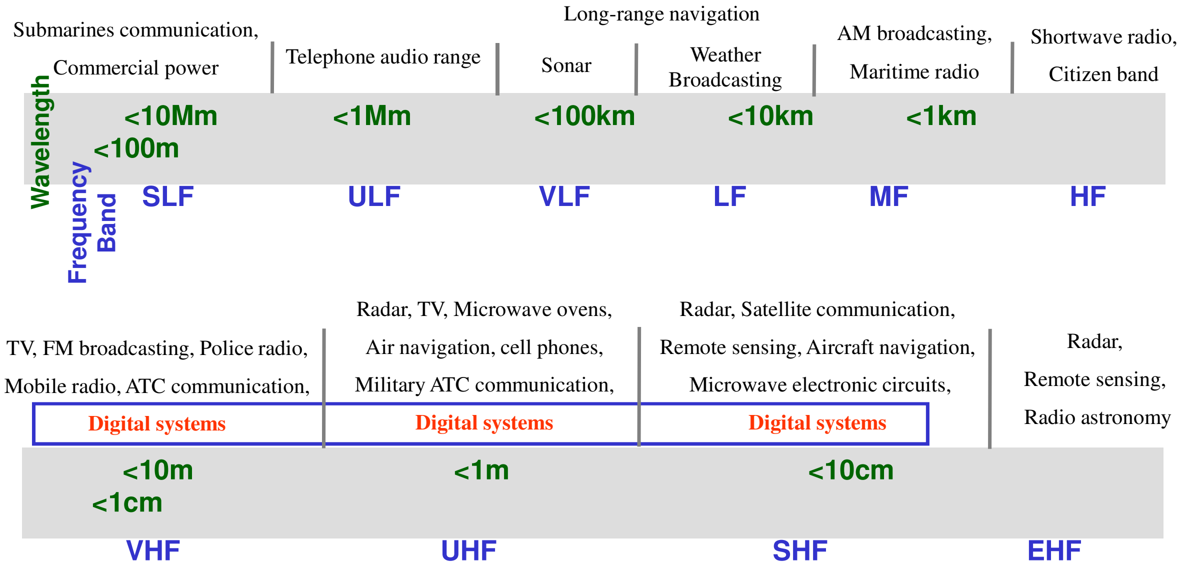

Figure 1.2 Frequency bands and corresponding wavelengths of electronic systems [7]. Bandwidth of digital systems extends to microwave frequency range.

range, which is of primary importance to accelerate the electrical design and prototyping process. In this context, the objective of this thesis is to make a contribution to efficient and accurate modeling of planar structures in high-speed digital systems by the extension of the contour integral method (CIM) [9].

Planar structures, specifically power planes are widely used in today's electronic packages and printed circuit boards (PCBs), which is a key element of the power distribution network (PDN) to provide a low impedance path for the power supply and to reduce interferences between different functional blocks. Traditionally, electrical design of power planes concerns mainly the simultaneous switching noises (SSN) on the power supply. However, with the increased system complexity and signal bandwidth, the PDN domain becomes tightly coupled to the signal distribution network (SDN) and the radiation field. For example, noise induced by switching currents on vertical vias can propagate and crosstalk to other signal and power vias or radiate from board edges, raising signal integrity (SI), power integrity (PI), and electromagnetic interference (EMI) issues. Proper modeling of power planes is essential to all the above three aspects. Especially for SI, where power planes act as references and is part of the signal return path, modeling of them must cover the whole spectrum of the signal bandwidth that can span from DC to the microwave region.

CIM is a fast numerical technique that is suitable for analysis of arbitrarily shaped planar structures, making it also a promising candidate for the task of power plane analysis. The extension of CIM presented in this work aims at an improvement in its accuracy and efficiency when modeling power planes with cylindrical vias as well as the combination with other approaches to enable system level simulations for handling of relatively complex multilayer structures. The goal is also to cover the scope of all three respects of the electric design including SI, PI, and EMI.

1.2. Organization of the Work

The remaining chapters of this thesis are organized as follows.

Chapter 2 reviews the function and role of power planes in SI, PI, and EMI. The excitation and propagation of cylindrical radial waves in the planar direction are illustrated. An example of a rectangular board is analyzed using a full-wave solver and the distributive behavior of power planes will be discussed. State of the art methods for modeling and simulation of power planes are reviewed in the last section. The definition and assumptions made for planar structures are clarified and the validity of the 2D assumption for power/ground plane pairs is discussed.

Chapter 3 presents a brief introduction to CIM including the basic formulation, the numerical procedure, and some salient features for retrieving of the field information. Particular attention is paid to the numerical modeling of circular ports that are needed for analysis of vias. The rectangular board example in chapter 2 is repeated using CIM and compared to full-wave results. Limitations of the method and motivations for extensions are listed at the end of the chapter.

Chapter 4 discusses the extension of CIM using analytical solutions for circular ports in order to improve its efficiency and accuracy, especially at high frequencies. Expressions for both isotropic and anisotropic modes are derived, first by assuming infinite planes, and then by combination with boundary line ports to form solutions for finite planes. Validation examples will be provided at the end of each section and the efficiency improvement will be briefly discussed.

Chapter 5 explains the hybridization of CIM with other approaches including equivalent circuits, the method of moments (MoM), and the physics-based via model. The fact that CIM represents a closed planar region surrounded by microwave ports allows it to be easily networked with other methods. Connection of CIM to one-port circuits, such as decoupling capacitors, is first presented, followed by the inclusion of radiation loss by hybridization with MoM. Finally, combination with the physics-based via model for simulations of multilayer substrates is described, which can be used to generate results in all perspectives of SI, PI, and EMI.

Chapter 6 provides a variety of application examples using the extended CIM. A set of pre-defined power/ground plane pair configurations is first analyzed to assess the efficiency and applicability of the method to complex shape power planes. Next, examples of multiplayer PCBs are presented and results concerning SI, PI, and EMI are shown. Application to dense via arrays ensues and the resolution of potential passivity problems is discussed.

Chapter 7 summarizes the most important results of this thesis. The contributions are briefly reviewed and some remarks concerning further developments of the method are given.

1.3. Conference and Journal Contributions

During this work, five conference [10]-[14] and one journal [15]-[17] publications have been made. They constitute a major part of this thesis and most of their content will appear in this work with explicit references.

2. Modeling of Planar Structures in Digital Systems

This chapter reviews functions of planar structures, in particular power planes, in digital systems with respect to signal propagation, power supply, and radiated emissions. As the signal bandwidth of digital systems stretches out further into the microwave spectrum, power planes appear to be electrically larger in their planar extents and exhibit distributive behavior. Thus, their modeling requires the consideration of electromagnetic wave propagations. Characteristics of wave phenomena within a pair of power/ground planes are demonstrated. A survey of state-of-the-art modeling methods is provided.

Nevertheless, the third dimension of today's power plane configurations remains electrically small, which allows us to regard them as planar circuits. Methods that were originally devised for planar circuit analysis can be in principle adjusted to power plane modeling. The definition of planar circuits, which are universally found in microwave component designs, and the assumptions made for power planes are briefly discussed.

2.1. Power Planes in Electronic Packages

2.1.1. Function for Power Delivery

Power planes belong to a part of the PDN that supplies voltage and current to integrated circuits (ICs). Typical components of a PDN include the voltage regulator module (VRM), decoupling capacitors (decaps), power/ground planes and other interconnections such as power vias, bonding wires, C4 bumps, etc., as depicted in Fig. 2.1. A successful power delivery requires an instantaneous supply of sufficient charge from the DC power source to the switching transistors on chip. Managing the path between them is the task of the PDN design [18],[19].

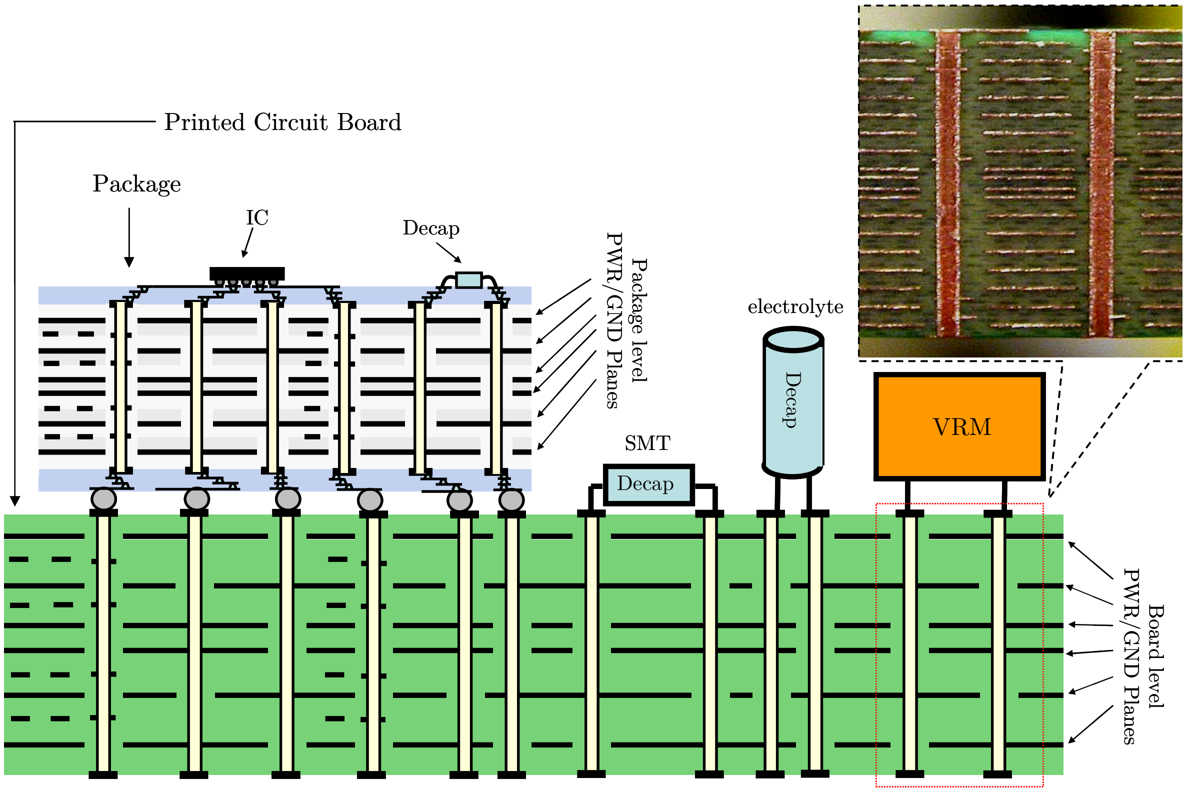

Figure 2.1 Illustration of a power delivery network that consists of VRM, decaps, and power planes. *Picture of PCB cross section courtesy of IBM Research, Yorktown Height, NY, USA.*

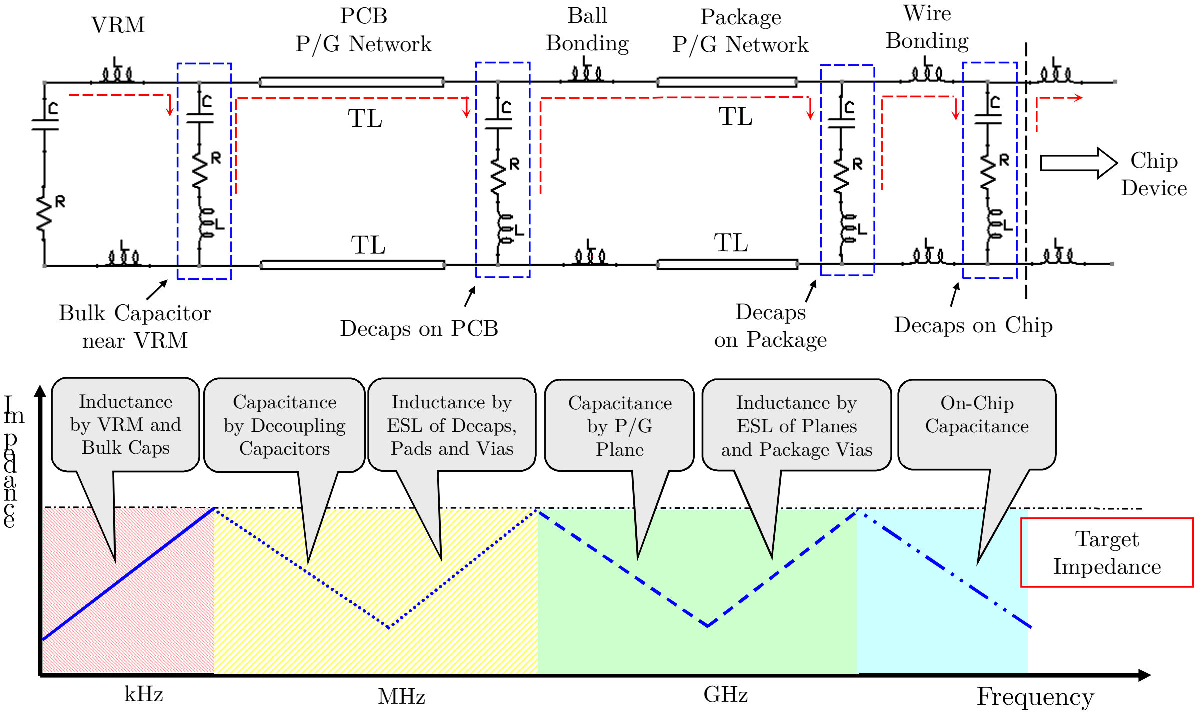

Figure 2.2 Equivalent circuit illustration of a power delivery hierarchy and its input impedance. Figure adapted from [18].

Since VRMs operate typically in the kilohertz (kHz) range, in comparison to multi-Gigahertz (GHz) frequencies, at which modern ICs switch, the VRMs are unable to respond to the transient current surges that the transistors demand. In addition, due to the physical separation between the VRM and ICs, parasitic inductances of the interconnections are inevitable, which increases the time delay for the charge to reach the switching transistors. Immediate charge deficiency can cause the power voltage level to ripple and the generation of SSN [20]. Both of the effects are detrimental to the system operation [21]. Therefore, decaps are commonly used in the PDN design to provide extra charge reservoirs, which supply currents to transistors during the switching cycles and recharging in the remaining cycles [22]. Since the speed at which decaps react to current changes is determined by the proximity of them to the transistors and the parasitics along the path, on-chip decaps are the fastest charge supply while the package decaps slower and the board decaps the slowest. On the other hand, due to the limitation of the real estate, the storage capacity of them is in a reversed order with board decaps the largest and on-chip decaps the smallest. Hence, a PDN is laid out in a hierarchical fashion, as shown in Fig. 2.2 (top), where the charge is relayed by capacitances at different package levels to ensure sufficient current supply to ICs at any time instant, when designed correctly [23],[24]. This picture can be translated to a target impedance concept in the frequency domain [18], where each PDN level is responsible for maintaining the impedance profile over a finite frequency band, as shown Fig. 2.2 (bottom). Using the target impedance concept allows the design of each PDN level individually and then cascading them together [25].

In the power delivery domain, one obvious advantage of using power planes is the reduction of parasitic resistances and inductances of the interconnections between different PDN elements. Also, the capacitance between power and ground planes serves as an extra bypassing capacitance that enhances the decoupling capacity. Although high frequency noise becomes more and more of an issue because of the parallel-plate waveguide mode propagation in the cavity formed by a pair of power/ground planes, solid planes are still the preferred strategy in modern electronic systems since they bring many benefits not only for the power supply but also for the signal transmission and the compliance with the electromagnetic compatibility (EMC) standards. They will be discussed in the next section.

2.1.2. Function for Signal Transmission and EMI Mitigation

The communication among different chip sets, such as processors, memories, optical modules, etc., is realized through off-chip interconnects between I/O circuitries. To ensure a sufficient signal fidelity and timing margin for proper functioning of the circuits, SI analysis is usually performed, which has undergone a significant development in the past few years [26]-[28]. Due to increased data rates, the signal links between drivers and receivers on PCBs or MCMs become electrically long, and thus, need to be treated as transmission lines (TLs). The signal traces in modern digital systems are almost exclusively designed as striplines or microstrips [28], for which the power planes serve as a part of the current return path and ensure a uniform TL mode across the reference plane. In addition, the power planes behave as shields preventing crosstalk between different signal layers by virtue of the skin effect; for example, a copper plane has a skin depth of about 2 micrometers (μm) at 1 GHz.

High speed signals experience many types of degradation in the passive channel such as frequency dependent conductor and dielectric losses, reflections from discontinuities and terminations, crosstalk from neighboring traces, and other noise sources. A proper characterization of these effects in the frequency domain is the premise of a reliable time domain analysis [29]. Although the electromagnetic fields of stripline and microstrip modes are distributed in a confined region near the TLs, discontinuities are usually not avoidable such as the vertical via transitions that induce and receive noises from the PDN by wave propagations in between power planes, which makes them an indispensable part of the signal net. Therefore, modeling of power planes has a major significance also to SI analysis.

The task of EMI/EMC design is to enhance the capability of preventing electronic devices from electromagnetic (EM) emissions and their immunity to external interferences [30]. The general EMI/EMC field is rather a broad discipline that covers issues in SI and PI regimes. In the context of this work, it is specific to an electronic system in a holistic perspective and deals with emission and susceptibility problems of the complete system that are otherwise not the subject of SI and PI. The EM emissions, either conducted or radiated, are regulated by government bodies, such as the Federal Communication Commission (FCC) in the United States and the International Special Committee on Radio Interference (CISPR) in the European Union [7]. Electrical designs with EMI/EMC awareness are of primary importance since no product can be released without the compliance to the standards.

In the early 90s while clock frequencies were mostly below 25 MHz, emissions came primarily from the attached cables since most wavelengths were long compared to the actual product [31]. Little emission was observed above 1 GHz, up to which the standards were specified [7]. Hence, early EMI/EMC engineering concerns mainly chocking and filtering common mode current from escaping the system. Today's digital systems operate in the GHz range and transmit data at several Gb/s making the product itself a potentially good antenna. Expansion of the testing spectrum to 10 GHz has been considered in the EMC standardization community [31]. Measures such as suppression of emission sources, filtering, differential signaling, and careful grounding

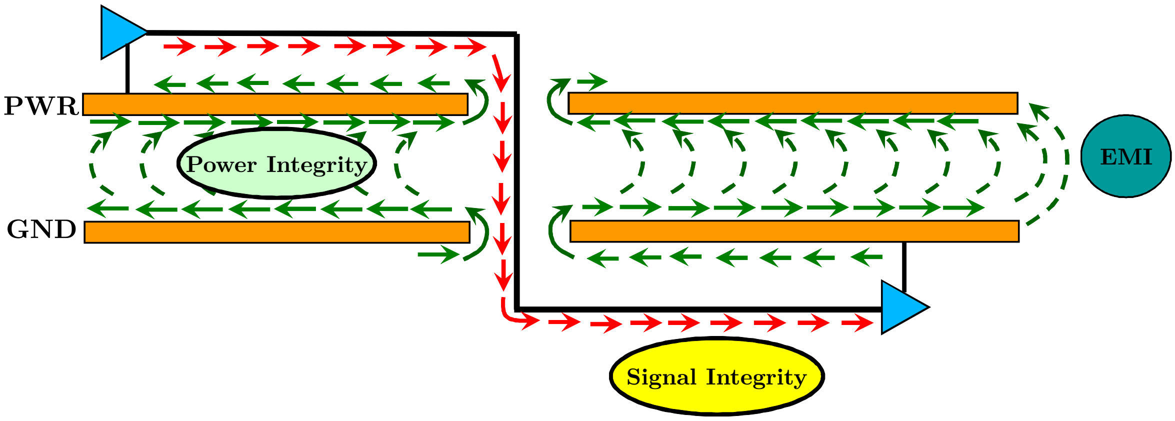

Figure 2.3 Current path and electromagnetic interaction among SI, PI, and EMI in a power/ground plane pair environment. Conduction currents (solid arrows) of the signal return between power planes in the form of distributed currents (dashed arrows) that induce noise interferences with the power supply and cause radiated emissions.

have been taken to improve EMC [31]-[34]. New concepts such as the electronic band gap structures have been introduced for suppression of the high frequency common mode noise [35].

Power planes can help reduce EM emissions and enhance system immunity, since they act as fences that restrain the radiations from internal traces and circuits and at the same time prevent the penetration of external noise into the system. However, radiated emissions can still be produced, especially at resonance frequencies of the power planes. The emission source could be traced back as far as noise generated in ICs and conducted to transition vias, which further travels down to the power plane edges and radiates from there. Since suppression at the noise source is not always feasible, proper designs of power planes and decap populations become critical to the EMI/EMC engineering, which in turn emphasizes the importance of power plane modeling in this field.

An illustration of how a pair of power/ground planes interacts with the signal net, the PDN, and the radiation field is depicted in Fig. 2.3. Due to the discontinuity at the via transition, the signal return current is distributed over the inner surfaces of the power planes causing noise propagation in the form of parallel-plate modes. This noise can be injected into the PDN or radiated from the edges. Conversely, external fields can couple through the board edge or the presence of SSN from other sources can spread out through the parallel-plate modes and eventually interfere with the signal net. The pair of power/ground planes is the link among the three issues.

2.1.3. Radial Wave Propagation in a Parallel-Plate Environment

The root cause of noise in a pair of power planes is attributed to its parallel-plate configuration that supports radial wave propagation. Since the source of the radial waveguide modes excitation is the via current flowing in the *z*-direction, only TM^z modes exist with $\mathcal{E}_x = \mathcal{E}_y = \mathcal{H}_z = 0$, as shown in Fig. 2.4, where $\mathcal{E}$ and $\mathcal{H}$ are the electric and magnetic field, respectively. The general solution for the *z*-component of the electric field for an outward traveling TM^z_{mn} wave is given in [36],[38],

$$\mathcal{E}_z^{mn}\left(r,\phi,z\right) = -jB_{mn}\frac{k_r^2}{\omega\mu\varepsilon}H_m^{(2)}\left(k_r r\right)\cdot\begin{Bmatrix}\cos\left(m\phi\right)\\ \sin\left(m\phi\right)\end{Bmatrix}\cdot e^{-jk_z z}\quad (n,m=0,1,2,\ldots), \tag{2.1}$$

with

$$k_z = \frac{n\pi}{d}, \tag{2.2}$$

$$k_r = \sqrt{\omega^2\mu\varepsilon - k_z^2}, \tag{2.3}$$

where $H_m^{(2)}$ represents the *m*-th order Hankel function of the second kind, B_{mn} is a constant, and *m* and *n* represent the mode order with respect to variations in ϕ- and *z*-direction, respectively. *d* is the height of the dielectric medium between the power planes. ω denotes the angular frequency. μ and ε are the permeability and permittivity of the medium, respectively. For $n \geq 1$, the TM^z_{mn} modes have a cutoff frequency [37]

$$\left(f_c\right)_{mn}^{TM^z} = \frac{n}{2d\sqrt{\mu\varepsilon}}. \tag{2.4}$$

For a typical power plane pair with d = 10mil, $\mu = \mu_0$, and $\varepsilon = 4\cdot\varepsilon_0$, the cutoff frequency of the first higher order (n = 1) mode is above 300 GHz, far beyond the bandwidth of today's digital systems. Therefore, only the fundamental mode (n = 0) is able to propagate. The higher order modes are evanescent and the fields associated with them can be considered as only local to the exciting via [36].

Due to the skin effect, high-speed signal currents are concentrated on surfaces of via barrels, which may be considered as an isotropic shell current, as shown in Fig. 2.5(a).

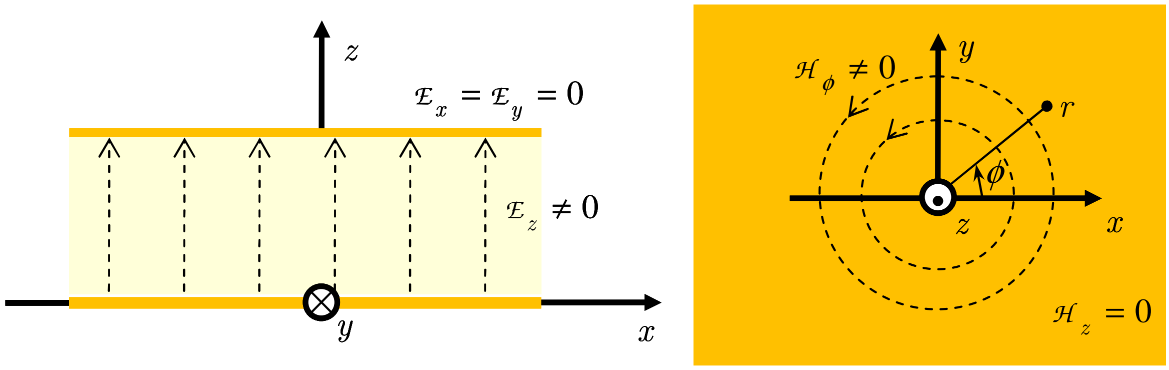

Figure 2.4 Illustration of coordinate systems and field elements of the fundamental TM^z mode. $\mathcal{E}_z$ and $\mathcal{H}_\phi$ are the tangential electric and magnetic fields, respectively.

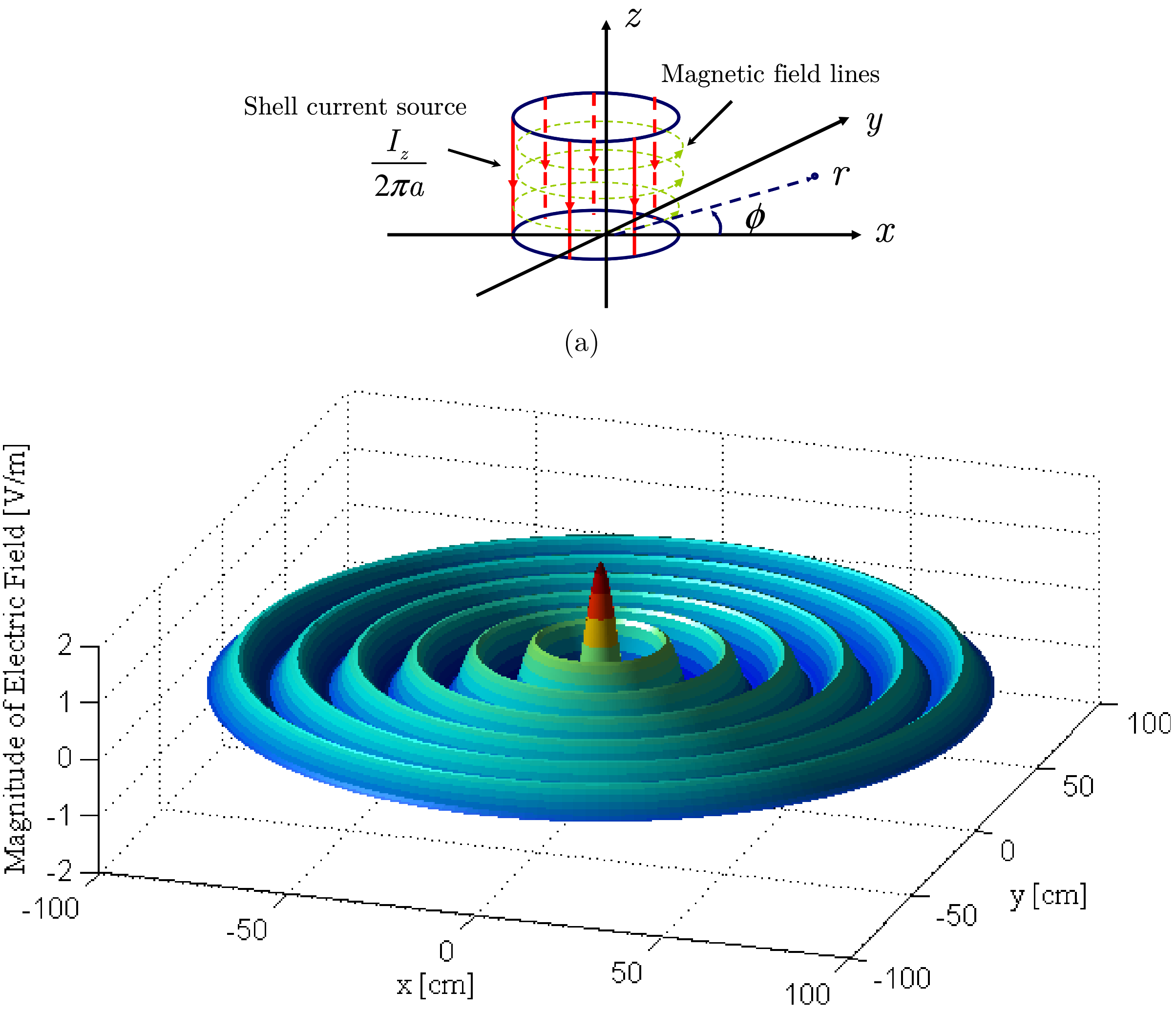

(a)

(b)

Figure 2.5 (a) Shell model of the via current. (b) Magnitude of the electric field of a radial wave at 1 GHz, excited by a 1 mA current shell with radius a = 5 mil in an infinite lossless parallel-plate environment with a relative dielectric constant of 4.0.

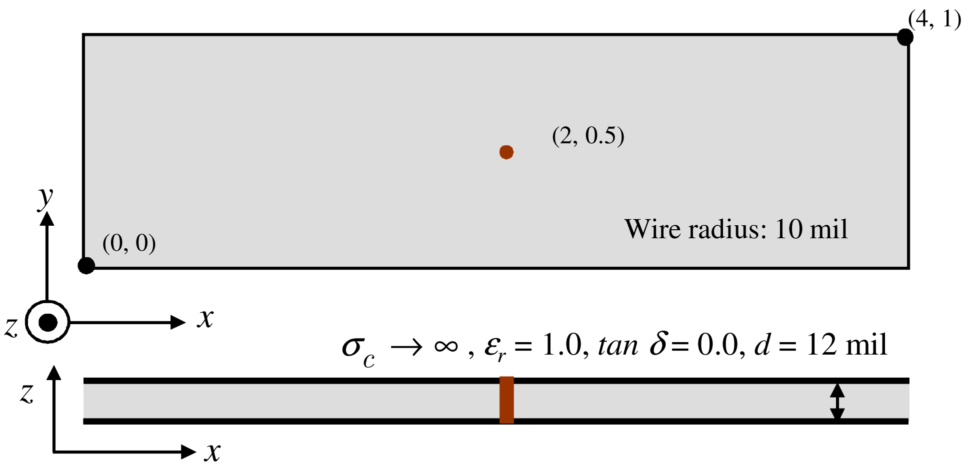

Figure 2.6 A rectangular board example consisting of a pair of perfect electric conducting (PEC) power/ground planes, excited by a cylindrical wire in the middle of the board. Dimensions are given in inches (1 inch 2.54 · 10^{-2} m).

For example, the skin depth of copper is about 20 μm at 10 MHz, much smaller than the board via radii, which are typically larger than 100 μm.

The solution of the radiation field from a shell current in an infinite parallel-plate environment can be found in [38],[39]. Fig. 2.5(b) plots the magnitude of the electric field distribution of a radial wave at 1 GHz, excited by a shell current of 1 mA in an infinite lossless parallel-plate environment with a relative dielectric constant of 4.0. The field pattern is similar to a cylindrical surface water wave [40]. The electric field first reduces its intensity rapidly in the vicinity of the source but only slowly ($\approx 1/\sqrt{r}$) in the far-field zone. This analysis manifests the fundamental noise propagation mechanism in power plane pairs and the fact that noise can spread out over the whole board area.

Notice that a lossless model is adopted here. In reality, the presence of conductor and dielectric losses as well as return vias will damp the wave and limit the noise propagation depending on the frequency.

2.1.4. Cavity Resonant Modes

Due the finite size and the open boundary of power planes, electromagnetic waves are mostly confined inside the cavity and form resonance modes [41],[42]. As an example, a rectangular 4-by-1 inch board excited by a wire current at the center is shown in Fig. 2.6. The cavity is assumed to be filled with air and the metal planes are of infinite conductivity. Magnitude and phase of the input impedance at the wire location

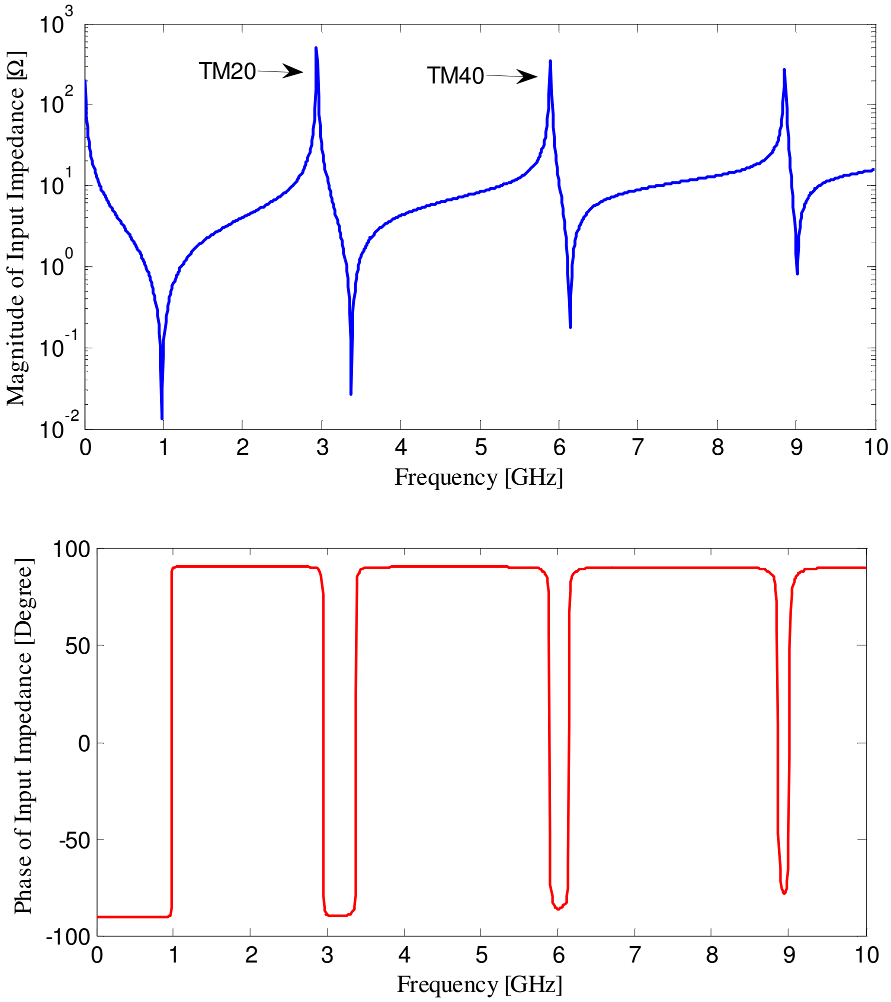

Figure 2.7 Magnitude and phase of the input impedance of the rectangular board in Fig. 2.6.

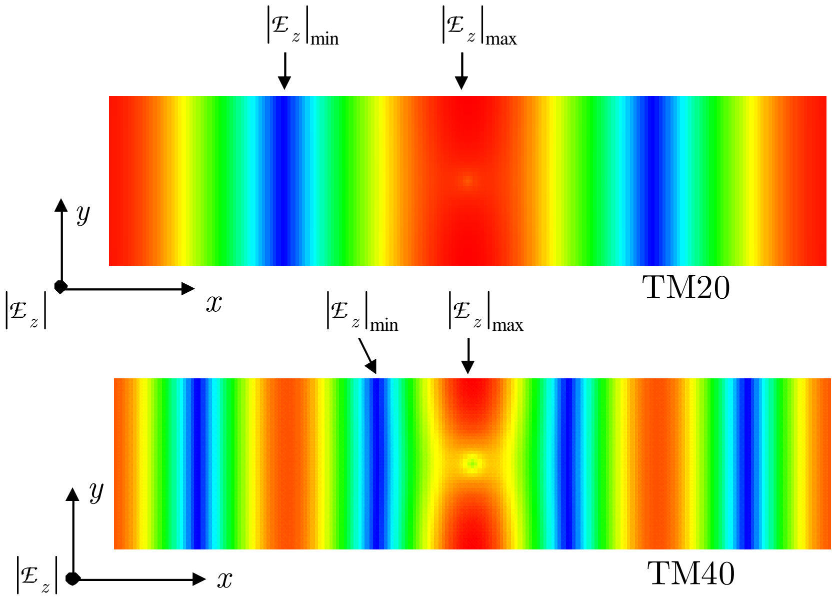

Figure 2.8 Electric field pattern of cavity modes of the rectangular board in Fig. 2.6.

simulated by a full-wave method of moments (MoM) solver [43] are plotted in Fig. 2.7. The impedance shows first a capacitive characteristic in the megahertz (MHz) range and then becomes inductive above 1 GHz. Cavity modes are formed at resonance frequencies such as the TM_{20} and TM_{40} modes at about 3 GHz and 6 GHz, respectively. For a pair of rectangular power planes, the resonance frequencies of TM_{mn} modes are given by

$$(f_r)_{mn} = \frac{1}{2\sqrt{\mu\varepsilon}} \sqrt{\left(\frac{m}{a}\right)^2 + \left(\frac{n}{b}\right)^2}, \tag{2.5}$$

where a and b are the board widths in x- and y-directions, respectively. Electric field distributions of the two modes are shown in Fig. 2.8. Noise induced at resonances is detrimental to the system operation. Its suppression may be realized by a proper design of decaps. However, due to parasitic inductances of decap interconnects, the effectiveness is limited to several GHz at maximum. Techniques for reducing resonances at high frequencies have also been proposed such as introducing losses, embedded capacitors, as well as electronic band gap structures [44]-[46].

2.2. State-of-the-Art Modeling Methods

A number of techniques has been proposed and applied to the modeling of planar structures and power planes in digital systems, which can be categorized as follows.

1. **Quasi-static solutions** – In early years when clock frequencies were still below 25 MHz, quasi-static analytical calculations were often used for performing frequency domain analysis of PDNs, where power planes were often approximated as simple capacitances [25]. Numerical quasi-static computations have also been performed, for example in [47]. Quasi-static solutions are limited though to electrically small structures and do not account for wave phenomena at high frequencies.

2. **General full-wave solvers** – A full-wave field solver is capable of solving Maxwell's equations without the quasi-static assumption at any given frequency or time. It is important when one must accurately account for displacement currents, electromagnetic radiations, and field coupling. Methods that fall into this category include, for example, the finite difference time domain method (FDTD) [48],[49] the finite element method (FEM) [50],[51] and the method of moments (MoM) [52]. Commercial tools based on the above methods are

available. Excellent accuracy and flexibility of full-wave methods, however, are often accompanied by massive resource demands and long computation times. Given the complexity of modern digital systems such as the one in Fig. 1.1, full-wave simulations are apparently too expensive when even feasible with today's computing power.

3. **2D numerical methods** – To overcome the resource and time hurdle of full-wave solvers, many 2D numerical approaches based on the planar circuit assumption (Section 2.3) have been proposed including e.g. the finite difference method (FDM) [53],[54], the contour integral method (CIM) [55],[56], the transmission matrix method (TMM) [57], and the transmission line matrix method (TLM) [58]. This class of methods offers reasonable efficiency while preserving the modeling flexibility of arbitrary planar structures.

4. **2D analytical formulas** – Further improvement of computational efficiency can be achieved by analytical formulations of specific 2D radiation problems. Examples of these algorithms are the radial waveguide method (RW) [59]-[63], the cavity resonator model (CRM) [64]-[66], and other improved formulations such as in [68]-[74]. Analytical formulas provide the best efficiency, but are restricted to simple structures such as infinite planes or regular shapes [75],[76].

5. **Equivalent circuits** – The development of equivalent circuits was inspired by the necessity of connecting package models to IC circuits that are mostly SPICE compatible models. Approaches in this category include the partial equivalent electric circuit method (PEEC) [77] and equivalent circuits derived from CRM [78],[79] as well as from quasi-static solutions [47]. The advantage of an equivalent circuit model is its compatibility to SPICE simulators that engineers are used to. However, it requires a fine grid granularity to capture transmission line effects at high frequencies and can also suffer from causality violation problems [80].

6. **Scattering methods** – General scattering methods are to some extend semi-analytical, which combine analytical solutions of cylindrical wave functions with the numerical computation for their interactions. The method based on foldy-lax equations can be found in [81],[82]. Other scattering methods have also been proposed in e.g. [83],[84]. In principle, scattering methods provide an accuracy comparable to full-wave solutions. However, it is difficult to handle finite power plane boundaries in this class of methods, and further, it does not distinguish propagating and non-propagating modes, which contributes to some redundancy in the numerical procedure.

7. **Segmented analysis** – By virtue of the microwave circuit theory and the segmentation technique [85]-[87] one may cut a system into blocks and analyze them separately. For example, different cavity models may be stacked together to generate a multilayer response, which is sometimes called a 2.5D approach. It allows us to combine the merits of different methods and choose the most appropriate approach for a specific element in the system. Abundant literature regarding this technique has been published in the past, for example [88]-[92].

This work focuses on the CIM, a 2D numerical method, based on the planar circuit assumption which is explained in the next section. More specifically, CIM has been extended in this thesis to include analytical expressions for circular ports for more efficient and more accurate modeling of cylindrical vias. Further, it has been combined with other efficient methods for simulating realistic applications of digital systems. The extension will explore the possibility of taking advantage of ideas behind techniques in category 4, 6, and 7.

2.3. Definition of Planar Circuits

The concept of a planar circuit was first introduced by Okoshi and Miyoshi [64],[93]. According to [93], microwave integrated circuits (MICs) can be classified into four categories: lumped elements (zero-dimension), uniform transmission lines (one-dimension), waveguides (three-dimension), and planar circuits (two-dimension). This classification is made by the number of dimensions that are comparable to the operating wavelength. A planar circuit has two dimensions extending longer than the wavelength, while the third dimension is a negligible fraction of the wavelength. The advantage of using this concept is that it reduces the modeling complexity and computational effort in comparison to a 3D full-wave model.

Since its introduction, the planar-circuit model has been applied to analysis of a wide variety of MICs and milli-wave integrated circuits (MMICs), such as microstrip antennas, couplers, matching networks [94]-[96], etc. In the early 90s, the concept has been ramified into the power plane analysis branch [65]. Due to rapid growth of the operating frequency of electronic systems, the planar dimensions of power planes can be comparable to or even many times long as the wavelength, whereas the third dimension (z-direction in the Cartesian or cylindrical coordinate overall in this work), specified by the distance between a pair of neighboring planes, remains electrically small. Take a PCB power/ground plane pair filled with the FR4 dielectric with a relative permittivity of 4.0 as an example, a typical cavity height of 10 mil corresponds to a quarter wavelength at a frequency of approximately 150 GHz, which is still far beyond the spectrum of modern digital systems. For instance, the content of a signal at a data rate of 20 Gb/s with 1 picosecond (ps) rise/fall time is below -20 dB when the frequency exceeds about 50 GHz [97]. Hence, the planar assumption of power planes is well justified for practically all digital applications.

2.4. Summary

Power planes will continue to be an important design practice of digital systems. They are an indispensable part of the signal link path, the PDN, and the EMC. In recent years, co-analysis of SI and PI has drawn more attentions in both the industry and the academia [98]. On top of that, additional capability of the EMI prediction has also been in consideration [31]. Furthermore, the advance of the semiconductor industry prompts electrical designs of even lower target impedances, smaller bit error rates (BERs), and less radiated emission over a broader frequency bandwidth. It has imposed greater challenges on the accuracy and efficiency of power plane modeling.

3. CIM – the Contour Integral Method

The contour integral method (CIM), a 2D numerical technique, was originally developed for analysis of arbitrarily shaped microwave planar circuits [9]. The method is based on a 2D integral equation derived from the scalar Green's theorem [93] and Weber's solution for cylindrical waves [99]. This chapter discusses the basics of CIM and its application to power plane analysis. The formulation of the numerical procedure is first introduced. Holes and cut-outs inside the power plane are considered intrinsically as part of the power plane boundary. Modeling of the cylindrical via ports can be realized by approximating them as polygons [100].

A distinctive feature of CIM is its ability to provide field information, as has been presented in [55]. This is particularly useful for analysis of power integrity and radiated emission problems. The computation of the cavity electric field distribution and the far-field radiation pattern will be addressed.

Limitations of the method will be discussed in the later sections and they serve as motivation for the extension of the method in next chapters.

3.1. Basic Formulation

Figure 3.1 shows a complex shaped power plane pair with the contour S, consisting of C the boundary contour of the planes and C' the contour of via barrels. Note that C encloses the boundary contour of both the external plane edge in a counterclockwise direction and the cut-out area in clockwise direction. $\boldsymbol{r}$ and $\boldsymbol{r}'$ are the observation and source points on S. $\hat{\boldsymbol{n}}'$ and $\hat{\boldsymbol{t}}'$ denote the unit normal and tangential vector. The normal vector is defined such that it always points away from the plane area. Neglecting field variation in z-direction results in a TM-mode field distribution with $\mathcal{E}_x = \mathcal{E}_y = \mathcal{H}_z = 0$. Therefore, the electric field between the planes $\mathcal{E}_z(\boldsymbol{r})$ satisfies the 2D scalar Helmholtz equation. Provided that the medium between the metal planes is homogeneous and applying the scalar Green's theorem with assistance of the 2D cylindrical wave solution, a contour integral equation [9] can be written as

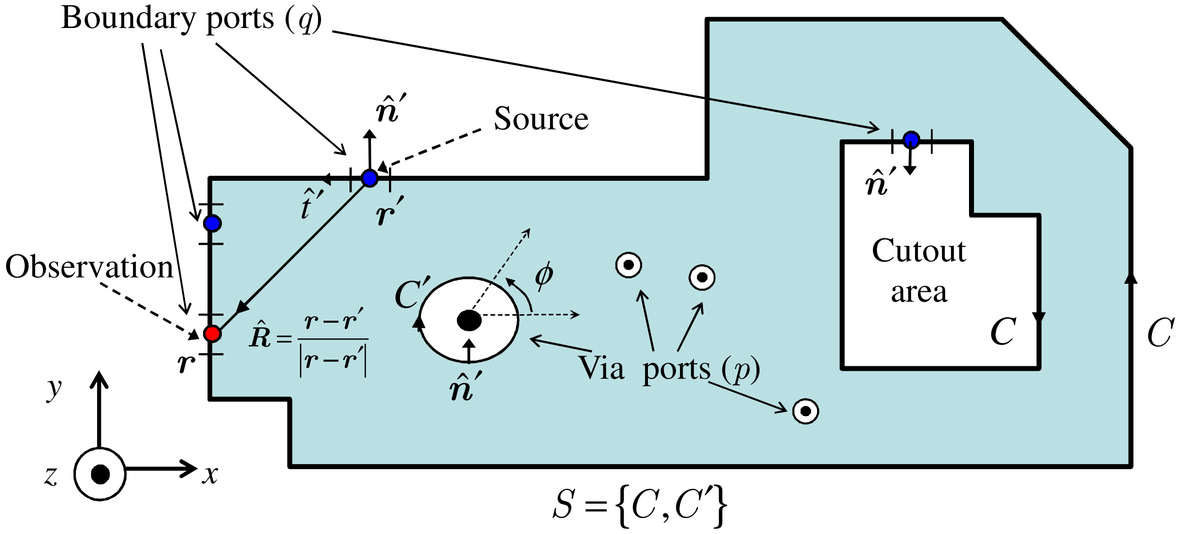

Figure 3.1 Computation domain and variable definition for the contour integral method. $\boldsymbol{r}$ and $\boldsymbol{r}'$ are the observation and source points on the contour S, which includes the plane boundary C and the via boundary C'. $\hat{\boldsymbol{n}}'$ and $\hat{\boldsymbol{t}}'$ denote the unit normal and tangential vectors on S, respectively.

$$\mathcal{E}_z(\boldsymbol{r}) = jF(\boldsymbol{r}) \oint_S \left[\frac{\partial H_0^{(2)}\left(k|\boldsymbol{r}-\boldsymbol{r}'|\right)}{\partial n'} \mathcal{E}_z(\boldsymbol{r}') - H_0^{(2)}\left(k|\boldsymbol{r}-\boldsymbol{r}'|\right) \frac{\partial \mathcal{E}_z(\boldsymbol{r}')}{\partial n'} \right] ds', \tag{3.1}$$

where $H_0^{(2)}$ is the zero-order Hankel function of the second kind. Some important properties of Bessel and Hankel functions are summarized in Appendix A.1. $|\boldsymbol{r}-\boldsymbol{r}'|$ is the distance between source and observation point. k is the complex wavenumber including dielectric and ohmic losses, defined as [64]

$$k = \omega\sqrt{\mu_0 \varepsilon_d}\left(1 - j\left(\tan\delta + t_s/d\right)/2\right) \qquad \left(t_s \le t_p\right) \tag{3.2}$$

with ε_d the dielectric permittivity, $\tan\delta$ the dielectric loss tangent, d the dielectric thickness, and $t_s = \sqrt{2/\omega\mu_0\kappa_c}$ the conductor skin depth, where ω denotes the angular frequency, μ_0 is the free space permeability, and $\kappa_c \approx 5.8\cdot 10^7$ S · m^{-1} is the conductivity of the copper planes. Here, the same metal is assumed for both the upper and lower plane with a thickness of t_p. Typical values of t_p range from 20 to 40 μm, and thus the loss model in (3.2) is applicable for frequencies above about 10 MHz for copper planes. The derivation of (3.2) is explained in [64]. The factor $F(\boldsymbol{r})$ depends on the position of the observation point [9],[101].

$$F(\boldsymbol{r}) = \begin{cases} 1/4, & \text{if } \boldsymbol{r} \text{ inside the contour,} \\ 0, & \text{if } \boldsymbol{r} \text{ outside the contour,} \\ 1/2, & \text{if } \boldsymbol{r} \text{ on a smooth contour.} \end{cases} \tag{3.3}$$

Equation (3.1) simplifies the complex 2D wave propagation problem to a line integral. One may consider (3.1) as corresponding to the Huygens equivalence principle [36], which states that the fields in a source-free region can be determined if the tangential electric and magnetic fields are completely known over a closed boundary.

Since only the boundaries of the power planes need to be considered, the modeling and computation effort can potentially be reduced. Combining (3.1) with the following relations [9]:

$$\frac{\partial \mathcal{E}_z(\boldsymbol{r}')}{\partial n'} = j\omega\mu_0 \mathcal{H}_{\tan}(\boldsymbol{r}'), \tag{3.4}$$

$$\frac{\partial H_0^{(2)}(k|\boldsymbol{r}-\boldsymbol{r}'|)}{\partial n'} = -\hat{\boldsymbol{R}} \cdot \hat{\boldsymbol{n}}' k H_1^{(2)}(k|\boldsymbol{r}-\boldsymbol{r}'|), \tag{3.5}$$

where $\hat{\boldsymbol{R}}$ represents the normalized vector of $\boldsymbol{r}' - \boldsymbol{r}$, as shown in Fig. 3.1. $H_1^{(2)}$ is the first order Hankel function of the second kind. $\mathcal{H}_{\tan}(\boldsymbol{r}')$ denotes the tangential magnetic field on a source point. Substituting (3.4) and (3.5) into (3.1), one obtains

$$\mathcal{E}_z(\boldsymbol{r}) = -jF(\boldsymbol{r}) \oint_S \left[k\hat{\boldsymbol{R}} \cdot \hat{\boldsymbol{n}}' H_1^{(2)}(k|\boldsymbol{r}-\boldsymbol{r}'|) \mathcal{E}_z(\boldsymbol{r}') + j\omega\mu_0 H_0^{(2)}(k|\boldsymbol{r}-\boldsymbol{r}'|) \mathcal{H}_{\tan}(\boldsymbol{r}') \right] ds'. \tag{3.6}$$

3.2. Numerical Procedure and Line Ports

For the numerical procedure to solve (3.6), the contour C is discretized into M segments with their widths W much smaller than the wavelength (usually a tenth of the wavelength $\lambda/10$). Each of the segments can be considered as a discrete line port. The boundary of each of the N via ports in the contour C' is approximated with L line segments. The tangential electric and magnetic fields are assumed to be constant over the segments and pulse basis functions can be used, as shown in Fig. 3.2. Over each line port, voltage and current definitions are established as

$$V = \mathcal{E}_z \cdot d, \tag{3.7}$$

$$I = \mathcal{H}_{\tan} \cdot W, \tag{3.8}$$

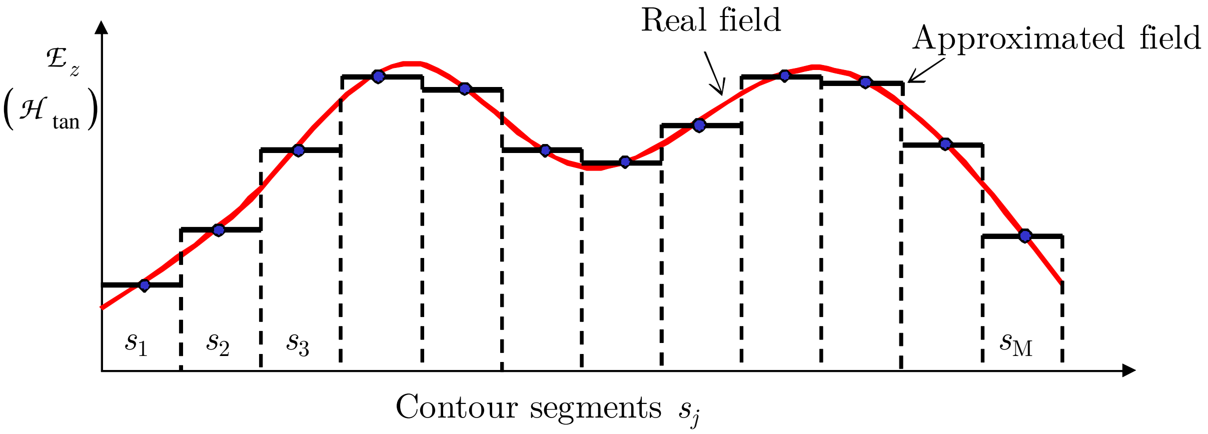

Figure 3.2 Pulse basis functions approximating a tangential electric (magnetic) field distribution.

where $\mathcal{H}_{\tan}$ is in the direction of $\hat{\boldsymbol{t}}'$ and I is the total port current flowing into the power plane region. The complex power transmitted through the line port is determined by

$$P = \frac{1}{2} V I^* = \frac{1}{2} \mathcal{E}_z \mathcal{H}_{\tan}^* A, \tag{3.9}$$

where $A = Wd$ is the port area and the asterisk * denotes the complex conjugate. This definition is consistent with a general microwave port definition [102].

Subsequently, one can write (3.6) for all the line ports in an equation system as

$$V_i = \frac{k}{j} F(\boldsymbol{r}) \sum_{j=1}^{M+L\times N} V_j \int_{s_j} \hat{\boldsymbol{R}} \cdot \hat{\boldsymbol{n}}' H_1^{(2)}\left(k\left|\boldsymbol{r}_i - \boldsymbol{r}_j\right|\right) ds_j + \omega\mu_0 d F(\boldsymbol{r}) \sum_{j=1}^{M+L\times N} \frac{I_j}{W_j} \int_{s_j} H_0^{(2)}\left(k\left|\boldsymbol{r}_i - \boldsymbol{r}_j\right|\right) ds_j,$$
$$\left(i = 1, \ldots, M + L\times N\right), \tag{3.10}$$

where the indices i, j denote observation and source line ports, respectively. The factor $F(\boldsymbol{r})$ here takes exclusively the value of 1/2, since the discretization is carried out so that observation points lie only on smooth contour segments.

One may interpret (3.10) as a 2D radiation field that is generated by multiple current and voltage sources on S. The radial wave pattern from a current source has been discussed in chapter 2 and illustrated in Fig. 2.5. Since usually the boundary contour C is subject to an open boundary condition, only voltage sources exist on C. The electric field pattern of a radial wave generated by a 1.5-cm wide line voltage source is depicted

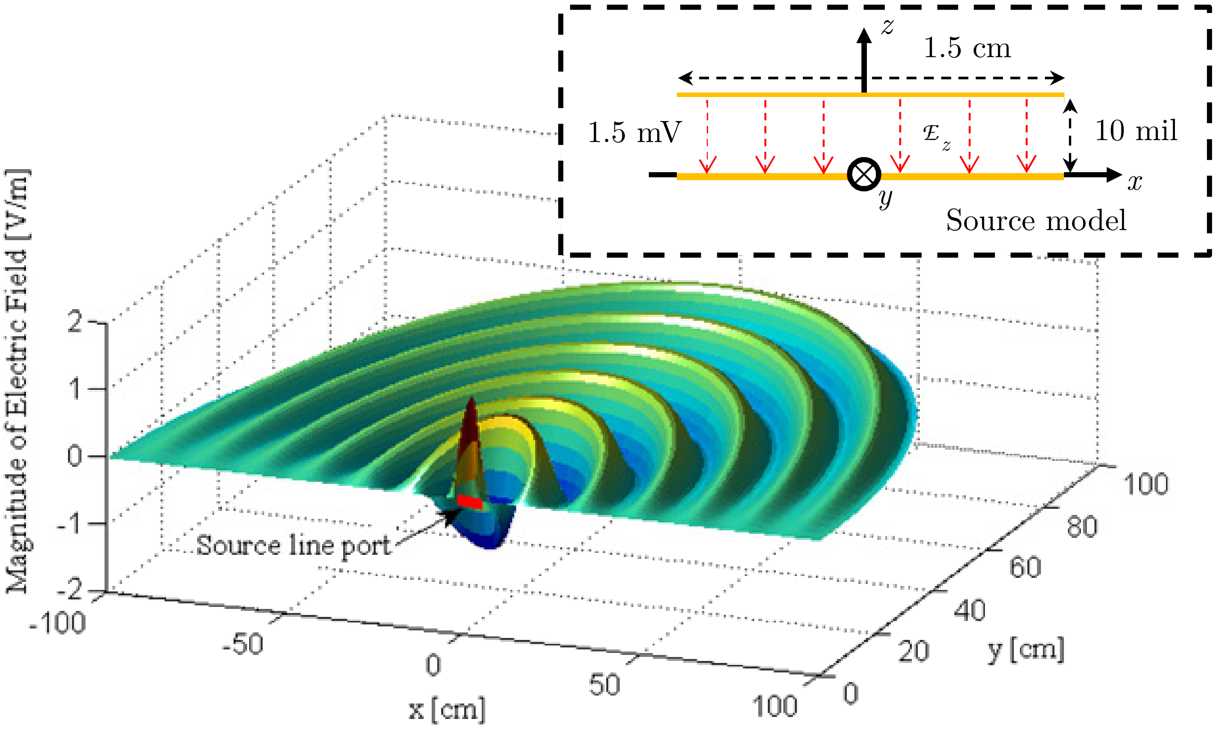

Figure 3.3 Magnitude of the electric field distribution at 1 GHz excited by a 1.5 cm wide voltage line port of 1 mV with regard to a lossless cavity of dielectric height of 10 mil and relative permittivity of 4.0. The source port is oriented in the x-axis with its center at the coordinate origin. The radiation field shows maxima on the y-axis and zero fields on the x-axis.

in Fig. 3.3. The field distribution is produced by exciting a 1 mV line source, oriented in the x-axis, in a lossless cavity with a dielectric height of 10 mil and the relative permittivity of 4.0. In contrast to the isotropic form of a current source radiation, the field pattern of a voltage line source exhibits the property of directivity with maxima at locations perpendicular to the source line and zero fields at positions aligned with the source line because of the $\hat{\boldsymbol{R}} \cdot \hat{\boldsymbol{n}}'$ term in the integral. Physically, the field pattern may be understood as the radiation field from a magnetic line current source [39].

In matrix form, the equation system (3.10) can be written as

$$\underbrace{\begin{bmatrix} \overline{\overline{U}}^{qq} & \overline{\overline{U}}^{qs} \\ \overline{\overline{U}}^{sq} & \overline{\overline{U}}^{ss} \end{bmatrix}}_{\overline{\overline{U}}} \cdot \begin{bmatrix} \overline{V}^{q} \\ \overline{V}^{s} \end{bmatrix} = \underbrace{\begin{bmatrix} \overline{\overline{H}}^{qq} & \overline{\overline{H}}^{qs} \\ \overline{\overline{H}}^{sq} & \overline{\overline{H}}^{ss} \end{bmatrix}}_{\overline{\overline{H}}} \cdot \begin{bmatrix} \overline{I}^{q} \\ \overline{I}^{s} \end{bmatrix} \tag{3.11}$$

where $\overline{V}^{q}$, $\overline{V}^{s}$ are unknown voltage vectors of sizes M and $N \times L$ on the contours C and C', respectively.

$$\overline{V}^q = [V_1, V_2, \ldots, V_M]^T, \quad \overline{V}^s = [V_{M+1}, V_{M+2}, \ldots, V_{M+L\times N}]^T, \tag{3.12}$$

and $\overline{I}^q$, $\overline{I}^s$ are the corresponding current vectors

$$\overline{I}^q = [I_1, I_2, \ldots, I_M]^T, \quad \overline{I}^s = [I_{M+1}, I_{M+2}, \ldots, I_{M+L\times N}]^T, \tag{3.13}$$

where T denotes matrix transpose. V_j and I_j are the corresponding j-th line port voltage and current, respectively, as defined in (3.7) and (3.8). The elements of matrices $\overline{\overline{U}}$ and $\overline{\overline{H}}$ in (3.11) are calculated as [64]

$$U_{ij} = \delta_{ij} - \frac{k}{2j} \int_{W_j} \hat{\boldsymbol{R}} \cdot \hat{\boldsymbol{n}}' H_1^{(2)}\left(k\left|\boldsymbol{r}_i - \boldsymbol{r}_j\right|\right) ds_j, \tag{3.14.a}$$

$$H_{ij} = \begin{cases} \dfrac{\omega\mu d}{2} \dfrac{1}{W_j} \displaystyle\int_{W_j} H_0^{(2)}\left(k\left|\boldsymbol{r}_i - \boldsymbol{r}_j\right|\right) ds_j & (i \neq j) \\ \dfrac{\omega\mu d}{2} \left[1 - \dfrac{2j}{\pi}\left(\ln\left(\dfrac{kW_i}{4}\right) - 1 + \gamma\right)\right] & (i = j), \end{cases} \tag{3.14.b}$$

where δ_{ij} is the Kronecker's delta and $\gamma = 0.5772$ is the Euler's constant. W_i and W_j are the widths of the i-th and j-th port, respectively. The line integrals in (3.14.a-b) can usually be evaluated by a simple mid-point rule with good accuracy, for which the off-diagonal terms in (3.14) are written as

$$U_{ij} = -\frac{kW_j}{2j} \hat{\boldsymbol{R}} \cdot \hat{\boldsymbol{n}}' H_1^{(2)}\left(k\rho_{ij}\right) \qquad (i \neq j), \tag{3.15.a}$$

$$H_{ij} = \frac{\omega\mu d}{2} H_0^{(2)}\left(k\rho_{ij}\right) \qquad (i \neq j), \tag{3.15.b}$$

where ρ_{ij} is the distance between the middle points of ports i and j. In the author's experience, the accuracy of the mid-point rule is poor at very low frequencies, typically in the kHz range. This is because the imaginary part of the Hankel function has a large gradient for small arguments. Numerical integration techniques such as the Gaussian quadrature rule [104] can be used to overcome the low frequency inaccuracy problem (see Appendix A.3).

By the impedance definition $\overline{V} = \overline{\overline{Z}}\,\overline{I}$, an impedance matrix can be found from (3.11),

$$\begin{bmatrix} \overline{\overline{Z}}^{qq} & \overline{\overline{Z}}^{qs} \\ \overline{\overline{Z}}^{sq} & \overline{\overline{Z}}^{ss} \end{bmatrix} = \begin{bmatrix} \overline{\overline{U}}^{qq} & \overline{\overline{U}}^{qs} \\ \overline{\overline{U}}^{sq} & \overline{\overline{U}}^{ss} \end{bmatrix}^{-1} \begin{bmatrix} \overline{\overline{H}}^{qq} & \overline{\overline{H}}^{qs} \\ \overline{\overline{H}}^{sq} & \overline{\overline{H}}^{ss} \end{bmatrix}. \tag{3.16}$$

The quantity of interest is the sub-matrix $\overline{\overline{Z}}^{ss}$ that represents the interaction among line segments on the vias by assuming a perfect magnetic conductor (PMC) boundary condition on the plane boundary C, i.e. $\overline{I}^{q} = \overline{0}$. The PMC boundary condition is an approximation neglecting a loading admittance from the fringing field and radiation at the edge of the plane. It is, however, usually justified for PCBs and packages with typical configurations since the effect of this loading admittance is small. Extension of the method to include the loading admittance will be presented in Section 5.2.

The method described above is suitable for lossy structures, i.e., k is complex, which is the case for most of the practical applications. For lossless structures, the method can be imprecise at frequencies very close to resonances due to bad conditioning of the matrix $\overline{\overline{U}}$ [105].

3.3. Modeling of Circular Ports

In the last section, the transfer characteristic among vias has been described by an impedance matrix $\overline{\overline{Z}}^{ss}$ with respect to discrete line segments on via perimeters. A more useful representation is instead the so-called parallel-plate impedance (Z_{pp}) [106] that regards vias as single circular ports by assuming constant currents over the via circumference, which is a good approximation when the via radii are much smaller than the wavelength. One may further assume constant voltages on these circular ports to extract Z_{pp} from $\overline{\overline{Z}}^{ss}$, as has been presented in [55]. The selection of the voltage probing point is rather arbitrary in [55]. Here, the port voltage is obtained by calculating an average of voltages on the segments of the via port for the extraction. It will be revealed in later sections that it is in fact corresponding to the isotropic mode of a circular port.

Consider N circular ports, each discretized into L segments as depicted in Fig. 3.4. Accordingly, the voltage and current vectors for the circular ports are expressed as

$$\overline{V}^{p} = \left[V_1^p, V_2^p, \ldots, V_N^p \right]^T, \tag{3.17}$$

$$\overline{I}^{p} = \left[I_1^p, I_2^p, \ldots, I_N^p \right]^T. \tag{3.18}$$

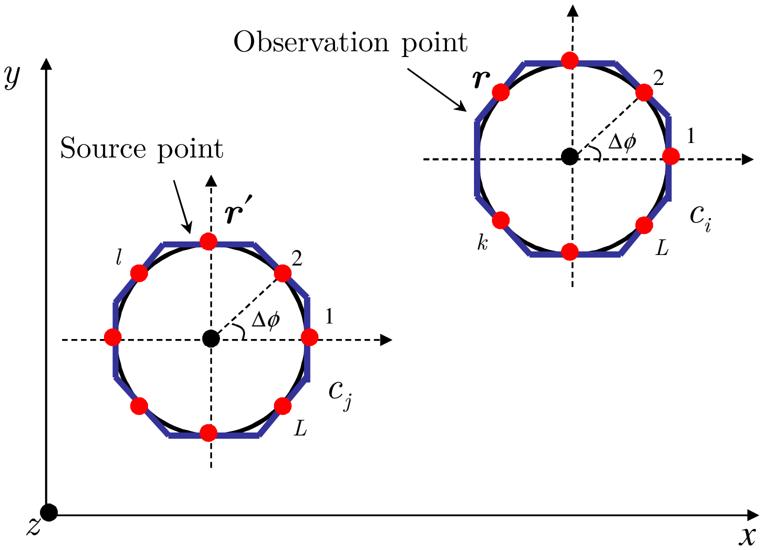

Figure 3.4 Notation of two circular ports discretized into $L = 8$ line segments. $\Delta\phi$ is the incremental azimuthal angle. c_i and c_j are the contours of the observation port and source port, respectively.

where the superscript p denotes the circular ports. Under the assumption of a constant current on each line segment, it is found that

$$I_j^p = \sum_{l=M+(j-1)L+1}^{M+jL} I_l = L\left(I^s\right)_j . \tag{3.19}$$

The voltage on the i-th circular port is established by averaging voltages on line segments, it follows that

$$V_i^p = \frac{1}{L}\sum_{k=M+(i-1)L+1}^{M+iL} V_k = \frac{1}{L}\sum_{k=1}^{L}\left(V_k^s\right)_i . \tag{3.20}$$

By using the relation $\overline{V}^s = \overline{\overline{Z}}^{ss}\,\overline{I}^s$, the Z_{pp} definition can be expressed accordingly as

$$Z_{ij}^{pp} = \frac{V_i^p}{I_j^p} = \frac{\frac{1}{L}\sum_{k=1}^{L}\left(V_k^s\right)_i}{L\left(I^s\right)_j} = \frac{\sum_{k=1}^{L}\sum_{l=1}^{L}\left(Z_{ij}^{ss}\right)_{kl}\left(I^s\right)_j}{L^2\left(I^s\right)_j} = \frac{1}{L^2}\sum_{k=1}^{L}\sum_{l=1}^{L}\left(Z_{ij}^{ss}\right)_{kl}, \tag{3.21}$$

where s denotes line ports on a particular via with corresponding observation and source port indices k and l, respectively. We may now rewrite (3.11) with regard to the circular port expressions as

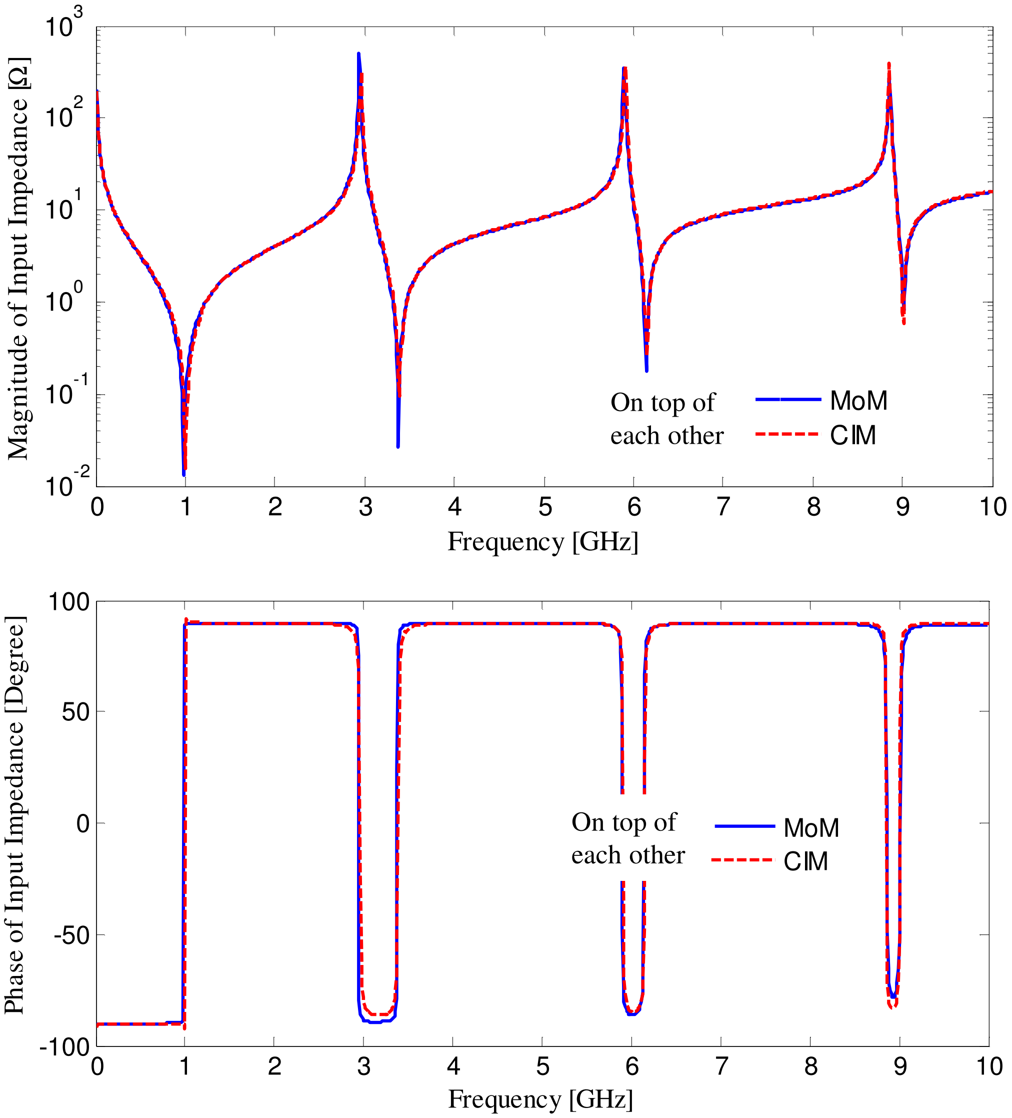

Figure 3.5 Magnitude and phase of the input impedance of the rectangular board example in Fig. 2.6, obtained by CIM and a full-wave MoM simulation.

$$\begin{bmatrix} \overline{V}^{q} \\ \overline{V}^{p} \end{bmatrix} = \begin{bmatrix} \overline{\overline{Z}}^{qq} & \overline{\overline{Z}}^{qp} \\ \overline{\overline{Z}}^{pq} & \overline{\overline{Z}}^{pp} \end{bmatrix} \cdot \begin{bmatrix} \overline{I}^{q} \\ \overline{I}^{p} \end{bmatrix}. \tag{3.22}$$

To show an application example, the rectangular board presented in Chapter 2 is analyzed again using CIM. The input impedance is plotted in Fig 3.5, together with that from the MoM simulation for comparison. The two curves lie on top of each other. However, CIM takes a CPU time of 25.3 milliseconds per frequency point using a 64-bit PC with 3.0 GHz CPU, which is more than 200 times faster than the MoM simulation.

3.4. Cavity Field Distribution and Radiation

A field distribution between power planes is sometimes desired, especially for power integrity analysis to help designers identify “hot spots” in the power plane. Generating a field distribution is relatively simple in CIM. It is not difficult to recognize that (3.6) and its discrete form (3.10) can be used to obtain the electric field at any point in the calculation domain provided that the sources on the right-hand side of them are known, which can be obtained by manipulating (3.22) depending on the excitations and boundary conditions. Once the source is determined, a field map can be produced by simple multiplications using (3.10).

According to the field equivalence principle [107], the radiated far fields from a pair of parallel planes can be approximated as the radiation from an equivalent magnetic surface current along the contour C [108],[109]. The electric far field at an observation point $\boldsymbol{r}$ in free space is expressed as [55],[103]

$$\mathcal{E}\left(\boldsymbol{r}\right) \approx \frac{jk_0}{4\pi} \cdot \frac{e^{-jk_0 r}}{r} \sum_{i=1}^{N} V_q\left(\boldsymbol{r}_i'\right) e^{jk_0\left(\boldsymbol{r}_i' \cdot \hat{e}_r\right)} \left(\hat{\boldsymbol{e}}_{\boldsymbol{r}} \times \hat{\boldsymbol{t}}_{\boldsymbol{i}}'\right) W_i, \tag{3.23}$$

where k_0 is the free space wavenumber. $\hat{\boldsymbol{e}}_{\boldsymbol{r}}$ is the unit vector of $\boldsymbol{r}$. $\boldsymbol{r}_i'$ is the location vector of the i-th port on the contour C. $V_q\left(\boldsymbol{r}_i'\right)$ can be obtained by (3.22). Application examples concerning cavity field distributions and radiation will be presented extensively in later chapters.

3.5. Limitations of the Method

The 2D nature of power planes and other planar structures in electronic systems makes the analysis of them by CIM possible, which in general provides a much more efficient computation when compared to 3D full-wave algorithms. Moreover, the fact that only the contour of the planar structure is concerned in CIM alleviates the modeling effort and potentially leads to a better efficiency than other 2D numerical methods. In comparison to analytical algorithms such as the radial waveguide (RW) method and the cavity resonator model (CRM), which are limited to simple and regular shapes, CIM is more flexible and can deal with planar structures, in principle, of any arbitrary shape.

However, CIM has also several limitations, especially when applied to multilayer structures with vertical via transitions.

- The presence of cylindrical via structures entails modeling of circular ports in CIM. As described above, conventional CIM is restricted to line ports and a discretization of the circular port circumference is required, which results in a rapidly increasing number of unknowns when more vias are in presence. It is not uncommon to find designs with thousands of vias in modern electronic packaging, for which modeling efficiency is critical. Discretization of circular ports obviously affects the computation speed of CIM and an extension for solving circular ports analytically is desired.

- CIM solves in essence a 2D field problem and the variations in the third dimension are neglected. In real power plane structures, 3D field distributions exist, for example, in the vicinity of via locations where the transition from a coaxial to a radial region induces a complex 3D near field pattern. Moreover, the radiated fields from plane edges are 3D in nature and their effect has been neglected by assuming an open PMC boundary condition. These 3D phenomena are not captured by CIM, and therefore, restrain its accuracy when applying to real structures.

- Electronic systems typically contain many multilayer structures. However, CIM only handles one pair of planes at each time and it alone does not give rise to multilayer responses. Therefore, hybridization with other methods is required in order to transfer the benefit of CIM to the analysis of multilayer substrates.

3.6. Summary and Discussions

The theory of the conventional CIM has been detailed in [9]. It is briefly reviewed here with emphasis on its application to the analysis of power planes and vias. Circular ports are needed for CIM to simulate cylindrical via transitions, and their modeling with line segments has been addressed. A much better efficiency of the method in comparison to full-wave solvers is revealed by a quick analysis of a rectangular board example. The limitations of the method are summarized, which will be investigated and correspondingly resolved by the extensions in the remaining chapters.

4. Extension using Analytical Solutions

In recognition of limitations of the conventional CIM, this chapter addresses the extension of it by incorporating analytical solutions for circular port modeling. As has been discussed above, conventional CIM treats circular ports by approximating them as polygons. Many line segments are required for an accurate modeling of the circular shape, which eclipses the efficiency benefit of CIM. The goal here is to derive sets of analytical expressions based on cylindrical wave functions to reduce the number of unknowns associated with each circular port and curtail the system matrix size for a faster computation.

An isotropic circular port definition is first explained, where the electric and magnetic fields on the exciting ports are assumed to be constant and uniform. Analytical expressions are then derived accordingly for both infinite and finite power planes [17]. The isotropic assumption may not hold in certain scenarios such as vias in very close proximity, where anisotropic modes can be excited. The port definition is next generalized to account for the non-uniform field distribution along the port perimeter and its associated anisotropic propagating modes, followed by derivations of formulas based on the general definition [16]. A few application examples using the extended CIM will be demonstrated and validated against the conventional CIM.

4.1. Isotropic Circular Port Definition

The excitation of an electromagnetic wave between the power planes can be associated with a field distribution induced by the vertical via current on a cylindrical surface, on which the circular port is defined accordingly. This port surface could lie on the via barrel, as adopted in [88], or some distance away as indicated in [110].

A power plane pair example with a separation of d is illustrated in Fig. 4.1. $\boldsymbol{r}$ represents the vector of a point on the port surface A. The circular port is specified as a cylindrical area facing towards the power bus, as shown in Fig. 4.1. In the following, it is assumed first that the excitation current is isotropic and constant over the

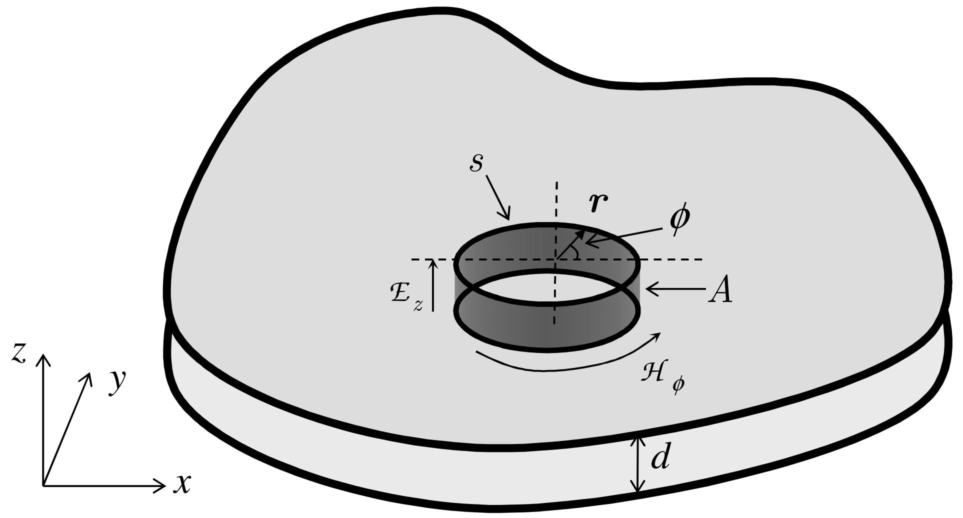

Figure 4.1 Illustration of the circular port definition in a pair of power/ground planes. A denotes the area of port surface. ϕ is the angle that vector r forms with the x-axis. $\mathcal{E}_z$ and $\mathcal{H}_\phi$ are the tangential electric and magnetic fields on the port surface, respectively.

rotationally symmetric circular port, i.e., the tangential electric and magnetic field $\mathcal{E}_z$ and $\mathcal{H}_\phi$ do not vary along the perimeter of the port. Hence, the total current through the port is found as

$$I = \mathcal{H}_\phi \cdot 2\pi a \, , \tag{4.1}$$

where a is the port radius. The voltage can be defined as a line average of the tangential electric fields [111]:

$$V = \frac{d}{2\pi a} \cdot \oint_s \mathcal{E}_z\left(\boldsymbol{r}\right) ds. \tag{4.2}$$

From (4.1) and (4.2), the parallel-plate impedance Z_{pp} can be written as

$$Z_{ij} = \frac{V_i}{I_j} = \frac{d}{2\pi a_i} \cdot \frac{\oint_s \mathcal{E}_z\left(\boldsymbol{r}\right) ds}{2\pi a \cdot \mathcal{H}_\phi\left(a_j\right)}, \tag{4.3}$$

where the indices i and j refer to an observation port and a source port, respectively. Since the line integral in (4.3) averages out any higher order anisotropic field distribution, Z_{pp} is here defined with respect to the fundamental isotropic mode of the fields on the port. Under the assumptions in (4.1), (4.2), and (4.3), the impedance expression for infinite plane pairs can be derived by taking advantage of the zeroth-order cylindrical wave expansion function, as applied in the radial waveguide (RW) method [59]-[63].

$$Z_{ij} = \frac{j\eta d}{2\pi a_j \cdot H_1^{(2)}\left(ka_j\right)} \cdot \begin{cases} H_0^{(2)}\left(ka_j\right) & (i = j) \\ J_0\left(ka_i\right) H_0^{(2)}\left(k\rho_{ij}\right) & (i \neq j), \end{cases} \tag{4.4}$$

where J_0 denotes the zeroth-order Bessel function. The distance between centers of the ports i and j is represented by ρ_{ij}. k is the complex wavenumber including dielectric and ohmic losses, as defined in (3.2). η denotes the complex wave impedance. In comparison to the formulation in [63], an additional zeroth-order Bessel function is included for the transfer impedance in (4.4), resulting from the integral over the circumference of the observation port in (4.3). This has also been reported in [72].

4.2. Derivations for Isotropic Ports

Based on the isotropic port definition above, novel analytical expressions are derived in this section for modeling of the circular ports. The goal is to reduce the computational complexity in contrast to the numerical modeling in the conventional CIM.

4.2.1. Infinite Planes

Consider first a plane pair with its outer boundary C, as shown in Fig. 3.1, extended to infinity. Since the electromagnetic waves decay to zero at infinity, only the reflections among circular ports themselves need to be considered. A configuration consisting of only circular ports is shown in Fig. 4.2.

As a starting point, the contour integral equation (3.1) over circular port contours is combined with the relation (3.4) yielding

$$\mathcal{E}_z\left(\boldsymbol{r}\right) = \frac{-1}{2j} \oint_{C'} \left[\frac{\partial H_0^{(2)}\left(k\left|\boldsymbol{r} - \boldsymbol{r}'\right|\right)}{\partial n} \mathcal{E}_z\left(\boldsymbol{r}'\right) - jk\eta H_0^{(2)}\left(k\left|\boldsymbol{r} - \boldsymbol{r}'\right|\right) \mathcal{H}_\phi\left(\boldsymbol{r}'\right) \right] ds', \tag{4.5}$$

where $\boldsymbol{r}$ and $\boldsymbol{r}'$ are the observation and source vectors on the contour C' including all the port perimeters $c_1, \ldots, c_N$, with N the total number of circular ports. Under the assumption of isotropic fields over the perimeter of the source port, the integral in (4.5) can be written as a sum of integrals over individual port perimeters as

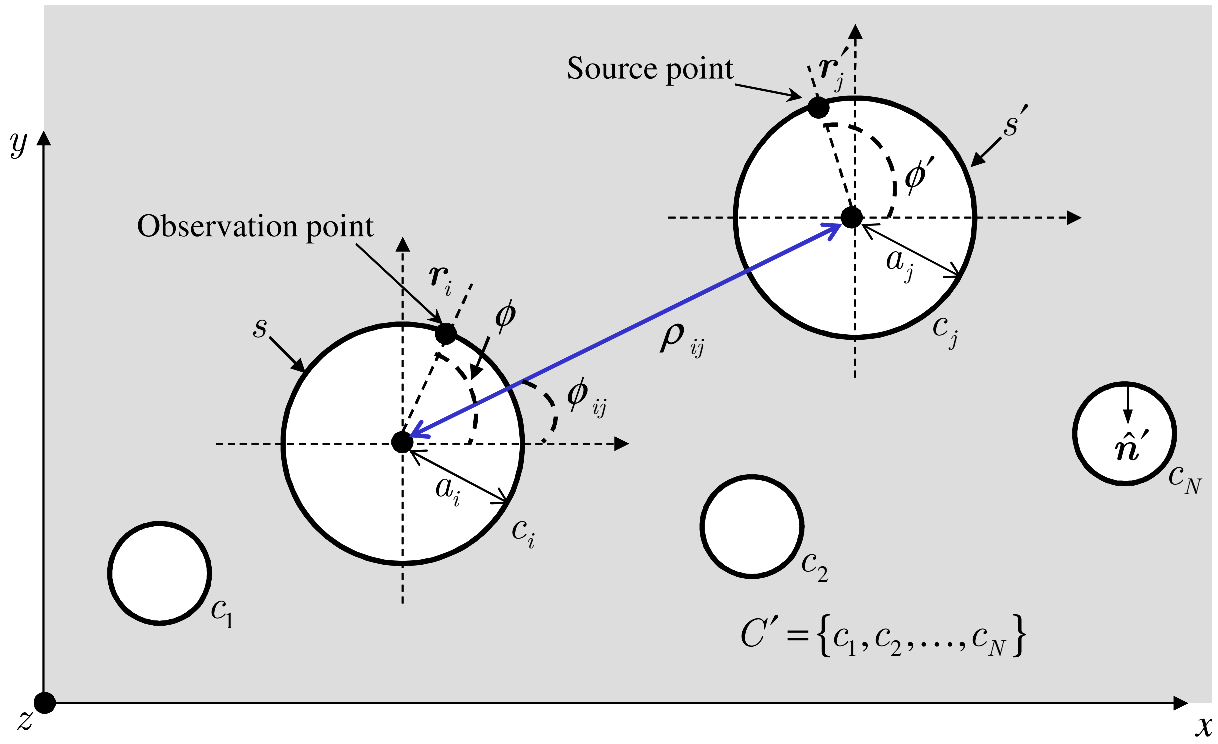

Figure 4.2 Notations of two circular ports in an infinite plane pair. c_i and c_j are the contours of the observation port and source port, respectively. a_i and a_j are the port radii. The distance between the centers of the ports is denoted as ρ_{ij}.

$$\mathcal{E}_z\left(\boldsymbol{r}_i\right) = -\sum_{j=1}^{N} \frac{1}{2j} \mathcal{E}_z\left(\boldsymbol{r}'_j\right) \underbrace{\oint_{c_j} \frac{\partial H_0^{(2)}\left(k\left|\boldsymbol{r}_i - \boldsymbol{r}'_j\right|\right)}{\partial n} ds'}_{\alpha_j} + \sum_{j=1}^{N} \frac{k\eta}{2} \mathcal{H}_\phi\left(\boldsymbol{r}'_j\right) \underbrace{\oint_{c_j} H_0^{(2)}\left(k\left|\boldsymbol{r}_i - \boldsymbol{r}'_j\right|\right) ds'}_{\beta_j}, \quad (4.6)$$

where the indices i and j denote the observation and source port locations, respectively, as shown in Fig. 4.2. Constant exciting voltages and currents on source ports are assumed, so that one obtains

$$I_j = \mathcal{H}_\phi\left(\boldsymbol{r}'_j\right) \cdot 2\pi a_j \qquad \text{and} \qquad V_j = \mathcal{E}_z\left(\boldsymbol{r}'_j\right) \cdot d\,. \quad (4.7)$$

According to the voltage definition (4.2), the voltage on the observation port is expressed as

$$V_i = \frac{d}{2\pi a_i} \oint_{c_i} \mathcal{E}_z\left(\boldsymbol{r}_i\right) ds. \quad (4.8)$$

By substituting (4.7) into (4.6), and in turn (4.6) into (4.8), an equation system is established as

$$
\begin{aligned}
V_i = &-\frac{1}{2j}\sum_{j=1}^{N}\frac{V_j}{2\pi a_i}\underbrace{\oint_{c_i}\oint_{c_j}\frac{\partial H_0^{(2)}\left(k\left|\boldsymbol{r}_i-\boldsymbol{r}_j'\right|\right)}{\partial n}ds'ds}_{\alpha_{ij}} \\
&+\sum_{j=1}^{N}\frac{k\eta d}{4\pi a_j}\frac{I_j}{2\pi a_i}\underbrace{\oint_{c_i}\oint_{c_j}H_0^{(2)}\left(k\left|\boldsymbol{r}_i-\boldsymbol{r}_j'\right|\right)ds'ds}_{\beta_{ij}}, \quad \left(i=1,\ldots,N\right),
\end{aligned}
\tag{4.9}
$$

Equations (4.9) can be expressed in matrix form given by

$$
\overline{\overline{U}}^{pp}\,\overline{V}^{p}=\overline{\overline{H}}^{pp}\,\overline{I}^{p},
\tag{4.10}
$$

where the identifier p denotes the circular ports, in contrast to line ports q on the boundary of a finite plane, as shown in Fig. 3.1. $\overline{V}^{p}$ and $\overline{I}^{p}$ are the voltage and current vectors of size (N × 1), as have been defined in (3.17) and (3.18). The integrals α_{ij} and β_{ij} describes the transfer functions from, respectively, a circular voltage and current source port to an observation port. They are obtained analytically (Appendix A.4 and A.5), where the elements in matrices $\overline{\overline{U}}^{pp}$ and $\overline{\overline{H}}^{pp}$ can be derived as

$$
H_{ij}^{pp}=\frac{k\eta d}{2}\begin{cases} J_0\left(ka_j\right)H_0^{(2)}\left(ka_j\right) & \left(i=j\right) \\ J_0\left(ka_i\right)J_0\left(ka_j\right)H_0^{(2)}\left(k\rho_{ij}\right) & \left(i\neq j\right), \end{cases}
\tag{4.11}
$$

$$
U_{ij}^{pp}=\frac{k\pi a_j}{j}\begin{cases} J_0\left(ka_j\right)H_1^{(2)}\left(ka_j\right) & \left(i=j\right) \\ J_0\left(ka_i\right)J_1\left(ka_j\right)H_0^{(2)}\left(k\rho_{ij}\right) & \left(i\neq j\right). \end{cases}
\tag{4.12}
$$

Equations (4.11) and (4.12) constitute novel analytical solutions for (4.10) in contrast to the numerical solution in the conventional CIM. The parallel-plate impedance Z_{pp} of an infinite plane pair is calculated by

$$
\overline{\overline{Z}}^{pp}=\left(\overline{\overline{U}}^{pp}\right)^{-1}\overline{\overline{H}}^{pp}.
\tag{4.13}
$$

In comparison to the Z_{pp} expression in (3.21) where multiple segments are involved, the new solution reduces the numerical complexity to only one unknown per circular port.

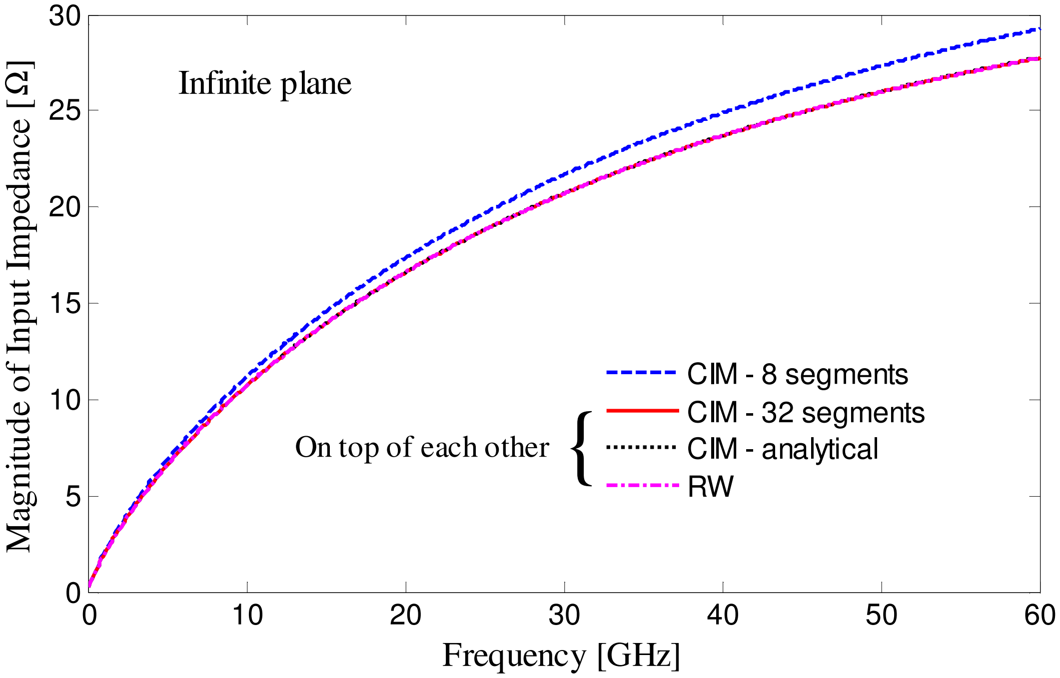

Figure 4.3 Input impedance of a 10-mil radius port on an infinite copper plane pair, obtained with the CIM by discretizing the port perimeter with 8 and 32 segments, the analytical solutions, as well as the RW method. The relative dielectric constant is $\varepsilon_r = 3.8$ and loss tangent is tanδ = 0.02. The cavity height d is 12 mil. The simulation times for the analytical CIM solutions and the discretized CIM with 32 segments are 10 μs and 1.9 ms per frequency point, respectively.

Fig. 4.3 shows the input impedance of a single circular port with 10 mil radius on an infinite plane pair, calculated using (4.13). The result is compared to the one obtained by discretizing the port into segments and taking the average of voltages on the segments assuming constant current excitation, as defined in (3.21). The impedance value predicted by modeling the port using 8 segments is higher than that calculated by (4.13), whereas it converges to the analytical result, when the port is finer discretized into 32 segments, as shown in Fig. 4.3. In the rest of this work, CIM with 32 segments will be used for validations of analytical expressions. The simulation time for CIM with analytical solutions is 10 microseconds (μs) per frequency point, which is more than 100 times faster than 1.9 millisecond (ms) per frequency point by the numerical port modeling with 32 segments.

Note that in the low frequency range, where $ka << 1$, small argument approximations for Bessel functions can be used and the off-diagonal terms in $\overline{\overline{U}}^{pp}$ vanish. Equation (4.13) is reduced to (4.4), the RW equation for infinite planes. Therefore, the RW method is a low frequency approximation of (4.13). According to the impedance

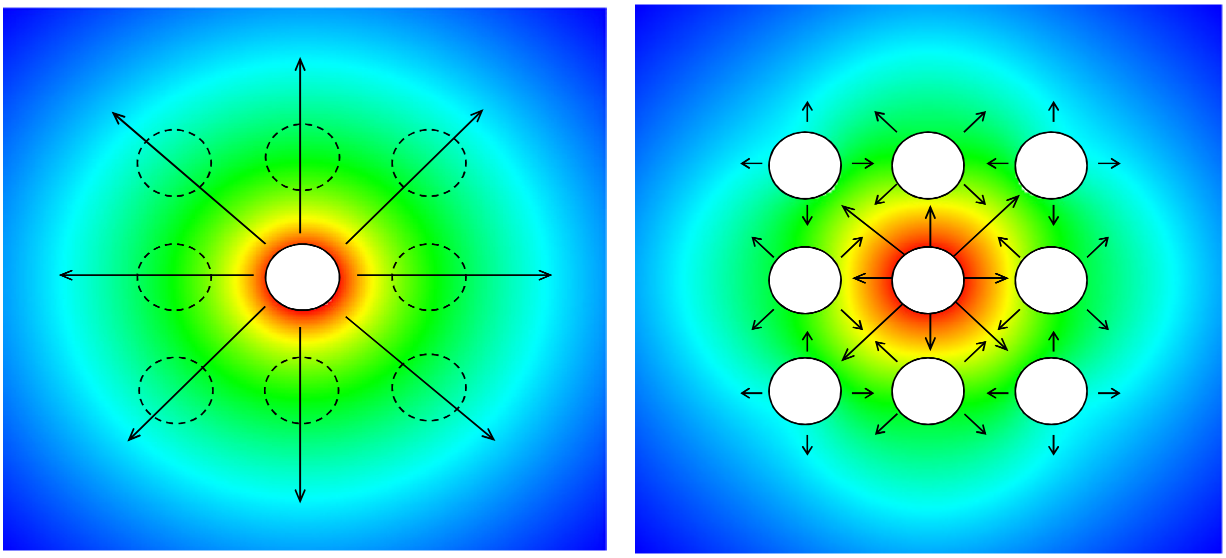

(a) (b)

Figure 4.4 Illustration of electromagnetic field amplitude of wave propagation inside a parallel-plate cavity (a) without and (b) with consideration of multiple scattering from open ports.

definition [111], the exact Z_{pp} should be computed in presence of PMC holes, i.e. with open ports. The RW method does not take into account the scattering from the PMC holes, whereas the effect has been considered in (4.13) by the off-diagonal terms of $\overline{\overline{U}}^{pp}$. A comparison to (4.4) reveals that the RW formula is only relevant to the corresponding ports i and j, and is not disturbed by ports with other indices, i.e., it does not consider the scattering from other ports. As illustrated in Fig. 4.4(a), the electric field pattern observed in the RW method is isotropic and all the ports, except for the exciting one at the center, are transparent to the field, whereas the reality is that these ports are open and can be considered as PMC holes in the plane which superimpose a scattered field as shown in Fig. 4.4(b). For input impedance calculation of a single port, the two methods are identical, as demonstrated in Fig. 4.3.

4.2.2. Finite Planes

Modeling of power plane boundaries has been described in the last chapter, where the boundary contour C, as shown in Fig. 4.5, is discretized into M line ports with their widths much smaller than the wavelength. The remaining task is to combine these linear ports with the analytical circular port solutions to form a complete equation system as in (3.14), for which the impedance matrix is obtained as

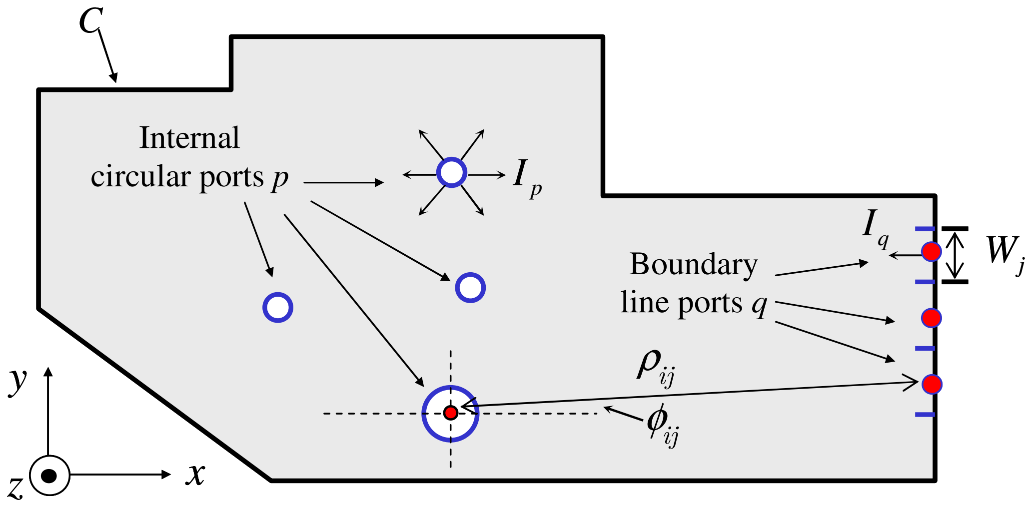

Figure 4.5 Illustration of boundary line ports with index q on the boundary contour C. The total number of line ports is M. ρ_{ij} denotes the distance between port centers.

$$\begin{bmatrix} \overline{\overline{Z}}^{qq} & \overline{\overline{Z}}^{qp} \\ \overline{\overline{Z}}^{pq} & \overline{\overline{Z}}^{pp} \end{bmatrix} = \begin{bmatrix} \overline{\overline{U}}^{qq} & \overline{\overline{U}}^{qp} \\ \overline{\overline{U}}^{pq} & \overline{\overline{U}}^{pp} \end{bmatrix}^{-1} \begin{bmatrix} \overline{\overline{H}}^{qq} & \overline{\overline{H}}^{qp} \\ \overline{\overline{H}}^{pq} & \overline{\overline{H}}^{pp} \end{bmatrix}. \tag{4.14}$$

where the supercript q still represents boundary line ports on contour C. In contrast to (3.12), where the contour C' is represented by $N\times L$ discrete line segments, circular ports with index p have a total number of N. The matrices $\overline{\overline{U}}^{pp}$ and $\overline{\overline{H}}^{pp}$ correspond to the analytical expression (4.12) and (4.11), respectively, whereas the matrices $\overline{\overline{U}}^{qq}$ and $\overline{\overline{H}}^{qq}$ deal exclusively with the interaction of line ports, the mathematical treatment of which has been addressed in Chapter 3. It remains to determine the off-diagonal matrices $\overline{\overline{U}}^{pq}$, $\overline{\overline{H}}^{pq}$, $\overline{\overline{U}}^{qp}$, and $\overline{\overline{H}}^{qp}$ that signify the interaction between circular and line ports. Since constant voltages and currents are assumed on the line ports, one can consider them as point sources, as shown in Fig. 4.5, for which only the fundamental mode is invoked. Under this assumption, we can find for the case that the source point $\boldsymbol{r}'$ lies on a circular port,

$$U_{ij}^{qp} = \frac{1}{2j} \oint_{c_j} \frac{\partial H_0^{(2)}\left(k\left|\boldsymbol{r}_i - \boldsymbol{r}_j'\right|\right)}{\partial n} ds', \tag{4.15}$$

$$H_{ij}^{qp} = \frac{k\eta d}{2} \frac{1}{2\pi a_j} \oint_{c_j} H_0^{(2)}\left(k\left|\boldsymbol{r}_i - \boldsymbol{r}_j'\right|\right) ds', \tag{4.16}$$

and for the case that the source point $\boldsymbol{r}'$ lies on a boundary line port,

$$U_{ij}^{qp} = \frac{1}{2j} \frac{1}{2\pi a_i} \oint_{c_i} \int_{W_j} \frac{\partial H_0^{(2)}\left(k\left|\boldsymbol{r}_i - \boldsymbol{r}_j'\right|\right)}{\partial n} ds' ds, \tag{4.17}$$

$$H_{ij}^{qp} = \frac{k\eta d}{2} \frac{1}{2\pi a_i} \frac{1}{W_j} \oint_{c_i} \int_{W_j} H_0^{(2)}\left(k\left|\boldsymbol{r}_i - \boldsymbol{r}_j'\right|\right) ds' ds\ . \tag{4.18}$$

Equations (4.15)-(4.18) are further simplified (Appendix A.6) as

$$U_{ij}^{qp} = \frac{k\pi a_j}{j} J_1\left(ka_j\right) H_0^{(2)}\left(\rho_{ij}\right), \tag{4.19}$$

$$H_{ij}^{qp} = \frac{k\eta d}{2} J_0\left(ka_j\right) H_0^{(2)}\left(\rho_{ij}\right), \tag{4.20}$$

$$U_{ij}^{qp} = -\frac{k}{2j} J_0\left(ka_i\right) \int_{W_j} \hat{\boldsymbol{R}} \cdot \hat{\boldsymbol{n}}' H_1^{(2)}\left(\rho_{ij}\right) ds', \tag{4.21}$$

$$H_{ij}^{qp} = \frac{k\eta d}{2W_j} J_0\left(ka_i\right) \int_{W_j} H_0^{(2)}\left(\rho_{ij}\right) ds', \tag{4.22}$$

which constitute the off-diagonal matrices in (4.14). In contrast to the original formulation of CIM, which contains only line port expressions as in (3.14), the novelty here is the equations (4.11), (4.12), and (4.19)-(4.22) that are additionally included as a result of the analytical solutions with regard to circular ports.

Fig. 4.7 plots the input impedance for the rectangular power plane case shown in Fig. 4.6, simulated using the approach described above, compared to the results from the conventional CIM by discretizing the port perimeter, and the RW method combined with image theory [63], as well as an extended cavity resonator model (CRM) for circular ports (Appendix B). The four methods yield nearly identical results. The simulation time for CIM with analytical solutions is 13.8 seconds per frequency point, a slight improvement in contrast to 14.3 seconds per frequency point with 32 segments around the circular ports since the number of unknowns associated with boundary ports dominates in this case.

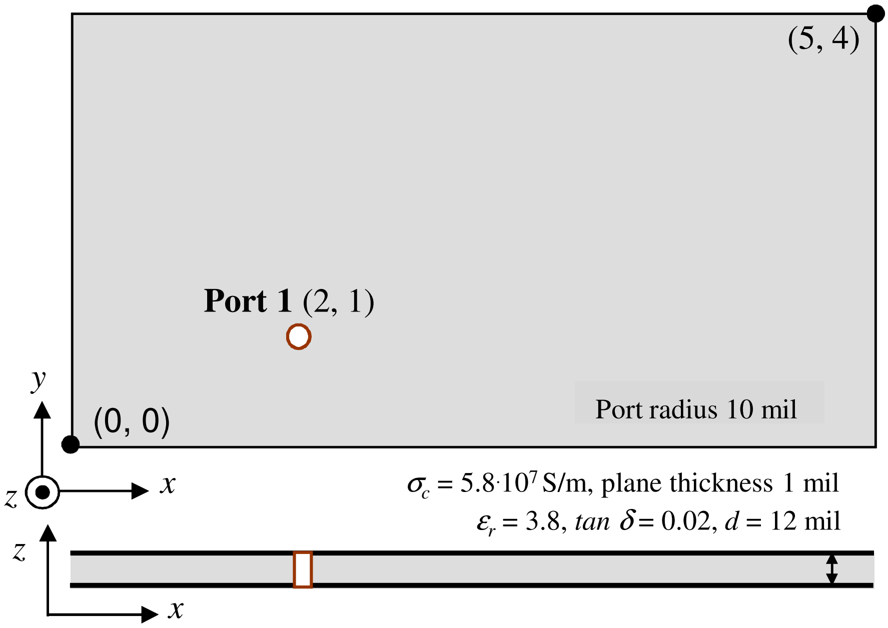

Figure 4.6 Rectangular plane pair example with a single port. Dimensions are given in inches (1 mil = 0.001 inch ≈ $25.4 \cdot 10^{-6}$ m).

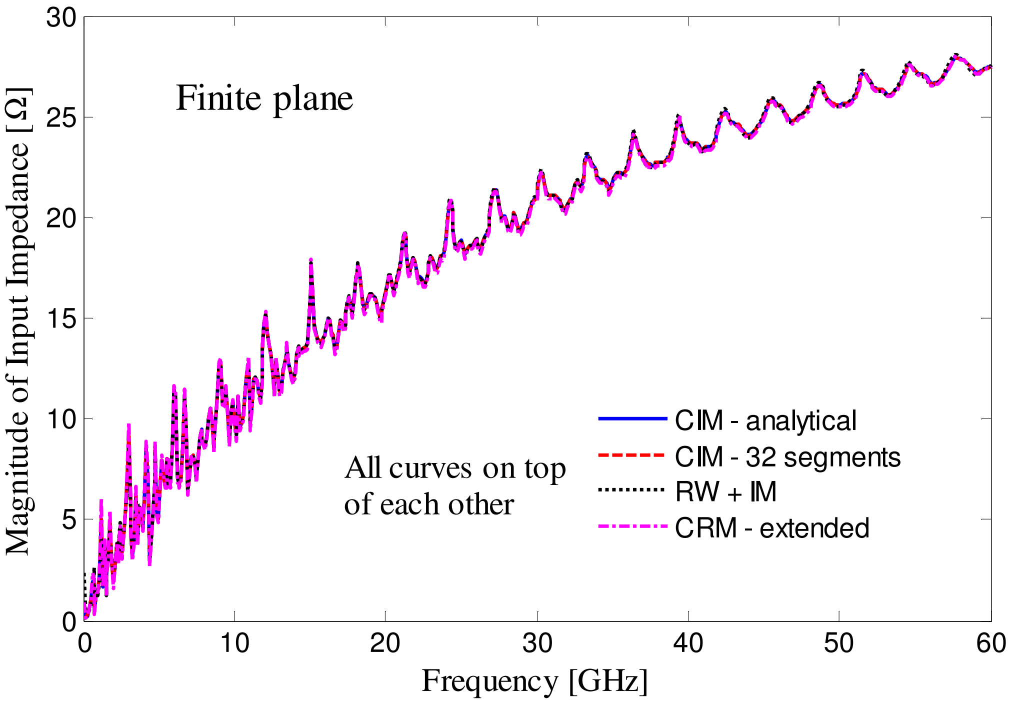

Figure 4.7 Input impedance computed for the case in Fig. 4.6, obtained with the CIM by discretizing the port perimeter, CIM with analytical circular port solutions, radial waveguide method plus image theory, and an extended cavity resonator model.

4.3. Identification of Non-uniform Currents

In previous sections, an isotropic circular port definition and its modeling have been addressed based on the assumption that the currents and voltages are constant along the port circumference. However, as has been discussed in [12], the isotropic assumption can be insufficient in certain scenarios, such as trace to via transitions and vias in very close proximity, where non-uniform currents on vias can develop. This leads to azimuth-dependent field distributions on circular ports, which can excite anisotropic modes, whose fundamental forms do not have cut-off frequencies [36]. As the I/O bandwidth and pin density continue to increase, the proximity effects become more prominent. Thus the inclusion of the anisotropic propagating modes becomes also more important [37].

To show the effect of anisotropy, two configurations that can lead to non-uniform currents on vias are analyzed [12]. The first structure, as shown in Fig. 4.8(a), consists of a via crossing two infinite solid reference planes. At the top and bottom ends, the via is connected to microstrip transmission lines. The current distribution on a via for the case of two reference planes was calculated by a full-wave time domain simulation with the Finite Integration Technique (FIT) [113], as shown in Fig. 4.8(b). A non-uniform current distribution along the via barrel is observed due to the vertical via transition that breaks the microtrip transmission line mode. The current on the upper part of the trace sees a different return path as the lower part, which builds an imbalanced current flow on the via barrel.

Similar structures have been analyzed before, e.g. in [114]-[116]. In [114], it has been found that for a via crossing one metallic layer, the angle between the top and the bottom line has a strong influence on the via propagation characteristics at higher frequencies. In [48], a via crossing two metal planes was investigated. It was shown that the electric field excited by the via current inside the cavity between the two planes was anisotropic.

The second configuration for identification of non-uniform currents is two vias in close proximity, as shown in Fig. 4.9(a). Full-wave simulation using an FEM solver [117] has been carried out with a uniform excitation on port A. Coaxial extensions of 10 mil length on the ports were used in the model and have been de-embedded. In Fig. 4.9(b), the results for the electric field strength values at the antipad rim of via A are plotted for different frequencies. The circle at which the electric field is evaluated has a radius of 15 mil and is placed at half the cavity height (6 mil). The results show that with increasing frequency, the electric fields around the via become more and more asymmetric, caused by non-uniform current distribution of the via. This non-uniformity

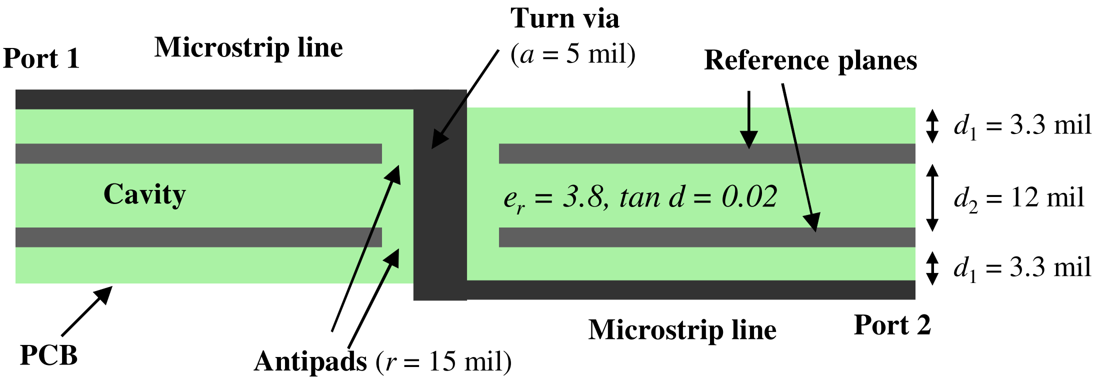

Traces: w = 6mil; traces and planes: t = 1mil, $s_c = 5.8\cdot10^7$ S/m

Plane size: 160 mil x 160 mil, boundary condition: absorbing

(a)

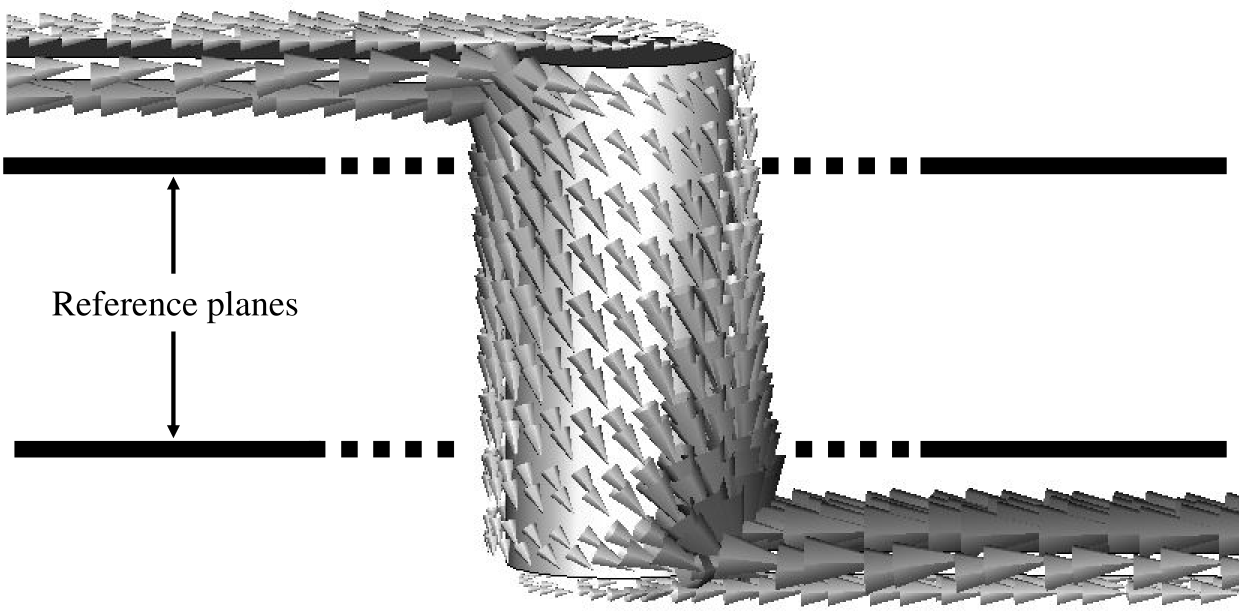

(b)

Figure 4.8 Signal via transition across two solid reference planes with the via barrel being connected to microstrip lines on both ends (a). Surface current on via and traces from a time domain FIT simulation (b). The excitation is a Gaussian pulse ($f_{\min} = 0$, $f_{\max} = 50$ GHz) applied to port 1. The surface current is shown at t = 50 picosecond. A pronounced non-uniform current distribution can be observed with this configuration. *Figure taken from* [12].

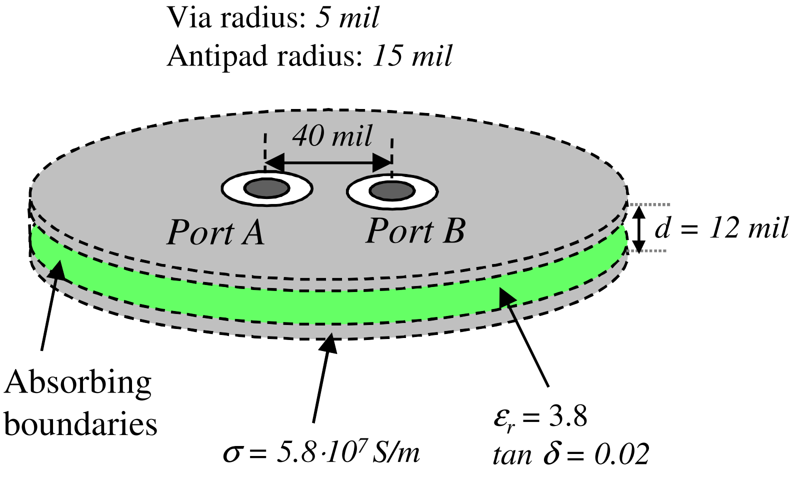

(a)

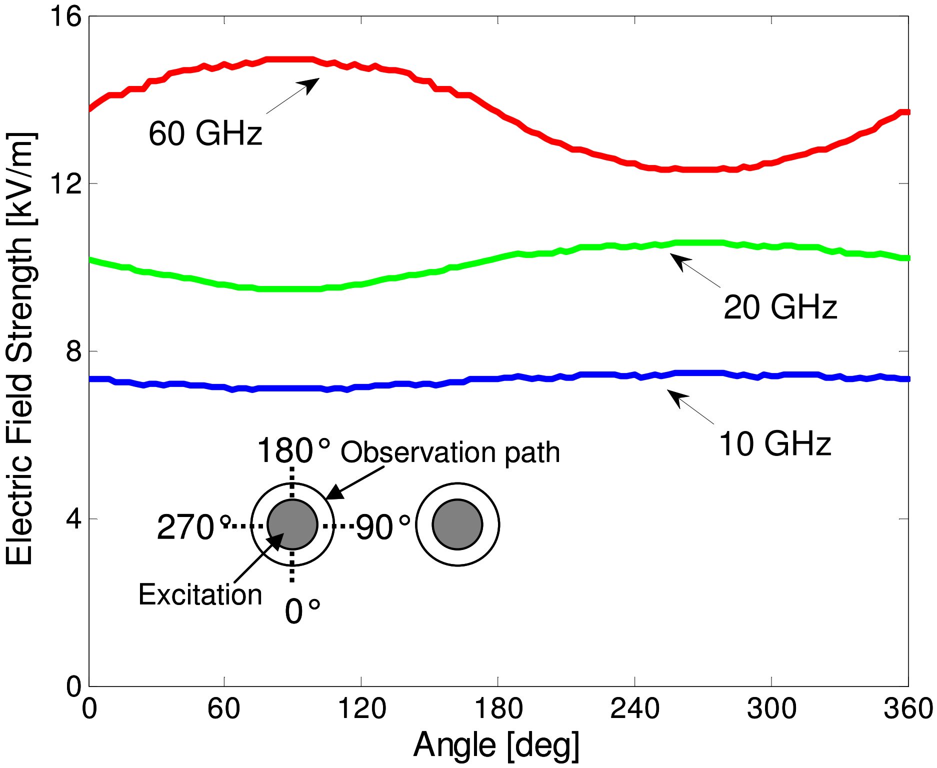

(b)

Figure 4.9 Example of two via segments in close proximity (a) and the electric field inside the cavity at the location of the antipad rim of via *A* (b), obtained with a full-wave method. The vias are connected to the lower reference plane and it is assumed that the planes are infinitely large. The complex amplitude of the electric field is plotted as a function of the angle around the via for different frequencies. The excitation is a 1-Watt power source on the left port *A*. *Figure taken from* [12].

is created by an imbalanced environment surrounding the observed via. In contrast to the microstrip-to-via transition example, the non-uniform currents are not generated by a non-uniform excitation, but by multiple reflections between the vias inside the cavity.

Similar effects to the above configurations can occur for vias close to plane edges. In this case, a non-uniform current on a via can be caused by multiple reflections between via and edge. In principle, any asymmetric environment that is “observable” to a via can lead to an anisotropic field distribution. In order to model these anisotropic effects using CIM, it is necessary first to formulate a correct representation of the anisotropic modes on circular ports, which is the topic of the next section.

4.4. Generalized Circular Port Definition

In contrast to a common port definition in [111], the assumption of isotropic port fields is abandoned in order to take non-uniform current excitations into account. That is, the port fields can vary with the azimuthal angle ϕ (Fig. 4.1) and the voltage and current waves along the port perimeter are not uniquely defined. Following the procedure in [118], one may relate the power associated with each azimuthal mode to an equivalent voltage and current. For that purpose, $\mathcal{E}_z$ and $\mathcal{H}_\phi$ on the port surface are first written in their azimuthal harmonics as [38]

$$\mathcal{E}_z(\boldsymbol{r}) = \sum_{n=-\infty}^{\infty} \tilde{\mathcal{E}}_n e^{jn\phi}, \qquad \mathcal{H}_\phi(\boldsymbol{r}) = \sum_{n=-\infty}^{\infty} \tilde{\mathcal{H}}_n e^{jn\phi}, \tag{4.23}$$

where

$$\tilde{\mathcal{E}}_n = \frac{1}{2\pi} \int_0^{2\pi} \mathcal{E}_z(\boldsymbol{r}) e^{-jn\phi} d\phi, \qquad \tilde{\mathcal{H}}_n = \frac{1}{2\pi} \int_0^{2\pi} \mathcal{H}_\phi(\boldsymbol{r}) e^{-jn\phi} d\phi, \tag{4.24}$$

are the Fourier coefficients of the n-th azimuthal mode of the electric and magnetic field, respectively. Due to the orthogonality of modes, the power transmitted through the port surface is given by

$$P = \frac{1}{2} \iint_A \mathcal{E}_z(\boldsymbol{r}) \mathcal{H}_\phi^*(\boldsymbol{r}) dA = \sum_{n=-\infty}^{\infty} \tilde{\mathcal{E}}_n \tilde{\mathcal{H}}_n^* \pi a d = \sum_{n=-\infty}^{\infty} P_n, \tag{4.25}$$

where a and A denote the radius and the area of the port surface, respectively. $P_n = \tilde{\mathcal{E}}_n \tilde{\mathcal{H}}_n^* \pi a d$ is the power transmitted by the n-th mode. It is clear from (4.25) that the total transmitted power through the port surface is a sum of the power contributed by each individual mode. This suggests that for each azimuthal mode, equivalent voltages and currents can be introduced in proportion to the modal electric and magnetic fields. Note that the mode of the n-th order ($n \neq 0$) is degenerate and consists of two modes with left- and right-handed angular dependences designated by minus and plus signs, respectively. Each of these two modes is characterized by a different mode voltage and current.

In principle, one can choose mode voltages and currents in a variety of ways. However, it is more reasonable to adopt the following modal definitions in order to keep the consistency with the isotropic definition (4.1) and (4.2):

$$V_n = \tilde{\mathcal{E}}_n \cdot d, \qquad\qquad I_n = \tilde{\mathcal{H}}_n \cdot 2\pi a. \tag{4.26}$$

The power obtained using the modal voltage and current are given by

$$P_n = \frac{1}{2} V_n I_n^{\,*} = \tilde{\mathcal{E}}_n \tilde{\mathcal{H}}_n^{*} \pi a d, \tag{4.27}$$

which is consistent with (4.25). Notice that the fundamental mode ($n = 0$) in (4.26) has the same physical significance as the isotropic definition (4.1), which corresponding to the net vertical current at the port location. The existence of anisotropic propagating modes ($n \neq 0$), caused by e.g. scattering from nearby structures, can alter the net current I_0 depending on the power transferred into those modes. The extended voltage and current definitions in (4.26) allow us to include and investigate this mode conversion effect. To quantify that, a new modal Z_{pp} definition is established in correspondence to (4.26)

$$\left(Z_{ij}\right)_{mn} = \left.\frac{V_{im}}{I_{jn}}\right|_{I_{kl}=0 \quad for\ k\neq j\ and\ l\neq n}, \tag{4.28}$$

where m and n denote the mode order of the ports associated with the i-th observation and j-th source port, respectively. The mode conversion effect is described as a transfer impedance by writing Z_{pp} in the form of (4.28), which represents the interaction of two circular ports in terms of their azimuthal modes. A modal impedance in (4.28) denotes the m-th modal voltage induced at port i by an n-th modal current excited at port j assuming an open condition, i.e., the modal currents are zero except for the exciting one.

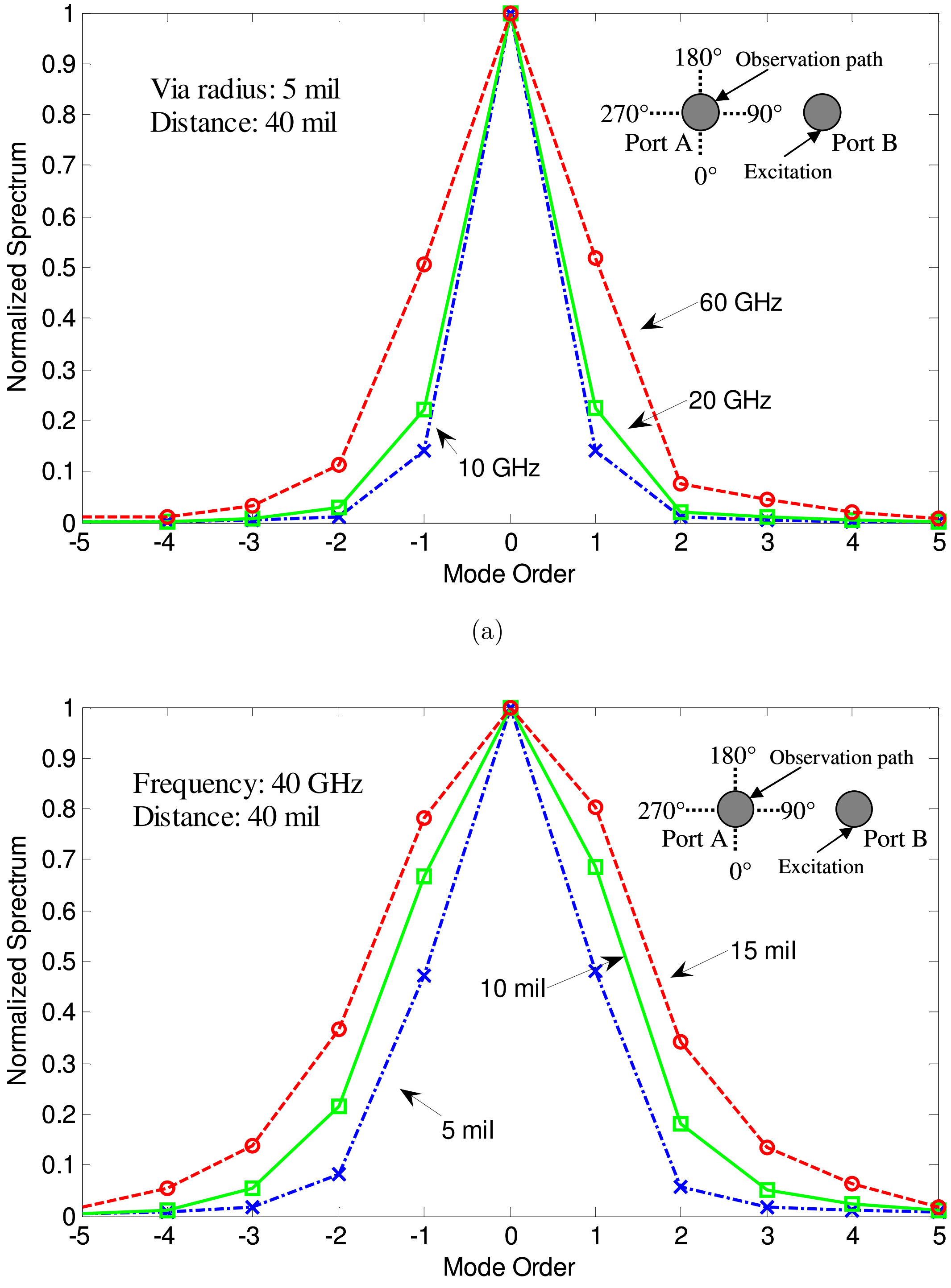

(a)

(b)

Figure 4.10 Amplitude spectrum of the electric field distribution on the circular port A with different frequencies (a), and different via radii (b), normalized to the zeroth-order uniform mode. The board configurations are the same as in Fig. 4.9. Port B on the right is excited with a uniform 1-mA current source and port A on the left is left open.

The conventional CIM, presented in Chapter 3, can be used to capture the field variation on the port perimeter due to non-uniform currents. However, as a 2D method, the CIM captures the effects of propagating modes only. In contrast to general-purpose full wave solvers, where the parallel-plate is usually excited by coaxial ports at the top plate, CIM ports are defined at the circumferences of the vias and fields in the antipad areas are neglected. Nevertheless, the current non-uniformity discussed here is mainly caused by the scattering of propagating modes, which can be simulated by the CIM.

The example depicted in Fig. 4.9 has been analyzed by the CIM with the circular via perimeters approximated using 32 line segments for each to capture the field variation in the azimuthal direction. A 1-mA uniform current source has been used to excite port B and port A was left open. The spectrum coefficients of the electric field distributions using (4.24) is plotted in Fig. 4.10. The coefficients are normalized to the isotropic zeroth-order mode for easy comparison. It can be seen that the higher order asymmetric modes become more prominent at higher frequencies and when the ports are larger. In these scenarios, disregarding the higher order modes may significantly affect the model accuracy.

4.5. Modeling of Anisotropic Modes

To include the anisotropic modes for CIM, novel expressions will be derived in this section to evaluate the modal impedance, defined in (4.28). The extraction of the modal impedance using results from the conventional CIM is first presented, followed by the derivation of analytical expressions for fast calculation of the modal impedance.

4.5.1. Numerical Modeling of Modal Impedance

In conventional CIM, circular ports have been modeled as discrete line segments circumscribing the port perimeters. In Chapter 3, the calculation of Z_{pp} was carried out under the isotropic assumption. Here, it is expanded in order to evaluate the modal impedance given by (4.28). Using the conventional CIM, one can obtain the field distribution along the port surface, and then the modal voltages and currents in (4.26) by performing the Fourier transformation (4.24) to evaluate the impedance expression (4.28). To perform that, the impedance matrix of line segments $\overline{\overline{Z}}^{ss}$ in (3.16) is first solved. Next, the modal voltages and currents in (4.26) can be written in their discrete forms as

$$V_{im} = \frac{d}{2\pi}\int_{0}^{2\pi} \mathcal{E}_z\left(\boldsymbol{r}_i\right) e^{-jm\phi} d\phi \approx \frac{1}{L}\sum_{k=1}^{L}\left(V_k^s\right)_i e^{-jmk\Delta\phi}, \tag{4.29}$$

$$I_{jn} = a\int_{0}^{2\pi} \mathcal{H}_{\phi}\left(\boldsymbol{r}_j\right) e^{-jn\phi} d\phi \approx \sum_{l=1}^{L}\left(I_l^s\right)_j e^{-jnl\Delta\phi}, \tag{4.30}$$

where the indices k and l denote line segments on observation and source circular ports, respectively, as depicted in Fig. 3.4. The discretization is assumed to be the same for all ports, so that the number of line segments per port L and the incremental angle $\Delta\phi$ are identical for all ports. According to the modal impedance definition (4.28), we obtain

$$\left(Z_{ij}\right)_{mn} = \frac{V_{im}}{I_{jn}} \approx \frac{\sum_{k=1}^{L}\left(V_k^s\right)_i e^{-jmk\Delta\phi}}{L\cdot\sum_{l=1}^{L}\left(I_l^s\right)_j e^{-jnl\Delta\phi}}. \tag{4.31}$$

Equation (4.31) can be written in vector notation as

$$\left(Z_{ij}\right)_{mn} L\overline{T_n}^T \overline{I_j}^s = \overline{T_m}^T \overline{V_i}^s, \tag{4.32}$$

where the current and voltage vectors $\overline{I_j}^s$ and $\overline{V_i}^s$ both have the size of 1×L. The vectors $\overline{T_n}$ and $\overline{T_m}$ represent the Fourier transformation operation with their entries written as

$$\left\{T_m\right\}_k = e^{-jmk\Delta\phi} \qquad \text{and} \qquad \left\{T_n\right\}_l = e^{-jnl\Delta\phi}, \tag{4.33}$$

respectively. Referring to (3.16) and substituting the relation $\overline{\overline{Z_{ij}}}^{ss}\,\overline{I_j}^s = \overline{V_i}^s$ into (4.32) leads to

$$\left(Z_{ij}\right)_{mn} L\overline{T_n}^T = \overline{T_m}^T \overline{\overline{Z_{ij}}}^{ss}. \tag{4.34}$$

Due to the property of exponential harmonics, we have $\overline{T_n}^T \cdot \overline{T_n}^{TH} = L,$ where the superscript H denotes the Hermitian transpose and

$$\left\{T_n^{TH}\right\}_l = e^{jnl\Delta\phi}. \tag{4.35}$$

The modal impedances are then derived as

$$\left(Z_{ij}\right)_{mn} = \frac{\overline{T_m}^{T}\, \overline{\overline{Z_{ij}}}^{ss}\, \overline{T_n}^{TH}}{L^2} = \frac{1}{L^2}\sum_{k=1}^{L}\sum_{l=1}^{L}\left(Z_{ij}^{ss}\right)_{kl} e^{j(nl-mk)\Delta\phi}. \tag{4.36}$$

One may recognize that (4.36) is reduced to (3.21) if $m = n = 0$, where constant voltages and currents are assumed on circular ports. It is obvious that this assumption is connected to the fundamental mode of the circular port.

Although (4.36) can be used for the analysis of anisotropic modes, discretzation of the port perimeter is still required for the conventional CIM. As a rule of thumb, one period of sinusoid may be approximated with 8 pulse basis functions, which indicates that, for each increment of the mode number, an additional 8 line segments are required for an accurate modeling of the mode. This results in significant amount of computation time, especially for systems with a large number of circular ports.

To alleviate that, the set of analytical solutions for isotropic circular ports will be extended to include any number of anisotropic modes based on definitions (4.26) and (4.28). Since only a few higher order modes are need in the calculation to achieve a sufficiently high accuracy, the overall computational efficiency of the extended CIM is much more advantageous over the conventional CIM described above.

4.5.2. Infinite Plane

The derivation starts by first considering infinite planes and neglecting the reflections from the outer boundary C, and thus the integral equation (4.5) is retained. However, (4.6) is no longer valid since the assumption of constant electric and magnetic fields over the port perimeter is dropped. Instead, the field variation has to be considered inside the integral as

$$\mathcal{E}_z\left(\boldsymbol{r}_i\right) = -\frac{1}{2j}\sum_{j=1}^{N}\underbrace{\oint_{c_j}\frac{\partial H_0^{(2)}\left(k\left|\boldsymbol{r}_i-\boldsymbol{r}_j'\right|\right)}{\partial n}\mathcal{E}_z\left(\boldsymbol{r}_j'\right)ds'}_{\alpha_j} + \frac{k\eta}{2}\sum_{j=1}^{N}\underbrace{\oint_{c_j}H_0^{(2)}\left(k\left|\boldsymbol{r}_i-\boldsymbol{r}_j'\right|\right)\mathcal{H}_\phi\left(\boldsymbol{r}_j'\right)ds'}_{\beta_j}. \tag{4.37}$$

The vector notations are correspondingly depicted in Fig. 4.2. By the modal voltage and current definition (4.26), equation (4.37) is expressed as

$$\begin{aligned} V_i\left(\boldsymbol{r}_i\right) = & -\frac{1}{2j} \sum_{j=1}^{N} \sum_{n=-\infty}^{\infty} \oint_{c_j} \frac{\partial H_0^{(2)}\left(k\left|\boldsymbol{r}_i - \boldsymbol{r}_j'\right|\right)}{\partial n} V_{jn} e^{jn\phi'} ds' \\ & + \sum_{j=1}^{N} \sum_{n=-\infty}^{\infty} \frac{k\eta d}{4\pi a_j} \oint_{c_j} H_0^{(2)}\left(k\left|\boldsymbol{r}_i - \boldsymbol{r}_j'\right|\right) I_{jn} e^{jn\phi'} ds', \end{aligned} \tag{4.38}$$

Further, we write $V_i\left(\boldsymbol{r}_i\right)$ also in its harmonics as

$$V_i\left(\boldsymbol{r}_i\right) = \sum_{m=-\infty}^{\infty} V_{im} e^{im\phi} \qquad \text{and} \qquad V_{im} = \frac{1}{2\pi a_i} \oint_{c_i} V_i\left(\boldsymbol{r}_i\right) e^{-im\phi} ds. \tag{4.39}$$

Substituting (4.39) into (4.38) yields the following equation system,

$$\begin{aligned} V_{im} = & -\frac{1}{2j} \sum_{j=1}^{N} \sum_{n=-\infty}^{\infty} \frac{V_{jn}}{2\pi a_i} \oint_{c_i} \oint_{c_j} \frac{\partial H_0^{(2)}\left(k\left|\boldsymbol{r}_i - \boldsymbol{r}_j'\right|\right)}{\partial n} e^{-jm\phi} e^{jn\phi'} ds' ds \\ & + \sum_{j=1}^{N} \sum_{n=-\infty}^{\infty} \frac{k\eta d}{4\pi a_j} \frac{I_{jn}}{2\pi a_i} \oint_{c_i} \oint_{c_j} H_0^{(2)}\left(k\left|\boldsymbol{r}_i - \boldsymbol{r}_j'\right|\right) e^{-jm\phi} e^{jn\phi'} ds' ds, \\ & \left(i = 1, \ldots, N, \quad m = -\infty, \ldots, 0, \ldots, \infty\right). \end{aligned} \tag{4.40}$$

It can be seen that the equation system (4.9) for the isotropic port is a subset of (4.40) assuming $m = n = 0$, which is related to the fundamental mode of the fields on circular ports. An “infinite matrix” expression can be formed from (4.40) as

$$\overline{\overline{U}}^{pp} \overline{V}^{p} = \overline{\overline{H}}^{pp} \overline{I}^{p}, \tag{4.41}$$

where the identifier p denotes the circular ports, each of which has an infinite number of modes. Although (4.41) is identical to (4.10) in their form, the sizes of the vector and matrices are different. The vectors $\overline{V}^{p}$ and $\overline{I}^{p}$ in (4.41) contain infinite numbers of modal voltages and currents, which are written as

$$\overline{V}^{p} = \left[\overline{V_1}^{p}, \ldots, \overline{V_i}^{p}, \ldots, \overline{V_N}^{p}\right]^T \quad \text{with} \quad \overline{V_i}^{p} = \left[V_{-\infty}, \ldots, V_0, \ldots, V_{\infty}\right]^T, \tag{4.42}$$

$$\overline{I}^{p} = \left[\overline{I_1}^{p}, \ldots, \overline{I_j}^{p}, \ldots, \overline{V_N}^{p}\right]^T \quad \text{with} \quad \overline{V_j}^{p} = \left[I_{-\infty}, \ldots, I_0, \ldots, I_{\infty}\right]^T. \tag{4.43}$$

The elements of the matrices $\overline{\overline{U}}^{pp}$ and $\overline{\overline{H}}^{pp}$ are obtained analytically, as described in Appendix A.7. They are expressed as

$$\left(U_{ij}^{pp}\right)_{mn}=\frac{k\pi a_j}{j}\cdot\begin{cases}J_m\left(ka_i\right)J_n'\left(ka_j\right)H_{m-n}^{(2)}\left(k\rho_{ij}\right)e^{-j(m-n)\phi_{ij}} & i\neq j,\\ J_m\left(ka_i\right)H_m'^{(2)}\left(ka_i\right) & m=n,\quad i=j,\\ 0 & m\neq n,\quad i=j,\end{cases}\tag{4.44}$$

$$i,j=1,2,\ldots,N,\quad m,n=-\infty,\ldots,-1,0,1,\ldots,\infty,$$

$$\left(H_{ij}^{pp}\right)_{mn}=\frac{k\eta\, d}{2}\cdot\begin{cases}J_m\left(ka_i\right)J_n\left(ka_j\right)H_{m-n}^{(2)}\left(k\rho_{ij}\right)e^{-j(m-n)\phi_{ij}} & i\neq j,\\ J_m\left(ka_i\right)H_m^{(2)}\left(ka_i\right) & m=n,\quad i=j,\\ 0 & m\neq n,\quad i=j,\end{cases}\tag{4.45}$$

$$i,j=1,2,\ldots,N,\quad m,n=-\infty,\ldots,-1,0,1,\ldots,\infty.$$

Here, a prime denotes a differentiation with respect to the argument of the Bessel and Hankel functions (Appendix A.1). The indices m and n signify the mode orders of the observation port i and source port j, respectively. It can be recognized that (4.44) and (4.45) are reduced to its isotropic form as in (4.12) and (4.11) when considering m=n=0 only.

As a consequence of (4.41), Z_{pp} for an infinite plane pair corresponding to definition (4.28) can be obtained by

$$\overline{\overline{Z}}^{pp}=\left(\overline{\overline{U}}^{pp}\right)^{-1}\overline{\overline{H}}^{pp}.\tag{4.46}$$

For the matrix inversion, $\overline{\overline{U}}^{pp}$ must be of finite size and square. Therefore, the mode series is truncated up to the Kth mode for both source and observation ports, i.e., both m and n take integer values from $-K$ to K. The determination of the truncation number K depends on frequency and port size, which will be discussed later.

For a single-port infinite plane pair, (4.46) can be evaluated analytically,

$$\left(Z_{11}^{pp}\right)_{mn}=-j\frac{\eta d}{2\pi a_1}\cdot\begin{cases}\dfrac{H_m^{(2)}\left(ka_1\right)}{H_m'^{(2)}\left(ka_1\right)} & m=n\\ 0 & m\neq n,\end{cases}\tag{4.47}$$

It is clear in (4.47) that the modes are independent of each other and mode conversion does not happen for a single-port case, as indicated by zero transfer impedance between modes. One can recognize that the input impedance of the fundamental mode (m=n=0) in (4.47) is identical to the radial waveguide formula [63]. The input impedances of

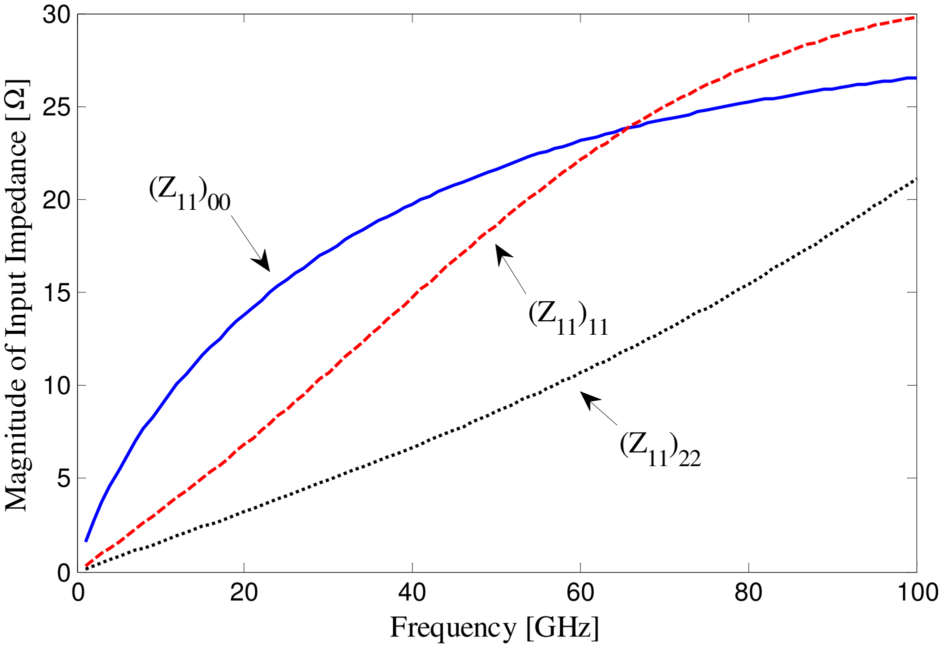

Figure 4.11 Magnitude of input impedances of different modes of a one-port infinite copper plane pair with port radius 10 mil and d = 10 mil (1 mil ≈ $25.4 \cdot 10^{-6}$ m), obtained with modal solutions (4.46). The relative permittivity and loss tangent of the dielectric are $\varepsilon_r = 3.8$ and $\tan\delta = 0.02$, respectively.

higher order modes for a single-port with 10-mil radius are shown in Fig. 4.11, whose magnitudes are smaller than the fundamental mode at low frequencies, however, develop with increasing frequency and can be even larger than the fundamental mode.

For more ports, mode conversions and multiple scattering take place and can alter the behavior of the fundamental mode. To show the effect, a two-port case is analyzed for a 10-mil thick infinite plane pair. The port radii of both ports are 10 mil and the distance between their centers ρ_{12} is 40 mil. The input and transfer impedances of the 0-th mode are shown in Fig. 4.12, with a different number of azimuthal modes (K = 0, 1, and 2) included in the computation. The results simulated by discretizing the port boundaries into 32 segments are also plotted for validation. The comparison indicates that only considering the isotropic mode (K = 0) is not sufficiently accurate for frequencies above 20 GHz, whereas adding one higher order mode in the calculation significantly improves the accuracy for both the input and transfer impedance. For K = 2, the modal solution obtained using (4.46) becomes indistinguishable to the one using the conventional CIM. Since the convergence can be achieved with only a few higher orders using the modal solution, the number of unknowns per port is much less, resulting in a much better computational efficiency than the conventional CIM. The

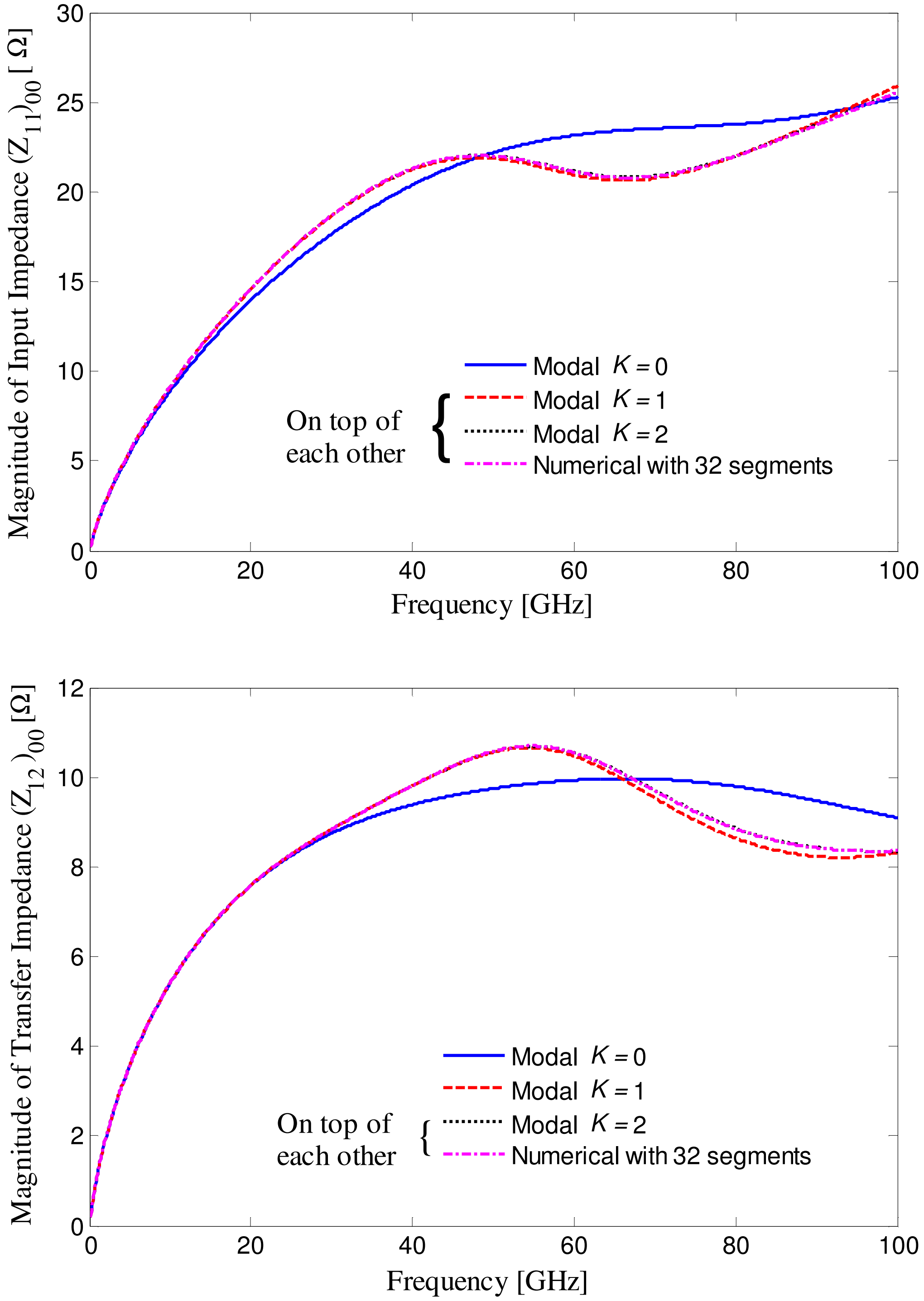

Figure 4.12 Magnitude of input and transfer impedance of the 0th mode of a two-port infinite copper plane pair with port radius 10 mil and d = 10 mil (1 mil ≈ $25.4 \cdot 10^{-6}$ m), obtained with modal solutions and the segmented approach. The distance between port centers is 40 mil. The relative permittivity and loss tangent of the dielectric are $\varepsilon_r = 3.8$ and $\tan\delta = 0.02$, respectively. The indices inside the bracket indicate port numbers, whereas the indices outside the bracket refer to mode numbers correspondingly.

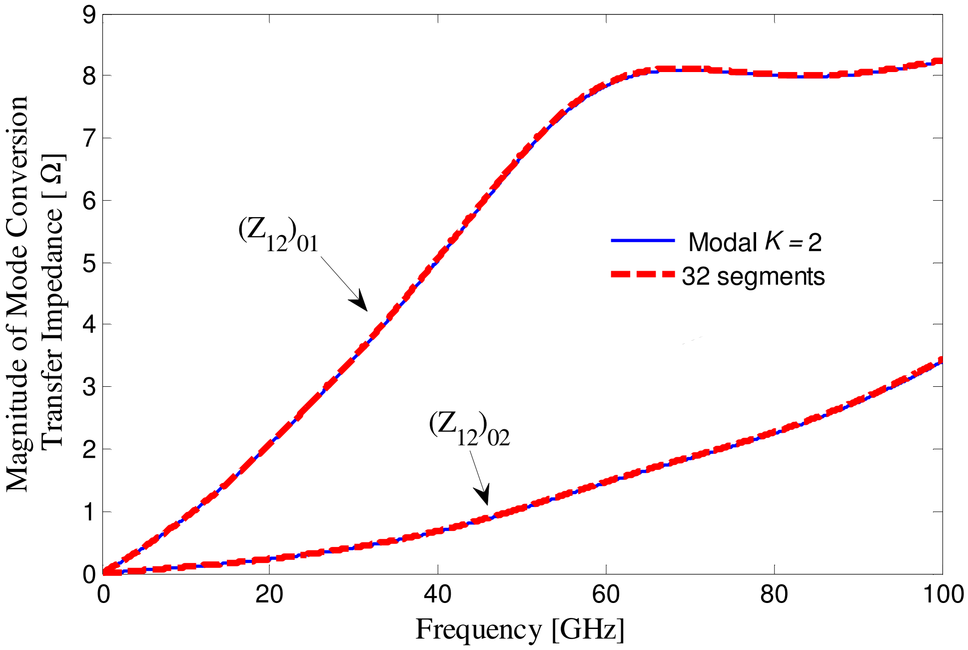

Figure 4.13 Mode conversion transfer impedance of the same two-port system, as described in the caption of Fig. 4.12. The modal solution (solid line) overlaps with the numerical solution (dashed line).

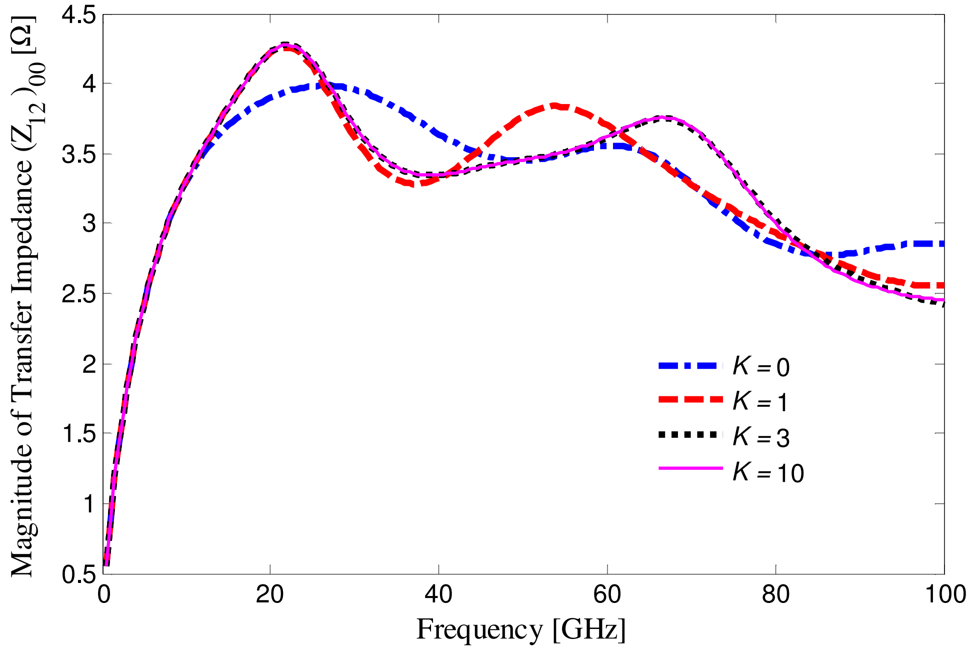

Figure 4.14 Magnitude of transfer impedance of the 0th mode of a two-port infinite copper plane pair with port radius of 25 mil and d = 10 mil, obtained with modal solutions of different K. The distance between port centers is 100 mil. The relative permittivity and loss tangent of the dielectric are $\varepsilon_r = 3.8$ and $\tan\delta = 0.02$, respectively. The impedance curves converge by increasing the truncation number K.

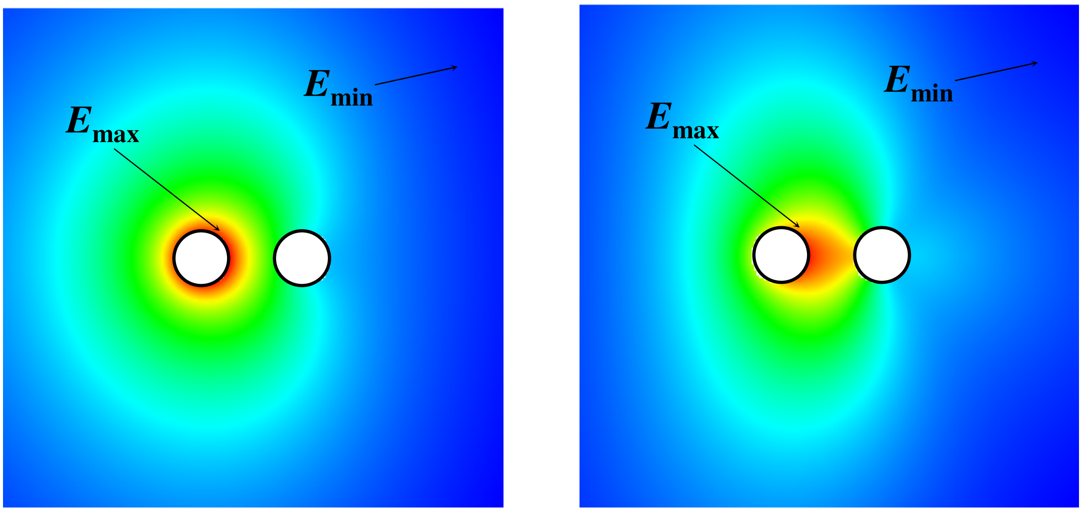

(a) $K = 0$ (b) $K = 2$

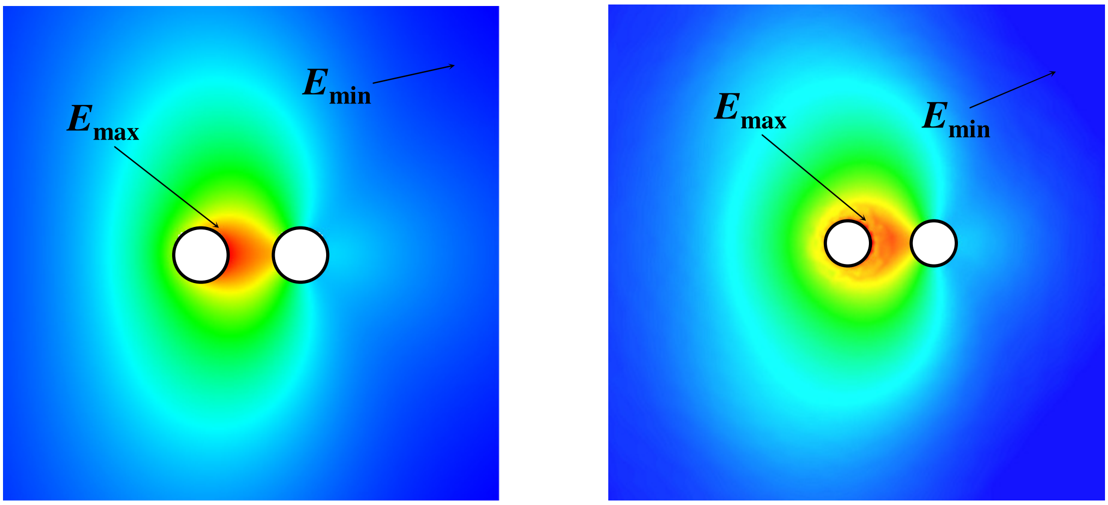

(c) 32 segments per port (d) full-wave

Figure 4.15 Normalized electric field distribution (magnitude in linear scale) at 50 GHz for the same two-port system, as described in the caption of Fig. 4.12, obtained with modal solution (a) $K = 0$, (b) $K = 2$, (c) numerical solution with 32 segments, and (d) full-wave solver. Port 1 (left) is excited with an isotropic current source and port 2 (right) is left open.

simulation time in this case is 0.2 ms per frequency point for the modal solution with $K = 2$ and 7.8 ms per frequency point for the discretized one using a 64-bit PC with 2.8 GHz CPU.

Fig. 4.13 shows the mode conversion transfer impedances between the two ports. The finite value of this impedance implies that a uniform current source can excite anisotropic modes on nearby ports, and vice versa. It is also obvious that the mode conversion increases with frequency and is stronger between lower order modes, as the magnitude of the transfer impedance between the mode 1 and mode 0 is much higher than the one between mode 2 and mode 0.

It has been observed that the mode conversion effects increase with frequency. Thus more modes have to be included in the computation for higher frequencies to obtain an accurate result. Fig. 4.14 shows the transfer impedance of mode 0 between two ports with a radius of 25 mil each and a distance of 100 mil between their centers, obtained with different truncation numbers K. The impedance curves converge by increasing K, whereas for each increment of K, the frequency range of accurate results is expanded by about 10 GHz in this case. As a rule of thumb for determining the mode truncation number K, one can say that K must be larger than the ratio of the port perimeter to a quarter wavelength.

The CIM can be used to generate an electric field distribution between the planes, as shown in Fig. 4.15. Here, port 1 (left) is excited with a 1-mA uniform current source and port 2 (right) is open. The same anisotropic field distribution around port 1 is observed at 50 GHz for the modal solution including higher order modes (b) and the numerical solution segmenting circular ports (c). Fig. 4.15(d) shows the electric field distribution obtained with a commercial full-wave finite element method based solver [117]. Although a minor difference from CIM results (b, c) exists due to the presence of via near fields, the same anisotropy is identified in the full-wave result. This anisotropy is attributed to the reflection and mode conversion caused by the open port 2. In contrast, only using mode 0 fails to account for this non-uniformity, as demonstrated in Fig. 4.15(a).

4.5.3. Finite Planes

For modeling of finite planes, equation (4.14) is recalled where the solution is formed by combining circular ports with boundary line ports. The difference from Section 4.2.2 is that the circular ports, denoted by superscript p, are represented by modal expressions. Similar to the procedure in Section 4.2.2, the expansion to finite planes is carried out by assuming boundary line ports as point sources. Expressions for the matrices $\overline{\overline{U}}^{pp}$ and $\overline{\overline{H}}^{pp}$ correspond to (4.44) and (4.45), respectively, whereas $\overline{\overline{U}}^{qq}$ and $\overline{\overline{H}}^{qq}$ are determined by (3.14.a) and (3.14.b), respectively. To find elements of the off-diagonal matrices $\overline{\overline{U}}^{pq}$, $\overline{\overline{H}}^{pq}$, $\overline{\overline{U}}^{qp}$, and $\overline{\overline{H}}^{qp}$ in (4.14), one may resort to the integrals in (4.37) to find interactions between a circular port and a point on the line port middle, as detailed in Appendix A.8. The coefficients of the off-diagonal matrices are written as

$$\left(U_{ij}^{qp}\right)_n = -\frac{k\pi a_j}{j} J_n'\left(ka_j\right) H_n^{(2)}\left(k\rho_{ij}\right) e^{jn\left(\phi_{ij}+\pi\right)}, \tag{4.48}$$

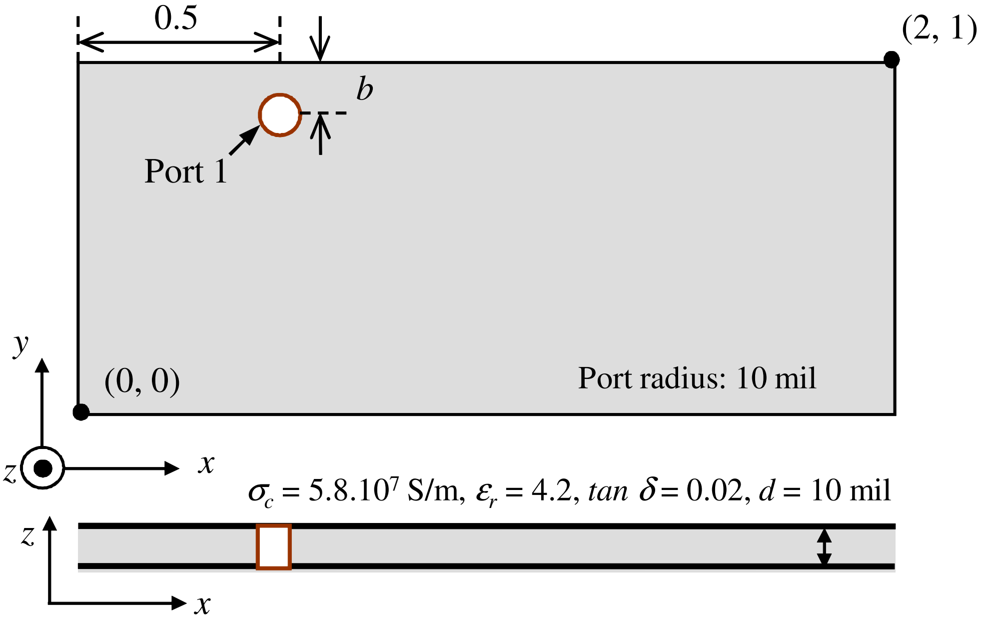

Figure 4.16 Rectangular plane pair example with a single port. Dimensions are given in inches (1 inch ≈ 2.54 · 10^{-2} m).

$$\left(H_{ij}^{qp}\right)_n = \frac{k\eta d}{2} J_n\left(ka_j\right) H_n^{(2)}\left(k\rho_{ij}\right) e^{jn\left(\phi_{ij}+\pi\right)}, \tag{4.49}$$

$$\left(U_{ij}^{pq}\right)_m = \frac{k}{2j} J_m\left(ka_i\right) \int_{W_j} \hat{\boldsymbol{R}}\cdot\hat{\boldsymbol{n}}' H_m'^{(2)}\left(k\rho_{ij}\right) e^{-jm\phi_{ij}} ds', \tag{4.50}$$

$$\left(H_{ij}^{pq}\right)_m = \frac{k\eta d}{2} J_m\left(ka_i\right) \frac{1}{W_j} \int_{W_j} H_m^{(2)}\left(k\rho_{ij}\right) e^{-jm\phi_{ij}} ds'. \tag{4.51}$$

A one-port rectangular plane pair, as shown in Fig. 4.16, is analyzed using the extended CIM. A circular port is placed close to the upper boundary of the plane with a distance of b. The input impedance results of the mode 0 for b = 50 mil is shown in Fig. 4.17, compared to that obtained by the conventional CIM with port perimeter discretized into 32 segments. Similar to the two-port infinite plane case, the extended CIM agrees with the conventional one, when higher order modes are included in the calculation. The influence of mode conversions on mode 0 is relatively small in this case since the dominant effect here is the plane resonances.

The mode conversion appears when the reflection from the plane boundary interferes with the local circular port field distributions. It depends on the distance of the port to

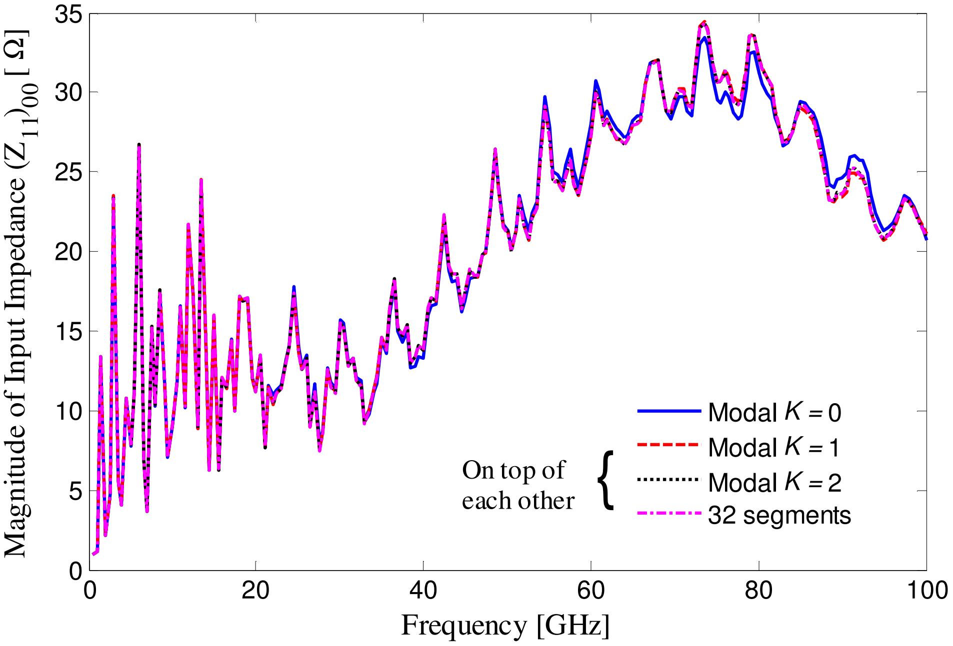

Figure 4.17 Magnitude of input impedance of the 0th mode of the case in Fig. 4.16 with $b = 50$ mil.

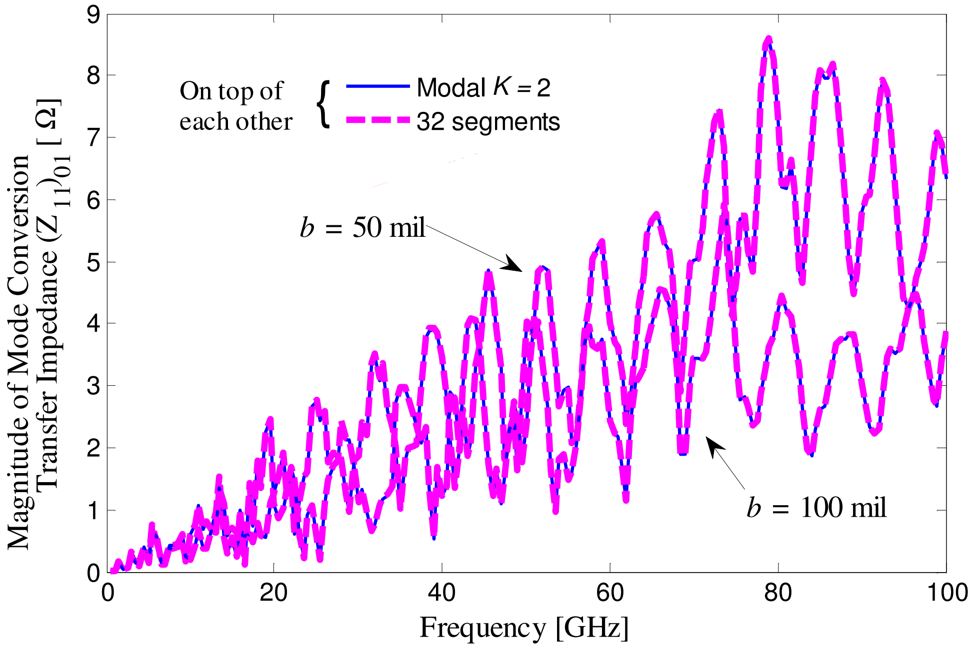

Figure 4.18 Magnitude of mode conversion of the case in Fig. 4.17 with $b = 50$ mil and 100 mil. Mode conversion is stronger when the port is closer to the boundary.

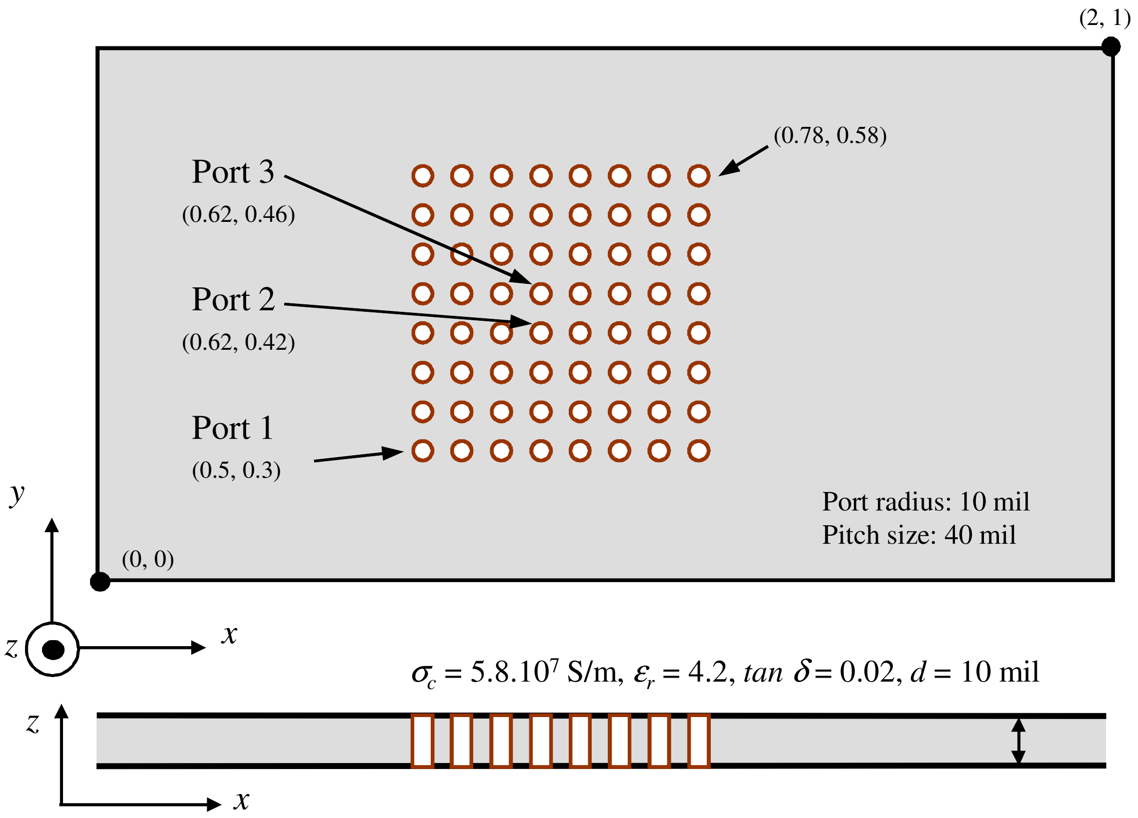

Figure 4.19 An 8 by 8 port array example. Both infinite and finite plane cases are studied. Dimensions are given in inches (1 inch ≈ $2.54 \cdot 10^{-2}$ m).

the boundary. The closer a port lies to the boundary, the more mode conversion is produced. The transfer impedance between the 0th and the 1st mode with b = 50 mil is compared to that with b = 100 mil, as shown in Fig. 4.18. As the port is moved further away from the boundary, the mode conversion becomes less significant.

4.5.4. Port Array Analysis

Based on the extended circular port definitions for taking into account the anisotropic propagating modes, analytical modal expressions have been derived in the last section to improve the efficiency of CIM. They have been validated using the conventional CIM for simple cases and the mode conversion effect and its impact on the Z_{pp} has been analyzed. In this section, the validation and comparison are extended to an 8 by 8 array 64-port case, as shown in Fig. 4.19. Simulation results with regard to ports 1, 2, and 3, as depicted in Fig. 4.19, will be shown for both the infinite and finite plane cases.

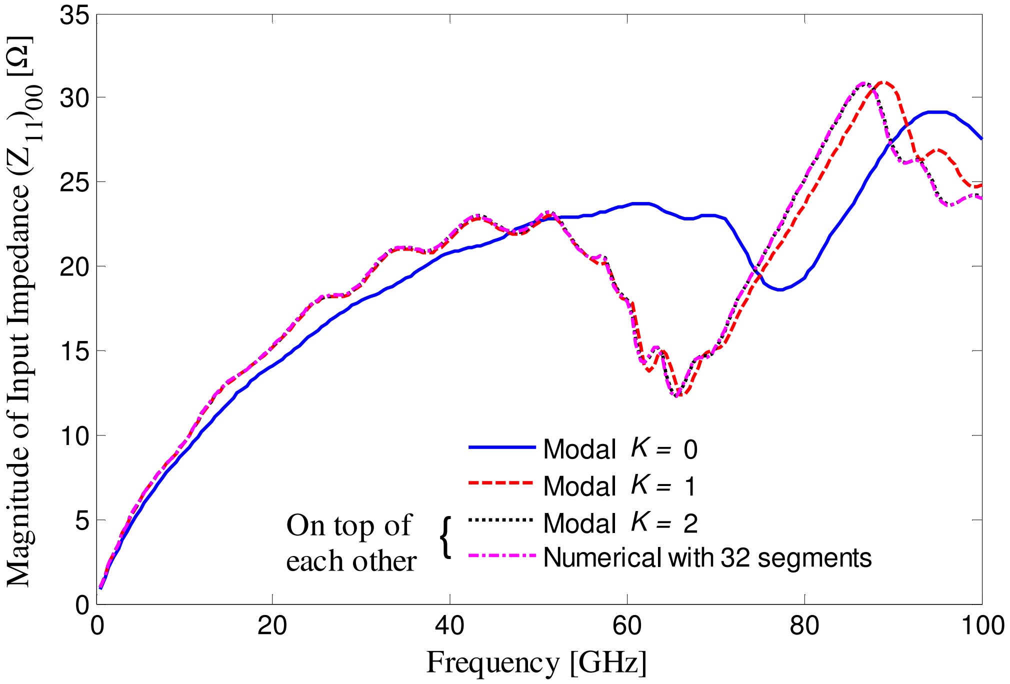

Figure 4.20 Magnitude of input impedance of the 0th mode of port 1 in the infinite plane case, shown in Fig. 4.19, obtained with CIM modal solutions and the conventional CIM considering discretized ports.

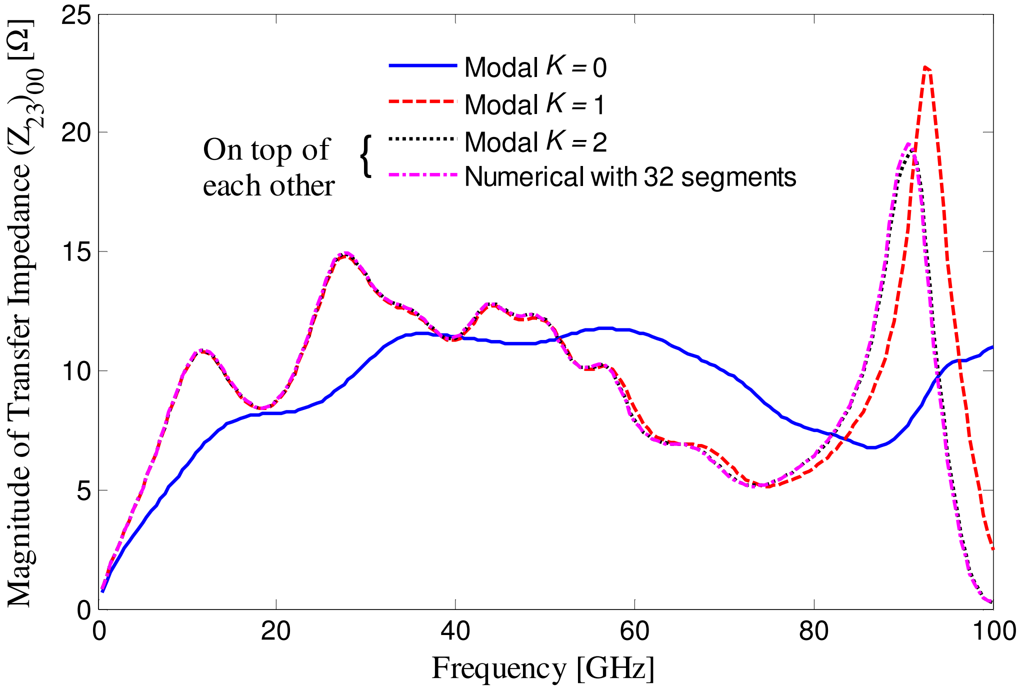

Figure 4.21 Magnitude of transfer impedance of the 0th mode between ports 2 and 3 for the infinite plane case in Fig. 4.19, obtained with CIM modal solutions and the conventional numerical CIM considering discretized ports.

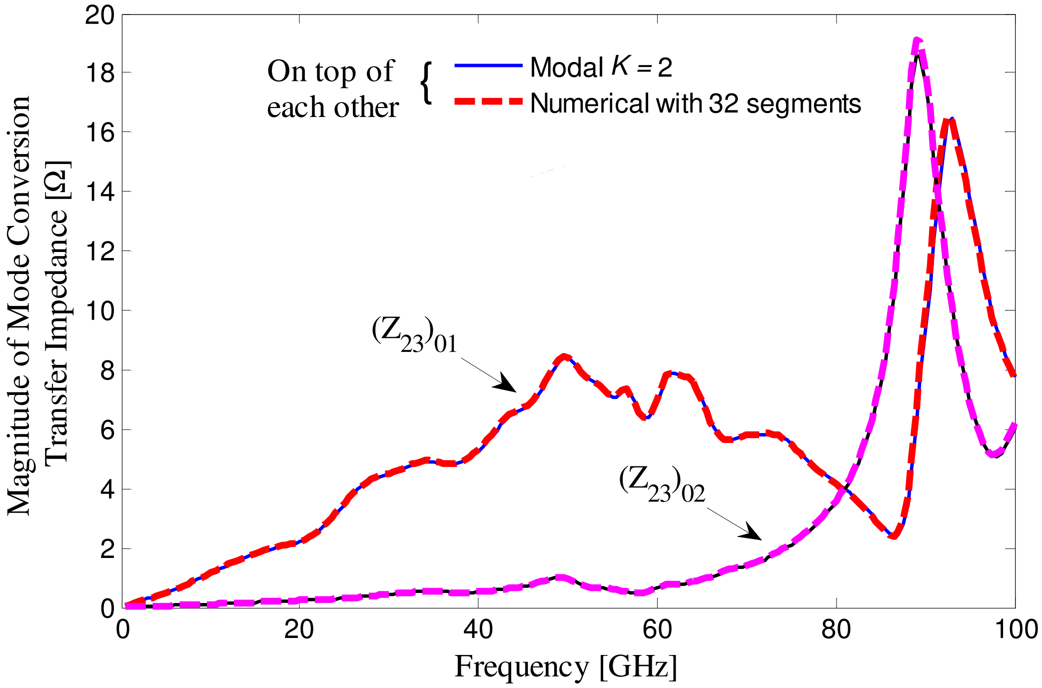

Figure 4.22 Mode conversion transfer impedance between ports 2 and 3 for the infinite plane case in Fig. 4.19, obtained with CIM modal solutions and the conventional CIM considering discretized ports. The modal solution (solid line) overlaps with the numerical solution (dashed line).

The infinite plane case is first studied. The input impedance of the 0th mode for port 1 and the transfer impedance of the 0th mode between port 2 and 3, obtained by the modal solutions and the conventional CIM, are plotted in Fig. 4.20 and Fig. 4.21, respectively. The results of the modal solution converge to the one calculated by the conventional CIM as more anisotropic modes are included in the computation, and they become visually indistinguishable when the mode truncation number K is increased to 2. With an isotropic port assumption ($K = 0$), the impedance results are inaccurate even at frequencies below 10 GHz, whereas adding one higher order mode significantly improves the correlation with the numerical CIM result by discretizing ports into 32 segments up to 60 GHz, as shown in Fig. 4.20 and 4.21.

The mode conversion transfer impedance between port 2 and 3 is shown in Fig. 4.22, where the conversion from the 2nd order mode to the fundamental mode is much less that from the 1st order mode for frequencies below 60 GHz. However, it shows a resonance peak at about 90 GHz, which causes the deviation of the $K = 1$ solution from the numerical CIM result near that frequency.

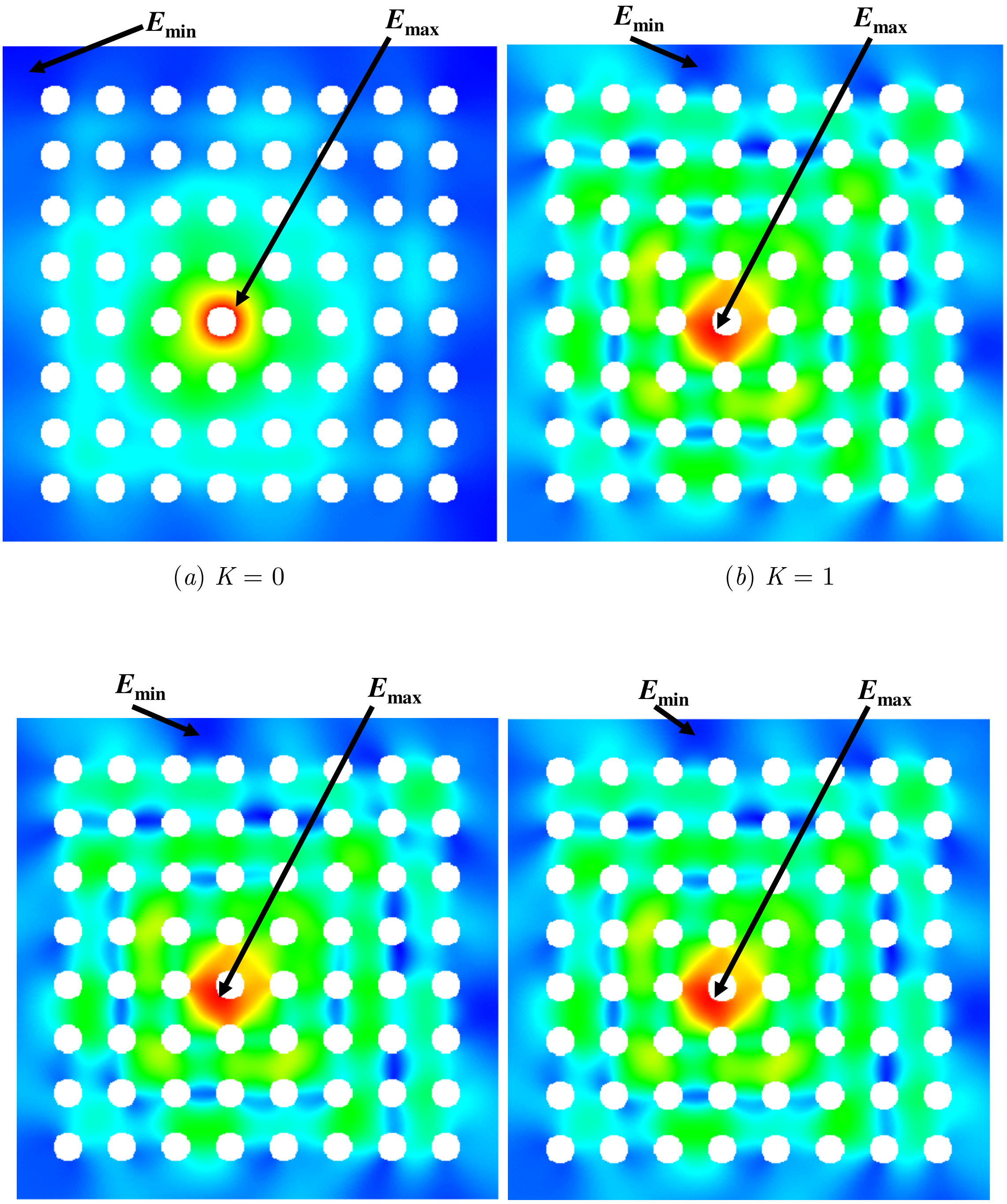

(a) $K = 0$ (b) $K = 1$

(c) $K = 2$ (d) with 32 segments

Figure 4.23 Electric field distribution (linear scale) at 50 GHz for the infinite plane case in Fig. 4.19, obtained with modal solution $K = 0$ (a), $K = 1$ (b), $K = 2$ (c), and numerical solution for ports with 32 segments (d). Port 2 is excited with a 1-mA isotropic current source and all other ports are left open.

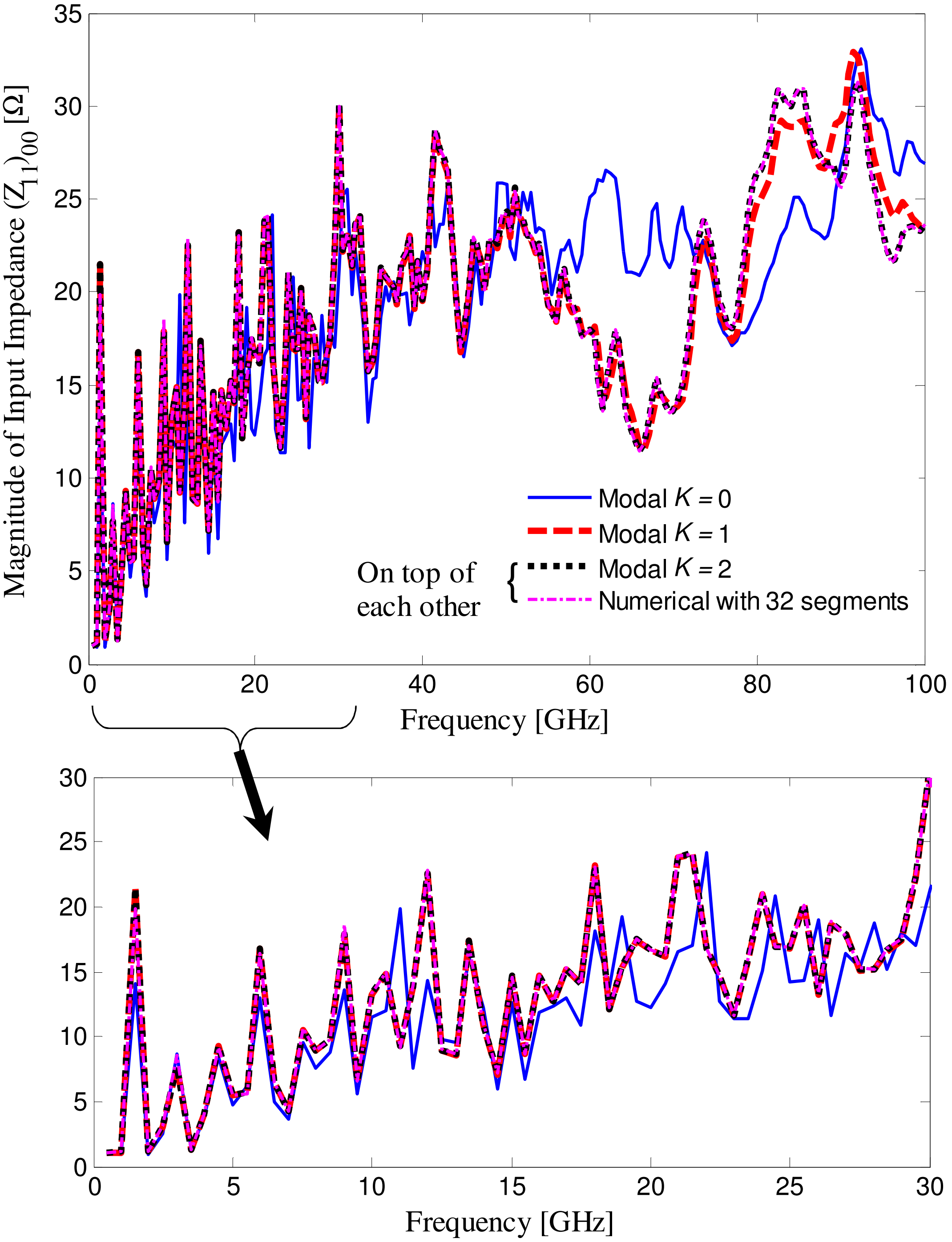

Figure 4.24 Magnitude of input impedance of the 0th mode of port 1 for the finite plane case, as shown in Fig. 4.19, obtained with CIM modal solutions and the pure numerical approach with circular ports discretized into 32 segments.

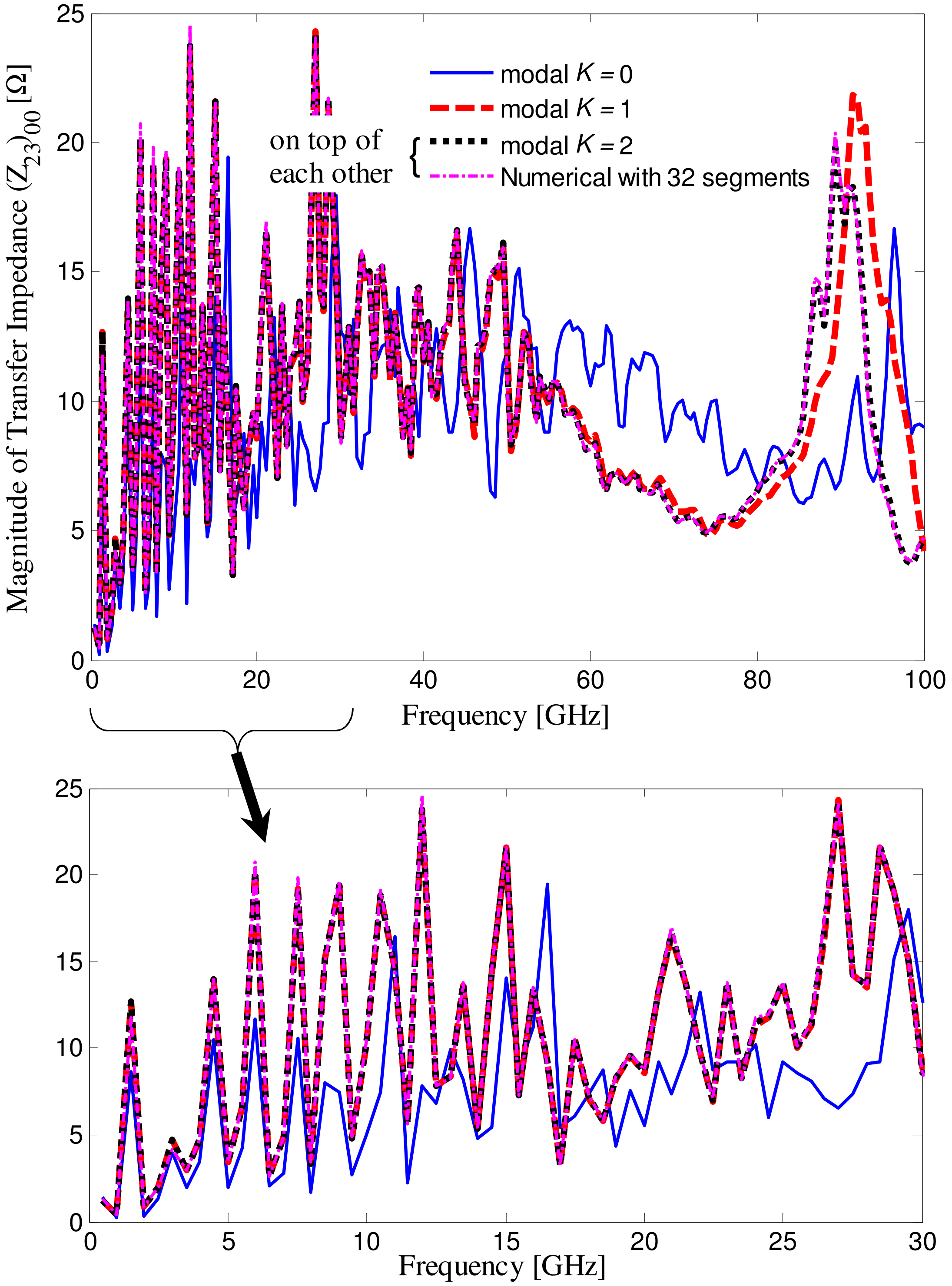

Figure 4.25 Magnitude of transfer impedance of the 0th mode between ports 2 and 3 for the finite plane case in Fig. 4.19, obtained with CIM modal solutions and the pure numerical approach with circular ports discretized into 32 segments.

TABLE 4.1. CPU Time for Computation of the 64-Port Array Case

Cases	MODAL $K = 0$	MODAL $K = 1$	MODAL $K = 2$	NUMERICAL 16 SEGMENTS	NUMERICAL 32 SEGMENTS
Infinite Plane	0.005	0.11	0.44	19.7	159
Finite Plane	5.2	7.8	11.2	56.0	210

Quantities are specified in second per frequency point.
Simulation was run on a 64-bit PC with a single 2.8-GHz CPU.

In comparison to the 2-port results in Fig. 4.12, where the curves are relatively smooth, the impedance results for the array case in Fig. 4.20 and 4.21 oscillate around a baseline due to multiple reflections from other open ports. The intensity and period of the fluctuation depend on the number of ports and pitch of the array. Disregarding the interference among anisotropic modes leads to an underestimation of the magnitude of this oscillation, as can be observed in Fig. 4.21. Therefore, including the anisotropic modes becomes even more important for analysis of large and dense arrays that can contain more than thousands of ports, e.g., in modern BGA via pin fields. The electric field distributions at 50 GHz for the 64-port array of infinite planes are demonstrated in Fig. 4.23 with an excitation of 1 mA isotropic current source at port 2 and all other ports open. Good agreement is achieved between the numerical CIM (d) and modal solution with $K > 0$ (b, c). A strong anisotropic field distribution is observed around the input port 2 and overall inside the array, which is absent in the $K = 0$ solution (a).

The port array analysis is next extended to a finite plane pair with its boundary shown in Fig. 4.19. Simulation results of the input impedance of the 0th mode for port 1 and the transfer impedance of the 0th mode between ports 2 and 3 are plotted in Fig. 4.24 and Fig. 4.25, respectively. In contrast to the one-port case in Fig. 4.17, where the difference between whether or not to include anisotropic modes is small, the results for the port array case show a significant difference between the solutions of $K = 0$ and $K > 0$, especially for frequencies over 20 GHz. This is because reflections from the port array itself become considerably large in comparison to reflections from the plane boundary, which again manifests the importance of considering anisotropic modes in modeling of large and dense arrays.

To evaluate the efficiency gain by extending CIM with analytical modal solutions, the simulation time used for both the infinite and finite plane cases is compared, as shown in Table 4.1. It can be concluded that the efficiency is improved by at least 300 times for the infinite plane case using the analytical solutions in contrast to the numerical one with 32 segments. For the finite planes, the improvement decreases to about 20 times, since the number of unknowns needed for modeling of the plane boundary is not reduced by the extension. In general, the efficiency gain can be expected to be more than 100 when modeling only the circular ports.

4.6. Summary and Discussion

Analytical solutions for circular ports have been derived to model cylindrical vias. The benefits of including the analytical expressions are two-fold. First, it improves the efficiency of CIM by reducing the system matrix size, and second, it enhances the accuracy by avoiding discretization errors such as that shown in Fig. 4.3.

Non-uniform current distribution surrounding vias has been identified by full-wave simulations of two scenarios. In order to model the anisotropy, the circular port definition has been extended to account for higher order azimuthal modes based on the general microwave port definition. Analytical solutions have been derived accordingly to include anisotropic modes. The magnitude of higher order modes depends on the electrical size of the circular port, i.e., the anisotropy is stronger when the frequency is higher or the port radius is larger. A rule of thumb for determining the number of modes for the computation is to ensure that the truncation number is larger than the ratio of the port perimeter to the quarter wavelength.

The efficiency improvement is only achieved for circular ports, whereas modeling of line ports on the boundary remains the same as in the conventional CIM. The number of line ports increases proportional to the frequency and can be very large in the microwave range. One may further expedite the method by exploring fast matrix solvers such as the fast multipole method (FMM) [120]. This is, however, not further investigated in this work. In many real-world applications, the presence of cavity losses and ground vias makes the reflection from board edges negligibly small at high frequencies and sufficient accuracy can be realized by assuming infinite planes.

5. Extension using Hybridization

Hitherto, modeling using CIM and its extension has been bounded to planar wave propagation problems, which means that its applicability is restricted to regions where the 2D assumption is still valid. However, real-world applications of digital systems are usually much more complex and can rarely be described as a pure 2D problem. For instance, in the vicinity of a via transition discontinuity, the conversion from a coaxial transverse electromagnetic (TEM) mode to a transverse magnetic (TM) radial waveguide mode causes a complex local near field distribution that may not be modeled by a 2D solver. Furthermore, analysis of multilayer substrates necessitates proper vertical connections of responses from each single planar structure, which inevitably requires hybridization of CIM with other methods. Another generic 3D-field example is the radiation through power plane edges, which has been neglected so far by assuming a perfect magnetic conductor boundary (PMC) condition.

One distinguishing characteristic of CIM is that it always models a closed contour, which can be arbitrarily defined, as long as the 2D assumption is still valid in the solution domain it encompasses. Combining with the fact that the modeled cavity is well isolated from the outside world by power planes in the vertical direction, we have for each power plane pair a closed system with well-defined boundary conditions. This feature allows us to decompose the system to sub-domains and cope with each of them separately using different techniques, and then join them together in a later stage for a complete system solution.

In this chapter, hybridizations of CIM with other methods will be presented based on the domain decomposition concept [121],[122]. The combining methods include one-port equivalent circuits for the modeling of decoupling capacitors (decaps) and ground vias [14], method of moments for inclusion of edge radiation losses [11], and physics-based models for vias and traces in a multilayer environment [15]. The segmentation technique [85] is selected for merging different sub-domains since the method can handle microwave ports that have been well defined in CIM in Chapter 3 and 4.

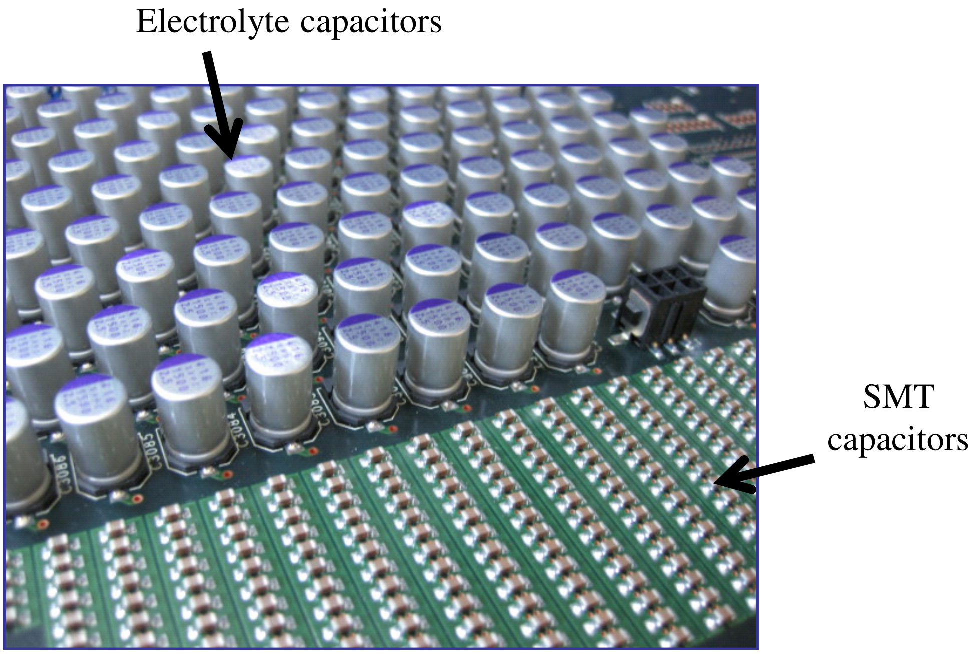

Figure 5.1 An overview of decoupling capacitor placement on a high performance motherboard.

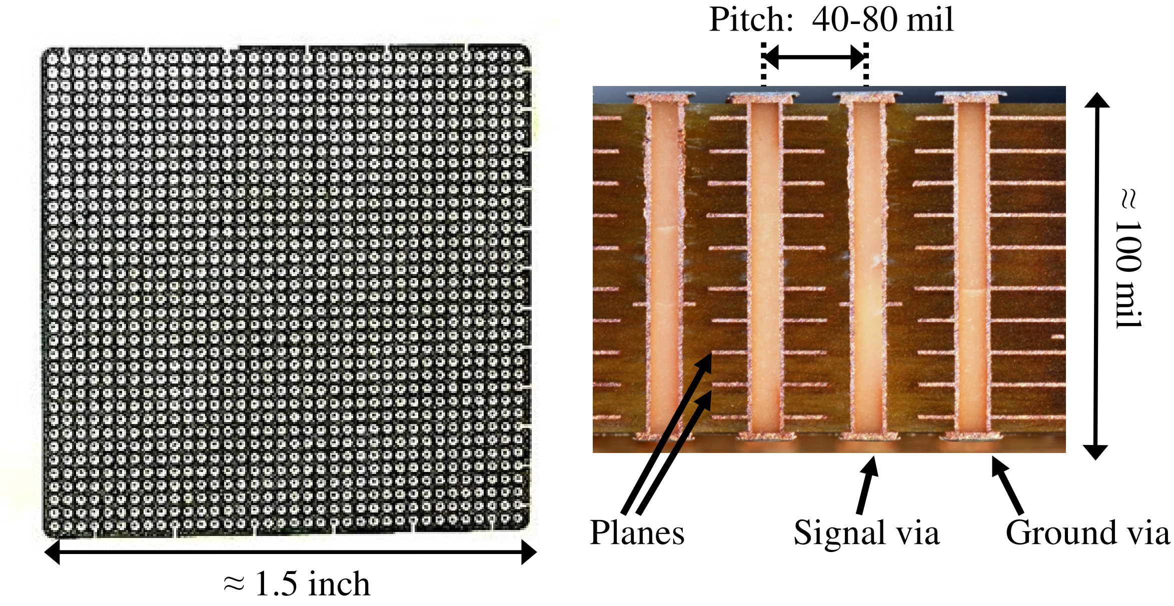

Figure 5.2 Top view of a via pin field on a printed circuit board with approximately 1300 vias (left), about half of which are ground vias. Cross section view of two signal and two ground vias traversing 10 power plane layers (right). *Figure courtesy of IBM Research, Yorktown Heights, NY, USA.*

5.1. Inclusion of One-Port Circuits

In real-world applications, PCBs and packages are populated with many devices such as decaps and other top and bottom layer terminations. The decaps are commonly used for the purpose of supplying extra charge storage and providing low impedance power delivery [22]. Fig. 5.1 shows an overview of part of a high performance motherboard, where a number of decaps are placed densely together to achieve effective power decoupling. On the other hand, power and ground vias are also common design practices for the suppression of SSN by connecting all power planes using power vias and ground planes using ground vias. They also provide a conducting return path for signals [123]-[125]. An exemplary dense via array with approximately 1300 vias is shown in Fig. 5.2, where about half of them are ground and power vias.

Both the decaps and ground via connectivity can be considered as one-port circuits. This section explains the inclusion of their effects in CIM. Decaps are taken as an example for the mathematical procedure, which can be applied to any one-port circuit.

5.1.1. Decoupling Capacitor Model

Decap models can be obtained through measurements, full-wave simulations, or a simple RLC serial resonance circuit [22],[126]. In this work, the RLC equivalent circuit model will be adopted, as shown in Fig. 5.3, where ESR and ESL denote the equivalent serial resistance and inductance, respectively, which are intrinsic parameters that only depends on the manufacturing process and materials. In addition, a parasitic inductance that results from the interconnect between the capacitor and power planes should also be included in the model. Techniques to minimize the parasitic inductance may be found in e.g. [127].

5.1.2. Inclusion of Decoupling Capacitors

The effect of decaps on the power impedance can be included in CIM using the segmentation technique [85]. The effect of the static via-plane capacitance as well as the higher order evanescent modes near the antipad are not considered for the moment since theirs values, typically several fF, are much smaller than the decoupling capacitor value. Modeling of the via-plate capacitance will be discussed in next sections.

With the equivalent model, the decoupling capacitors can be described by a diagonal impedance matrix $\overline{\overline{Z}}^{c}$, with $\overline{\overline{Z}}^{c}\overline{I}^{c} = \overline{V}^{c}$. $\overline{I}^{c}$, $\overline{V}^{c}$ are the current and voltage vectors,

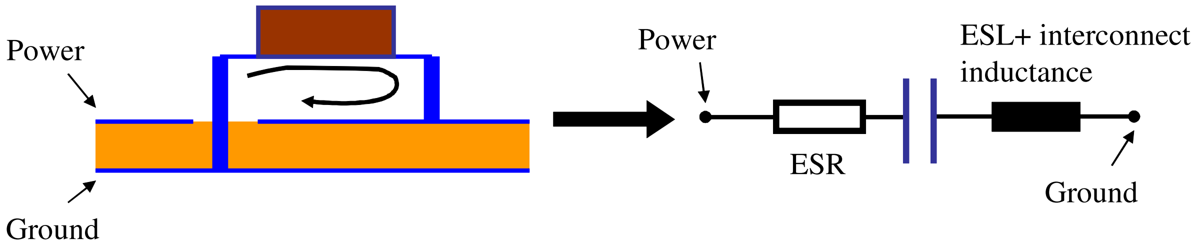

Figure 5.3 Decoupling capacitor model with a serial resonance circuit. ESR and ESL are the equivalent serial resistance and inductance, respectively. The via-plane capacitance is not considered in this illustration.

respectively, on the decoupling capacitors. The diagonal terms in $\overline{\overline{Z}}^{c}$ are calculated as

$$Z_{ii}^{c} = R_i + j(\omega L_i - 1/\omega C_i)\,. \tag{5.1}$$

Here, the circular ports p in CIM are categorized into two groups, ports terminated with decoupling capacitors and not terminated, designated with upper indices t and u, respectively. The impedance matrix $\overline{\overline{Z}}^{pp}$ is next written as

$$\overline{\overline{Z}}^{pp} = \begin{bmatrix} \overline{\overline{Z}}^{uu} & \overline{\overline{Z}}^{ut} \\ \overline{\overline{Z}}^{tu} & \overline{\overline{Z}}^{tt} \end{bmatrix}, \quad \text{and} \quad \begin{bmatrix} \overline{\overline{Z}}^{uu} & \overline{\overline{Z}}^{ut} \\ \overline{\overline{Z}}^{tu} & \overline{\overline{Z}}^{tt} \end{bmatrix} \cdot \begin{bmatrix} \overline{I}^{u} \\ \overline{I}^{t} \end{bmatrix} = \begin{bmatrix} \overline{V}^{u} \\ \overline{V}^{t} \end{bmatrix}. \tag{5.2}$$

Equating the voltages and currents on the connected ports, $\overline{V}^{t} = \overline{V}^{c}$ and $\overline{I}^{t} = -\overline{I}^{c}$, the following expression can be derived

$$\left[\overline{\overline{Z}}^{uu} - \overline{\overline{Z}}^{ut}\left(\overline{\overline{Z}}^{tt} + \overline{\overline{Z}}^{c}\right)^{-1}\overline{\overline{Z}}^{tu}\right] \cdot \overline{I}^{u} = \overline{V}^{u}. \tag{5.3}$$

The resulting matrix in the bracket is then the parallel-plate impedance of the observation ports including the decoupling capacitor effect.

Equation (5.3) is applicable to any one-port circuit in general, for which $\overline{\overline{Z}}^{c}$ is modified to the corresponding circuit model. For example the effect of ground vias can be obtained by making $\overline{\overline{Z}}^{c} = \overline{\overline{0}}$, assuming that they are short circuits.

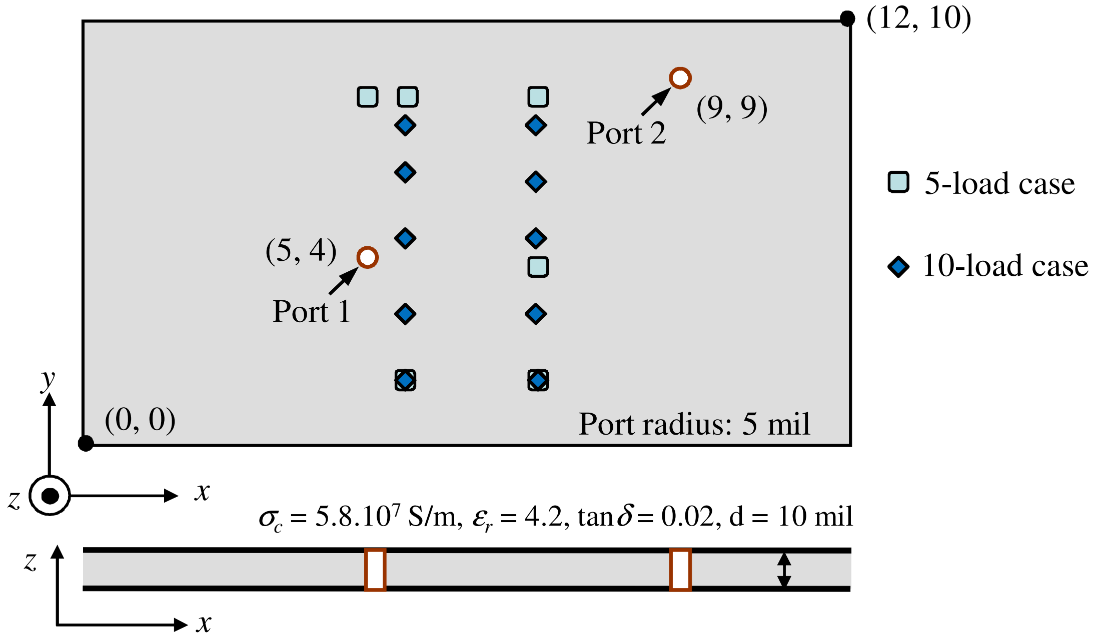

Figure 5.4 Two-port rectangular power plane pair example. The loads can be either decaps or ground vias. Dimensions are given in inches (1 inch ≈ $2.54 \cdot 10^{-2}$ m).

5.1.3. A Rectangular Board Example

A 2-port rectangular power plane configuration is shown in Fig. 5.4. The input and transfer impedances of the bare board are shown in Fig. 5.5, obtained by CIM and full-wave simulations using an FEM solver [117] assuming a PMC boundary condition. Isotropic circular ports for CIM are applied here since the simulated frequencies are low enough and the distances between ports are sufficiently far so that anisotropic modes can be neglected. For the full-wave simulation, a lumped port is used and placed on an antipad region of 15-mil radius. Although the via near field is not accounted for in the CIM, the results from the two methods overlap, indicating a minimal influence of via-plate capacitance in the MHz frequency range.

The computation efficiency of CIM is 112 times better than that of the full-wave solver in this case. Also, CIM has been shown to be more efficient when simulating multiple vias. For instance, if 7 via ports are computed for this case, the full-wave solver is more than 300 times slower than CIM due to the progressive meshing in the full-wave method for small vias that yields many unknowns while the complexity only increases by one unknown per isotropic port in CIM.

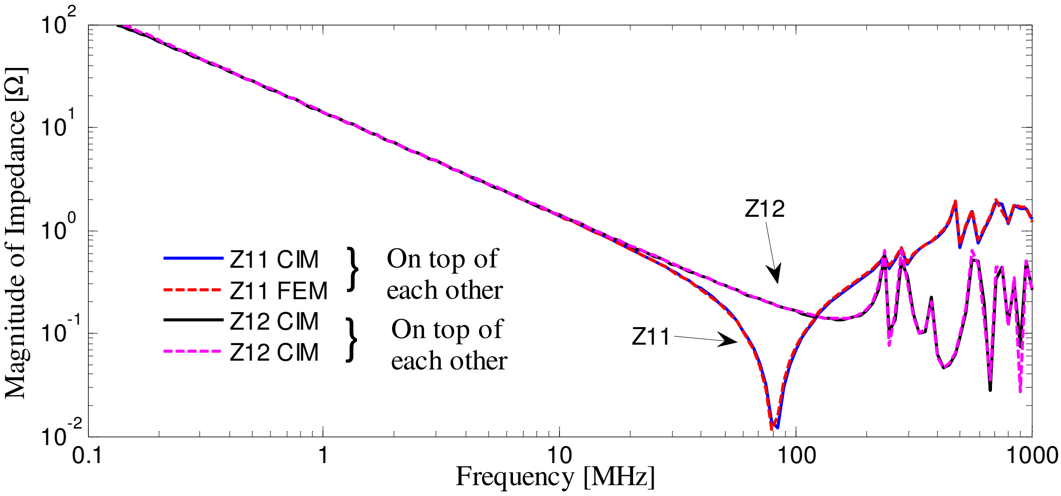

Figure 5.5 Input and transfer impedances of the bare board case in Fig. 5.4, obtained by CIM and compared to FEM full-wave simulation.

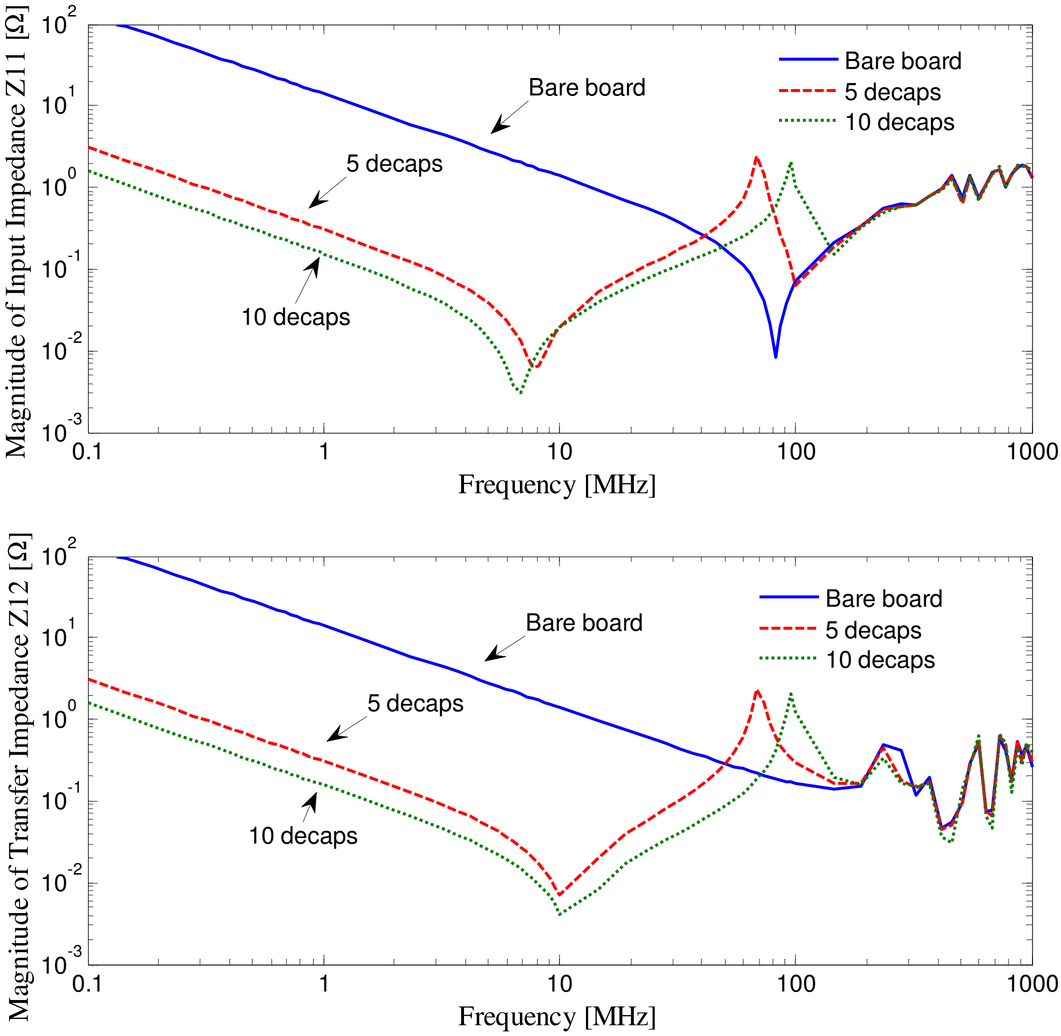

Figure 5.6 Input and transfer impedances of the case in Fig. 5.4 with different numbers decaps, obtained by CIM. The decaps are modelled as 0.1µF capacitors with 30-mΩ ESR and 2-nH total inductance. The decaps reduce the board impedance up to about 30 MHz.

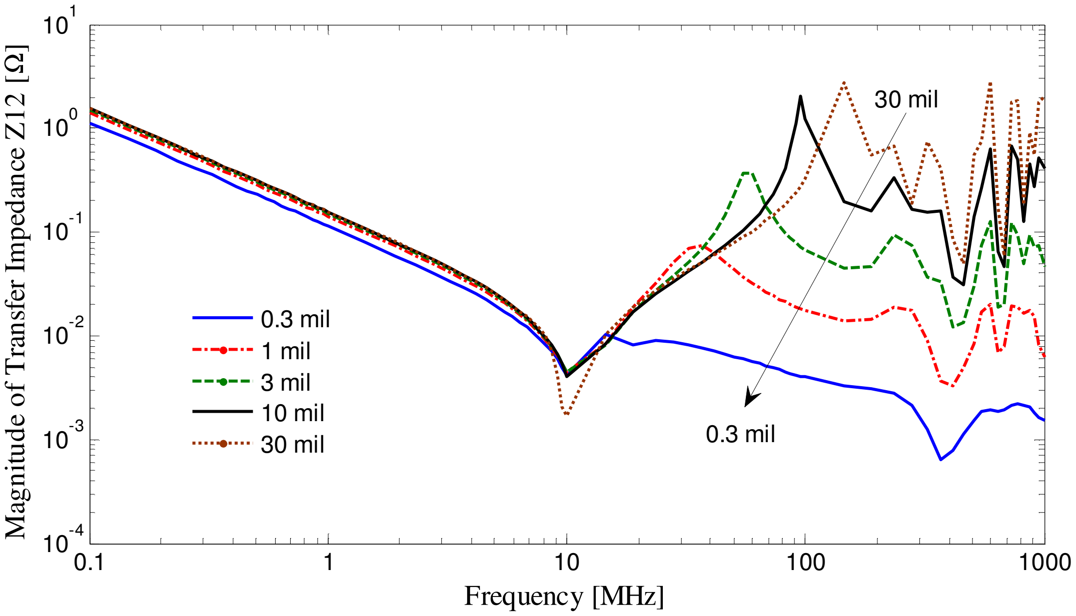

Figure 5.7 Transfer impedance for the rectangular board in Fig. 5.4 for different dielectric thicknesses with 5 decoupling capacitors. The impedance reduction can be achieved by decreasing the dielectric height. The cavity resonances are damped for thinner dielectrics due to the increased conductor loss.

The effect of different numbers of decaps on both input and transfer impedances is plotted in Fig. 5.6, obtained using the technique described above. The decaps are modelled as 0.1 μF capacitors with 30-mΩ ESR and the total parasitic inductance of 2 nH, i.e., the ESL plus the interconnect inductance. The impedances are reduced by about 2 decades up to 10 MHz by placing 5 decaps, whereas doubling the number of decaps cuts the impedance further by a half. A serial resonance is formed at around 10 MHz by the decap capacitances and parasitic inductances. Beyond that, the inductance of the decaps dominates and contributes to an unwanted parallel anti-resonance with the board capacitance at about 80 MHz. Suppression of the anti-resonances can be achieved by decaps that are resonating at those frequencies. In practical design, decap values are arranged in a hierarchical fashion, e.g., 3 values per decade, to accomplish a flat impedance profile for a wideband frequency range [23].

Due to manufacturing and layout restrictions, it is impossible to eliminate parasitic inductances of decaps. The frequency range of the effectiveness of board decaps is usually limited up to 1 GHz. Although high frequency power supplies may be provided by package and IC decaps, low impedance at the board level is still desired in the GHz frequency range to mitigate high frequency SSN. One solution to this is to reduce the distance between power and ground planes [128],[129]. Fig. 5.7 shows the impact of different dielectric heights on the transfer impedance between port 1 and 2 with 5 decaps. For frequencies above 10 MHz where decaps are no longer in effect, the impedance reduction is only realized by decreasing the dielectric thickness. In essence, moving the power plane closer to the ground plane magnifies the electric field strength between them. The benefits of that are two-fold: First, it enhances the charge capacity for the decoupling; second, it increases the conductor loss, as seen in (3.2), that reducing d leads to an increase of the imaginary part of k, which helps damping the cavity resonances.

One utility of CIM is to generate field plots that give an overview on the influence of a particular noise source on the complete board rather than the impedances on discrete spots. The electric field distribution between power and ground planes of the bare board in Fig. 5.4 is illustrated in Fig. 5.8 at 300MHz, obtained by CIM and a full-wave FEM solver [117]. The structure is excited at port 1 with 1 Watt and port 2 is terminated with a 50-Ω resistance. On the right side of Fig. 5.8, the blue frame that encloses the field plot indicates the board edge. The fields at the positions that are very close to the board edge are not calculated in CIM due to poor precision of the numerical integrals near the board boundaries. In principle, the fields in these areas could be extrapolated. One may observe from the field plot that, although the area near the noise source is quiet, hot spots are found in the left lower corner of the board.

Figure 5.9 illustrates the electric field distribution of the board with 5 decaps, as depicted in Fig. 5.4, at 10 MHz with port 1 excited by 1 Watt power and port 2 terminated with 50 Ω. The locations of the capacitors can be recognized in the field map. The amplitude of the electric field across the board area ranges from 9 to 18 V/m, which is much smaller in comparison to a uniform 2.2 kV/m over a bare board with the same excitation and termination, showing an effective bypassing of decaps for a low impedance power supply.

Radiated emissions can also be mitigated by placing decaps. Fig. 5.10 compares the far-field radiation diagrams between the bare board and that with 5 decaps for the same simulation configuration at 10 MHz with port 1 excited by 1 Watt power and port 2 terminated with 50 Ω. The unit Volt is used in Fig. 5.10 since the far-field zone is assumed for the radiation diagram and the electric field is inversely proportional to the distance from the source. Therefore, the actual field strength should be calculated by dividing by the distance. At 10 MHz, the bare board can be considered as a dipole antenna and thus generates a toroid (doughnut) shaped radiation pattern with the maximum electric field lying on the x-y plane. By placing decaps, the electric field distribution around the plane boundary changes, as shown in Fig. 5.9, hence the radiation pattern changes as shown in Fig. 5.10. The maximum electric field strength for the 5-decap case is about 6.55 μV that is around 27 dB lower than 152.45 μV for the bare board.

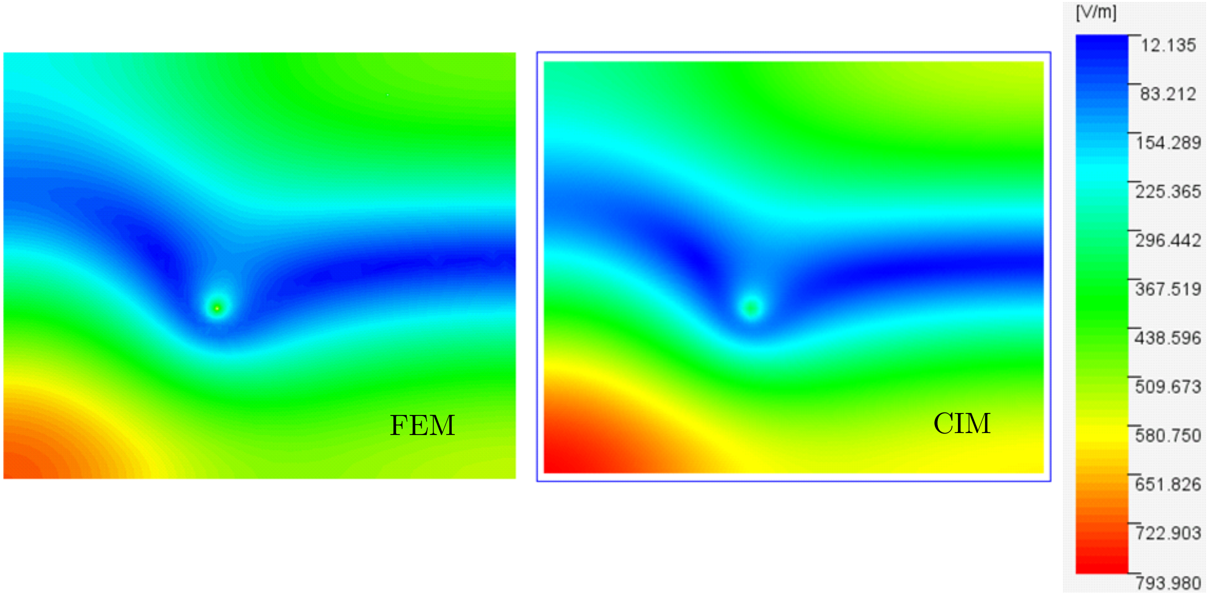

Figure 5.8 Magnitude of the electric field distribution between power and ground planes of the bare board in Fig. 5.4 at 300 MHz with port 1 excited by a 1-Watt power source and port 2 terminated with 50 Ω, using CIM (right) and a full-wave FEM solver (left). The dielectric thickness is 10 mil.

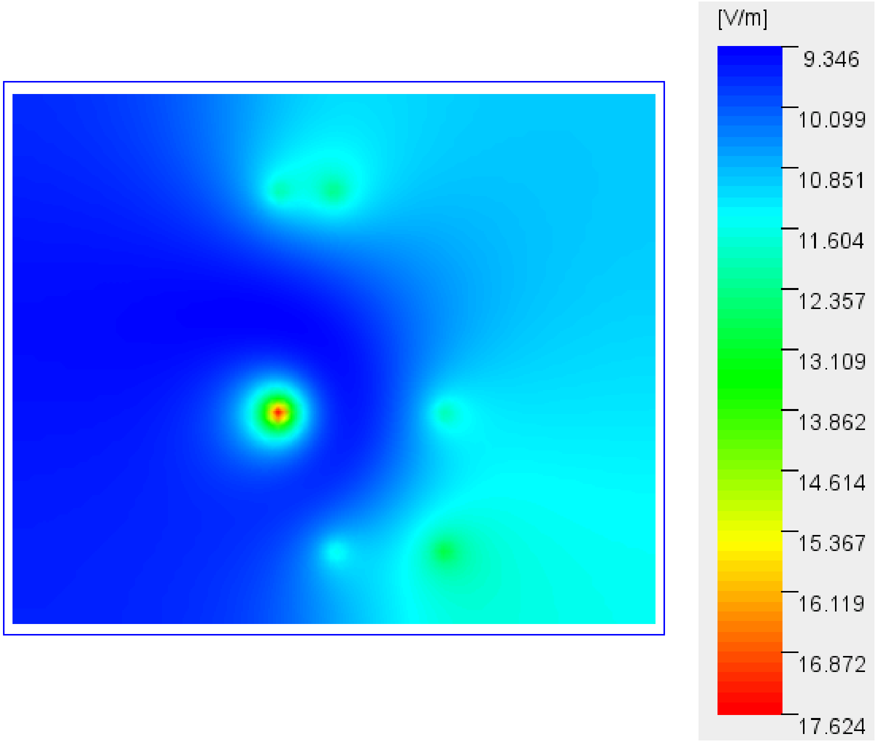

Figure 5.9 Magnitude of the electric field distribution between power and ground planes for the rectangular board in Fig. 5.4 with 5 decaps at 10 MHz with port 1 excited by a 1-Watt power source and port 2 terminated with 50 Ω, obtained using CIM. The dielectric thickness is 10 mil.

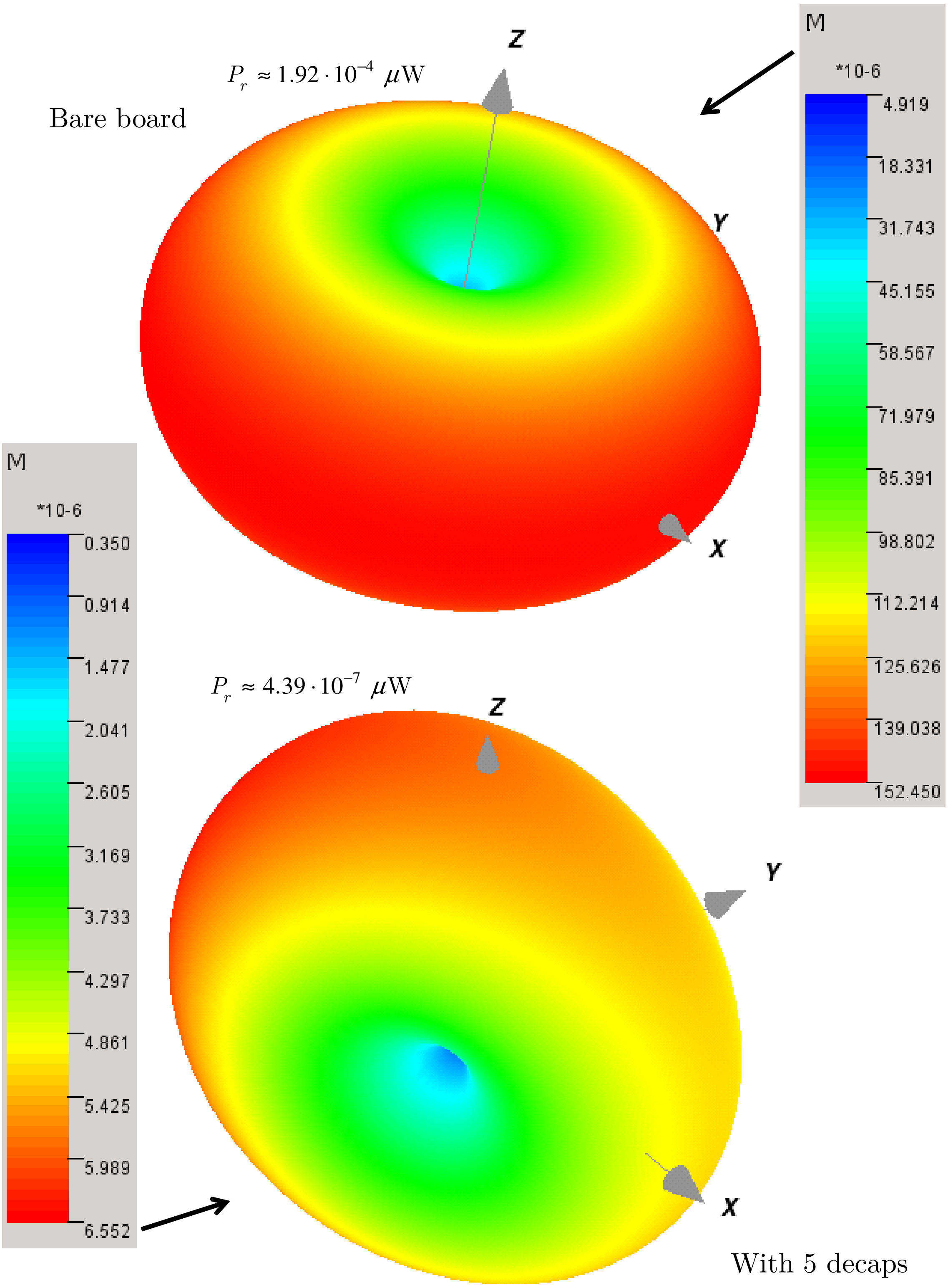

Figure 5.10 Radiation diagram of the bare board and that with 5 decaps, as shown in Fig. 5.4, at 10 MHz with port 1 excited by 1 Watt power and port 2 terminated with 50 Ω, using CIM. The dielectric thickness is 10 mil. The radiated power is calculated by numerical integration of the Poynting vector over a unit sphere.

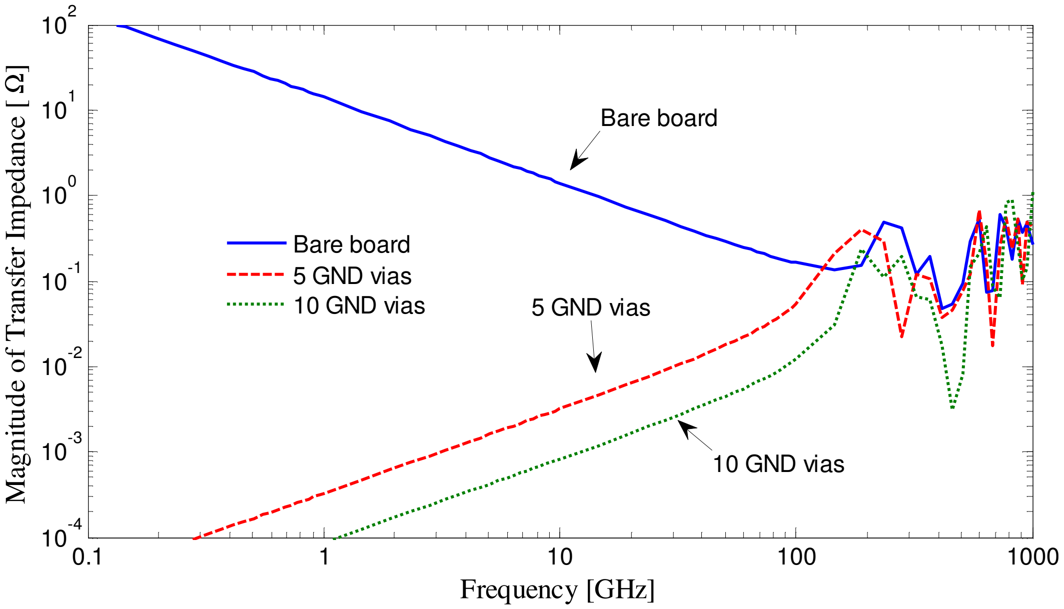

Figure 5.11 Input and transfer impedances of the case in Fig. 5.4 with different numbers of ground vias, obtained by CIM. The ground vias are modelled as short circuits.

From the radiation diagram in Fig. 5.10, one may also obtain the total radiated power by an integral of the Poynting vector over a unit sphere A_u as

$$P_r = \frac{1}{2} \oiint_{A_u} \vec{S} \cdot d\vec{A}_u = \frac{1}{2\eta_0} \oiint_{A_u} \left|\mathcal{E}\right|^2 dA_u \tag{5.4}$$

where $\vec{S}$ denotes the complex Poynting vector and η_0 is the vacuum wave impedance. The radiated power is also reduced by about 27 dB with 5 decaps in comparison to a bare board.

The decaps are the connection between power and ground planes, for which a DC potential difference must be maintained. For neighboring power or ground planes, power or ground vias are usually used, respectively, for the mitigation of SSN. Fig. 5.11 plots the transfer impedance between ports 1 and 2 of the rectangular board configuration in Fig. 5.4 with different numbers of ground vias, assuming that both of the upper and lower planes are grounds. The ground vias are modeled as short circuits in CIM. As observed in Fig. 5.11, the impedance starts inductive at low frequencies owing to the mutual inductance between two current loops that the ports form with ground vias. At frequencies higher than 100 MHz, the impedance is again dominated by board resonances. Usually, ground vias are placed much closer to the signal vias to reduce parasitic inductances for a broader bandwidth.

5.2. Inclusion of Radiation Loss

So far, it has been assumed that the power planes are surrounded by a perfect magnetic conductor (PMC), i.e., an ideal open boundary condition. Under this approximation, a magnetic current distribution can be obtained using CIM, and the radiated emission can also be estimated as the radiation from an equivalent magnetic current around the board boundary [14]. However, the finite impedance of the radiation field may not be neglected for the cases of thick and low loss cavities [130]. Also, it was found in [15] that for the radiation emission calculation the PMC boundary approximation leads to less accurate results at high frequencies for multilayer structures. Therefore, it becomes necessary to include the radiation loss into the power plane modeling for low loss and multilayer applications in order to obtain accurate power impedances and the radiation fields.

In principle, full-wave solvers can be used to analyze power planes including radiation losses. However, high computational burden limits the application of these solvers. It has been shown in [130],[131] that the effect of the radiation loss can be accounted for analytically in the cavity resonator model by modifying the complex wavenumber. The drawback of this approach is that it is restricted to rectangular power planes where an analytical calculation of the field distribution around the edges is possible. Therefore, for including the radiation loss of arbitrary shaped power planes, a hybridization of CIM with the method of moments (MoM) is presented. The solution domain is divided into interior and exterior subdomains. The interior domain is solved using CIM, whereas the exterior radiated fields can be obtained by considering solely the magnetic currents around the board circumference. In both subdomains, only the cavity boundary is necessary to be discretized, and thus can be solved efficiently.

5.2.1. Domain Decomposition

A typical power plane pair configuration with dielectric thickness d is shown in Fig. 5.12. The division of the solution domains is depicted by the dashed line. Since the electric current flows dominantly on the inner side of the power planes, the interaction between the interior and exterior subdomains occurs only through the coupling at the boundary of the cavity, denoted as C, as shown in Fig. 5.12. Thus, the two subdomains can be treated independently. The internal domain is 2D in nature and can be solved by CIM, whereas the external domain constitutes a 3D radiation problem that is best suited to the MoM. The final solution is found by matching boundary condition at the contour C by forcing continuity of tangential electrical and magnetic fields.

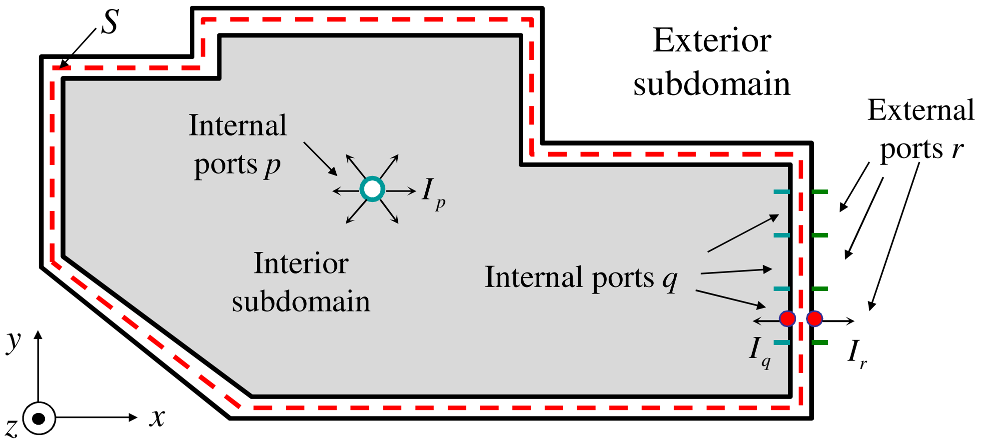

(a) Top view

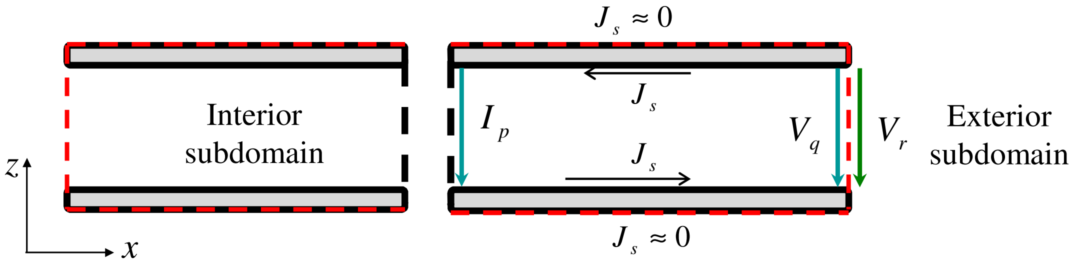

(b) Cross section view

Figure 5.12 Power plane structure and definition of the solution domains for inclusion of the radiation loss. (a) Top view, (b) cross section view.

5.2.2. Modeling of the External Domain

The exterior domain consists of the cavity boundary as well as the upper and lower metal planes. An exact solution would involve discretization and computation of both, which would as complex as the original problem. However, since the power planes lie approximately on the symmetry plane of the radiation field, currents on the outer surfaces of the planes may be neglected. Hence, the radiation fields can be seen as only produced by the magnetic surface current on the boundary C without considering the metal planes. This approximation is illustrated in Fig. 5.13. Due to the short distance between two power planes, the electric field lines have nearly rotational symmetry around the magnetic current source. Therefore, one may neglect the board thickness and the computation is only related to magnetic currents.

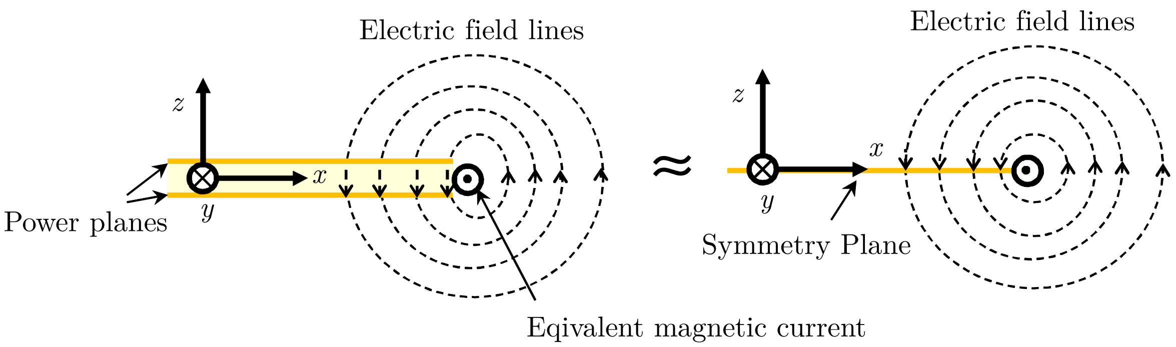

Figure 5.13 Illustration of the approximation of the radiation field from power planes to that from a magnetic current source. Due to the short distance between two power planes, the electric field lines have nearly rotational symmetry around the magnetic current source. Therefore, the board thickness is neglected for the radiation admittance calculation.

In order to connect the exterior to the interior domain, it is necessary to obtain the radiation admittance associated with the outer boundary, which is equivalent to solve a radiation problem from a magnetic current source. It is well-known for electric surface currents that the electric field integral equation (EFIE) can be applied [36].

$$\left.\vec{\mathcal{E}}(\boldsymbol{r})\right|_{\tan} = \frac{1}{4\pi}\iint_A \left.\left[j\omega\mu_0\vec{\mathcal{J}}_s(\boldsymbol{r}')\frac{e^{-jk|\boldsymbol{r}-\boldsymbol{r}'|}}{|\boldsymbol{r}-\boldsymbol{r}'|} + j\frac{\nabla'\cdot\vec{\mathcal{J}}_s(\boldsymbol{r}')}{\omega\varepsilon_0}\nabla\frac{e^{-jk|\boldsymbol{r}-\boldsymbol{r}'|}}{|\boldsymbol{r}-\boldsymbol{r}'|}\right]dA'\right|_{\tan}, \tag{5.5}$$

where $\boldsymbol{r}$ denotes an observation point in free space. $\vec{\mathcal{J}}_s(\boldsymbol{r}')$ represents an electric surface current density on the surface A. ε_0 and μ_0 are the free space permittivity and permeability, respectively. Based on the duality theorem [36]

$$\vec{\mathcal{E}} \sim \vec{\mathcal{H}}, \quad \vec{\mathcal{J}}_s \sim \vec{\mathcal{M}}_s, \quad \varepsilon \sim \mu, \tag{5.6}$$

one can rewrite (5.5) with regard to magnetic surface currents on the cavity boundary,

$$\left.\vec{\mathcal{H}}(\boldsymbol{r})\right|_{\tan} = \frac{d}{4\pi}\cdot\oint_C \left.\left[j\omega\varepsilon_0\vec{\mathcal{M}}_s(\boldsymbol{r}')\frac{e^{-jk|\boldsymbol{r}-\boldsymbol{r}'|}}{|\boldsymbol{r}-\boldsymbol{r}'|} + \frac{j\nabla'\cdot\vec{\mathcal{M}}_s(\boldsymbol{r}')}{\omega\mu_0}\nabla\frac{e^{-jk|\boldsymbol{r}-\boldsymbol{r}'|}}{|\boldsymbol{r}-\boldsymbol{r}'|}\right]ds'\right|_{\tan}, \tag{5.7}$$

where $\vec{\mathcal{M}}_s(\boldsymbol{r}') = \mathcal{E}_z(\boldsymbol{r}')\cdot(\vec{\boldsymbol{e}}_z \times \vec{\boldsymbol{n}}')$ is the magnetic surface current density on boundary C with $\vec{\boldsymbol{n}}'$ the normal vector of the boundary surface pointing into the exterior subdomain. Here, it is assumed that the magnetic current is constant in the z-direction.

For solving the exterior domain, the EFIE (5.7) is written in the following equation system

$$\overline{\overline{Y}}^{rr}\,\overline{V}^{r} = \overline{I}^{r}, \tag{5.8}$$

where the index r denotes the external ports, as shown in Fig. 5.12. $\overline{V}^{r}$ and $\overline{I}^{r}$ are voltage and current vectors of the same sizes as $\overline{V}^{q}$ and $\overline{I}^{q}$ in the CIM formulation (3.22), provided that the discretization is the identical for boundaries of both internal and external domain. To match the CIM line port definitions (3.7) and (3.8), one may similarly apply pulse basis functions and define the voltages and currents for the external domain as

$$V_r = \mathcal{M}_s \cdot d, \tag{5.9}$$

$$I_r = -\mathcal{H}_{\tan} \cdot W, \tag{5.10}$$

where W is the port width. Notice the minus sign in (5.10), which is a result of different definitions of current directions for the CIM and MoM domains, as depicted in Fig. 5.12. Followed by a point matching procedure [52], the admittance matrix of the radiation fields $\overline{\overline{Y}}^{rr}$ can be found.

For a more accurate computation, triangular basis functions followed by a razor-blade testing procedure is actually applied in this work for the establishment of (5.8). Detailed explanation of that can be found in [132]. However, a misalignment of port definitions occurs as shown in Fig. 5.14(a), where the CIM line ports are shifted by half port width to the MoM basis functions. This can be resolved by applying an approximation of triangular basis using pulse basis functions in CIM [52], as depicted in Fig. 5.14(b), for which the triangle shape is approximated by 4 line pulses. This operation brings the approximated triangular CIM port to the exact position of the MoM ports, as shown in Fig. 5.14(c). One disadvantage here is that the boundary C has to be discretized finer by a factor of 2, and thus the computational efficiency of CIM is compromised.

5.2.3. Merging of Sub-domains

To join the solutions of the two subdomains, the continuity of the tangential electric and magnetic field on boundary C is enforced, by which one can eliminate the

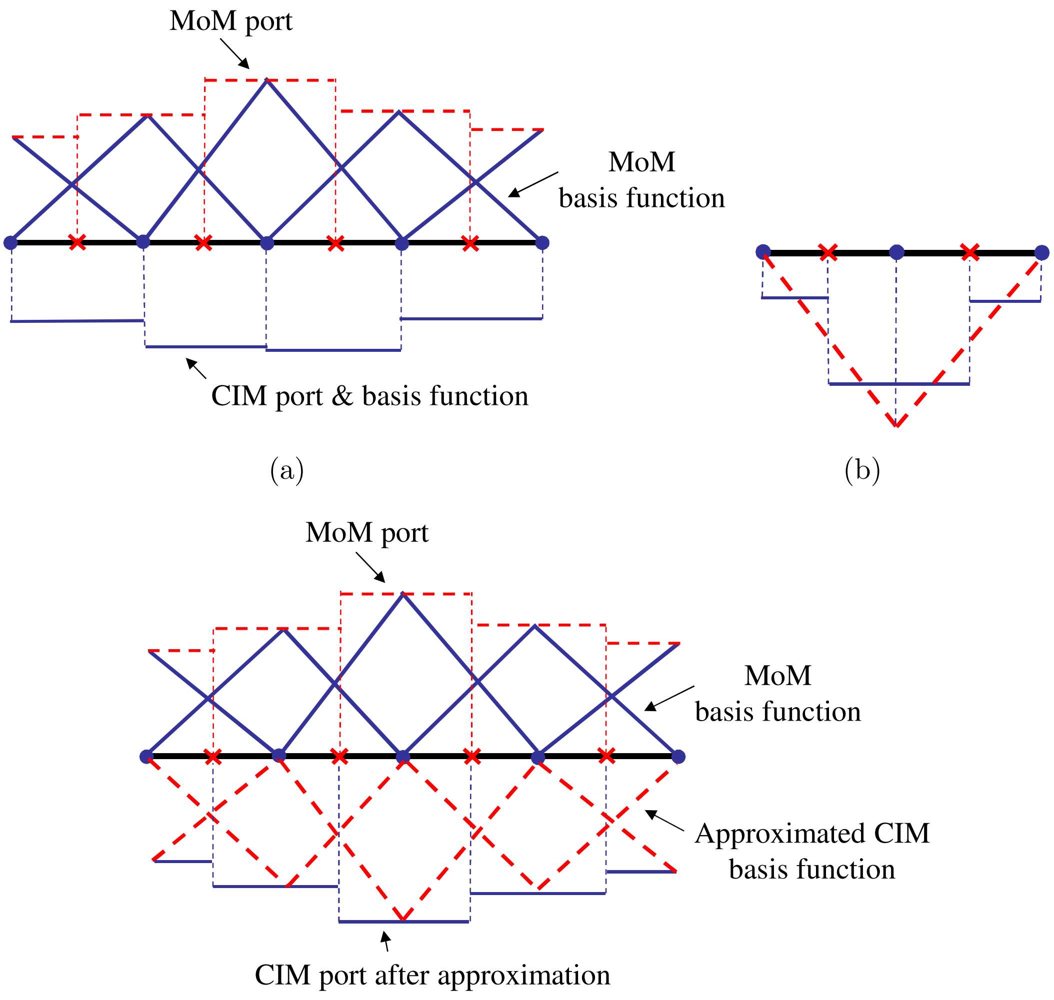

(a) (b)

(c)

Figure 5.14 Approximation of MoM triangular basis functions using CIM pulse basis functions. (a) Illustration of misalignment between CIM and MoM ports. (b) Approximation of one triangular basis function using four CIM ports. (c) Illustration of aligned CIM ports with MoM basis functions.

boundary ports to form the solution of the complete domain including radiation fields. In terms of voltages and currents, the following conditions apply:

$$\overline{V}^{q} = \overline{V}^{r}, \qquad \overline{I}^{q} = -\overline{I}^{r}. \tag{5.11}$$

Combining (5.11) with (5.8) and (3.22), one obtains the following relations

$$\overline{I}^{q} = \left[\overline{\overline{Z}}^{qq} + \left(\overline{\overline{Y}}^{rr}\right)^{-1}\right]^{-1} \overline{\overline{Z}}^{qp}\,\overline{I}^{p}, \tag{5.12}$$

$$\bar{\bar{Z}}^{pq}\bar{I}^{q} + \bar{\bar{Z}}^{pp}\bar{I}^{p} = \bar{V}^{p}. \tag{5.13}$$

Substituting (5.12) into (5.13) leads to

$$\bar{\bar{Z}}^{pq}\left(\bar{\bar{Z}}^{qq} + \bar{\bar{Z}}^{rr}\right)^{-1}\bar{\bar{Z}}^{qp}\bar{I}^{p} + \bar{\bar{Z}}^{pp}\bar{I}^{p} = \bar{\bar{Z}}^{p}\bar{I}^{p} = \bar{V}^{p}, \tag{5.14}$$

where $\bar{\bar{Z}}^{rr} = \left(\bar{\bar{Y}}^{rr}\right)^{-1}$ is the radiation impedance matrix. The result is an impedance matrix $\bar{\bar{Z}}^{p}$ that only concerns the circular ports, expressed as

$$\bar{\bar{Z}}^{p} = \bar{\bar{Z}}^{pp} \underbrace{-\bar{\bar{Z}}^{pq}\left(\bar{\bar{Z}}^{qq} + \bar{\bar{Z}}^{rr}\right)^{-1}\bar{\bar{Z}}^{qp}}_{\bar{\bar{Z}}_{corr}}. \tag{5.15}$$

This joining procedure is in fact the segmentation technique, described in [85]. In comparison to the solution of a PMC boundary, the new expression (5.15) includes an additional correction term $\bar{\bar{Z}}_{corr}$ that summarizes the contribution of the radiation loss to the power impedance at the internal ports *p*. The correction impedance is inversely related to the radiation impedance $\bar{\bar{Z}}^{rr}$ and the self-impedance of boundary ports $\bar{\bar{Z}}^{qq}$ that are determined by the boundary profile of power planes. More importantly, it is proportional to the transfer functions between internal and boundary ports, $\bar{\bar{Z}}^{pq}$ and $\bar{\bar{Z}}^{qp}$, which depends on the distance from vias to the boundary as well as the loss in the cavity. Apparently, $\bar{\bar{Z}}_{corr}$ will have a more significant contribution for vias close to the boundary and for low loss dielectrics.

As explained in Section 3.4, by virtue of the field equivalence principle, the radiated far fields from the power planes can be approximated as being radiated from the equivalent magnetic surface current on *C*. So far, the magnetic current has been obtained by calculating a voltage distribution around the boundary with PMC condition as $\bar{V}^{q} = \bar{\bar{Z}}^{qp}\bar{I}^{p}$, which is only an approximation. In this hybrid approach, the voltage distribution can be calculated by substituting (5.11) and (5.12) into (5.8) as

$$\bar{V}^{q} = \bar{\bar{Z}}^{rr}\left(\bar{\bar{Z}}^{qq} + \bar{\bar{Z}}^{rr}\right)^{-1}\bar{\bar{Z}}^{qp}\bar{I}^{p}. \tag{5.16}$$

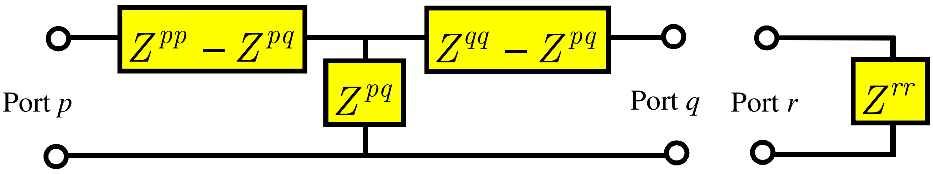

Figure 5.15 An equivalent circuit illustration of the parallel connection between radiation impedance and the power plane impedance. Port q can be assumed open (PMC boundary) only if $Z^{rr} \gg Z^{qq}$, which may not be true for low loss cavities at resonances.

It can be concluded from (5.16) that the radiation impedance is in parallel with the power impedance. An equivalent circuit model is shown in Fig. 5.15 by assuming single entries for the ports p, q, and r in the corresponding impedance matrices. For the radiation computation, the boundary voltage obtained by assuming the PMC condition is a good approximation if the external radiation impedance is much larger than the internal impedance observed at the boundary. However, this may not be true, especially for low loss cavities where the internal impedance at resonance frequencies can be very high. Boundary voltages obtained by (5.16) should be used in those cases to calculate the equivalent surface magnetic current for a correct determination of the far field radiation.

5.2.4. Validation and Examples

A rectangular power plane pair with a port of 10 mil radius at the center, as shown in Fig. 5.16, is simulated using the hybrid method. The power planes are configured as perfect electric conductors (PEC) and the dielectric is lossless, thus the real part of the input power is only dissipated by the radiation field. This is not captured by methods assuming the PMC boundary condition that prevents radiation from the structure. As a consequence, the real part of the input impedance is zero using CIM alone. However, the hybrid method predicts a nonzero real part of the input impedance, as shown in Fig. 5.17, owing to the radiation loss.

The same configuration is simulated using a MoM full-wave solver [43]. The proposed method shows a good agreement with the MoM solution except for the very low frequencies, possibly due to the instability of the CIM system matrix near DC in lossless cases. The efficiency of the proposed method is, however, much better due to the fact that only the boundary needs to be discretized, as shown in Fig. 5.18(b). In contrast, the whole plane has to be discretized in MoM, as shown in Fig. 5.18(a). The

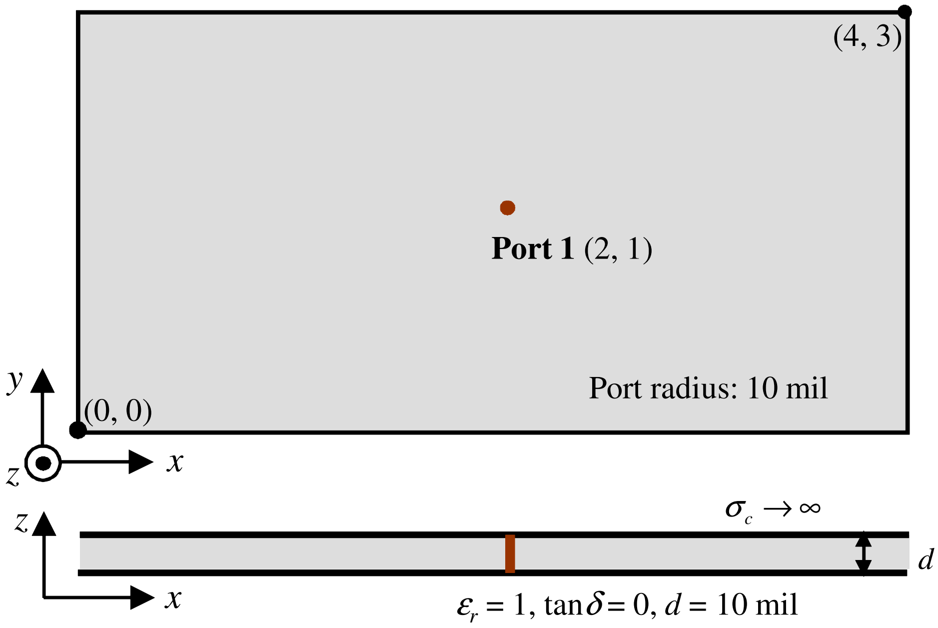

Figure 5.16 Rectangular plane pair example with one port at the center. Dimensions are given in inches (1 inch ≈ $2.54 \cdot 10^{-2}$ m).

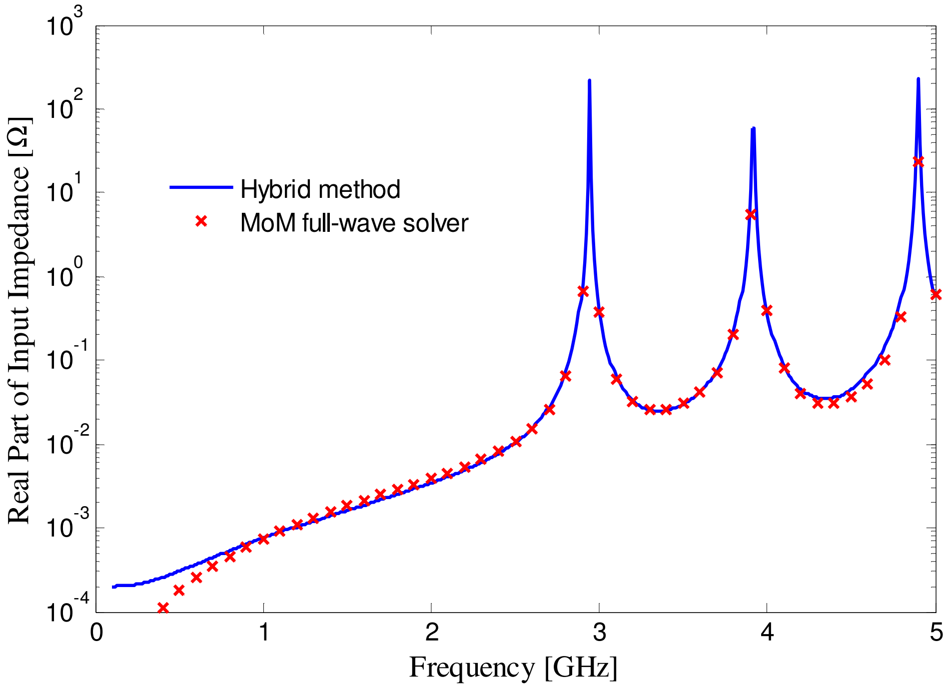

Figure 5.17 Real part of the input impedance computed for the case in Fig. 5.16, obtained with the proposed hybrid method and a full-wave MoM simulation. Real part of the input impedance indicates the radiated power for this case.

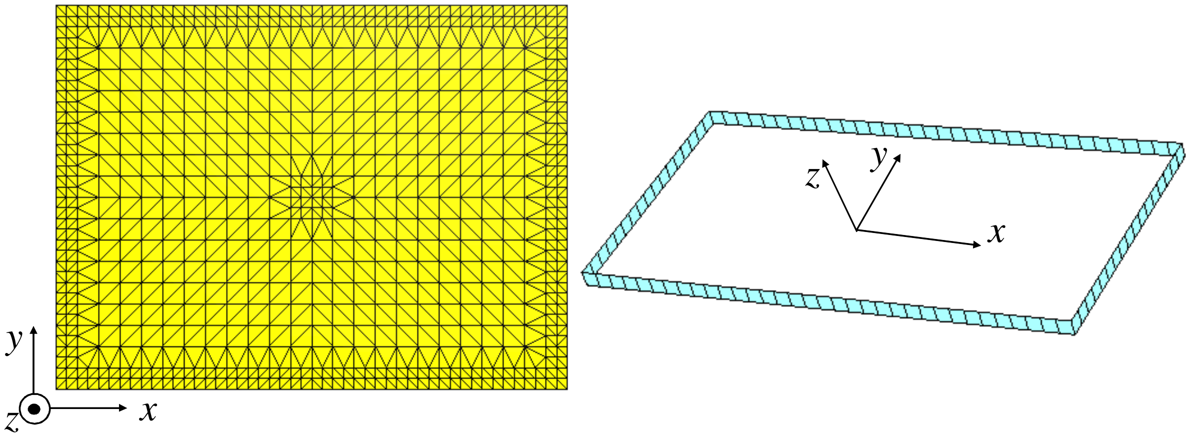

(a) MoM discretization (b) Hybrid method discretization

Figure 5.18 Discretization at 5 GHz of the power plane pair case in Fig. 5.16 by (a) MoM full-wave solver and (b) the hybrid method. The hybrid method needs much fewer unknowns since only the boundary is discretized.

solving time of the MoM solver is about 22 second per frequency point (s/freq), whereas the hybrid approach takes less than 0.1 s/freq.

The second example is an irregular shaped copper plane pair with a 60 mil thick lossless dielectric layer, shown in Fig. 5.19. An FEM based full-wave solver [117] is used to validate the simulation results. In the FEM simulation, a coaxial lumped port is defined as excitation, leading to a capacitive parasitic via near field that is not taken into account by the proposed hybrid method. This extra capacitance is handled with the physics-based via model in the next section. Its value is analytically calculated to be about 85 fF [133]. An airbox is defined to account for the radiation loss in the FEM simulation.

The input impedances calculated by both the hybrid method and the FEM solver are plotted in Fig. 5.20, which shows a good agreement. The simulation time for the FEM solver is over 4 minutes per frequency, whereas about 0.6 s/freq is needed for the hybrid method. The magnitude of the correction impedance, defined in (5.15), is shown in Fig. 5.21. The FEM result is obtained by subtracting the input impedance simulated with a PMC boundary condition from the result with an airbox, which corresponds to the definition in (5.15). This correction impedance manifests the difference between the two boundary conditions seen by the input port. As shown in Fig. 5.21, it increases with the frequency and can be particularly high near and at the resonance frequencies.

Fig. 5.22 shows the radiated power of the structure in Fig. 5.19, obtained by an integral of the Poynting vector as in (5.4). The excitation is 1-Watt power at the input port.

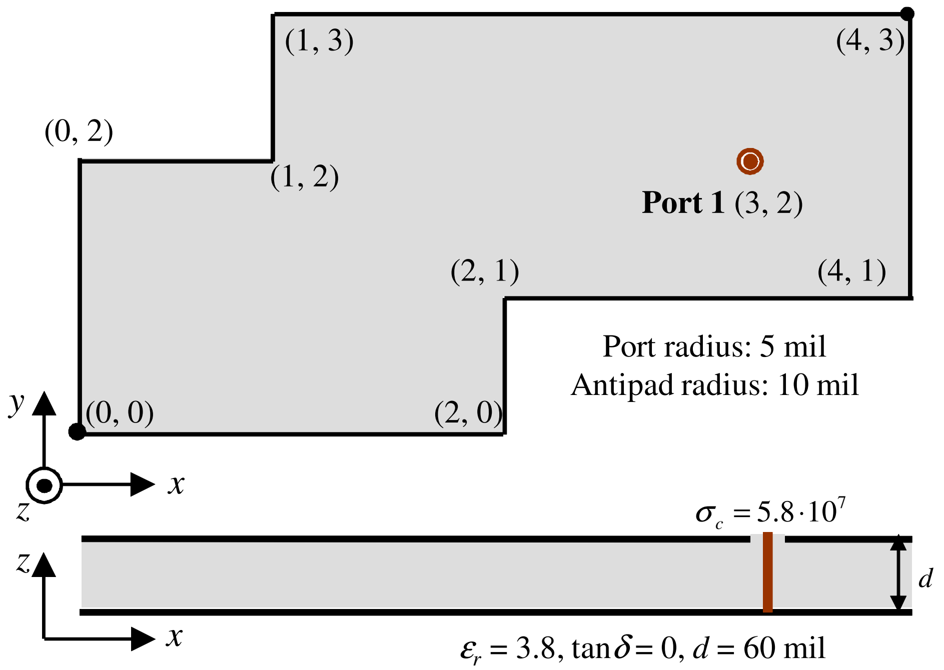

Figure 5.19 An irregular copper plane pair example with a thick cavity. Dimensions are given in inches (1 inch ≈ $2.54 \cdot 10^{-2}$ m).

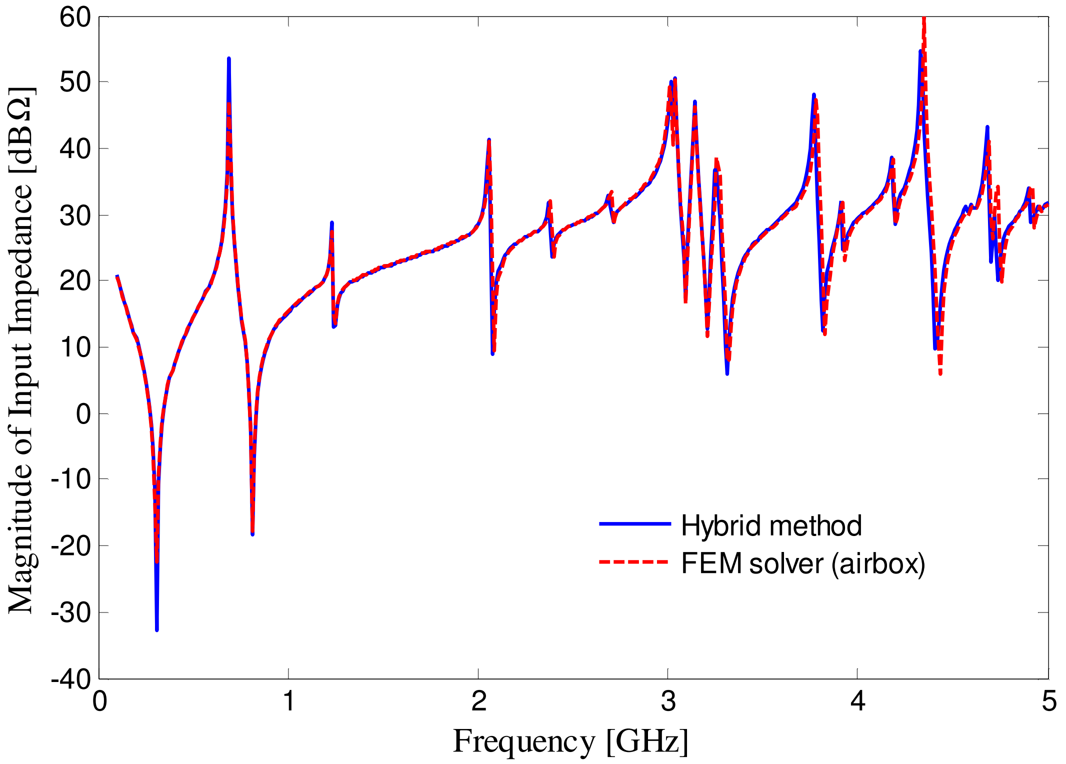

Figure 5.20 Magnitude of the input impedance computed for the case in Fig. 5.19, obtained with the proposed hybrid method and a full-wave FEM simulation.

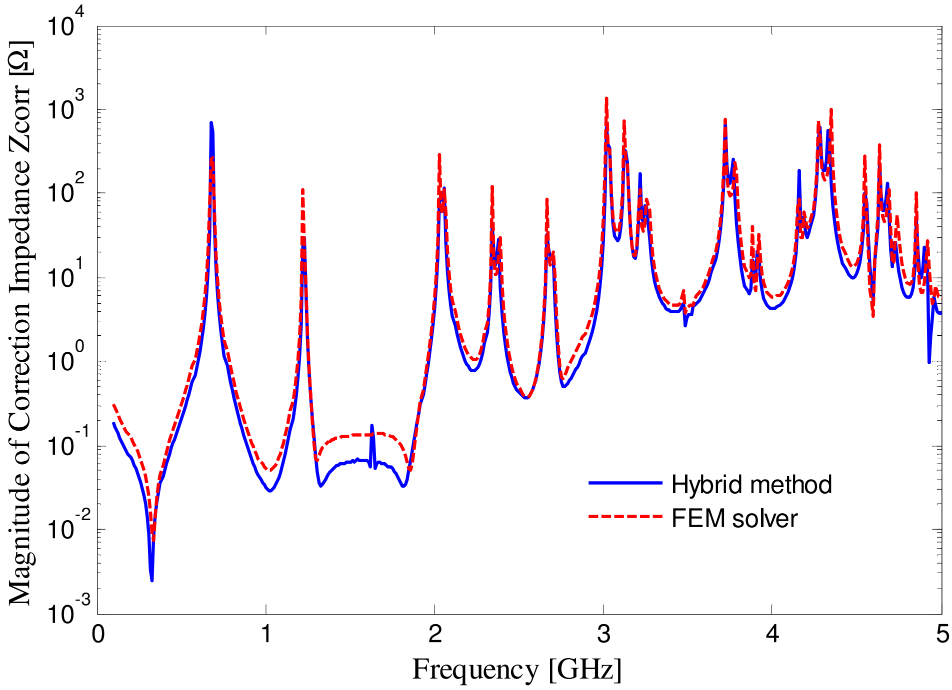

Figure 5.21 Magnitude of the correction impedance, as defined in (5.15), computed for the case in Fig. 5.19, obtained with the proposed hybrid method and a full-wave FEM simulation.

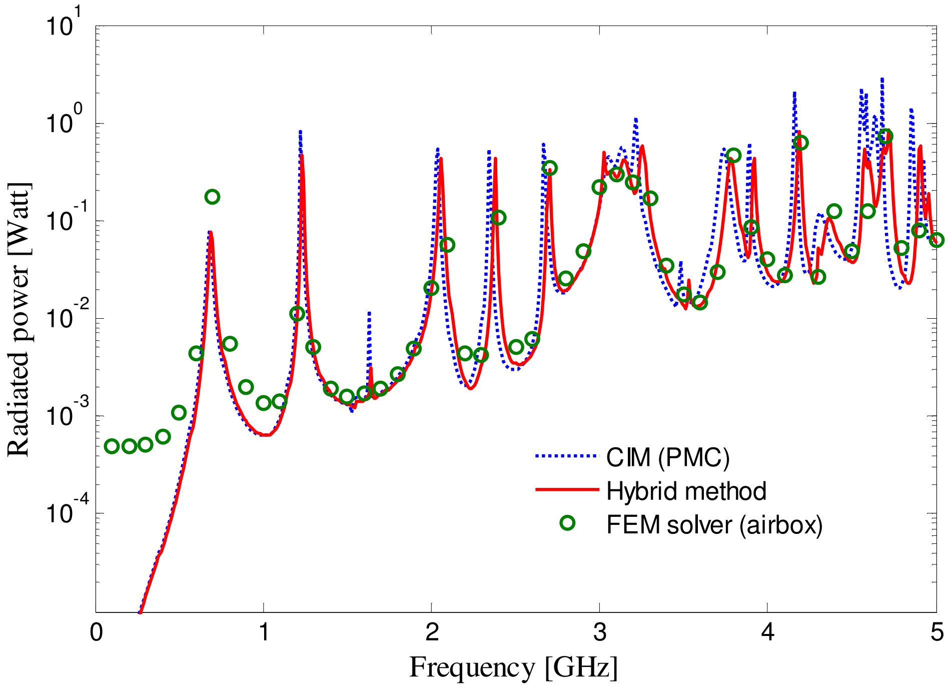

Figure 5.22 Radiated power computed for the case in Fig. 5.19 excited by a 1-Watt power source, obtained with the proposed hybrid method, a full-wave FEM simulation, and a two-step approach using CIM.

The results are obtained with the hybrid method, a FEM solver, as well as a two-step approach where the boundary voltage distribution is first computed assuming a PMC boundary condition. The hybrid method shows a good correlation with the FEM simulation. The discrepancy at the low frequencies might be explained by an insufficient size of the airbox in the FEM simulation. The results from the two-step approach deviates from the other two at frequencies over 2 GHz. In particular, a higher radiated power is predicted at resonance frequencies and some of the peaks even exceed the 1 Watt input power. This may be explained by an overestimated boundary under the PMC condition. It is then necessary to consider the radiation loss in these cases.

5.3. Hybridization with Via and Trace Model

As has been mentioned before, CIM is restricted to modeling of planar wave propagation problems. 3D field distributions, formed e.g. in the vicinity of via transitions, cannot be captured by CIM. Moreover, transmission line modes, that involve power planes as return paths, build field distributions that are not constant in the vertical direction, and thus are not generic problems for CIM. All these elements are essential to digital systems and proper hybridization with modeling schemes of them is necessary to leverage CIM for the modeling of a complete system.

5.3.1. Physics-based Via Model

A rich selection of via models exists in the literature, such as the Williamson model [134], the intrinsic via model [110], and multiple scattering methods [82],[83]. A summary of via models can be found in [106]. In principle, all these via models can be utilized for the connection to CIM. In the frame of this work, the physics-based via model [88],[106],[135]-[141] is adapted for the hybridization since the equivalent circuit structure makes the insertion of CIM impedance matrix results obvious and easy. The isotropic circular port expressions derived in Section 4.2 will be used for the power plane modeling in this section.

The physics-based via model is first briefly described here. Detailed explanation that covers the full range of this approach has been presented in [142]. The term “physics-based” stems from the fact that this model was developed by constructing circuit elements along the physical current return path of the via. Fig. 5.23 depicts a signal link crossing multilayer power planes, which consists of two through-vias and a stripline connection. An initial assumption is that the field penetration through the solid planes can be neglected due to the skin effect. Hence, vias provide the only coupling path

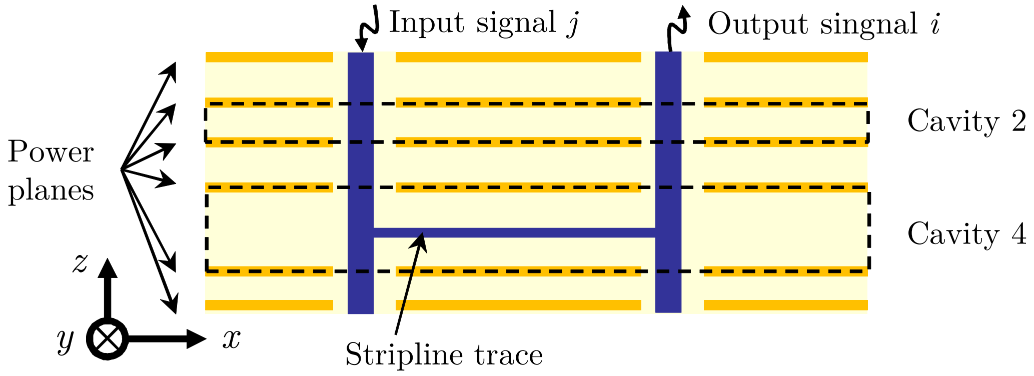

Figure 5.23 Cross section view of a signal traversing a multilayer substrate. The signal link consists of i-th and j-th through-via and a stripline connection.

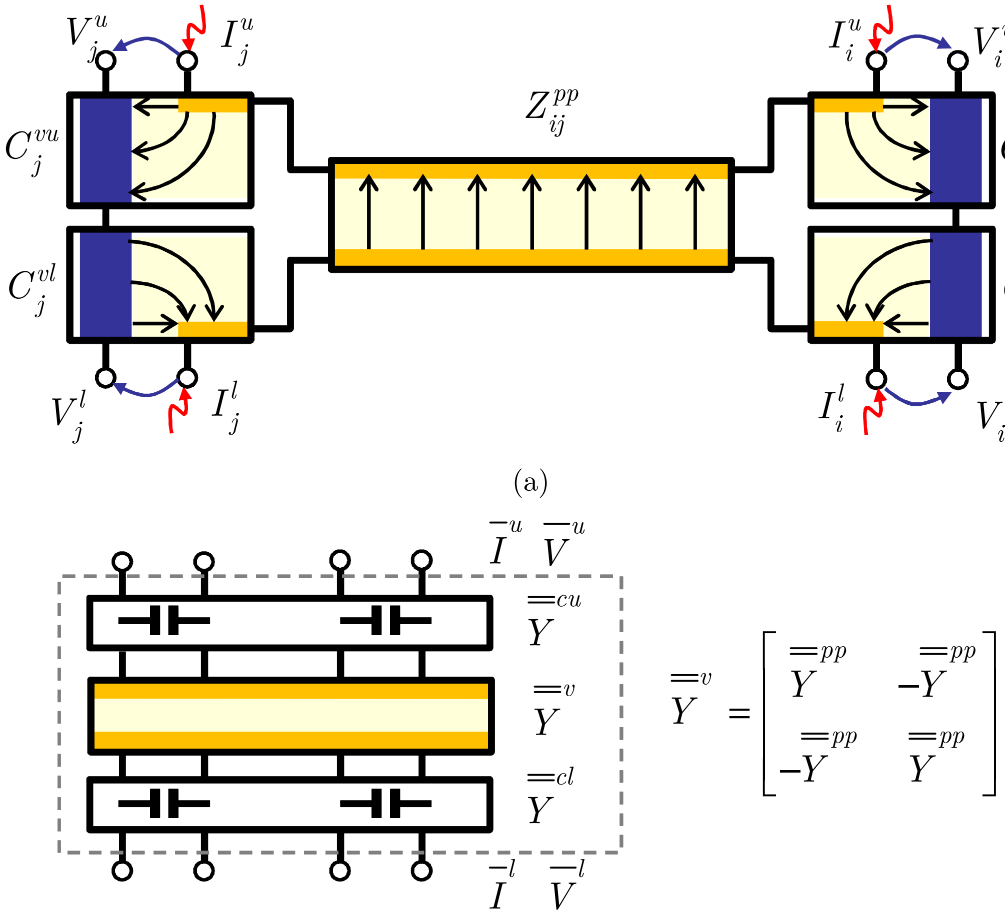

(a)

$$\overline{\overline{Y}}^{v} = \begin{bmatrix} \overline{\overline{Y}}^{pp} & -\overline{\overline{Y}}^{pp} \\ -\overline{\overline{Y}}^{pp} & \overline{\overline{Y}}^{pp} \end{bmatrix}$$

(b)

Figure 5.24 Description of the via model for cavity 2 in Fig. 5.23. (a) Elements in the current return path consisting of the via capacitance C^v and the parallel-plate impedance Z^{pp}. (b) Its equivalent network representation. $\overline{\overline{Y}}^{v}$ denotes the expanded cavity matrix and $\overline{\overline{Y}}^{c}$ the admittance matrix associated with the via capacitances. Superscripts u and l refer to the *upper* or *lower* cavity sides, respectively.

between cavities. For each of the transitions through a pair of power planes, a π-type equivalent circuit model can be built. The two building blocks of the model are the parallel-plate impedance Z^{pp} and the via-to-plane capacitances C^{v} [106]. Fig. 5.24(a) illustrates the basic circuit elements on the current return path for cavity 2 of the multilayer substrate in Fig. 5.23. The via capacitances are used to approximate the near-field around vias penetrating reference planes through clearance holes (antipads). The parallel-plate impedance represents the planar propagation modes inside the cavities formed between adjacent power planes that is exactly modeled by CIM. For n via transitions, $\overline{\overline{Z}}^{pp}$ describes an n-port network with ports defined at each via location, which corresponds to the impedance matrix of circular ports of the 0th mode in CIM.

The circuit diagram in Fig. 5.24(a) can be further translated to a network representation as shown in Fig. 5.24(b). To provide upper (u) and lower (l) connection nodes, the parallel-plate impedance is expanded for n via transitions to a $2n$-port network, for which Z-parameters cannot be used and Y-parameters must be applied with $\overline{\overline{Y}}^{pp} = \left(\overline{\overline{Z}}^{pp}\right)^{-1}$ [143]. For the general case of a single cavity, the via model can be written as [88]

$$\begin{bmatrix}\overline{I}^{u}\\ \overline{I}^{l}\end{bmatrix} = \left(\underbrace{\begin{bmatrix}\overline{\overline{Y}}^{cu} & 0\\ 0 & \overline{\overline{Y}}^{cl}\end{bmatrix}}_{\overline{\overline{Y}}^{c}} + \underbrace{\begin{bmatrix}\overline{\overline{Y}}^{pp} & -\overline{\overline{Y}}^{pp}\\ -\overline{\overline{Y}}^{pp} & \overline{\overline{Y}}^{pp}\end{bmatrix}}_{\overline{\overline{Y}}^{v}}\right)\cdot\begin{bmatrix}\overline{V}^{u}\\ \overline{V}^{l}\end{bmatrix}, \tag{5.17}$$

where the vectors $\overline{I}^{u}$, $\overline{I}^{l}$, $\overline{V}^{u}$, and $\overline{V}^{l}$ denote the currents and voltages defined at each via location, for the upper and lower side, respectively, as shown in Fig. 24(b). $\overline{\overline{Y}}^{v}$ represents the expanded parallel-plate admittance $\overline{\overline{Y}}^{pp}$. The matrix $\overline{\overline{Y}}^{c}$ includes the via capacitances including the diagonal submatrices $\overline{\overline{Y}}^{cu}$ and $\overline{\overline{Y}}^{cl}$, with entries $Y_i^{c(u/l)} = j\omega C_i^{v(u/l)}$, where C^{vu} denotes the via-barrel to antipad-rim capacitance for the upper side, and C^{vl} for the lower side. For power and ground vias connected to a plane, the corresponding capacitance entry is replaced with a short circuit [137]. The via capacitance values can be calculated with quasi-static solvers or analytical formulas [144],[145].

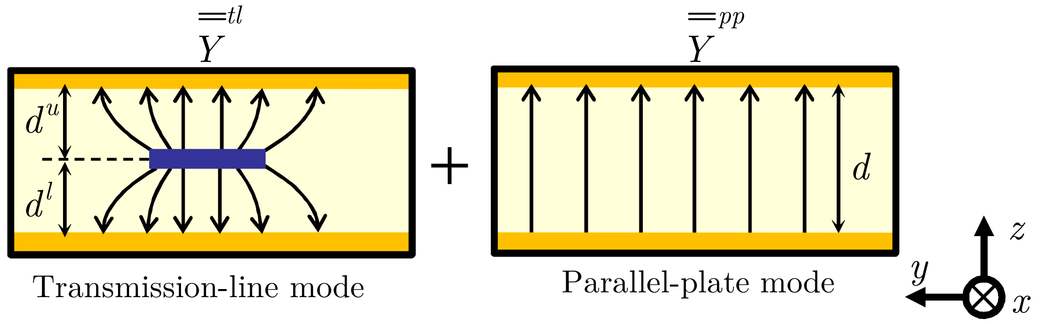

Transmission-line mode

Parallel-plate mode

Figure 5.25 Description of the stripline transmission-line mode and the parallel-plate mode for cavity 4 in Fig. 5.23. It is assumed that the two modes are decoupled in the power plane region and the coupling appears only at via locations.

5.3.2. Via and Trace Transition Model

The physics-based via model has been extended to include vias connected to internal traces in [146], by applying the modal decomposition technique presented in [147]. The via transition is described for these cases by two modes: the stripline transmission-line mode [148] and the parallel-plate impedance mode, as illustrated in Fig. 5.25. It is assumed that the coupling between the two modes appears only at via locations. Therefore, the modal decomposition technique [147] can be used to provide a solution to decouple the two modes at each via location. It can be shown that the matrix term $\overline{\overline{Y}}^{v}$ in (5.17) can be substituted with the following expression for transitions associated with striplines [88],

$$\overline{\overline{Y}}^{v} = \begin{pmatrix} k^2 \cdot \overline{\overline{Y}}^{tl} + \overline{\overline{Y}}^{pp} & (-k^2 - k) \cdot \overline{\overline{Y}}^{tl} - \overline{\overline{Y}}^{pp} \\ (-k^2 - k) \cdot \overline{\overline{Y}}^{tl} - \overline{\overline{Y}}^{pp} & (k^2 + 2k + 1) \cdot \overline{\overline{Y}}^{tl} + \overline{\overline{Y}}^{pp} \end{pmatrix}, \tag{5.18}$$

where $\overline{\overline{Y}}^{tl} = \left(\overline{\overline{Z}}^{tl}\right)^{-1}$ represents the admittance matrix of the stripline model. The factor k is defined as $k = -d^l \big/ \left(d^l + d^u\right)$ with d^l and d^u the heights from the trace to the lower and upper plane inside the cavity, respectively, as shown in Fig. 5.25. The factor k is a result of the modal decomposition [147], under the assumption that the trace thickness can be neglected.

5.3.3. Connection to CIM Matrices

The physics-based via model in conjunction with the trace model focus on SI analysis. It has been extended to cover PI applications in [89]. However, computation of radiated emissions, which is also an important design aspect of digital systems, is not covered in the model. On the other hand, upon calculation of the end-to-end port response, the electromagnetic behavior at intermediate layers is lost due to the segmentation procedure. Therefore, the goal here is also to hybridize CIM with the via model to recover field information and to form a collective tool for simultaneous analysis of all respects of SI, PI, and EMC applications. Similar hybrid approaches can be found in the literature [149],[150]. In contrast to them, by virtue of CIM, the method presented in this work is capable of computing cavity field distributions of each layer including their far-field radiation. In comparison to other hybrid techniques, for example a commercial solver [151], the advantage of this formulation is that only the boundaries need to be discretized in CIM. In principle, this simplifies the meshing and potentially results in a better numerical efficiency.

It is not difficult to recognize that CIM can be fit into the via model by using the CIM impedance matrix of circular ports to replace the Z^{pp} matrix in Fig. 5.24. To extend the method to also compute the noise distributions between power planes and the far field radiation for PI and EMC applications, it is necessary to obtain the currents flowing on all the vias of each intermediate layer and the electric field distribution on each boundary of the cavities, as indicated in Section 3.3. For that purpose, the boundary line ports in CIM must be incorporated for each individual cavity.

Fig. 5.26 shows the cross section of a five-layer three-cavity PCB example (a) and its equivalent network and port definitions (b). It is assumed that adjacent cavities are only connected through the via transitions. The capacitance matices $\overset{=}{Y}^{cu}$, $\overset{=}{Y}^{cl}$ and models of the cavities $\overset{=}{Y}^{v}$ bear the same meaning as before. The difference here is an h-parameter matrix $\overset{=}{h}^{c}$ for the second cavity that includes additionally the boundary ports from CIM in order for the calculation of cavity and radiated fields. The formulation of $\overset{=}{h}^{c}$ will be explained next.

The starting point here is the CIM impedance matrix in (3.22). As described in the last section, an expansion of via port is required to account for the upper and lower layer connections, which were carried out in the Y-parameter form before. However, the boundary ports q are subject to an open condition that is best described by Z-parameters. Therefore, it is most convenient to address the via-port expansion using an h-parameter expression, defined as

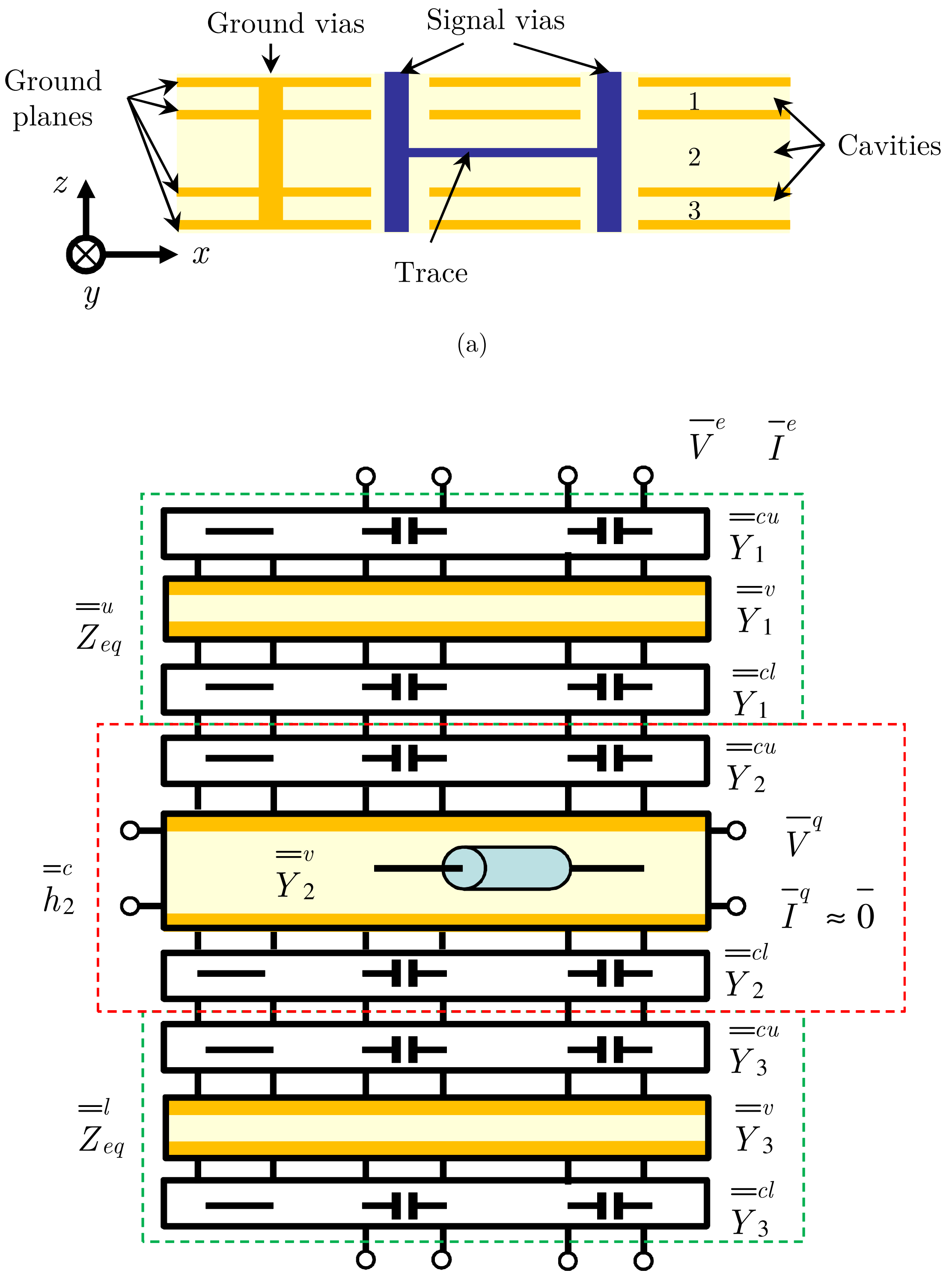

(a)

(b)

Figure 5.26 Description of the combination process for a multilayer case. (a) Example of a board cross-section with three cavities. (b) Network-level representation of the example, including the port definition for via and boundary ports.

$$\begin{bmatrix} \overline{\overline{h}}^{qq} & \overline{\overline{h}}^{qp} \\ \overline{\overline{h}}^{pq} & \overline{\overline{h}}^{pp} \end{bmatrix} \cdot \begin{bmatrix} \overline{I}^{q} \\ \overline{V}^{p} \end{bmatrix} = \begin{bmatrix} \overline{V}^{q} \\ \overline{I}^{p} \end{bmatrix}, \tag{5.19}$$

where the h-matrix can be obtained from the impedance matrix (3.22) by the transformation [152]

$$\begin{bmatrix} \overline{\overline{h}}^{qq} & \overline{\overline{h}}^{qp} \\ \overline{\overline{h}}^{pq} & \overline{\overline{h}}^{pp} \end{bmatrix} = \begin{bmatrix} \overline{\overline{Z}}^{qq} - \overline{\overline{Z}}^{qp} \left(\overline{\overline{Z}}^{pp}\right)^{-1} \overline{\overline{Z}}^{pq} & \overline{\overline{Z}}^{qp} \left(\overline{\overline{Z}}^{pp}\right)^{-1} \\ \left(\overline{\overline{Z}}^{pp}\right)^{-1} \overline{\overline{Z}}^{pq} & \left(\overline{\overline{Z}}^{pp}\right)^{-1} \end{bmatrix}. \tag{5.20}$$

Note that $\overline{\overline{h}}^{pp}$ has the same significance as the parallel-plate admittance matrix $\overline{\overline{Y}}^{pp}$ with the boundary ports open $\overline{I}^{q} = \overline{0}$, i.e., the PMC boundary condition. For the voltages and currents on the upper and lower via ports, the following relation holds: $\overline{V}^{u} - \overline{V}^{l} = \overline{V}^{p}$ and $\overline{I}^{u} = -\overline{I}^{l} = \overline{I}^{p}$. Therefore, the h-matrix can be expanded as

$$\underbrace{\begin{bmatrix} \overline{\overline{h}}^{qq} & \overline{\overline{h}}^{qp} & -\overline{\overline{h}}^{qp} \\ \overline{\overline{h}}^{pq} & \overline{\overline{h}}^{pp} & -\overline{\overline{h}}^{pp} \\ -\overline{\overline{h}}^{pq} & -\overline{\overline{h}}^{pp} & \overline{\overline{h}}^{pp} \end{bmatrix}}_{\overline{\overline{h}}^{c}} \cdot \begin{bmatrix} \overline{I}^{q} \\ \overline{V}^{u} \\ \overline{V}^{l} \end{bmatrix} = \begin{bmatrix} \overline{V}^{q} \\ \overline{I}^{u} \\ \overline{I}^{l} \end{bmatrix}. \tag{5.21}$$

Note that this expansion process may also be done using S-parameters. It is, however, most straightforward and concise using h-parameters. In $\overline{\overline{h}}^{c}$, the sub-matrix

$$\overline{\overline{h}}^{v} = \begin{bmatrix} \overline{\overline{h}}^{pp} & -\overline{\overline{h}}^{pp} \\ -\overline{\overline{h}}^{pp} & \overline{\overline{h}}^{pp} \end{bmatrix} \tag{5.22}$$

is identical to the expanded parallel-plate admittance matrix $\overline{\overline{Y}}^{v}$ in (5.17). As a reminder, the impedance matrix in (3.22) represents a cavity including both via and boundary ports, implied by the indices p and q, respectively. Therefore, the via capacitance and stripline models can be incorporated according to (5.18). Consequently, the following *h*-parameter expression can be found to describe the second cavity including all the elements in Fig. 5.26,

$$\overline{\overline{h}}^{c} = \begin{bmatrix} \overline{\overline{h}}^{qq} & \overline{\overline{h}}^{qp} & -\overline{\overline{h}}^{qp} \\ \overline{\overline{h}}^{pq} & \overline{\overline{Y}}^{pp} + \overline{\overline{Y}}^{cu} + k^2 \overline{\overline{Y}}^{tl} & -\overline{\overline{Y}}^{pp} + (-k^2 - k)\overline{\overline{Y}}^{tl} \\ -\overline{\overline{h}}^{pq} & -\overline{\overline{Y}}^{pp} + (-k^2 - k)\overline{\overline{Y}}^{tl} & \overline{\overline{Y}}^{pp} + \overline{\overline{Y}}^{cl} + (k^2 + 2k + 1)\overline{\overline{Y}}^{tl} \end{bmatrix}. \tag{5.23}$$

It is also assumed that the stripline is not located in the vicinity of the boundary so that such coupling effects are negligible. Equation (5.23) describes the general network representation for an individual cavity. Its difference to (5.18) is manifested by the additional transfer function $\overline{\overline{h}}^{pq}$ that represents the noise propagation from vias to the cavity boundary, which in turn leads to radiated emissions.

For a single-cavity system, (5.23) is ready to be connected to source ports and terminations on the top and bottom sides of the cavity. The terminations, such as decoupling capacitors and ground vias, are reduced using the technique described in Section 5.1. For that purpose, *h*-parameters are transformed to *Z*-parameters, for which formulas to conduct segmentation are available [85]. As a result, only the source ports, denoted as *e*, and the boundary ports *q*, as shown in Fig. 4.5, remain in the final system matrix as

$$\begin{bmatrix} \overline{\overline{Z}}^{qq} & \overline{\overline{Z}}^{qe} \\ \overline{\overline{Z}}^{eq} & \overline{\overline{Z}}^{ee} \end{bmatrix} \cdot \begin{bmatrix} \overline{I}^{q} \\ \overline{I}^{e} \end{bmatrix} = \begin{bmatrix} \overline{V}^{q} \\ \overline{V}^{e} \end{bmatrix}. \tag{5.24}$$

Assuming a PMC boundary condition, the voltage distribution on the boundary ports $\overline{V}^{q}$ can be computed as

$$\overline{V}^{q}\Big|_{\overline{I}^{q}=0} = \overline{\overline{Z}}^{qe} \cdot \overline{I}^{e}. \tag{5.25}$$

The radiated far fields are then obtained using (3.23) for the single-cavity case. In order to find the field distribution inside the cavity, the currents flowing on each via, including those connecting to the terminations, must be known. The voltages on the upper and lower via ports $\overline{V}^{u}$ and $\overline{V}^{l}$ can be retrieved by storing an auxiliary matrix when applying the segmentation [85]. The via currents are calculated by

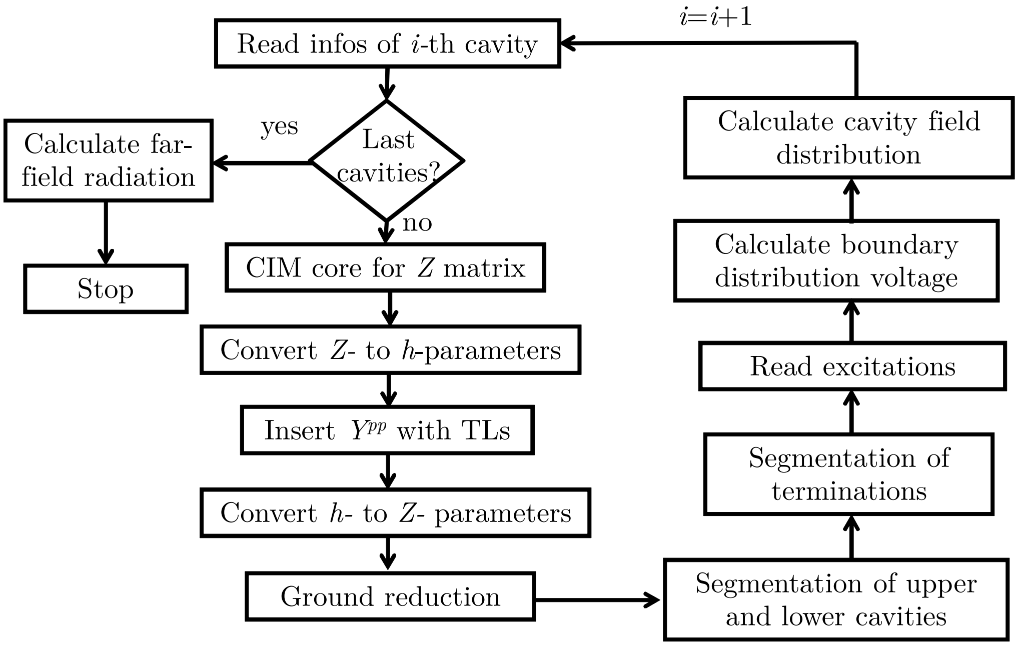

Figure 5.27 Flow diagram of the cavity-by-cavity approach. Each cavity is solved independently one after another. The far-field radiation is obtained after the voltage distributions on all cavity boundaries have been computed.

$$\overline{I}^{p} = \overline{\overline{Y}}^{pp} \cdot \overline{V}^{p} = \overline{\overline{Y}}^{pp} \cdot \left(\overline{V}^{u} - \overline{V}^{l}\right), \tag{5.26}$$

and the voltage distribution inside the cavity is obtained by (3.22).

5.3.4. Merging of Multiple Layers

For multilayer systems, each individual cavity is described using (5.23). In principle, the cavities, including all the boundary ports, can be segmented, i.e., concatenated sequentially from top to bottom in one step to generate a transfer function between top-/bottom-layer source ports and the boundary ports of all the cavities. However, for the retrieval of voltages and currents on the intermediate via ports, it is required that auxiliary matrices be stored each time a cavity is appended. Hence, the amount of storage can be very large, especially for many layer systems.

Alternatively, the implementation can follow a cavity-by-cavity approach and each cavity is solved independently, as shown in the flow diagram in Fig. 5.27. For the i-th cavity, the parallel-plate impedance Z^{pp} including boundary ports is first obtained using

CIM, which is then converted to an h-parameter matrix as in (5.19). Via-plate capacitances and transmission line models are then inserted to form a complete description of that cavity as in (5.23). For the next segmentation procedures, it is converted back to a Z-parameter matrix. The layers on its upper and lower sides are accounted for by two equivalent blocks, $\overline{\overline{Z}}{}^{u}_{eq}$ and $\overline{\overline{Z}}{}^{l}_{eq}$, as depicted in Fig. 5.26, which are obtained using the methods described in Sections 5.3.1 and 5.3.2. The cavities within the equivalent blocks are represented using (5.18), without boundary ports. Terminations, such as decaps and resistors, are segmented next. As a consequence, one obtains the transfer function between the top/bottom source ports and the boundary ports of only one intermediate cavity, and thus the voltage distribution on that cavity boundary by (5.25). This process is repeated for every cavity to obtain the complete voltage distribution around the PCB sidewalls. Here, since the boundary ports are only needed for the calculated cavity, the amount of storage is reduced in exchange for a slightly longer calculation time. The total electric far-field is obtained as a superposition of the radiation from each cavity as

$$\mathcal{E}^{tot}(\boldsymbol{r}) \approx \sum_{i=1}^{N} \mathcal{E}_i(\boldsymbol{r}), \tag{5.27}$$

where N denots the total number of cavities here. The radiations from individual cavities $\mathcal{E}_i(\boldsymbol{r})$ are calculated using (3.23). In this chapter, the validation examples will be restricted to single cavity cases. Advanced multilayer applications will be presented in Chapter 6.

5.3.5. Validation and Examples

In this section, the combined method is applied to simulate two single-cavity configurations and compared against full-wave simulations. The first explored example is a rectangular single cavity board, described in Fig. 5.28.

The input impedance seen at port 1, whose internal pin is connected to the lower plane, has been obtained using the hybrid method, the cavity resonator model (single sum, 100 iterations [69]), and a finite element method (FEM) based full-wave electromagnetic solver [117], as shown in Fig. 5.29. The compared results of the methods agree well. The via-plate capacitance is calculated to be 26 fF using formulas in [144], which is too small to have an impact on the impedance for single cavities over the simulated frequency range. As shown in Fig. 5.29, the result from the hybrid method overlaps with the cavity model, which does not include the via capacitance.

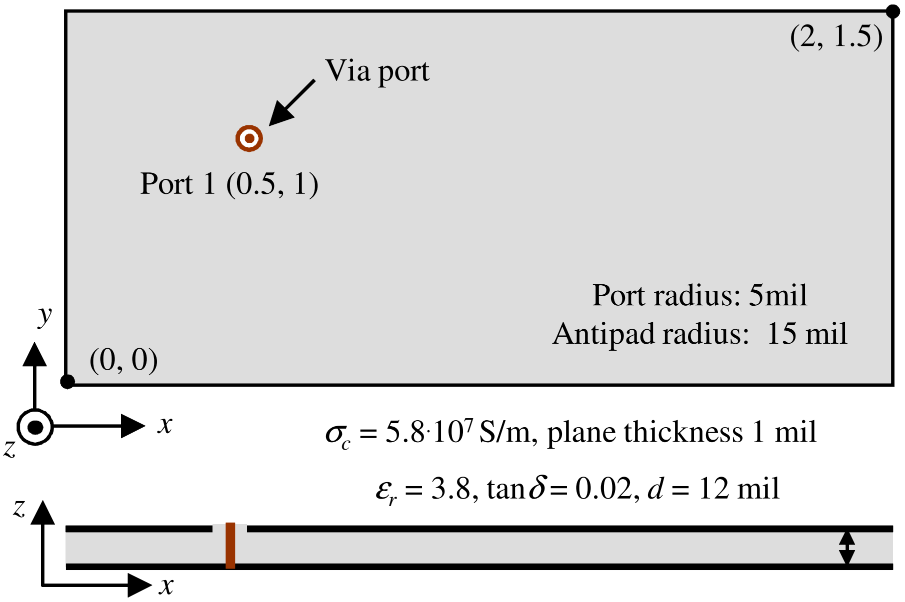

Figure 5.28 Single-cavity example with one single port. Dimensions are given in inches (1 inch ≈ $2.54 \cdot 10^{-2}$ m).

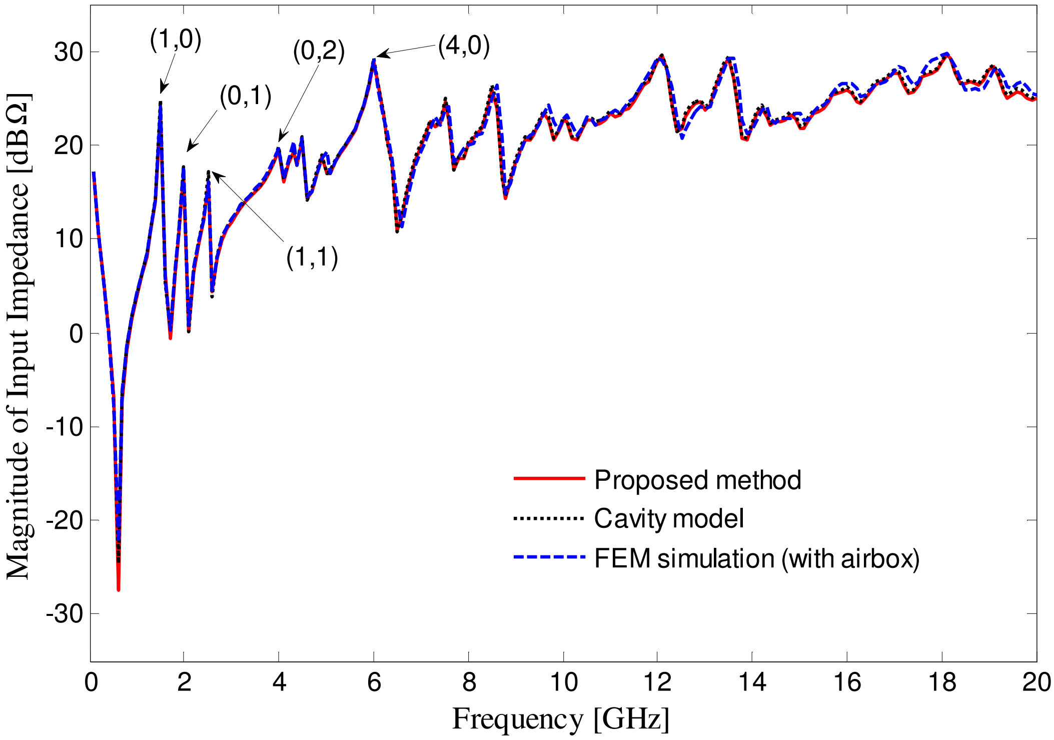

Figure 5.29 Input impedance and resonance modes for the example in Fig. 5.28, obtained with the hybrid method, the cavity model, and a full-wave simulation.

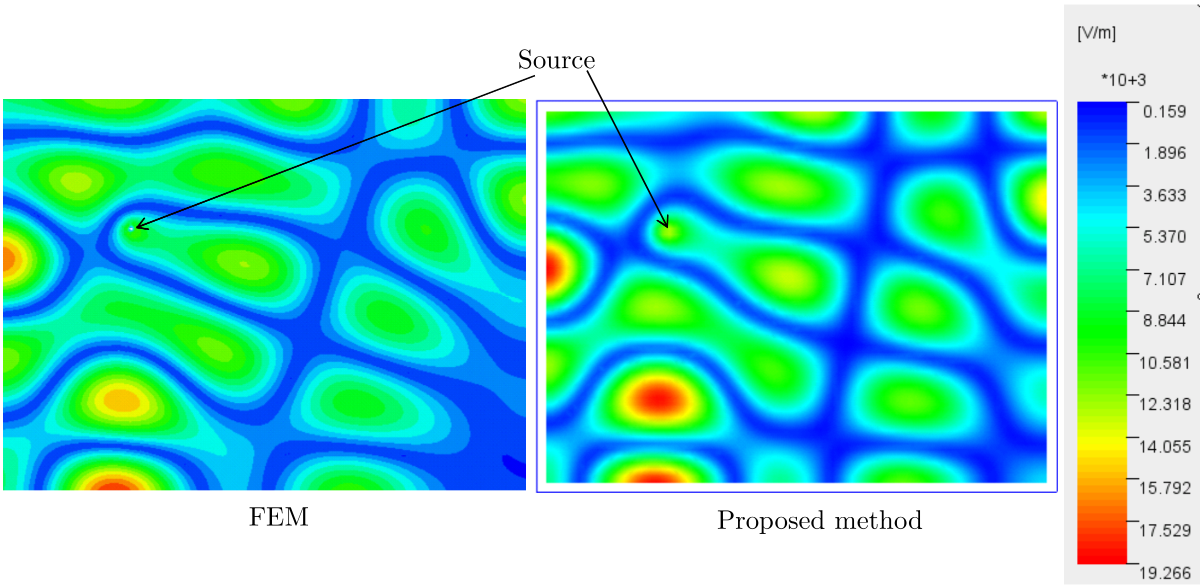

Figure 5.30 Electric field distribution between power and ground planes of the case in Fig. 5.28 at 10 GHz with port 1 excited by a 1-Watt power source, using the proposed hybrid method (right) and a full-wave FEM solver (left). Multiple resonances are observed in the cavity.

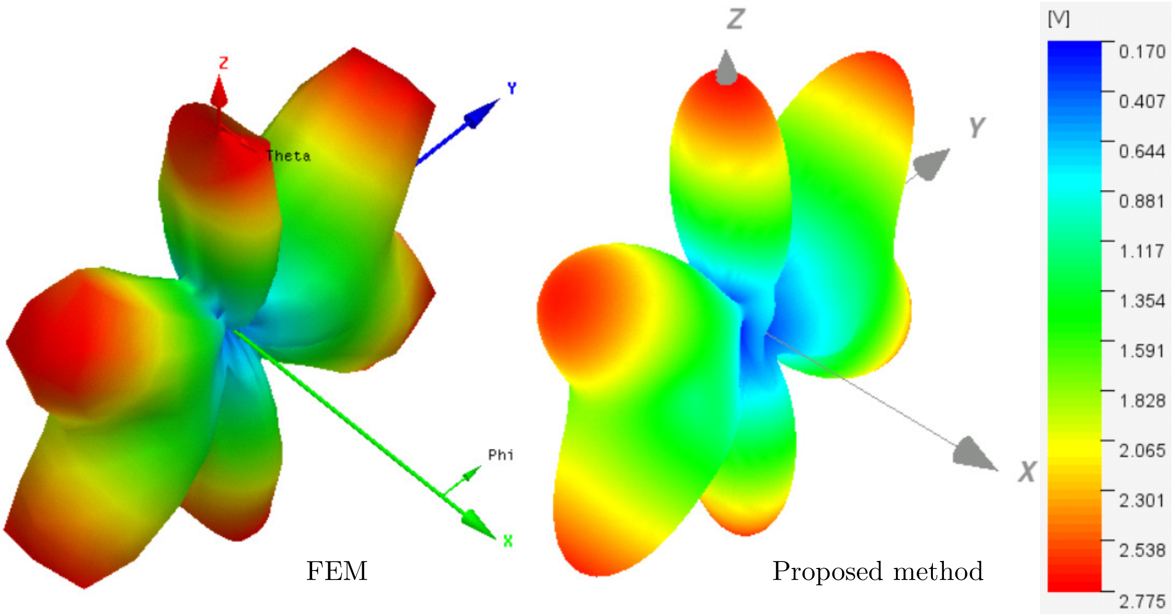

Figure 5.31 Radiation diagram of the case in Fig. 5.28 at 10 GHz with port 1 excited by an 1-Watt power source, using the proposed hybrid method (right) and a full-wave FEM solver (left).

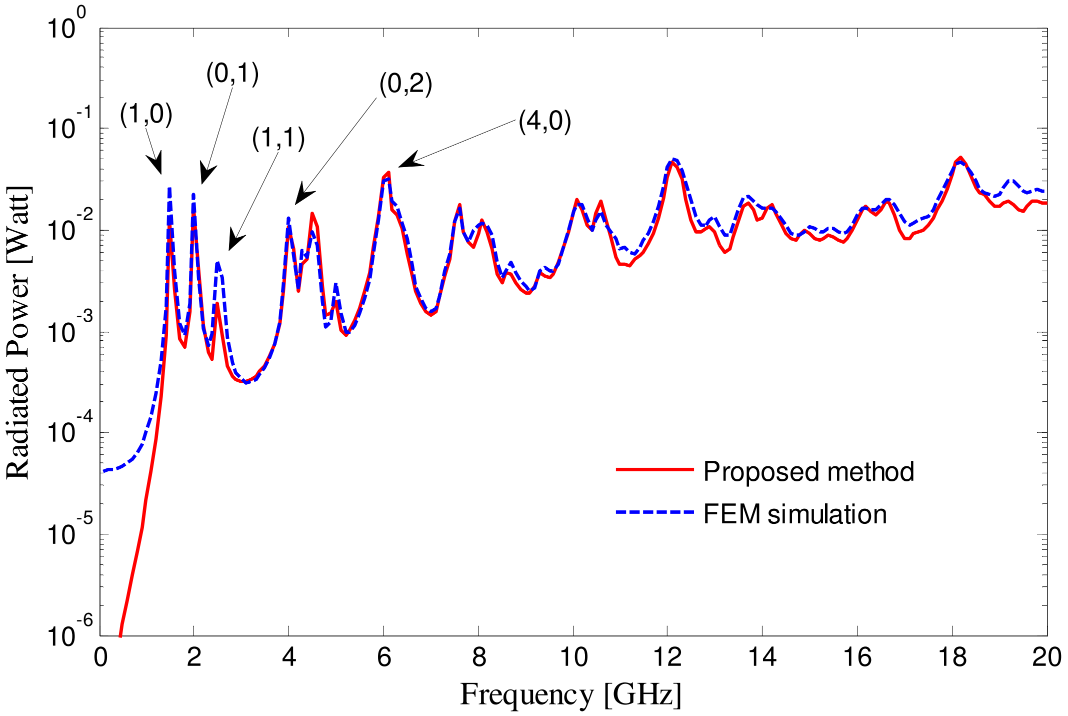

Figure 5.32 Radiated power computed for the case in Fig. 5.28, obtained with the proposed method and a full-wave simulation. The input port 1 is excited with a 1-Watt power source.

Since the FEM solver is a volume method, an air box surrounding the structure is required in order to compute radiation. The minimum distance from the structure to the boundary, typically $\lambda/4$ for absorbing boundaries, imposes a limitation on the minimum size of the model and therefore impairs the computation efficiency. In contrast, by virtue of the equivalence principle, the proposed method allows a fast estimation of the radiated far fields. The simulation time for this case, with 200 frequencies, took about 9.4 seconds with the proposed method and about 3 hours with the full-wave simulation (CPU time, 3.0-GHz PC, 4-GB RAM).

The electric field distribution inside the cavity and the radiated far-field at 10 GHz are plotted in Fig. 5.30 and Fig. 5.31, respectively, obtained by both the proposed method and the FEM full-wave solver. The input port 1 is excited with a 1-Watt power source. Similar field patterns are produced by both of the methods. At 10 GHz multiple peaks and valleys of the electric field in the cavity are observed, since the wavelength is much smaller than the power plane dimensions. Also, the radiation field exhibits six maxima in the y-z plane in contrast to the doughnut pattern in the low frequency range, as shown in Fig. 5.10.

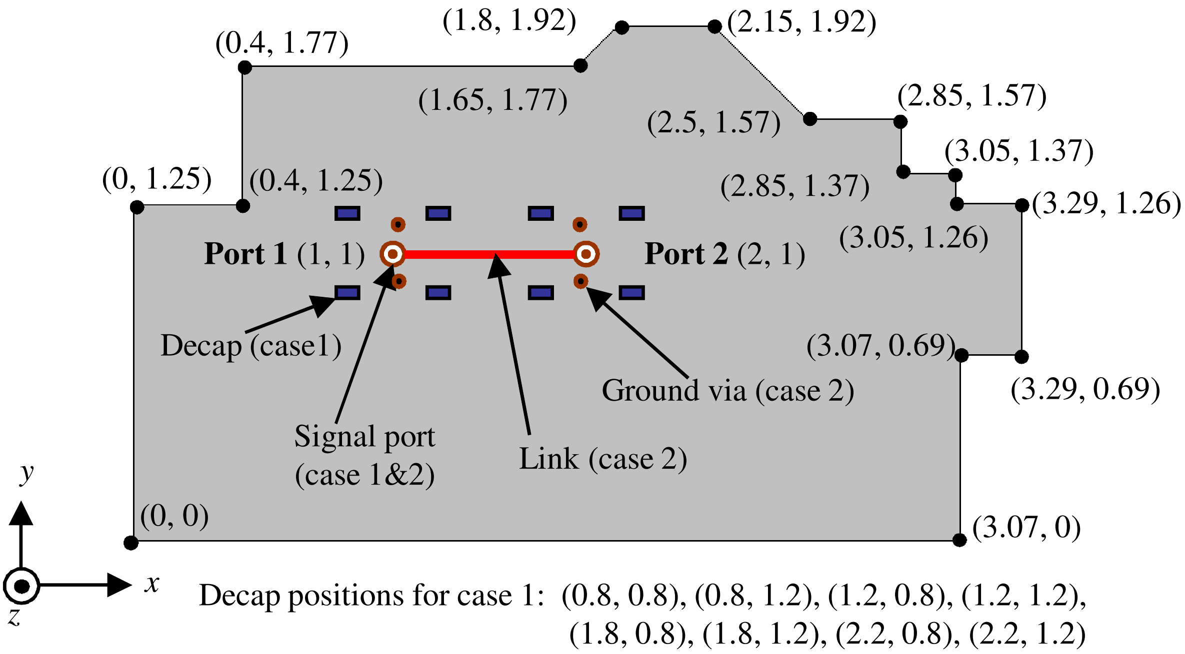

Decap positions for case 1: (0.8, 0.8), (0.8, 1.2), (1.2, 0.8), (1.2, 1.2),
(1.8, 0.8), (1.8, 1.2), (2.2, 0.8), (2.2, 1.2)

Ground via positions for case 2: (1, 1.04), (1, 0.96), (2, 1.04), (2, 0.96)

Figure 5.33 Two-port irregular shaped single-layer board example. Two cases are analyzed: case 1 with 8 decaps, and case 2 with 4 ground vias and a link connecting the two ports. The vias are shorting the bottom plane for the first case and open at the bottom side for the second case. Dimensions are given in inches (1 inch ≈ $2.54 \cdot 10^{-2}$ m). Port geometry, board cross-section, and material properties correspond to the ones defined for the case in Fig. 5.28.

With the hybrid method the total radiated power can be calculated as the integral of the Poynting vector over a unit spherical surface, as in (5.4). Fig. 5.32 shows that the hybrid method predicts similar values in the frequency range from 1.5 GHz up to 20 GHz in comparison to the FEM simulation. For lower frequencies, the full-wave simulation predicts higher radiation. This is probably due to an insufficient distance to the absorbing boundary that results in loss of accuracy for the full-wave solver. It was observed that the full-wave results tend to correspond to the ones predicted by the proposed method, if the size of the air box is increased. However, the computation burden increases very rapidly with the model size.

For the second example, a single-cavity irregular shaped board is explored, as shown in Fig. 5.33. Two scenarios will be analyzed. For the first case, the board was populated with decaps. Fig. 5.34 shows the transfer impedance between Port 1 and 2 with eight ideal 10 nF capacitors located at positions shown in Fig. 5.33, calculated using both the proposed method and the full-wave FEM solver. The two vias are shorting the bottom

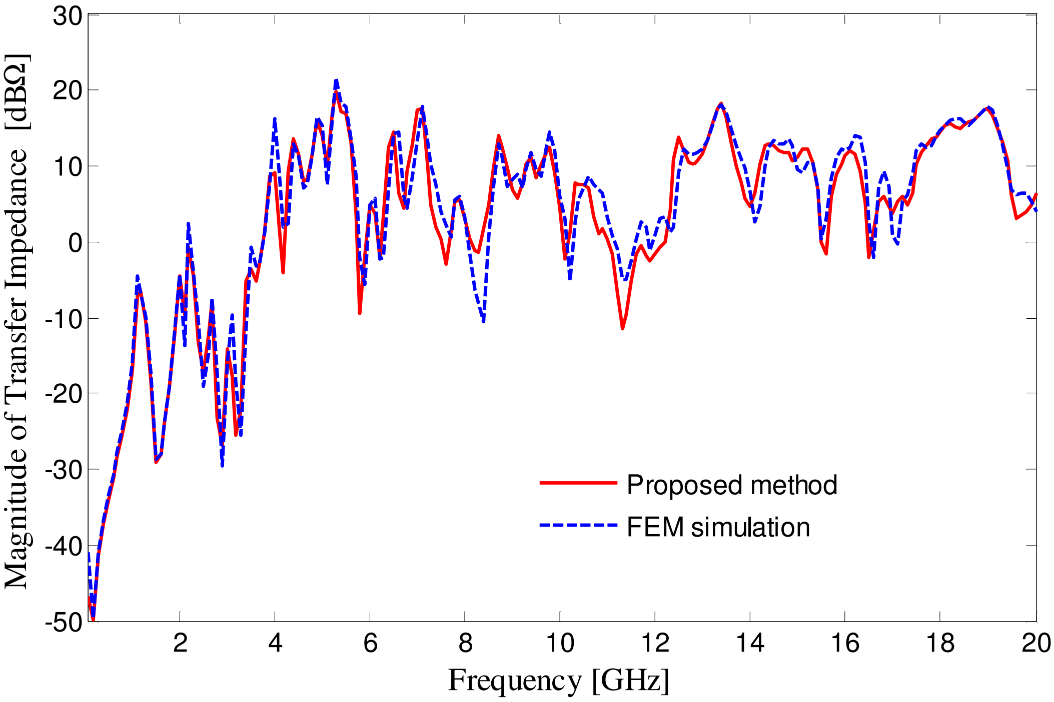

Figure 5.34 Correlation to full-wave simulation for the transfer impedance Z12, for case 1 of the example in Fig. 5.33 with 8 10-nF ideal decoupling capacitors.

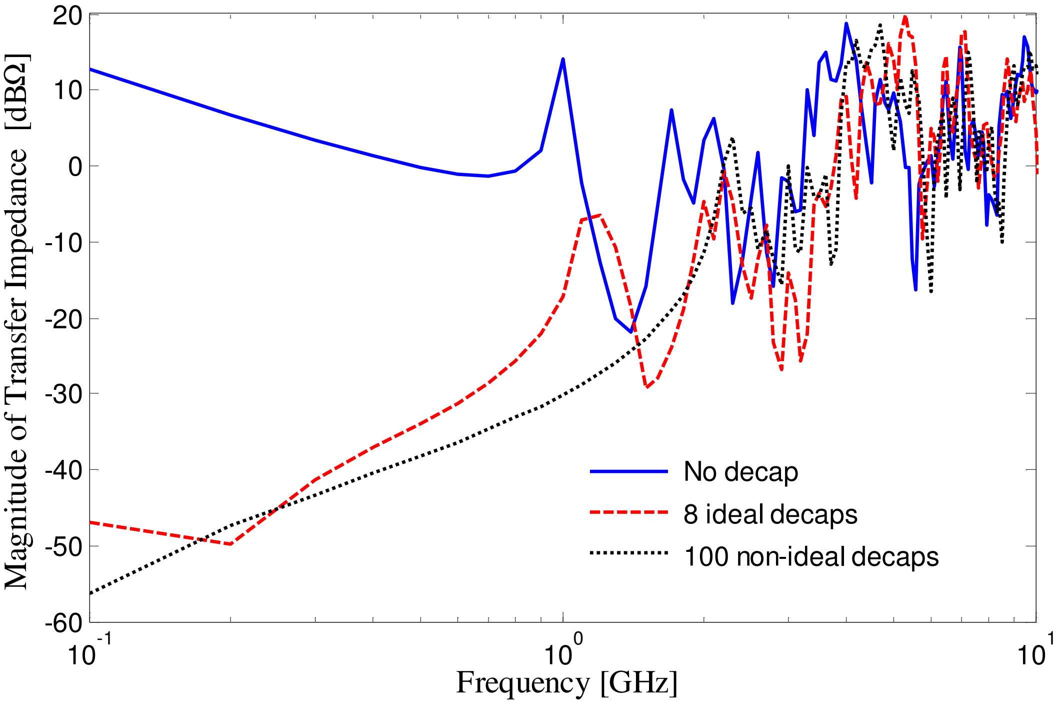

Figure 5.35 Transfer impedance for case 1 of the example in Fig. 5.33 and different numbers of 10 nF decoupling capacitors, computed with the proposed method. Non-ideal decap parasitics were modeled with $ESR = 100\ \mathrm{m}\Omega$, $ESL{+}L_{interc} = 1\ \mathrm{nH}$.

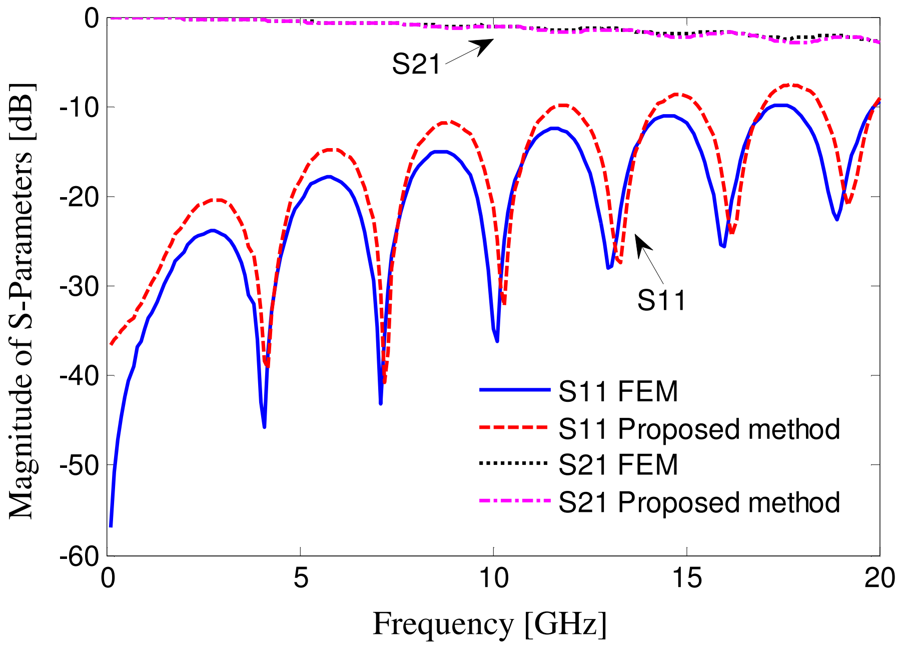

Figure 5.36 Reflection and transmission S-parameters for case 2 of the example in Fig. 5.33, obtained with the proposed method and an FEM full-wave analysis.

plane and the boundary is assumed to be PMC. Lumped ports were used for the full-wave simulation and the capacitors were included as lumped elements placed on top of additional pins.

The effect of different numbers of decaps is shown in Fig. 5.35. The impedance is reduced noticeably for frequencies below 1 GHz, however the decoupling becomes less effective in the GHz range even with 8 ideal decaps that are not sufficient for damping of cavity resonances. If more decoupling capacitors are added, the bandwidth of the decoupling effect is extended to higher frequencies. This is illustrated in the example with the simulation of one hundred 10-nF non-ideal capacitors, uniformly distributed on the board. The equivalent series resistance (ESR) was set to 100 mΩ and the total equivalent parasitic inductance ($ESL+L_{interc}$) to 1 nH for each non-ideal decap. This case shows a further reduction on the transfer impedance and makes the decoupling effect observable up to 2 GHz. Note that this case was not simulated with the full-wave solver due to insufficient resources of a single 32-bit PC. The simulation time using the hybrid method for 200 frequency points was 25 seconds, 27.5 seconds, and 64.5 seconds for the board without decaps, with 8 ideal decaps, and with one hundred non-ideal decaps, respectively. In contrast, the full-wave simulation took more than 6 hours of CPU time for the case with 8 ideal decaps.

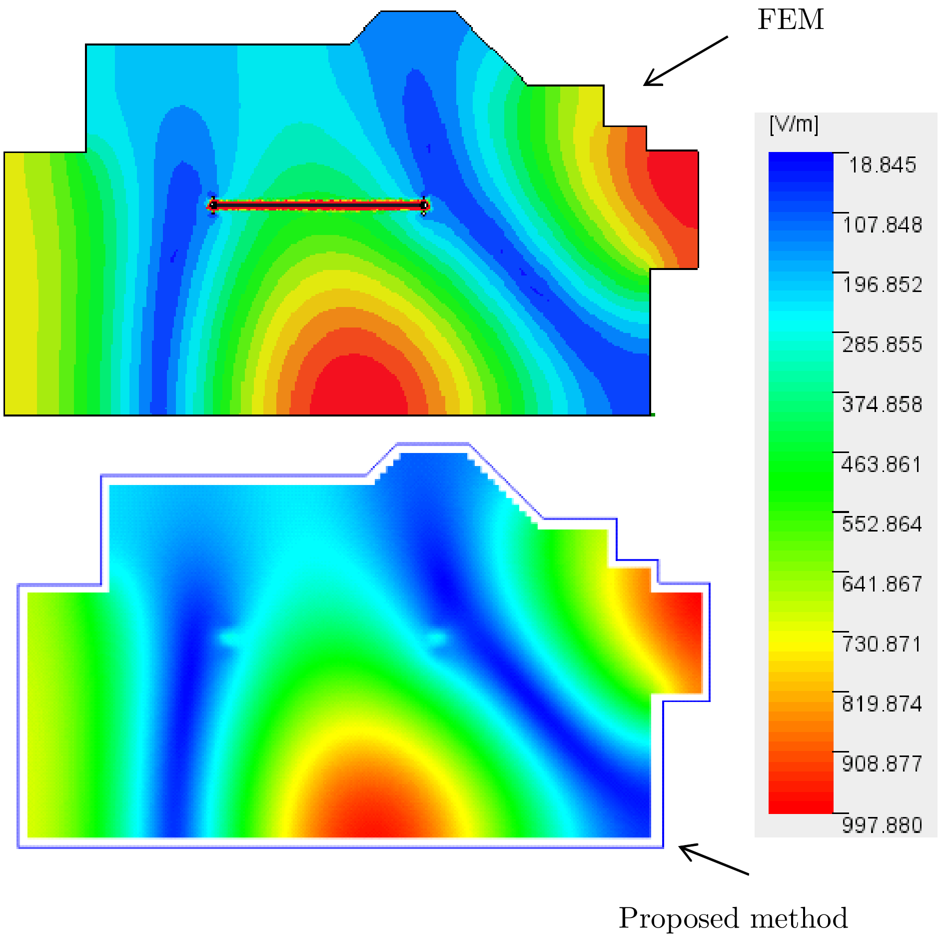

Figure 5.37 Cavity electric field distribution for case 2 of the example in Fig. 5.33 at 2 GHz with port 1 excited by a 1-Watt power source and port 2 terminated with 50 Ω, using the hybrid method (lower) and a full-wave FEM solver (upper). The field distribution of the transmission line mode is not calculated by the hybrid method.

For the second scenario of this example, a 4-mil wide stripline link located in the middle of the cavity is used to connect the two ports. Each port is accompanied by two ground vias, as shown in Fig. 5.33. The signal vias are assumed open at the bottom side. Both methods predict similar transmission and reflection behaviors of the link as shown in Fig. 5.36. The deviation of the reflection curves may be explained as the characteristic impedance used in the hybrid method was 50 Ω, which differs from the one that is seen by the full-wave solver. Also, the distortion of via near fields by the stripline conductor is not considered in the hybrid method.

For this case, the electric field distribution inside the cavity at 2 GHz is illustrated in Fig. 5.37, obtained by both the proposed method and the FEM full-wave solver. The input port 1 is excited with a 1-Watt power source and port 2 is terminated with 50 Ω.

Similar cavity field patterns are observed. Essentially, the difference between the two results is the transmission line field, as observed in the full-wave result, which is absent in the hybrid method result, since it only computes the cavity field distribution. The magnitude of the electric field in this case is much smaller in comparison to the ones without the link, such as in Fig. 5.30, because a large portion of the input current flows on the trace and less energy is coupled into the cavity than the cases without traces.

5.4. Summary and Discussion

The extensions presented in this chapter take advantage of the segmented analysis, which is a divide and conquer scheme that combines the merit of CIM with other efficient approaches. Combinations with one-port circuits, external radiation fields, as well as multilayer via and trace structures have been explained in this chapter. In general, CIM provides a fast solution for a closed planar domain that can be connected to any other system blocks. Further hybridization with methods listed in Section 2.2 is in principle possible.

The segmentation of the system requires a proper port definition and correct modeling of the sub-domains under reasonable assumptions. For example, the hybridization with MoM in Section 5.2 relies on the assumption that the external field is symmetric with regard to the power planes. If the symmetry breaks, by e.g. a nearby 3D structure, one needs also to account for currents flowing on metal planes. Moreover, the vertical transition of higher order modes is possible as shown in the example in Fig. 4.7. The combination with the physics-based via model in Section 5.3 assumes that only the isotropic mode is coupled from the coaxial region to the radial waveguide region, since the effect of higher order coaxial modes is small in the vertical direction [153].

6. Advanced Applications

Advanced application examples using CIM and its extensions will be presented in this chapter, covering a wide range of aspects in the electrical design of digital systems including SI, PI, and radiated emission analyses. Simulations of arbitrary shape power/ground plane pairs and computations of the parallel-plate impedance for classic PI applications are first presented. A set of power plane shapes is analyzed and the computational efficiency will be discussed. Then, dense via arrays in a multilayer environment will be analyzed. The resolution of a potential passivity problem using the extended CIM will be discussed. Finally, the hybridized method with physics-based via and trace models is applied to multilayer printed circuit boards to evaluate its ability for generating useful parameters covering SI, PI, and EMI in a concurrent fashion.

6.1. Arbitrary Shaped Power Planes

The extended CIM is applied here to calculate the parallel-plate impedances of three selected complex shaped power plane configurations in order to assess its usefulness and limitations. The results are validated with full-wave simulations. The comparison to measurement data is presented for the last two cases. The focus is on the PI analysis and the frequency range is chosen up to 1 GHz for easy comparisons. Isotropic port solutions from Section 4.2 will be used. Electric field distributions between the power planes will be shown and their implication to the PDN design will be briefly discussed. The simulation time and memory demand are reported for the comparison to other techniques. At this point, CIM is incapable of predicting the radiation from cut-outs and slots over solid planes. Therefore, radiation is not considered here.

All three configurations consist of a two-port single cavity, sandwiched by a pair of power planes consisting of power on the upper side and ground on the lower side, surrounded by a PMC boundary. It is assumed that the vias are shorted to the ground plane. The material constants and via dimension parameters are set as in Table 6.1. All field plots shown in this section are generated by exciting port 1 with a 1-Watt power source and by terminating port 2 with a 50-Ω resistance.

Table 6.1. Material constants and via dimension parameters.

Relative dielectric permittivity ε_r	4.2
Relative permeability μ_r	1.0
Loss tangent $\tan\delta$	0.02
Plane conductivity κ (S/m)	5.8e+7
Plane thickness (mil)	1.2
Dielectric thickness d (mil)	10
Via diameter (mil)	10
Via pad diameter (mil)	20
Via keepout/antipad (mil)	36

6.1.1. L-Shape Board with Cut-Out Area

The first power plane case is an L-shape board with a cut-out area as shown in Fig. 6.1. The bottom side is a complete piece of solid plane. Since the PMC boundary condition is assumed for the cut-out area, the ground metal in the cut-out area has no effect on the impedance calculation.

The magnitude of input and transfer impedances of the bare board using both CIM and a full-wave FEM solver [117] is shown in Fig. 6.2. For the full-wave simulation, a wave port is applied on the coaxial antipad region. As has been discussed in section 5.1, the effect of the via-plate capacitance is negligibly small in the MHz frequency range and thus not included in the CIM simulations here. Fig. 6.3 compares the electric field distribution between the power and ground planes at 300 MHz obtained by the FEM solver with that obtained by CIM solutions.

Fig. 6.4 plots the transfer impedances of the bare board for the cases with and without the cut-out area. Since a cut-out in the power plane reduces the capacitance of the board, the impedance is higher with a cut-out area at frequencies lower than 10 MHz. Furthermore, the first resonance is shifted to a higher frequency with the cut-out due to an increased inductance between the two ports resulting from the prolonged current path between them.

The effect of 176 decoupling capacitors (decap) on the input and transfer impedances is shown in Fig. 6.5. The decaps are modeled as 0.1-µF capacitors with 30-mΩ ESR and the total parasitic inductance of 2 nH (ESL plus the interconnect inductance). They are uniformly distributed on the board area with 1-inch pitch in both x- and y-directions. For this simulation, 178 via ports are needed, which is for the full-wave simulation beyond the resource limit of a 32-bit PC. However, the simulation was achieved using

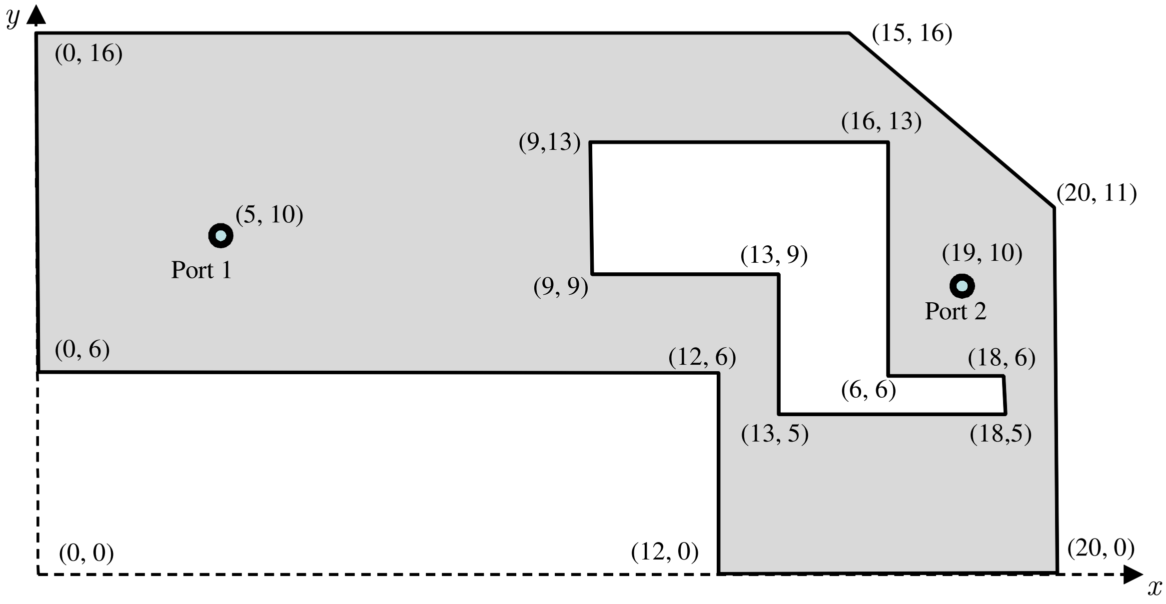

Figure 6.1 Configuration of an L-shape board with a cut-out area. Material constants are specified in Table 6.1. Dimensions are given in inches (1 inch ≈ $2.54 \cdot 10^{-2}$ m).

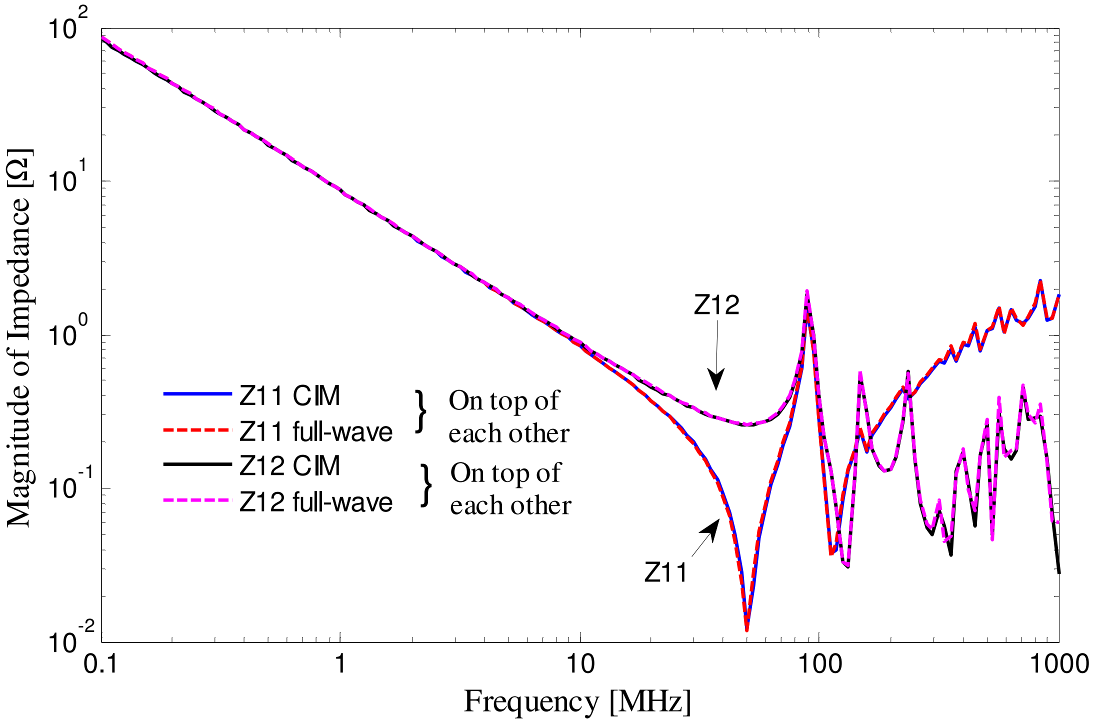

Figure 6.2 Comparison of input and transfer impedances of the bare board case in Fig. 6.1, obtained by CIM and an FEM full-wave solver.

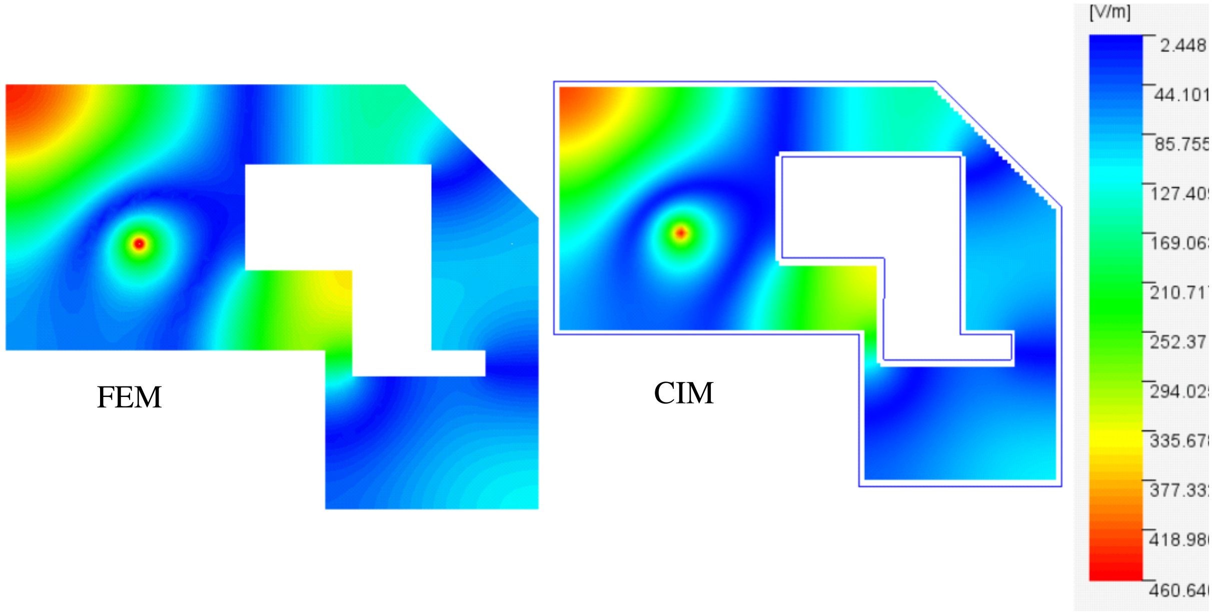

Figure 6.3 Magnitude of the electric field distribution between power and ground planes at 300 MHz for the board configuration in Fig. 6.1 with port 1 excited by a 1-Watt power source and port 2 terminated with 50 Ω, obtained by an FEM full-wave solver and CIM.

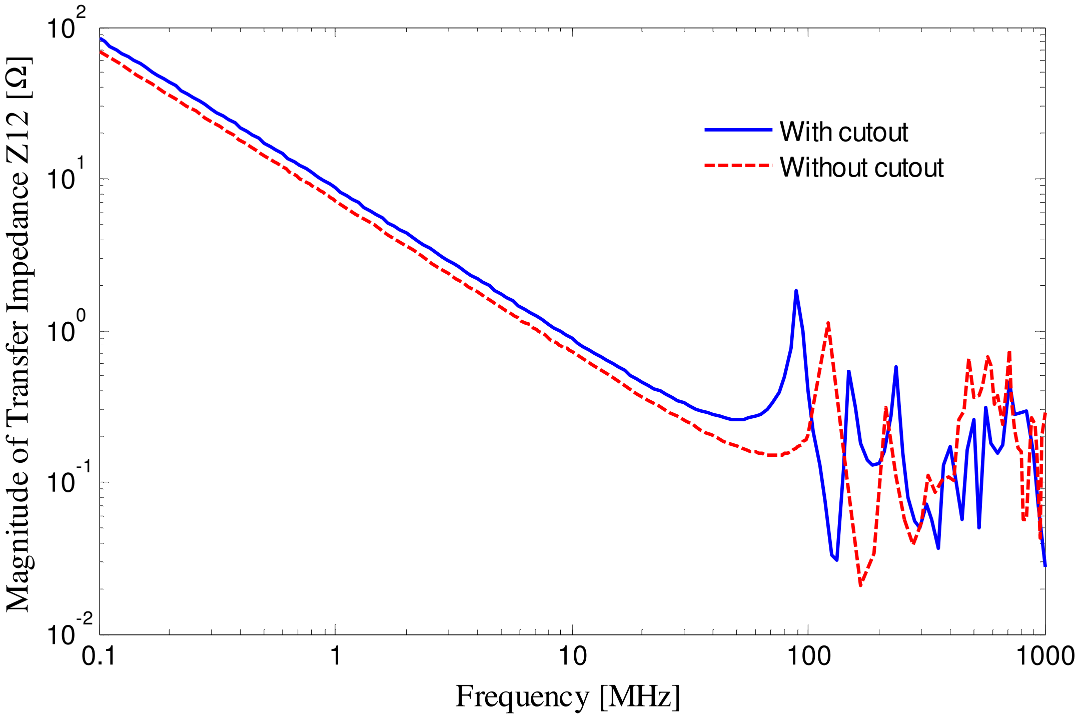

Figure 6.4 Comparison of transfer impedances of the bare board in Fig. 6.1 with that without the cut-out area, obtained by CIM. The cut-out shifts the resonances to lower frequencies comparing to that without the cut-out.

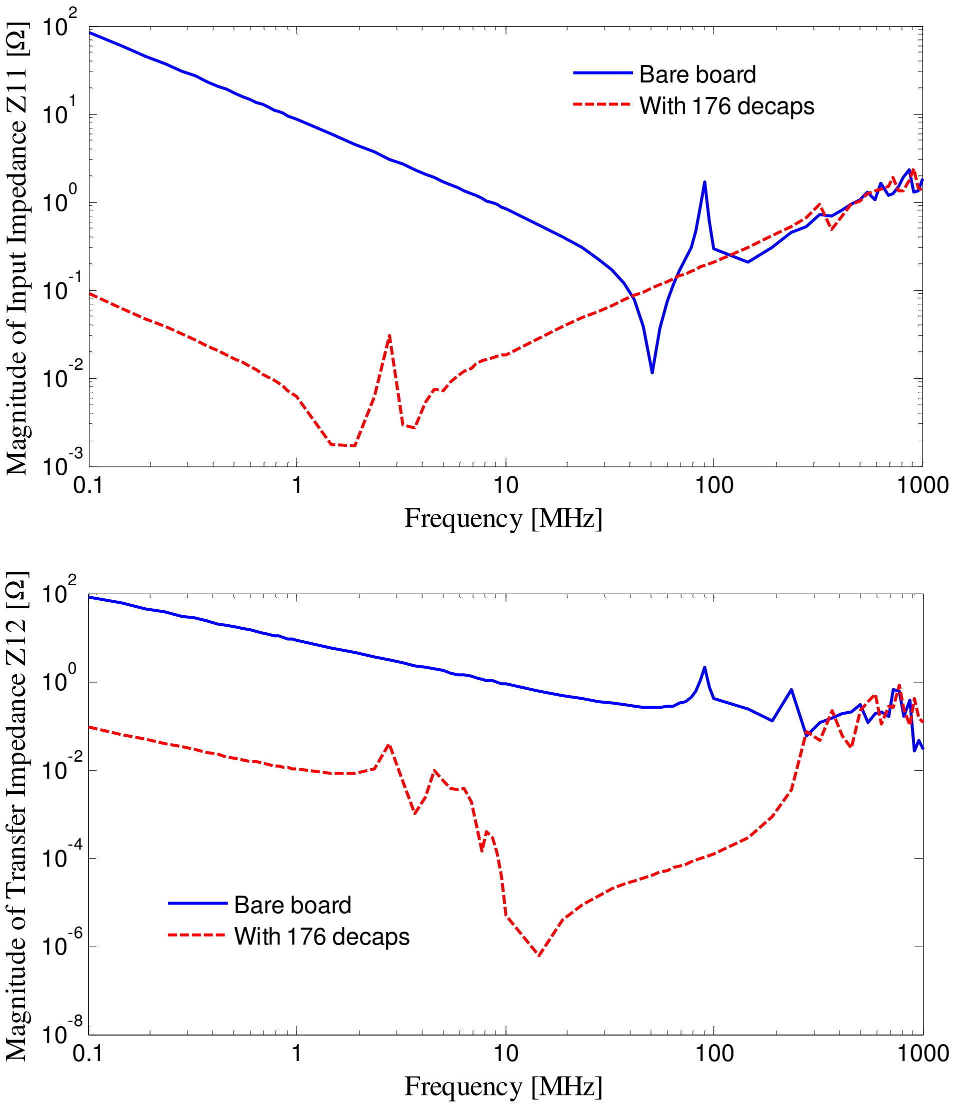

Figure 6.5 Comparison of input (upper) and transfer (lower) impedances of the bare board in Fig. 6.1 to that with 176 decaps, obtained by CIM.

CIM at a reasonable speed of 0.856 seconds per frequency step (s/freq) using only 4.1 MByte RAM. By placing decaps across the board, the input impedance of the board is reduced below 100 mΩ up to 30 MHz, whereas the transfer impedance is reduced up to 300 MHz. Notice that the first few board resonances are shifted to several MHz with decaps, e.g., from about 90 MHz for the bare board to 2.8 MHz for the board with decaps. This phenomenon stresses the importance of cavity resonance modeling for a precise calculation of the power plane impedance even at very low frequencies.

As shown in Fig. 6.6, the electric field distribution between power and ground planes at the first resonance frequency for the bare board at 90 MHz is similar to that with 176 decpas at 2.8 MHz. The electric field amplitude with decaps is, however, more than 40 times less than that of the bare board.

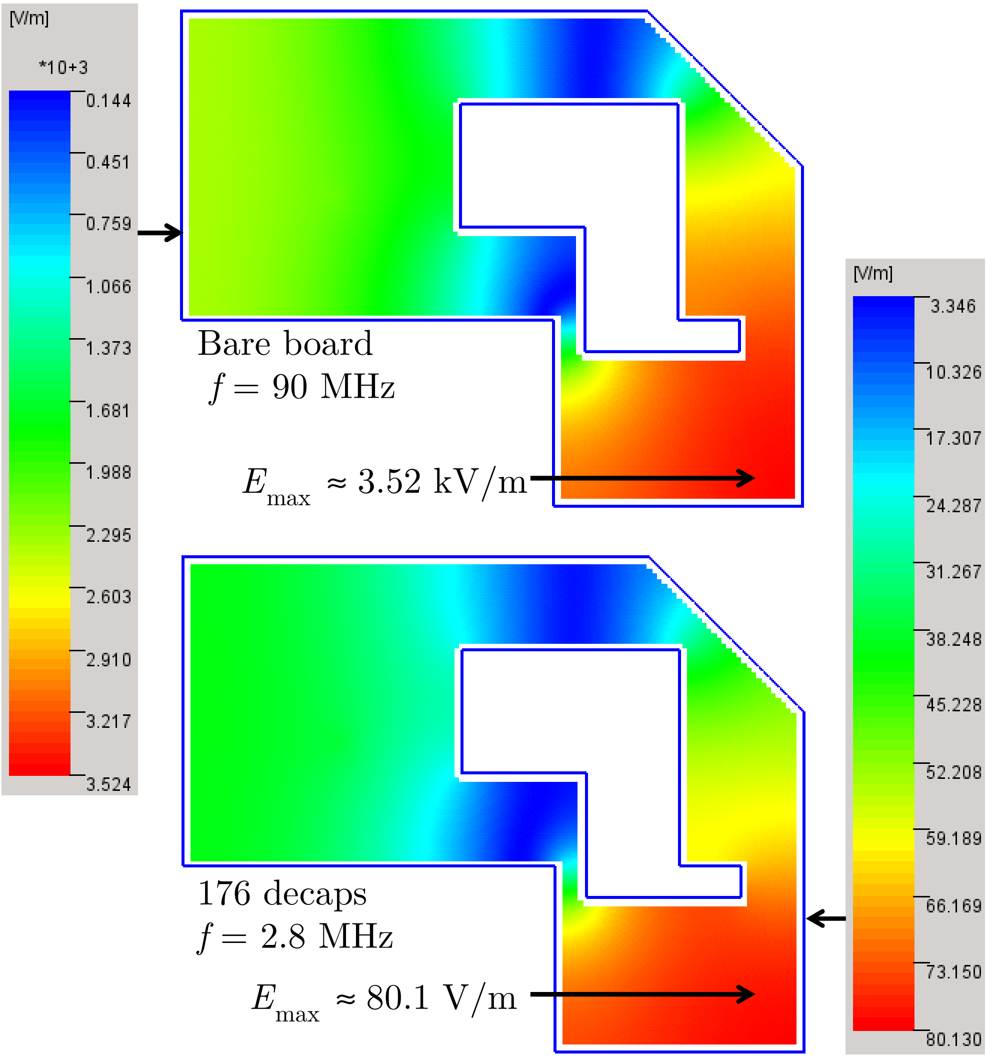

Figure 6.6 Magnitude of the electric field distribution between power and ground planes at 90 MHz for the bare board and at 2.8 MHz for the board with 176 decpas, obtained by CIM. The board configuration is shown in Fig. 6.1. Port 1 is excited by a 1-Watt power source and port 2 terminated with 50 Ω.

6.1.2. Board with Narrow Slot

The next case is a narrow slot structure as shown in Fig. 6.7, which is usually used to prevent noise coupling between two different circuit blocks. Here, PMC conditions are assumed for the board boundary as well as for the edges of the slot, and thus the field coupling across the slot line is neglected, since its effect is minimal in the examined frequency range. At higher frequencies, this field coupling can have a distinguishable effect on the noise propagation in the cavity [155],[156].

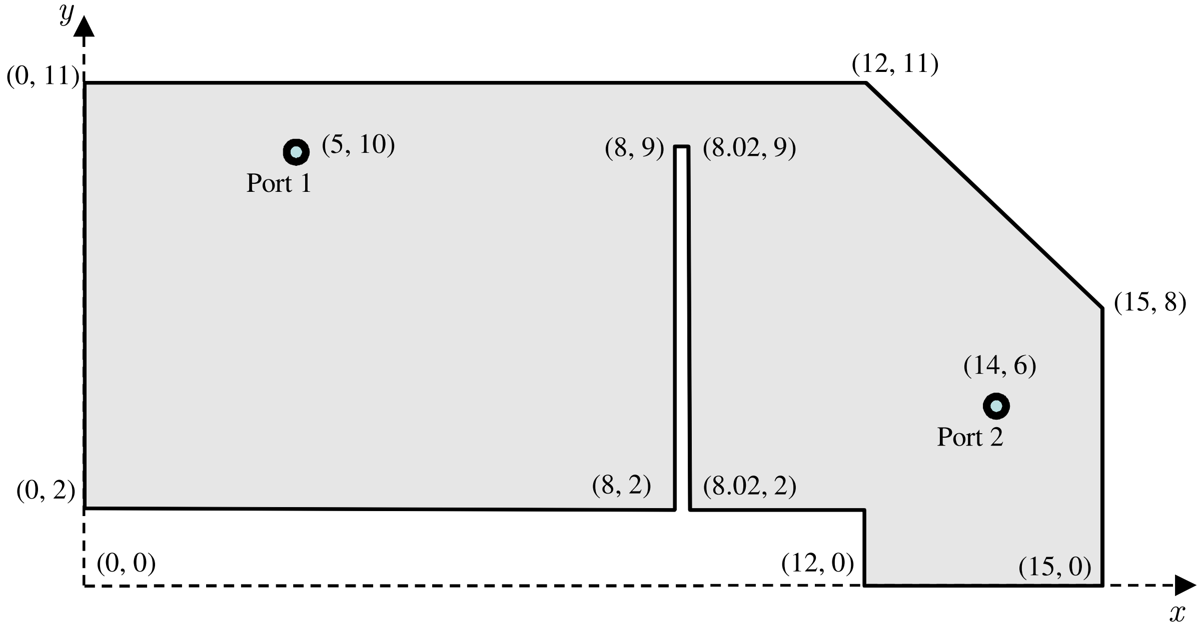

Figure 6.7 Configuration of a board with a narrow slot. Material constants are specified in Table 6.1. Dimensions are given in inches (1 inch ≈ $2.54 \cdot 10^{-2}$ m).

In this configuration, the distance between the two sides of the narrow slot is so small that a discretization of its edges with the tenth-of-wavelength rule does not yield a sufficiently precise result due to the limitation of the numerical integral. The edges of the slot line have to be discretized finer in order to obtain a correct response. A rule of thumb can be made as the length of each discrete segment does not exceed twice the slot width. Obviously, the fine discretization is accompanied with an increased matrix size and affects the computational efficiency.

Input and transfer impedances of the bare board with the narrow slot are plotted in Fig. 6.8, obtained by CIM and the full-wave FEM solver. The two edges of the narrow slot are discretized into 175 segments each, whereas the remaining board boundary is discretized using the tenth-of-wavelength rule. In this way, CIM agrees with the full-wave solver as shown in Fig. 6.8. The effectiveness of the isolation by the narrow slot can be observed by a deep trench at around 190 MHz in the transfer impedance.

Fig. 6.9 shows the electric field distribution of the bare board at 190 MHz simulated using both CIM and a full-wave solver. The two methods predict a similar behavior that the electric field is constrained on the exciting half of the board. The slot line can effectively block the noise penetration to the other half of the plane near the simulated frequency.

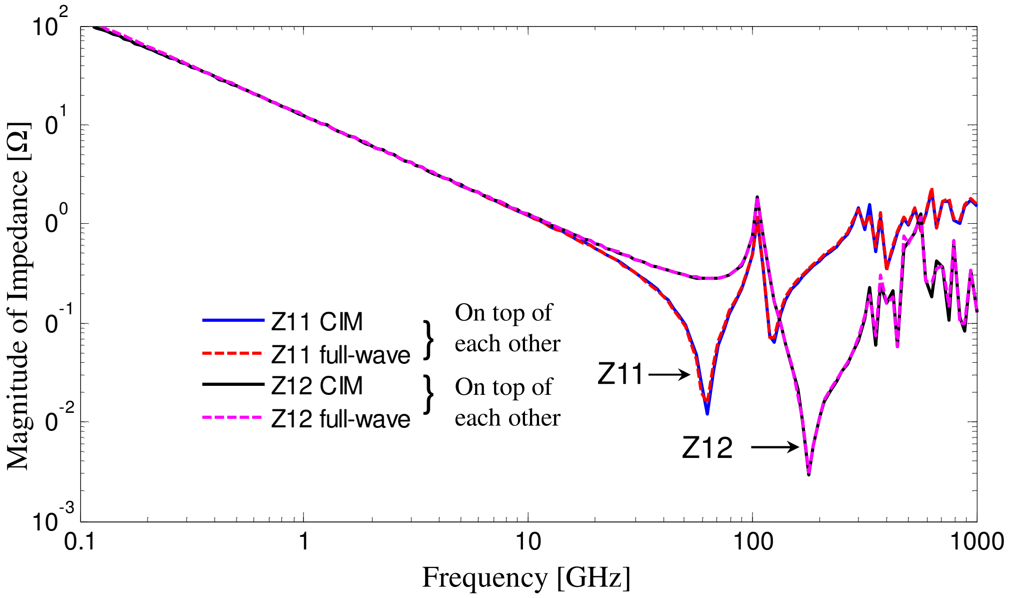

Figure 6.8 Comparison of input and transfer impedances of the bare board case in Fig. 6.7, obtained by CIM and an FEM full-wave solver. The slot line is discretized into 175 segments for each side of the slot. A deep trench is observed at around 200 MHz for the transfer impedance, owing to the isolation effect of the narrow slot.

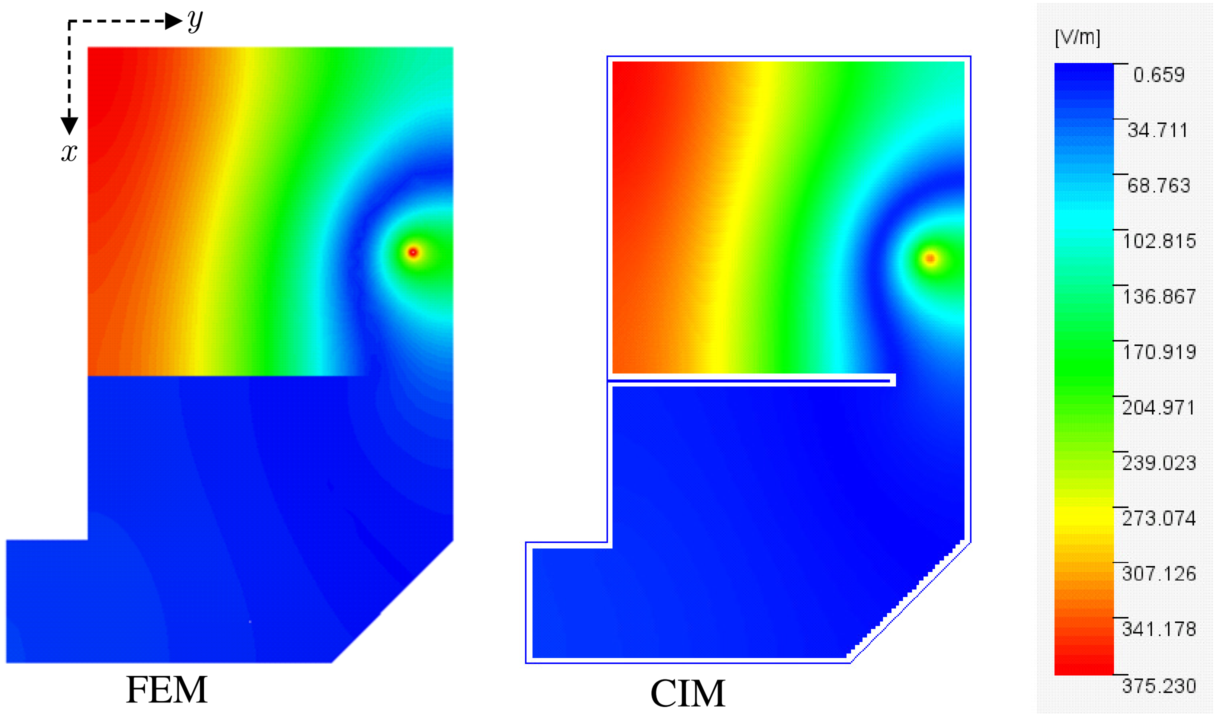

Figure 6.9 Electric field distribution between power and ground planes at 190 MHz for the bare board case in Fig. 6.7 with port 1 excited by a 1-Watt power source and port 2 terminated with 50 Ω, using a full-wave FEM solver and CIM. Both methods show the isolation by the slot line.

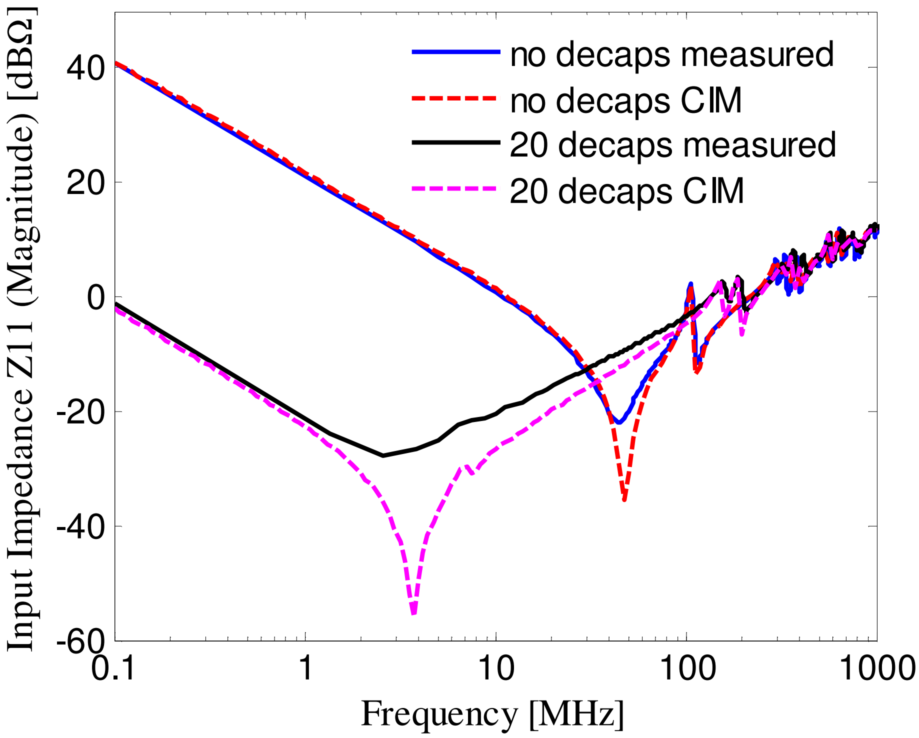

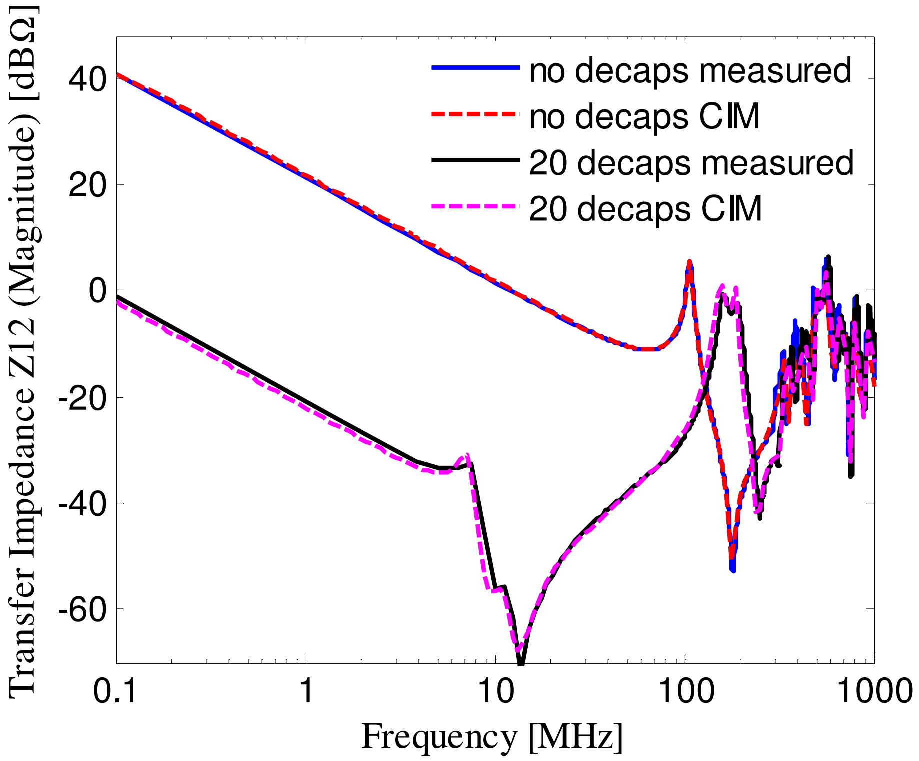

Figure 6.10 Comparison of input and transfer impedances to measurement data for the configuration in Fig. 6.7 in cases of a bare board and a board with 20 decaps.

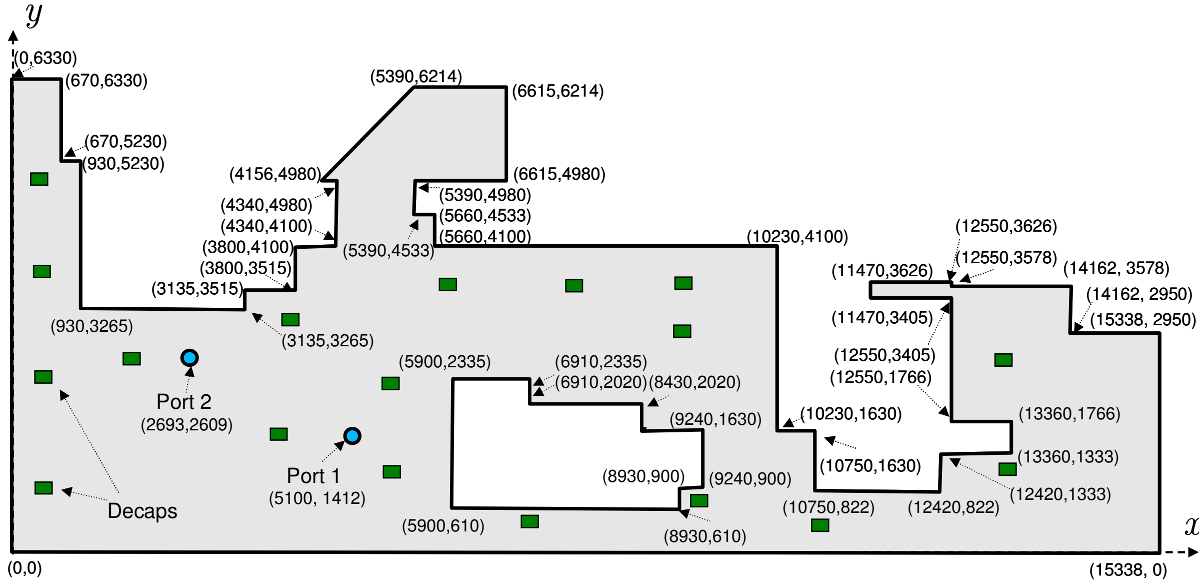

Figure 6.11 Configuration of a complex shaped board. Material constants are specified in Table 6.1. Dimensions are given in mils (1 mil ≈ $2.54 \cdot 10^{-5}$ m).

The configuration of this particular case was manufactured and measured for both cases of the bare board and the board with 20 decaps in [154]. The decaps used in this case are 0.1-µF SMT capacitors with 30-mΩ ESR and 1.3-nH total parasitic inductance. The decaps are located uniformly on the board with a 2.5-inch pitch in the x-direction and a 2-inch pitch in y-direction. For the measurement, the SMA port inductance is estimated to be 380 pH and its pad resistance is neglected. Fig. 6.10 shows the correlation between CIM simulations and the measurement data.

6.1.3. Complex Shaped Board

The configuration of the last case in this section, as shown in Fig. 6.11, is a pair of very complex shaped power planes whose outer boundary and cut-out area consist of 38 and 20 edges, respectively. Modeling of such a complex geometry would be a difficult task for segmented methods with analytical solutions such as in [157]-[159] due to a cumbersome preprocessing where the board has to be partitioned into regular shapes with line ports defined at the junctions. In CIM, no partition is needed and only the contour coordinates are necessary to be given for the computation, which greatly mitigates the modeling effort.

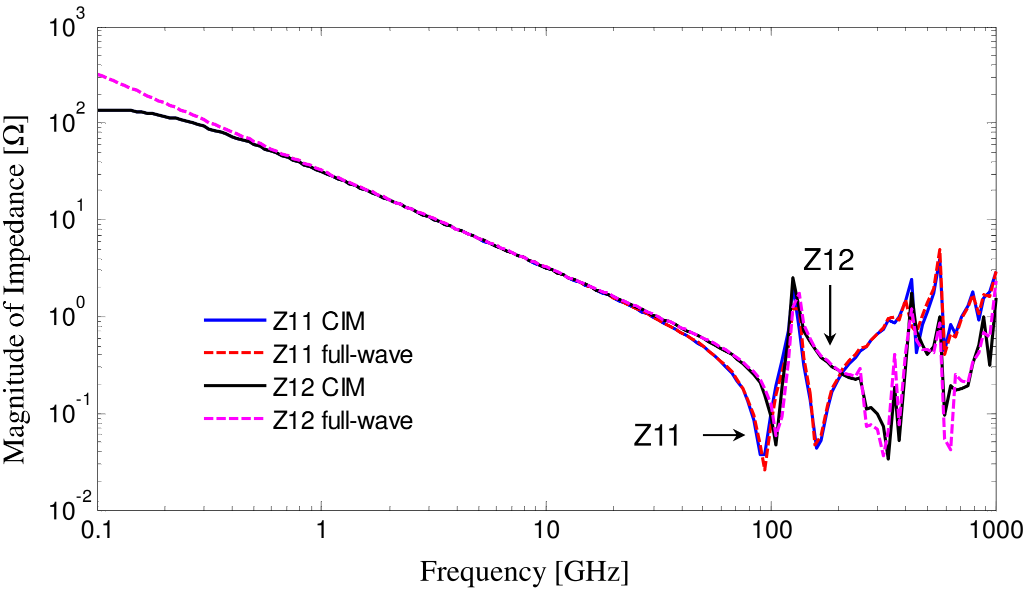

Figure 6.12 Comparison of input and transfer impedances of the bare board case in Fig. 6.11, obtained by CIM and an FEM full-wave simulation.

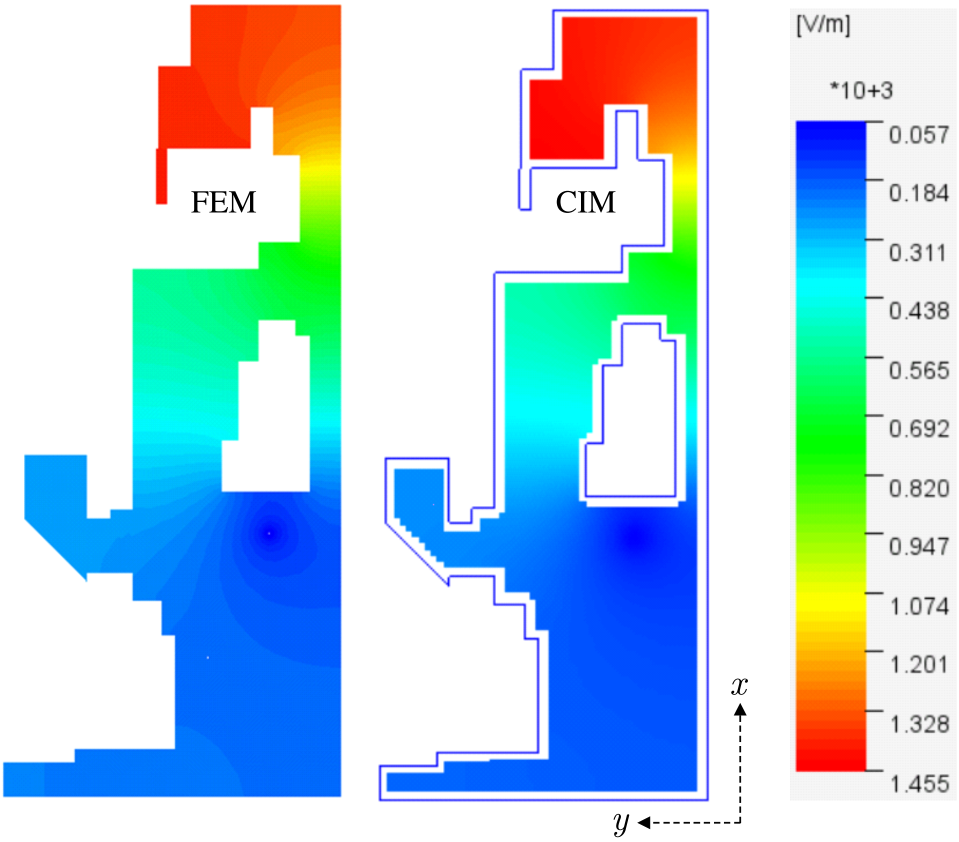

Figure 6.13 Magnitude of the electric field distribution at 100 MHz for the bare board case in Fig. 6.11 with port 1 excited by a 1-Watt power source and port 2 terminated with 50 Ω, using CIM and a full-wave FEM solver.

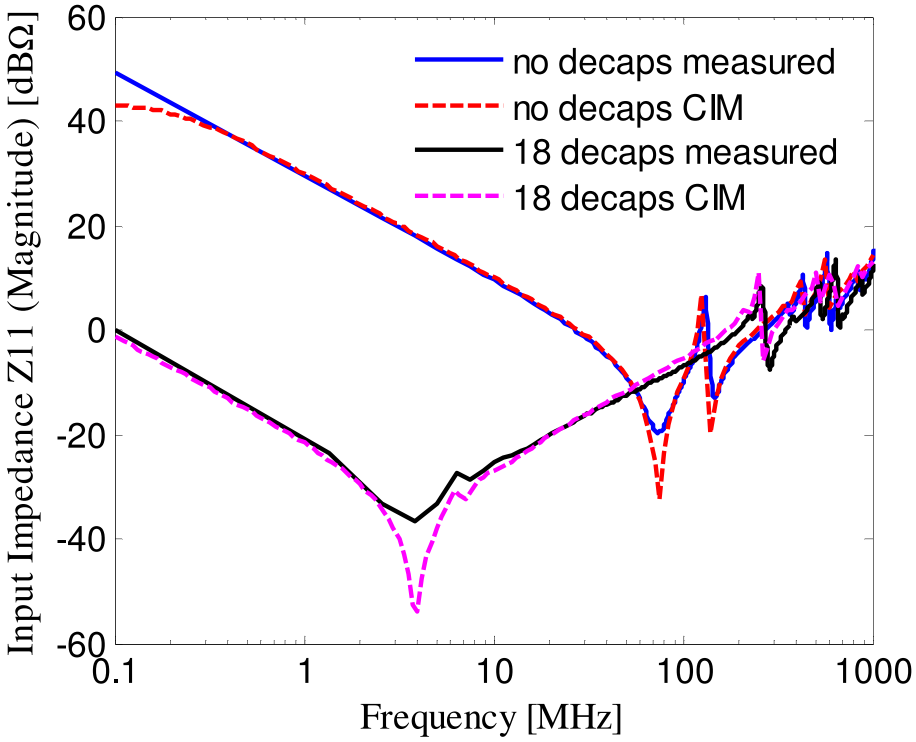

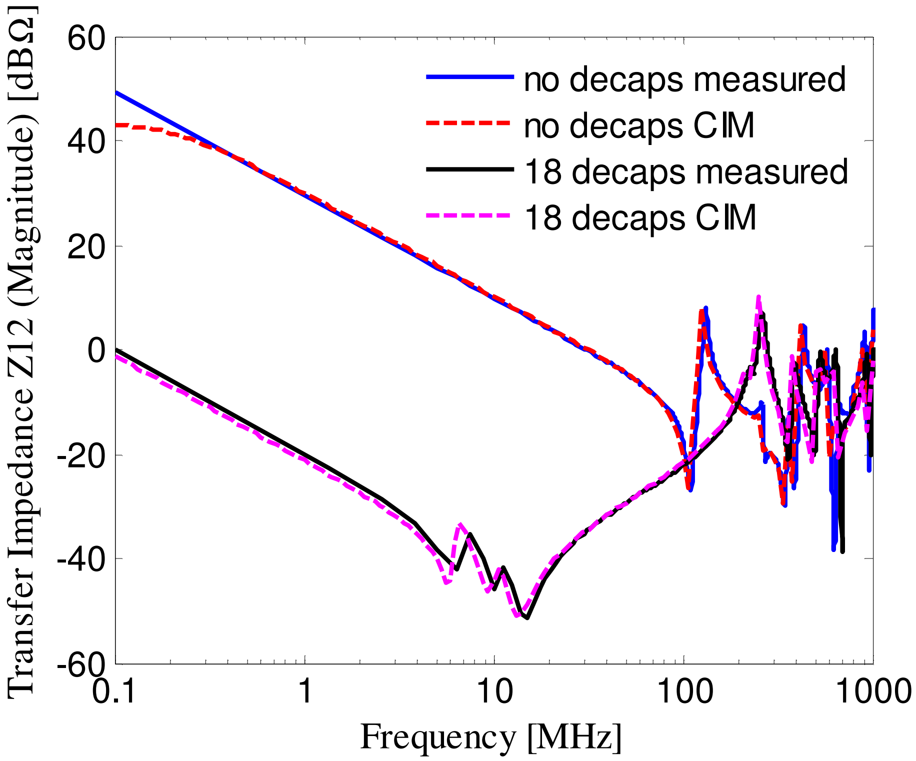

Figure 6.14 Comparison of input and transfer impedances to measurement data for the complex board configuration in Fig. 6.11 in cases of a bare board and a board with 18 decaps.

The input and transfer impedances of the bare board obtained by CIM are compared in Fig. 6.12 to the full-wave FEM results. The overall agreement between them is good except for a small deviation in the kHz frequency range, which does not appear in the previous two cases. This may be explained by a limited numerical precision of CIM at very low frequencies due to the high complexity of the board contour. However, it can be easily corrected, since the bare board behaves as a parallel-plate capacitance in that frequency range.

In Fig. 6.13, the electric field distributions of the bare board at 100 MHz, simulated with both CIM and a full-wave solver, are illustrated. Although both input and transfer impedances are low at 100 MHz as shown in Fig. 12, a “hot area” can be identified at the far end of the board beyond the neck-down region. Fig. 6.14 shows the correlation between CIM simulations and measurement data [154] in case of the bare board and with 18 decaps whose locations are depicted in Fig. 6.11.

6.1.4. Discussion on Applicability and Limitations

Table 6.2 summarizes the simulation time and the amount of RAM required, including the three cases in this section as well as the rectangular board case in section 5.1.3. The simulations for the study cases were run on a 32-bit 3-GHz PC with 2 GByte RAM.

Table 6.2. Summary of simulation time and memory demand using the contour integral method. (s/freq = second per frequency point, decaps = decoupling capacitors)

Board Configuration	**CPU time (s/freq)**	**Memory (MBytes)**
Rectangular (bare board)	0.034	< 1
Rectangular (5 decaps)	0.037	< 1
Rectangular (10 decaps)	0.041	< 1
L-shape without cut-out (bare board)	0.070	< 1
L-shape without cut-out (7 decaps)	0.077	< 1
L-shape without cut-out (15 decaps)	0.087	< 1
L-shape with cut-out (bare board)	0.218	1.1
L-shape with cut-out (176 decaps)	0.856	4.1
Narrow slot (bare board)	1.430	6.1
Narrow slot (20 decaps)	1.494	6.6
Complex (bare board)	0.127	< 1
Complex (18 decaps)	0.155	< 1

For PI applications, the extended CIM has been shown to be highly accurate for the presented examples and can be applied to any arbitrary shaped power planes. The efficiency of this approach is, in general, very good, as shown in Table 6.2. The simulation time was under 1 s/freq for most of the configurations, except for the case with the narrow slot line where the slot boundary has to be fine discretized to achieve a sufficient accuracy. Besides, it is relatively easy to create a model using CIM, since only the contour of the power plane has to be specified. Furthermore, CIM can provide field distributions inside the cavity, which is very useful to PI analyses. It allows the designer to control noise propagation over the whole board. For instance, in the complex shape example, the input and transfer impedances of port 1 and 2 are both low at 100 MHz. However, it can be seen in Fig. 6.13 that the electric field can be high on the other half of the board.

Despite of the extensions in this work, CIM still suffers from some limitations. The simulation becomes slow in case of narrow slots. Also, noise coupling across slots is not captured at present. The calculation of radiation is restricted to solid parallel planes. At this point, the field radiated from openings and cut-outs cannot be handled.

6.2. Stacked Power Planes

To evaluate the applicability of the hybrid method combing CIM with the physics-based via and trace models to stacked power planes, as described in section 5.3, two multilayer examples are presented in this section. A dense via array example is first analyzed with the focus on SI results and passivity issues. Then, a multilayer PCB example is simulated to obtain SI, PI, and EMI related results such as S-parameters, field distributions inside the cavity, and radiated powers. The isotropic port formulations in Section 4.2 will be used for the analysis here.

6.2.1. Dense Via Array and Passivity Issue

Modern via pin fields can contain thousands of vias in a small area, as shown earlier in Fig. 5.2. Modeling such large and dense via arrays using general-purposed full-wave solvers remains impractical prompting the development of faster approaches such as multiple scattering methods [81]-[83] and equivalent-circuit based via models [106],[110].

In principle, equivalent-circuit based approaches provide the best efficiency thanks to analytical solutions available for the evaluation of the circuit elements. In particular, the radial waveguide (RW) method [59],[63] is often used to calculate the parallel-plate

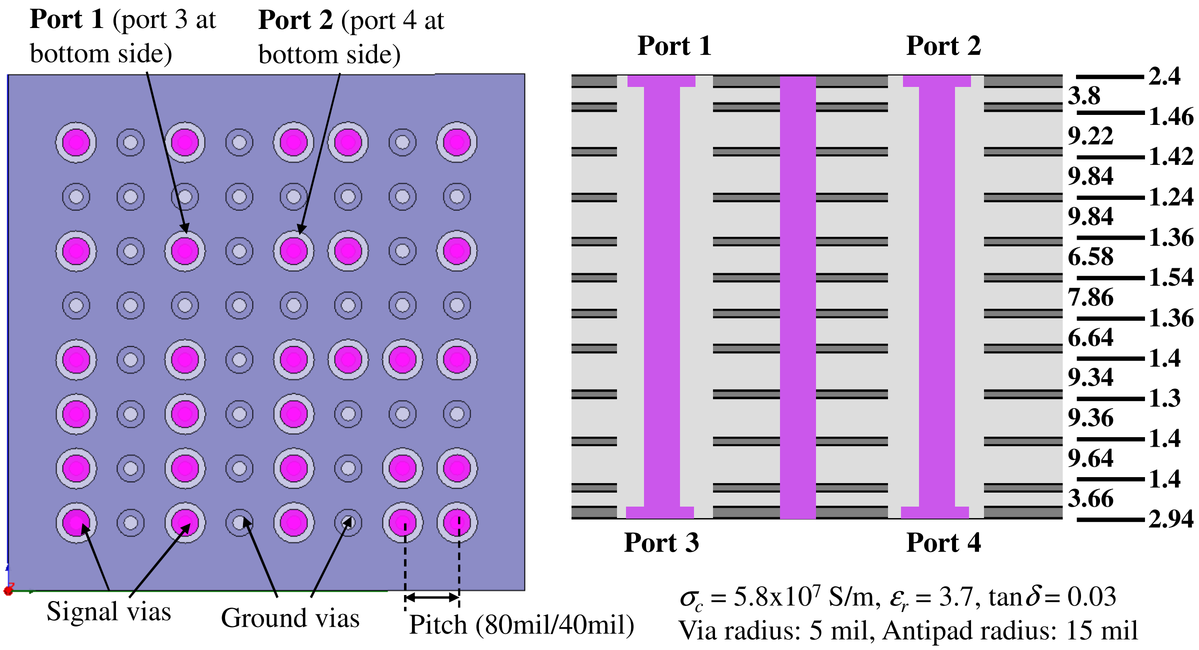

Figure 6.15 Top view (left) and cross section view (right) of an 11-cavity 8-by-8 via array example. The boundary is assumed to be a perfectly matched layer (PML). Dimensions are given in mils (1 mil ≈ $2.54 \cdot 10^{-5}$ m).

impedance Z_{pp}, which is modeled by CIM in this work. The RW method uses the Green's function for solid planes and is not consistent with the open condition of an impedance definition [110]. The scattered field becomes larger for vias with smaller separations, which may significantly affect model results in the case of dense via arrays with small pitches.

Passivity violations, where the singular values of the S-parameter matrix can exceed 1 [29] due to neglect of this multiple scattering effect can occur. As will be shown in the next example with an 8-by-8 via array, as shown in Fig. 6.15, analyzed using the physics-based via model with the RW method, significant passivity violations can occur in the simulation result. In contrast, the Z_{pp} obtained by CIM takes into account this scattering effect from open ports. The passivity violation can be suppressed by using CIM formulation for the Z_{pp} calculation.

Fig. 6.16 shows the transmission results S_{13} and S_{24} for a pitch size of 80 and 40 mils, obtained from both the physics-based via model with the RW method and a full-wave FEM solver [117]. The results show a good correlation. However, the physics-based via model results exhibit a clear passivity violation for the 40-mil pitch case. Both S_{13} and S_{24} exceed 0 dB by about 0.1 dB in the frequency range from 25 to 30 GHz and from 20 to 25 GHz, respectively, in spite of the losses introduced in the cavity. Fig. 6.17 plots singular values of the S-parameter matrix from the physics-based via model. Non-

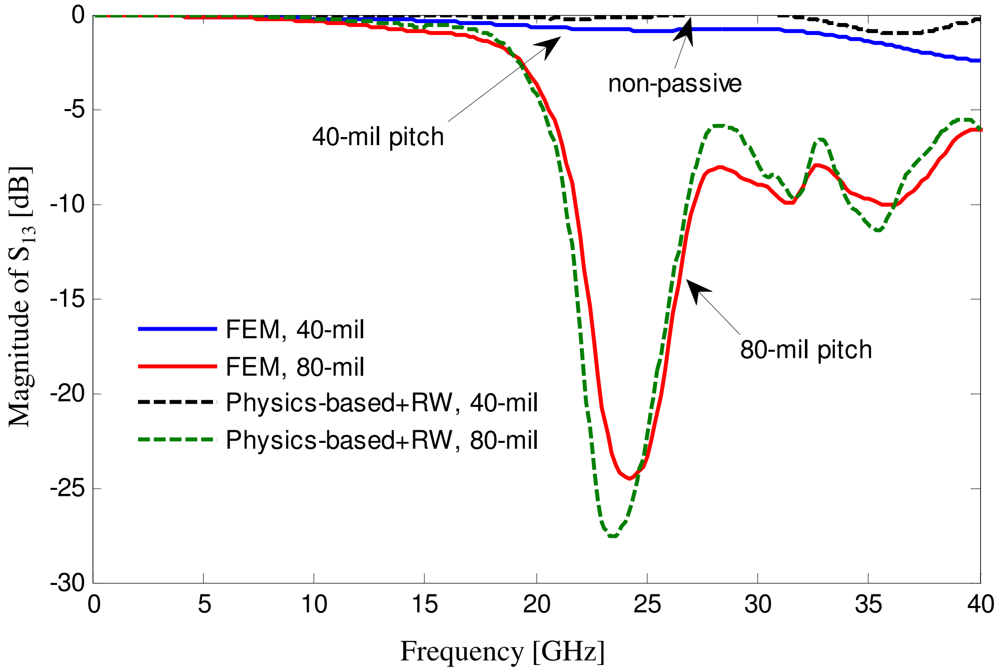

(a)

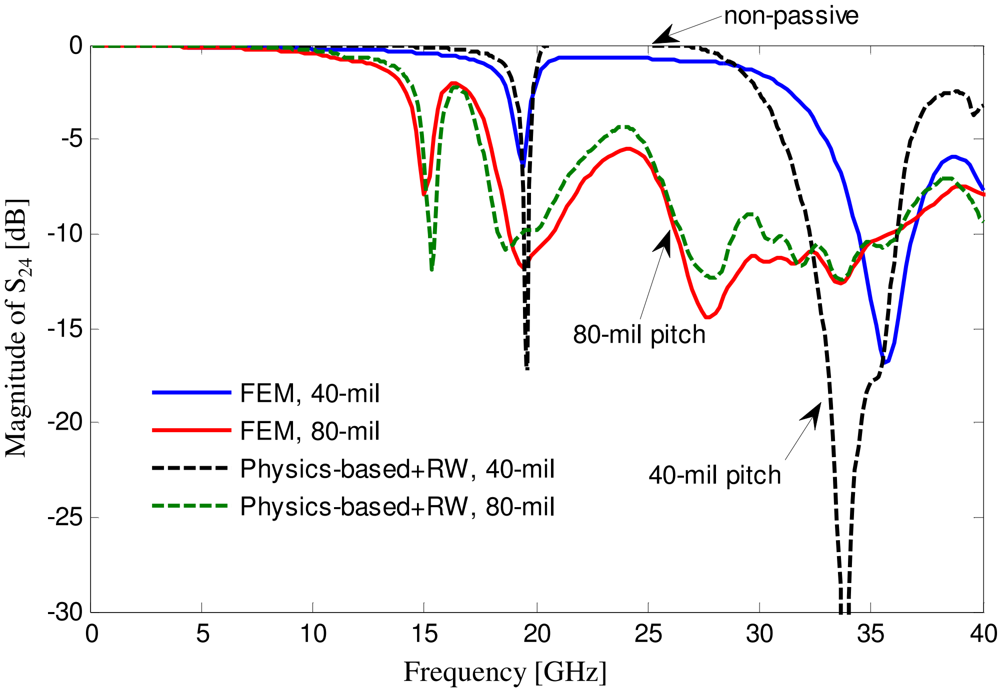

(b)

Figure 6.16 Magnitude of transmission (a) S_{13} and (b) S_{24} for the via array case in Fig. 6.15, obtained by the physics-based via model with the RW formula and a full-wave FEM solver. The result from the physics-based via model for the 40-mil pitch shows non-passive behavior in the frequency range from 20 to 30 GHz.

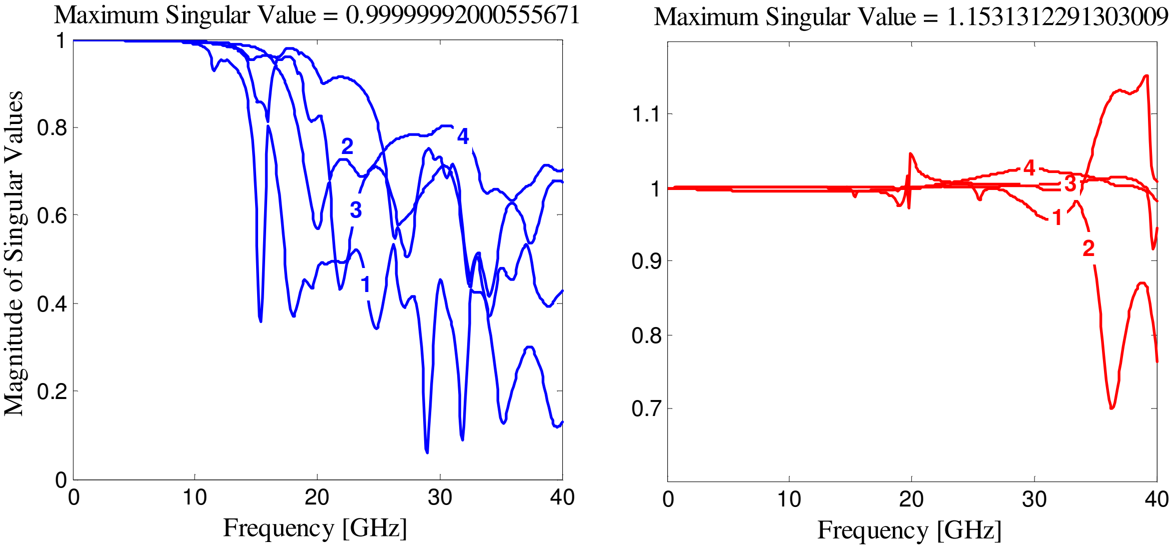

Figure 6.17 Singular values extracted from S-parameter matrix obtained by the physics-based via model with the RW formula for the via array example in Fig. 6.15 for cases of (left) 80-mil pitch and (right) 40-mil pitch. Passivity violation is observed for S-parameters of the 40-mil pitch case.

passivity does not appear in the 80-mil pitch data, whereas strong passivity violations are identified for the 40-mil pitch case near 20 GHz and over 30 GHz, which may not be tolerated for a meaningful time domain analysis.

The analysis shows the potential of passivity problems for via array modeling using the RW method. It is also observed that the occurrence of the passivity violation depends on the pitch size, which is only related to Z_{pp} in the model. The cause of the passivity violation may be attributed to neglecting the energy of the scattered field from open ports, which is considered in CIM.

It is recognized that CIM can be reduced to the RW formula by leaving out the off-diagonal elements of $\overline{\overline{U}}^{pp}$ in (4.12), which are responsible for the inclusion of scattered fields from open ports. The off-diagonal elements of $\overline{\overline{U}}^{pp}$ depend on the frequency, the via radius, and the distance between vias. Taking a 2-port single cavity with a relative dielectric constant of 3.7 as an example, Fig. 6.18 plots the magnitude of U_{12}/U_{11} with different port radii and different distances between the two ports, which signifies the influence of the scattered field from one open port to the incident field. It is observed that the impact of the scattering increases with frequency and becomes more significant for larger ports and ports in closer proximity. This indicates that the multiple scattering can have a larger effect in via arrays with smaller pitches, since the vias lie closer to each other.

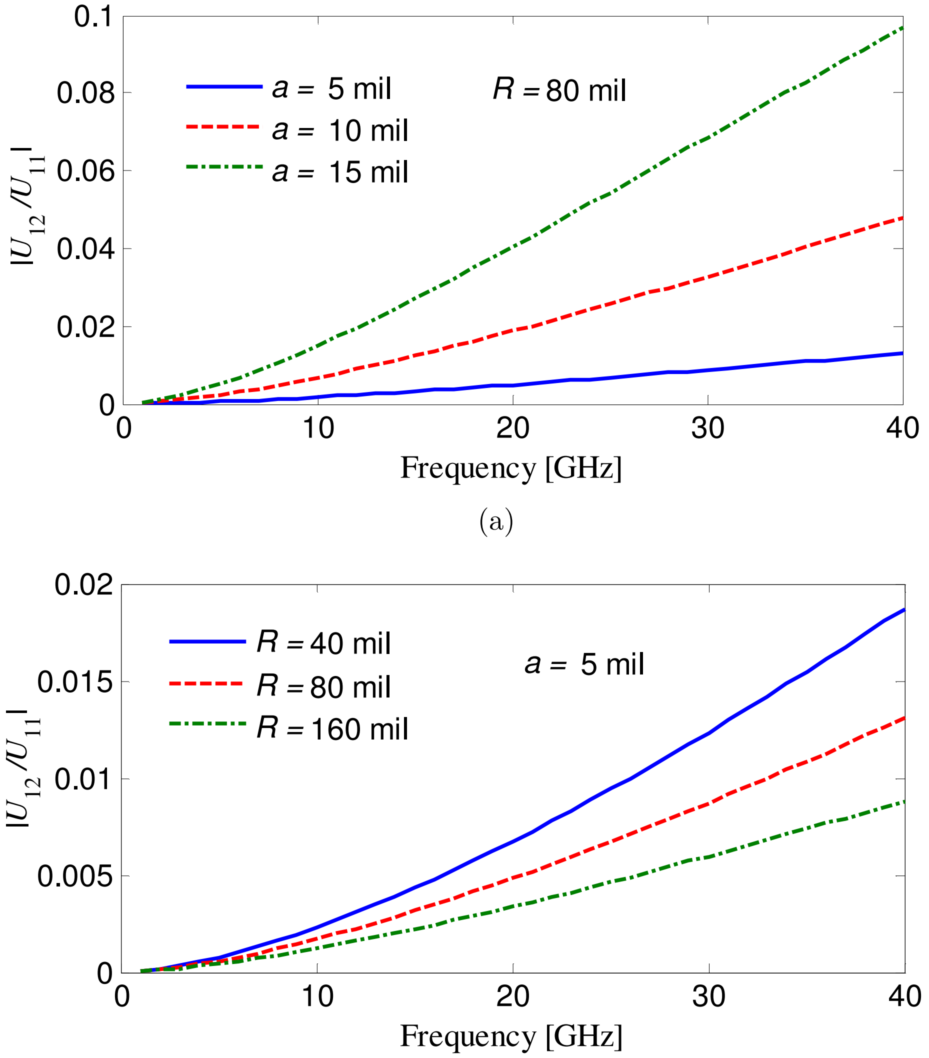

(a)

(b)

Figure 6.18 Magnitude of U_{12}/U_{11} of a two-port system, obtained by **(4.12)**. It implies the influence of the scattered field from one open port on the incident field. The impact is larger for (a) ports with bigger radius and (b) ports with shorter distance.

The via array example, as shown in Fig. 6.15, is re-simulated here using the physics-based via model again with CIM, as formulated in Section 5.3. The transmission results S_{13} and S_{24} with the CIM for both the pitches of 80 and 40 mils are plotted in Fig. 6.19 and compared to that with the RW. For the 80-mil pitch, the difference between the two approaches is barely observable, indicating that the solid plane approximation in the RW method is sufficiently accurate for this pitch size. For the 40-mil pitch, although the deviation is also not large, more importantly, the S-parameter results with the CIM are physically more meaningful since they have been brought down to less than 0 dB for all frequencies.

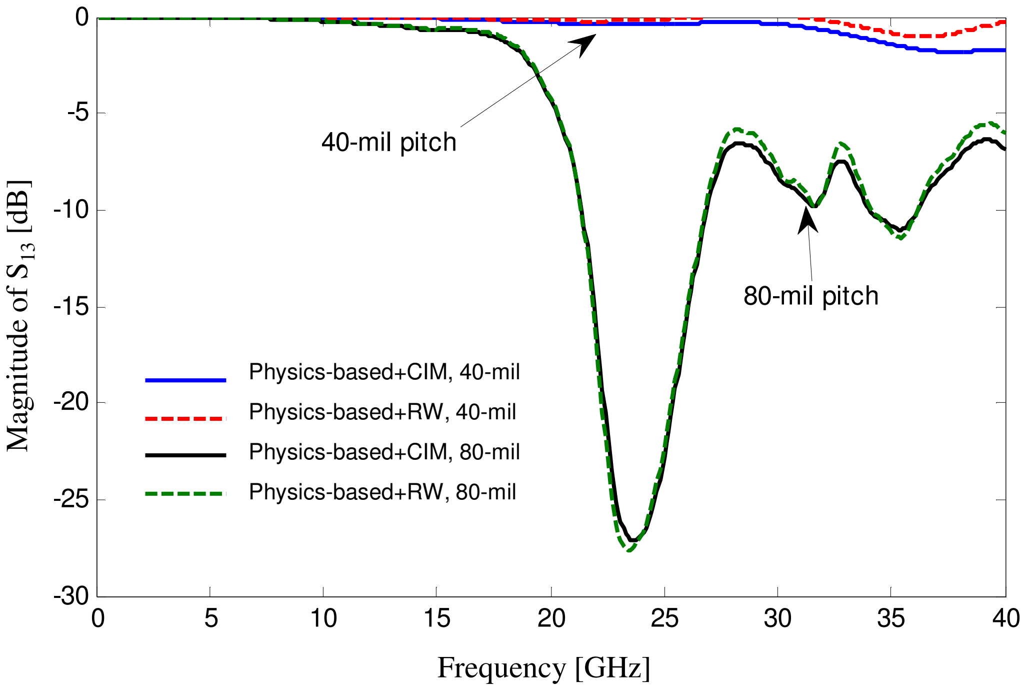

(a)

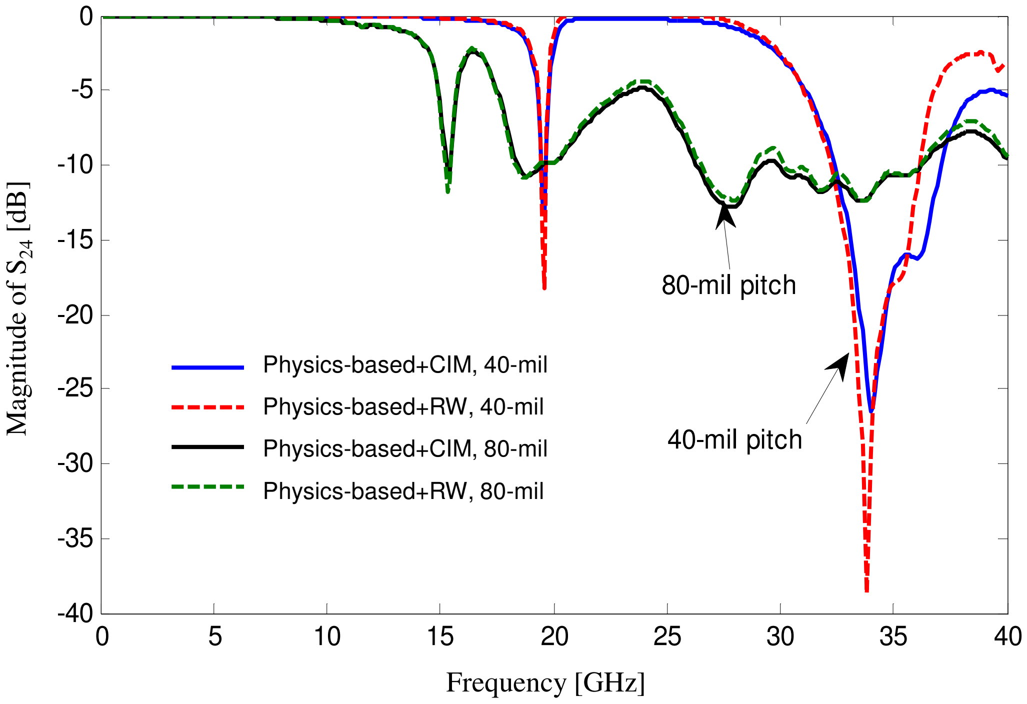

(b)

Figure 6.19 Magnitude of transmission (a) S_{13} and (b) S_{24} for the via array case in Fig. 6.15, obtained by the physics-based via model with RW formula and with the CIM. The non-passive behavior has been corrected by using CIM.

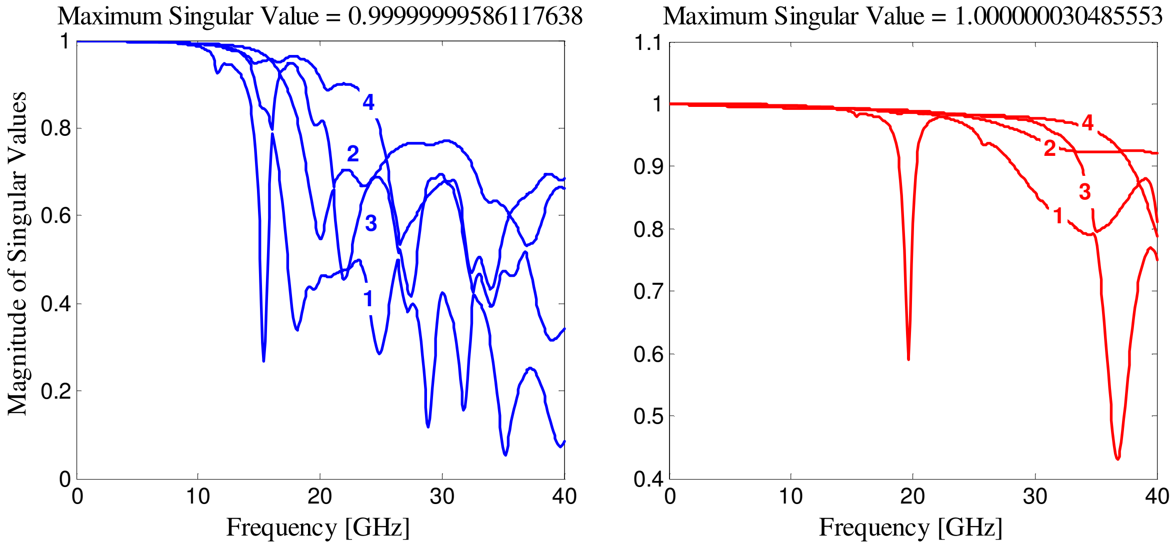

Figure 6.20 Singular values extracted from the S-parameter matrix obtained by the physics-based via model with CIM for the via array example in Fig. 6.15 for cases of (left) 80-mil pitch and (right) 40-mil pitch. Only a negligible passivity violation is observed for the 40-mil case at very low frequencies with a maximum singular value of 1.0000000305 due to the finite numerical precision of the Hankel function evaluation.

The singular values of the S-parameter matrix, obtained by the physics-based via model with the CIM, are shown in Fig. 6.20. No severe passivity violation is present for either pitch. Only a slight violation is observed for the 40-mil data at very low frequencies due to the finite numerical precision of the Hankel function evaluation. This is, however, easily corrected by a passivity enforcement algorithm [160],[161].

It can be concluded from the case studied here that the effect of multiple scattering may have a rather small impact on the accuracy of equivalent-circuit based models, but is critical for the model passivity, especially for via arrays with small pitch sizes. The total simulation for a single-core 3 GHz CPU with 4 GB memory for this example using the physics-based via model with the CIM required 85 seconds, which is slightly slower when compared to the 65 seconds required for the RW formula due to an additional matrix inversion. However, this is still very efficient considering the complexity of this example. In contrast, the FEM solver takes several days to solve this problem with the same hardware resource.

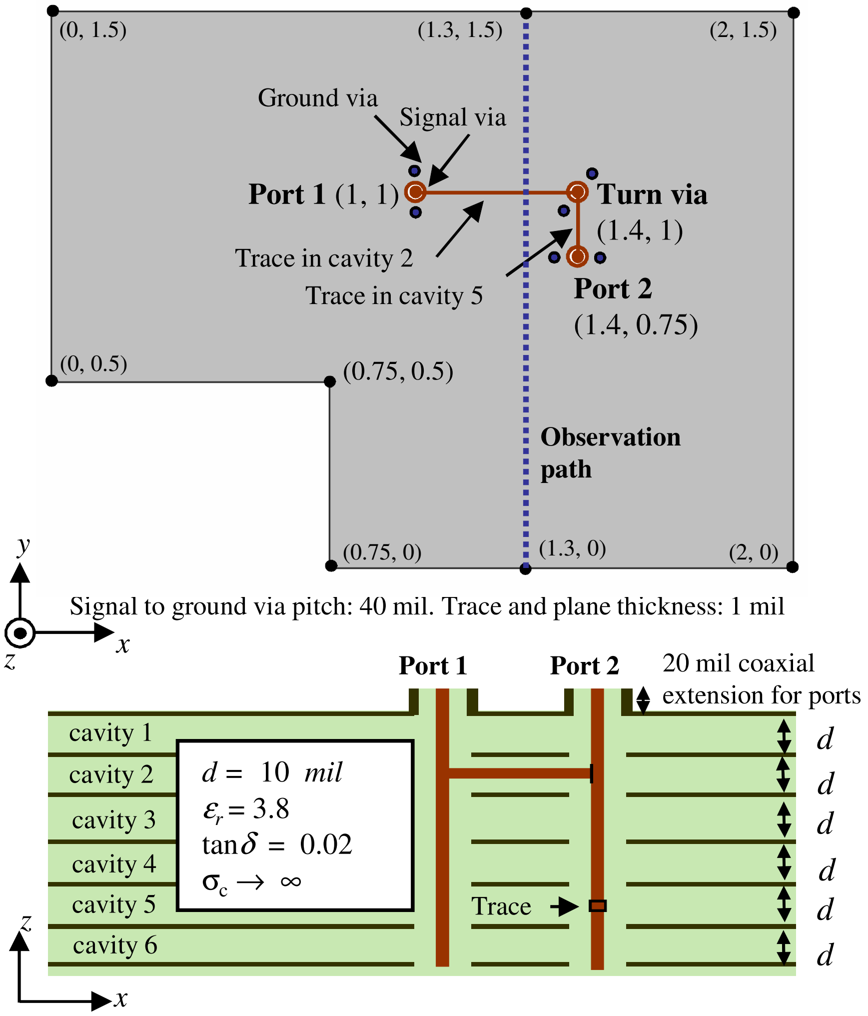

Figure 6.21 An L-shaped multilayer printed circuit board with two traces at different cavities and six ground vias. The ground vias are shorted to all seven ground planes. Dimensions are given in inches (1 inch ≈ $2.54 \cdot 10^{-2}$ m).

6.2.2. Analysis of Multilayer Printed Circuit Board

The hybrid method in Section 5.3 has been applied to several single-cavity cases. This section will explore a multilayer structure including stripline traces and ground vias. The goal of the analysis is to simultaneously generate different metrics that are useful for SI, PI, and EMI applications such as S-parameters, field distributions, radiation diagrams, and radiated power. The results will be validated with full-wave simulations. More application examples may be found in [13],[15], and [142].

A six-cavity L-shape board example is shown in Fig. 6.21. A single-ended signal link is connected with three through-hole signal vias and traverses the turn via from cavity 2 to cavity 5. Both traces are 4-mil wide and vertically centered in the cavities. The

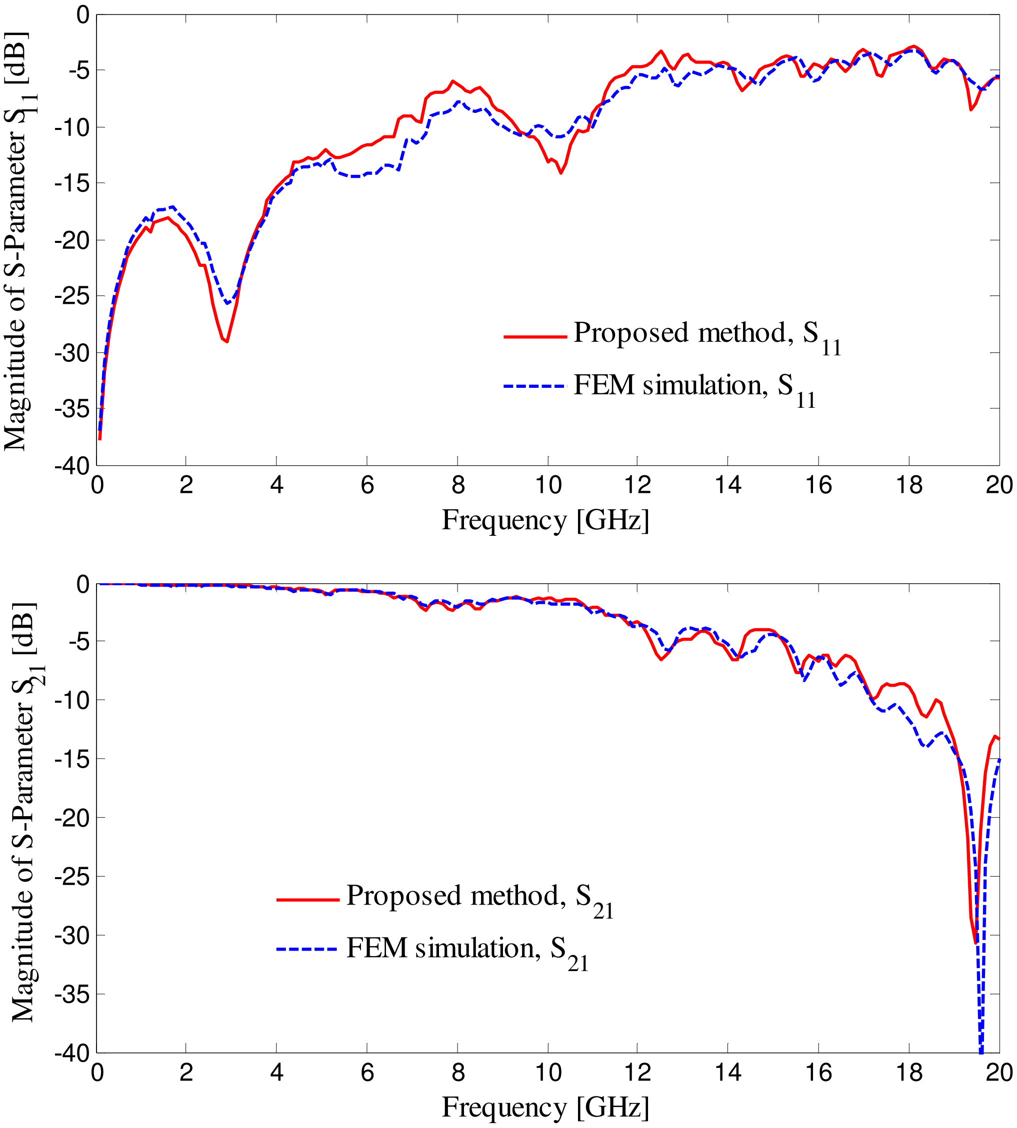

Fig. 6.22 S-parameters at defined ports for the example in Fig. 6.21, obtained with the proposed method and a full-wave FEM analysis.

signal vias are left open on the bottom side of the board with the turn via open also on the top side. The reference planes are assumed to be all ground planes. Six ground vias, shorting all the reference planes, are placed near the through-hole vias with a pitch of 40 mil. Two ports are defined on the top side with coaxial extensions of 20 mil, as shown in Fig. 6.21. The coaxial extensions are modeled as ideal transmission lines in the hybrid method.

S-parameter results are plotted in Fig. 6.22, obtained using both the hybrid method and a full-wave finite element (FEM) based solver [117]. The full-wave simulation is configured with an air box surrounding the board, so that radiation effects are included. Both methods predict a similar behavior of the link. The transmission S_{21} decreases at higher frequencies and reaches the minimum at around 20 GHz, which is attributed to the via stub resonance of the first via [162]. The deviation of the two curves could be explained by the following: The characteristic impedance used in the combined method was analytically calculated as 47Ω, which might be different in the full-wave simulation. The thickness of the coaxial region at the antipads is neglected in the proposed method. Although the thickness of a single metal plane is small, they may have a visible effect cumulatively in a multilayer environment. Also, the ground vias are relatively close to the traces, which might deform the local fields that are not captured by the proposed method; furthermore, the proposed method assumes a PMC boundary condition, which neglects the finite impedance of the air. This causes a deviation with respect to the full-wave simulation, especially in the high frequency range where the power leakage through board edge can be considerable.

Figure 6.23 shows the surface maps of the electric field distribution inside the first cavity at 4 GHz, obtained by both the proposed method and the full-wave simulation. An incident power of 1 W was used to excite port 1, and port 2 is terminated with 50 Ω in both of the simulations. Similar field pattern can be observed using both of the methods. A slight mismatch of peak locations may be explained by the neglected radiation loss by CIM that shifts the resonance frequencies. The high electric field amplitude in the via antipad areas in the FEM result is attributed to the via-plate capacitance. The electric field in this area is not explicitly included in the proposed method.

The electric field amplitudes along the observation path, shown in Fig. 6.21, for different layers are plotted in Fig. 6.24. It is reasonable that the noise amplitude inside the cavities becomes less for lower layers, since most of the signal current flows through the traces leaving little current on the via stubs to excite lower cavities.

The radiated power is plotted in Fig. 6.25, obtained by first calculating the boundary voltage distribution under the PMC condition and then a superposition of the radiation from each cavity. For low frequencies in the MHz range, the full-wave simulation predicts higher radiation due to an insufficient distance to the absorbing boundary that results in loss of accuracy for the full-wave solver. Similar resonance peaks are observed for both methods from 1 GHz up to 10 GHz. Beyond that, the resonances predicted by the proposed method are more noticeable than by the FEM simulation and the correlation becomes slightly worse at higher frequencies. This is possibly due to the omission of the power leakage from board edges by the hybrid method that results in higher Q resonances, as seen in Fig. 6.25. Despite of that, the overall tendency agrees well with the full-wave result. Further extension of the method may involve techniques in Section 5.2 to account for the radiation loss in multilayer applications. The radiation diagram at 4 GHz obtained by both methods is compared in Fig. 6.26.

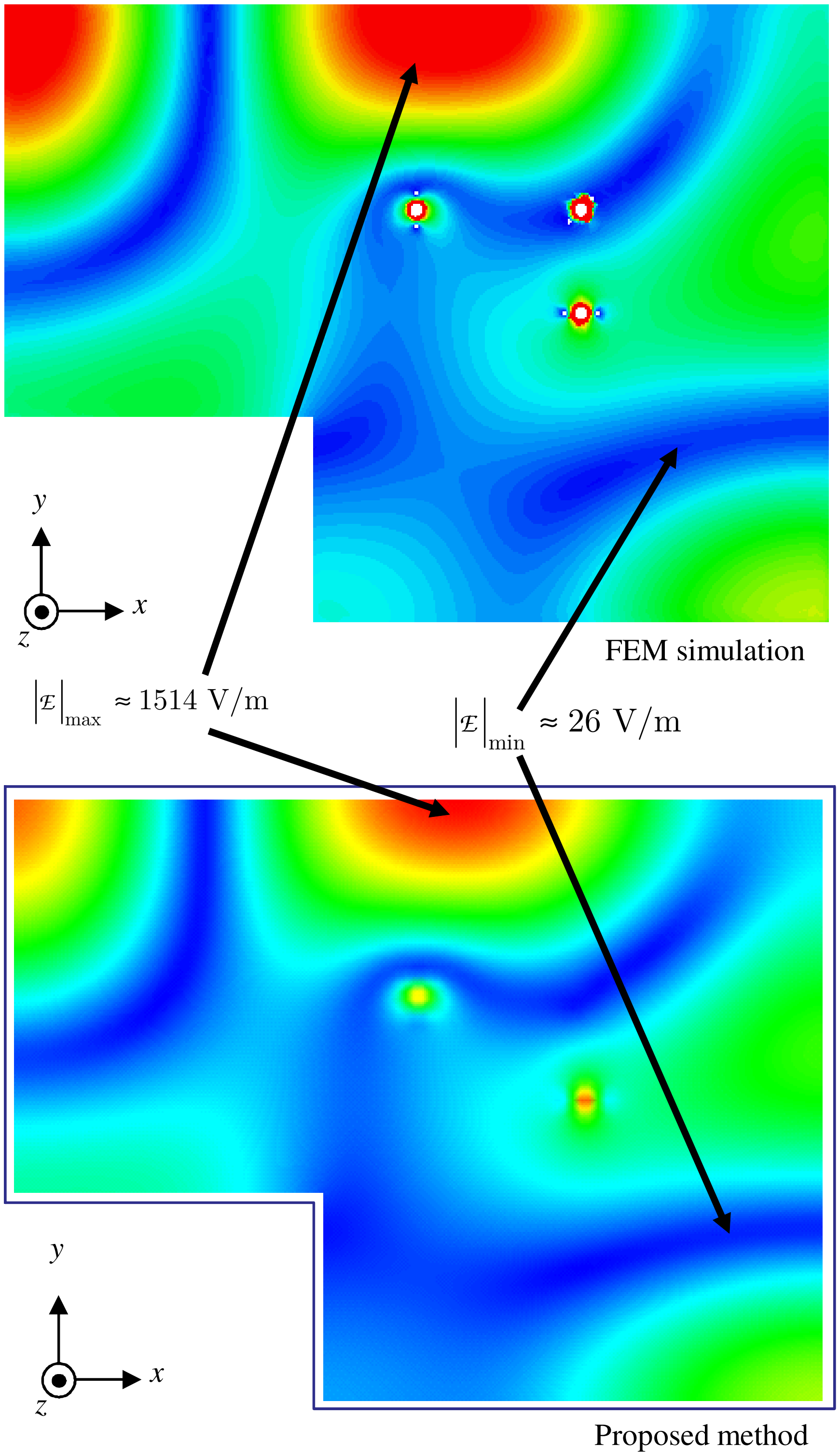

Figure 6.23 Electric field distribution (complex amplitude) in the first cavity at 4 GHz for the example in Fig. 6.21, obtained with the proposed method and a full-wave FEM simulation. Port 1 is excited with an incident power of 1 Watt and port 2 is terminated with 50 Ω.

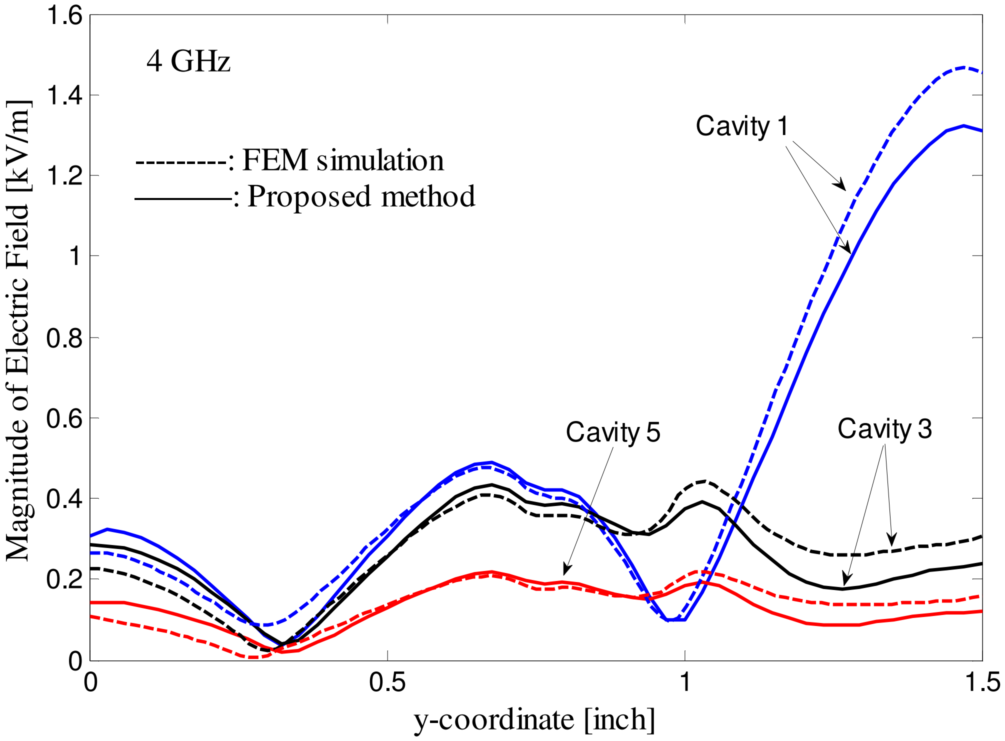

Figure 6.24 Electric field distribution (complex amplitude) along the observation path, as defined in Fig. 6.21, inside cavity 1, 3, and 5 at 4 GHz, obtained by both the proposed method and a full-wave FEM simulation.

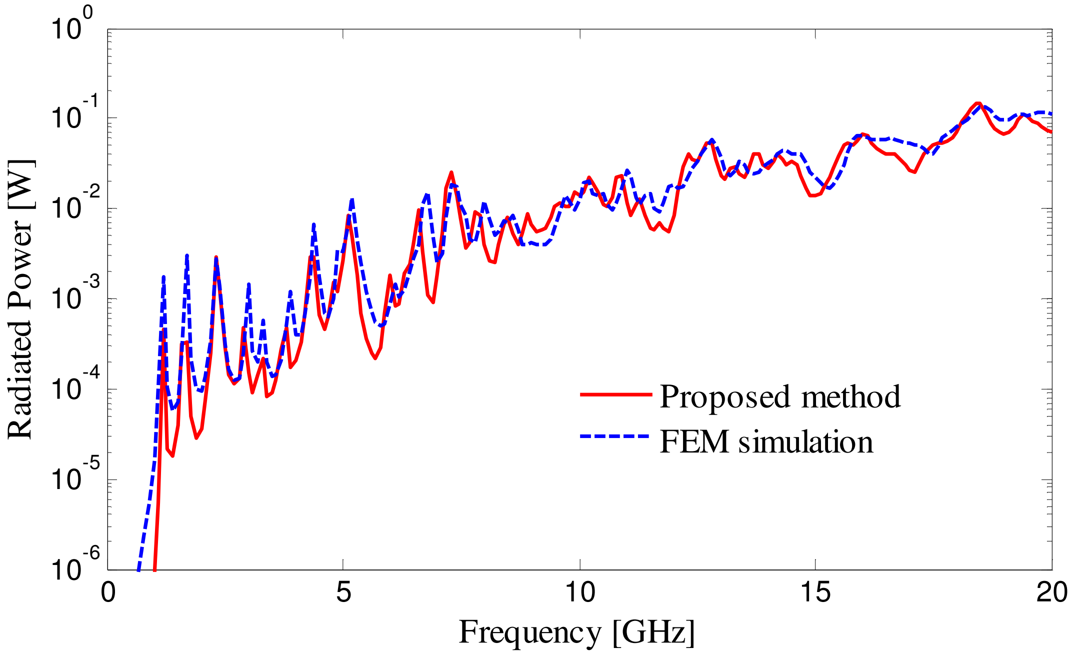

Figure 6.25 Radiated power for the multilayer example in Fig. 6.21, obtained by both the proposed method and a full-wave FEM simulation.

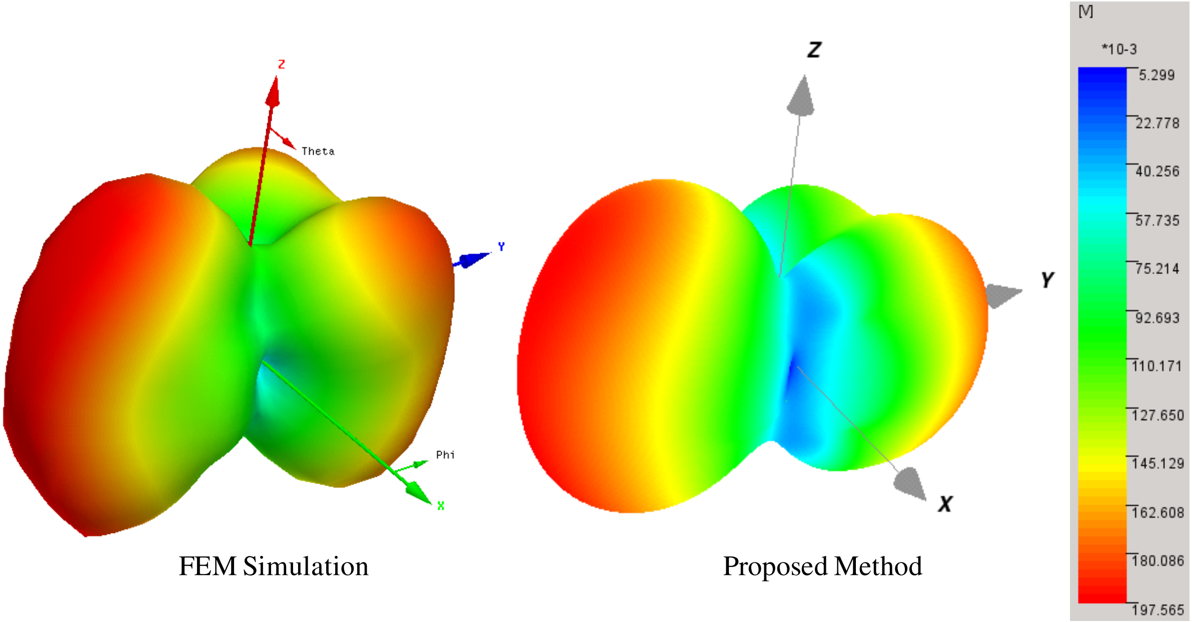

FEM Simulation

Proposed Method

Figure 6.26 Radiation diagram of the case in Fig. 6.21 at 4 GHz with port 1 excited by a 1-Watt power source and port 2 terminated with 50 Ω, using the hybrid method (right) and the full-wave FEM solver (left).

The total computation time for the full-wave solver in this case was over 20 hours for 200 frequency points on a 3.0-GHz CPU, 4-GB RAM, 32-bit PC. However, the proposed method took only 129 seconds to generate the same set of results using the same computer configuration. The high efficiency of the proposed method allows simulations of more complex structures. In general, the hybrid method is more than a hundred times faster than a full-wave solver.

6.3. Summary and Discussion

The application of the extended CIM to complex power planes has revealed an overall good accuracy and efficiency of the method. A speed-up of 10 to 1000 times against full-wave solvers can be expected, depending on configurations. The suitability of the extended CIM for dense via array analysis and a resolution of passivity violation by CIM have been discussed. A range of simulations has been demonstrated for the multilayer examples covering SI, PI, and EMI. The results correlate well with the full-wave results. For the examples in this chapter, sufficient accuracy has been achieved with the isotropic port formulation. Anisotropic modes may have an effect for even more complex applications at higher frequencies. Further extension of the method may include considerations of the radiation loss also for multilayer substrates.

7. Conclusions and Outlook

This thesis is a contribution to the modeling of planar structures in digital systems in response to the need of efficient EDA tools in the semiconductor and packaging sectors. In this work, the conventional contour integral method (CIM) has been extended to realize a fast and accurate analysis of power planes with many cylindrical vias. It has been connected to other efficient methods for a feasible system-level analysis of relatively complex structures including effects of decoupling capacitors, multilayer PCBs, and dense via arrays. Useful parameters for the full spectrum of the electrical design including SI, PI, and EMI can be produced covering a frequency range up to at least 20 GHz. In principle, the method is applicable to planar structures for higher frequencies as long as the planar circuit assumption is still valid. Various application examples and benchmarks have been presented to prove the validity of the extensions and to clarify its advantages and limitations.

In summary, novel scientific contributions can be summarized as follows:

- Analytical expressions for circular ports have been derived based on cylindrical wave expansions in order to improve the efficiency and accuracy of the method by preventing discretization of the circular ports (Chapter 4). The efficiency improvement ranges from 10 to 1000 times depending on the number of circular ports when comparing to the conventional CIM.
- The circular port definition has been generalized to account for anisotropic modes that are important for modeling of vias in close proximity (Section 4.4). The effect of anisotropic modes on the parallel-plate impedance and cavity field pattern with regard to port configurations has been shown (Section 4.5).
- The combination of CIM with equivalent circuits and the physics-based via model has been proposed (Section 5.1, 5.3), which has enabled simulations of more complex structures for various design objectives (Chapter 6).
- The importance of radiation losses has been shown for power planes with low losses and thick cavities, whose effect has been included by hybridization of CIM with the MoM (Section 5.2).

- The capability of the combined method for a concurrent co-analysis of SI, PI, and EMI for multilayer structures has been demonstrated (Section 6.2).
- It has been shown that the extended CIM is effective and efficient in simulations of dense via arrays. Potential passivity problems can be prevented by using the extended CIM for its correct interpretation of the scattering physics that is otherwise omitted by analytical methods.

In the framework of electrical analysis of digital systems, possible further extensions of the method have also been explored based on the foundation laid out in this work. Prospective developments can include the following:

- The application of the method has been limited to single-board scenarios so far. Digital systems often consist of multiple boards joint together by connectors. An attempt to investigate radiated emissions of such a system has been made by the author in [163], in which a high-speed differential signal crossing a motherboard daughter-card configuration was analyzed using a full-wave MoM solver [43]. The structure in [163] was relatively simple and the boards were approximated by metal planes, since the costly numerical computation limits the model complexity. A more realistic analysis requires the consideration of multilayer boards and multiple vias. To achieve that, an extension of CIM may employ the domain decomposition (Section 5.2.1) together with the hybridization with physics-based via models (Section 5.3).
- The DC IR drop of power planes can have significant impact on high-performance systems [164]. Swiss-cheese effects, neck-downs, and cut-outs on power planes increase the DC resistance and reduce the voltage margin. Thus, it is desired to extend CIM for the DC resistance calculation of planar metal planes. Furthermore, the transition from DC to the 2D wave frequency range requires further studies, since the skin depth may not be smaller than the metal plane thickness any more.
- The through-silicon-via (TSV) technology is one of the key technologies to enable vertical connections for 3D ICs and packaging [165],[166]. In contrast to dielectric materials surrounding vias in PCBs or conventional packages, TSVs are embedded in silicon. CIM may be extended to model quasi-TEM modes of TSVs.
- CIM may be further accelerated by exploiting fast solvers such as the FMM [120]. In particular, modeling of the plane boundary remains to be a major handicap of the efficiency. Moreover, due to the periodicity of via array arrangements, fast Toeplitz matrix inversion algorithms [167] may be utilized to improve the computation speed.

Appendix A: Mathematical Appendix

A.1. Bessel and Hankel Functions

Bessel functions are canonical solutions $r\left(x\right)$ of the Bessel's differential equation [38],

$$x\frac{dr}{dx}\left(x\frac{dr}{dx}\right)+\left(x^2-v^2\right)r=0, \tag{A.1.1}$$

where v, a real or complex number, is the order of Bessel functions. The Bessel's equation arises when finding separable solutions of the Helmholz equation in the cylindrical coordinate, for which one obtains Bessel functions of integer order (v=n). The integer orders represent cylindrical harmonics and are of particular interest for this work. Therefore, the following discussion focuses on integer orders. The Bessel function of the first kind $J_n\left(x\right)$ and of the second kind $Y_n\left(x\right)$ constitute two linearly independent solutions of (A.1.1), where

$$Y_n\left(x\right)=\lim_{v\to n}\frac{J_v\left(x\right)\cos v\pi-J_{-v}\left(x\right)}{\sin v\pi}. \tag{A.1.2}$$

$Y_v\left(x\right)$ is sometimes called Neumann function denoted by $N_v\left(x\right)$. Fig. A.1 shows curves for the lowest orders of the two kinds of Bessel functions. For negative orders, the following relations are valid,

$$J_{-n}\left(x\right)=\left(-1\right)^n J_n\left(x\right), \tag{A.1.3}$$

$$Y_{-n}\left(x\right)=\left(-1\right)^n Y_n\left(x\right), \tag{A.1.4}$$

The Bessel functions have the following asymptotic forms for non-negative n. For small arguments $0<x\ll\sqrt{n+1}$, one obtains

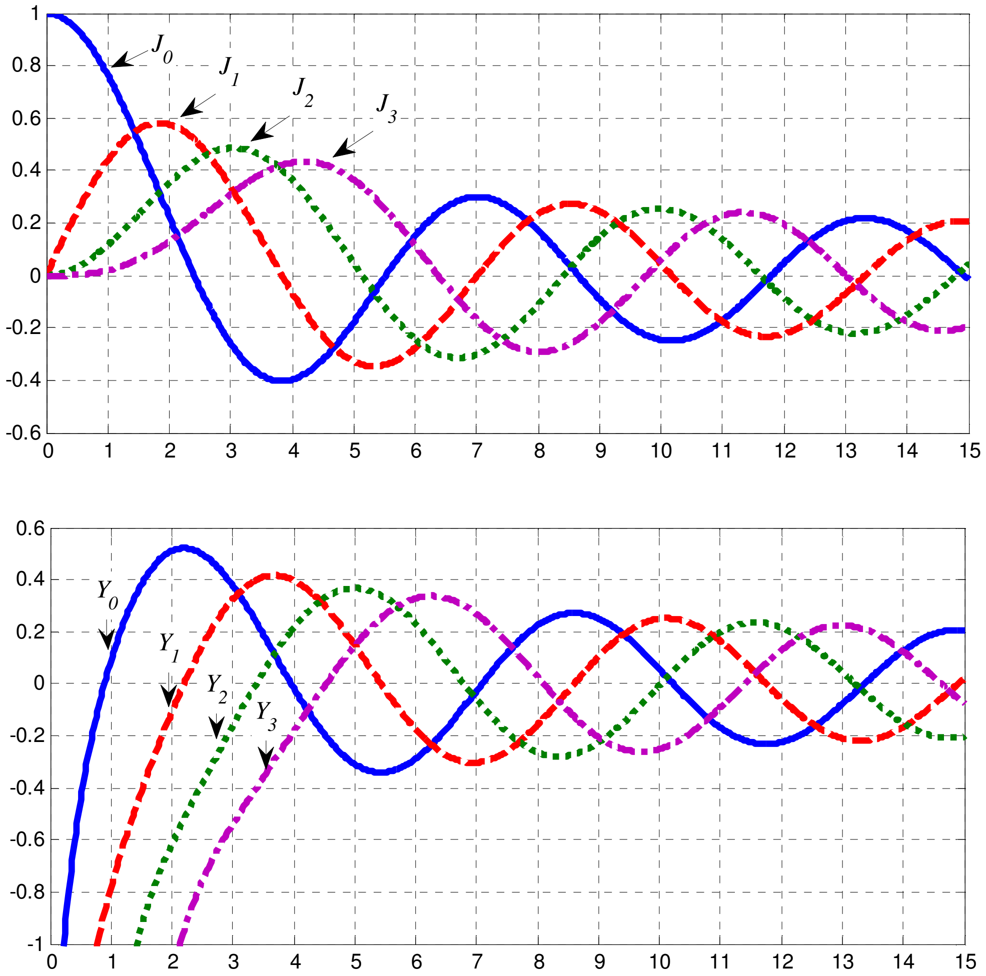

Figure A.1 Bessel functions of the first kind (upper) and of the second kind (lower).

$$J_n(x) \approx \frac{1}{n!}\left(\frac{x}{2}\right)^n, \tag{A.1.5}$$

$$Y_n(x) \approx \begin{cases} \dfrac{2}{\pi}\left[\ln(x/2)+\gamma\right] & \text{if } n = 0 \\ -\dfrac{(n-1)!}{\pi}\left(\dfrac{2}{x}\right)^n & \text{if } n > 0, \end{cases} \tag{A.1.6}$$

where $\gamma \approx 0.5772$ is the Euler constant. For large arguments $x \gg \left|n^2 - 1/4\right|$,

$$J_n(x) \approx \sqrt{\frac{2}{\pi x}}\cos\left(x - \frac{\pi}{4} - \frac{n\pi}{2}\right), \tag{A.1.7}$$

$$Y_n(x) \approx \sqrt{\frac{2}{\pi x}} \sin\left(x - \frac{\pi}{4} - \frac{n\pi}{2}\right). \tag{A.1.8}$$

For the convenience of expressing harmonic wave phenomena, Hankel functions are defined as linear combinations of the Bessel functions,

$$H_n^{(1)}(x) = J_n(x) + jY_n(x), \tag{A.1.9}$$

$$H_n^{(2)}(x) = J_n(x) - jY_n(x), \tag{A.1.10}$$

where $H_n^{(1)}$ and $H_n^{(2)}$ are Hankel functions of the first and second kind, respectively, which represent inward- and outward-propagating cylindrical wave solutions, respectively. The asymptotic forms of Hankel functions can be obtained from those for J_n and Y_n. In particular, the large-argument formulas are expressed as

$$H_n^{(1)}(x) \approx \sqrt{\frac{2}{j\pi x}} j^{-n} e^{jx}, \tag{A.1.11}$$

$$H_n^{(2)}(x) \approx \sqrt{\frac{2j}{\pi x}} j^{n} e^{-jx}, \tag{A.1.12}$$

showing the wave character of Hankel functions.

The above Bessel functions all satisfy the recurrence relation [119],

$$Z_n(x) = \frac{x}{2n}\left[Z_{n-1}(x) + Z_{n+1}(x)\right], \tag{A.1.13}$$

$$Z_n'(x) = \frac{1}{2}\left[Z_{n-1}(x) - Z_{n+1}(x)\right], \tag{A.1.14}$$

where the prime denotes a differentiation with respect to the argument. Z_n represents either one of J_n, Y_n, $H_n^{(1)}$, or $H_n^{(2)}$.

Another useful relation that is often encountered in problem solving is the Wronskian of Bessel's equation [36],

$$H_n^{(2)}(x) J_n'(x) = \frac{2j}{\pi x} + H_n'^{(2)}(x) J_n(x). \tag{A.1.15}$$

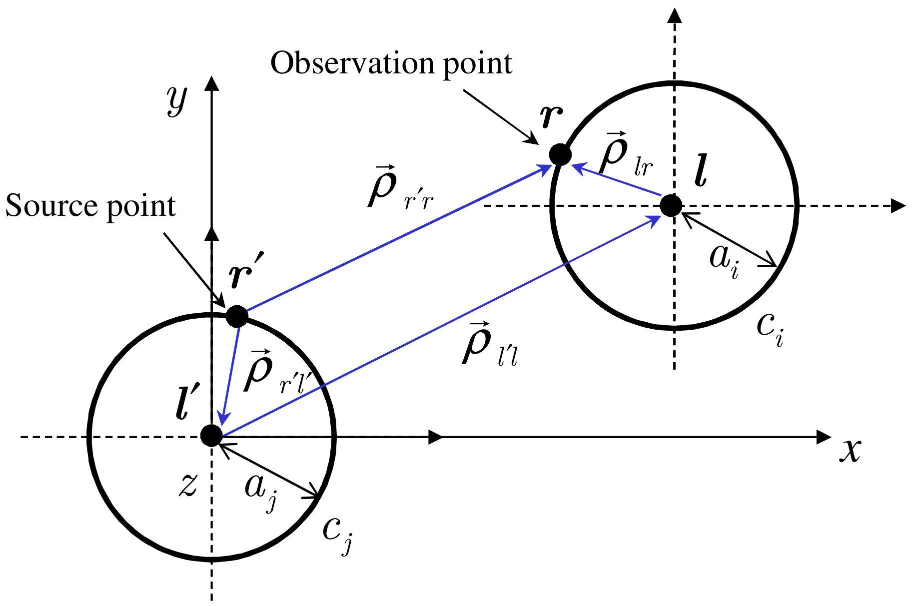

Figure A.2 Vector notations for addition theorems and derivation of circular port expressions. The vector from observation point to source point is decomposed into the sum of 3 vectors passing through the port centers.

A.2. Addition Theorems for Hankel Functions

The addition theorem is often applied to solve cylindrical scattering problems [36]. Take Hankel function of the second kind as an example,

$$H_0^{(2)}\left(k\left|\boldsymbol{r}-\boldsymbol{r}'\right|\right)=\begin{cases}\sum\limits_{n=-\infty}^{\infty} J_n\left(k\rho_{l'r}\right)H_n^{(2)}\left(k\rho_{l'r'}\right)e^{jn\left(\phi_{l'r}-\phi_{l'r'}\right)} & \left(\rho_{l'r}\le\rho_{l'r'}\right)\\ \sum\limits_{n=-\infty}^{\infty} J_n\left(k\rho_{l'r'}\right)H_n^{(2)}\left(k\rho_{l'r}\right)e^{jn\left(\phi_{l'r}-\phi_{l'r'}\right)} & \left(\rho_{l'r}\ge\rho_{l'r'}\right)\end{cases} \tag{A.2.1}$$

where ϕ_{ab} is the angle that the corresponding vector $\vec{\rho}_{ab}=\boldsymbol{b}-\boldsymbol{a}$ forms with the x-axis and $\rho_{ab}=\left|\vec{\rho}_{ab}\right|$. The vector notations are shown in Fig. A.2. Basically, it expresses the fields from a source located at $\boldsymbol{r}'$ by cylindrical wave functions originating from the coordinate origin $\boldsymbol{l}'$. Here the case of $\rho_{l'r}\ge\rho_{l'r'}$ is of particular interest. Use the Graf's formula [119],

$$H_n^{(2)}\left(k\rho_{l'r}\right)e^{jn\left(\phi_{l'r}-\phi_{l'l}\right)}=\sum_{m=-\infty}^{\infty} J_m\left(k\rho_{lr}\right)H_{m+n}^{(2)}\left(k\rho_{l'l}\right)e^{j(m+n)\left(\phi_{ll'}-\phi_{lr}\right)}, \tag{A.2.2}$$

that can be further written as,

$$H_n^{(2)}\left(k\rho_{l'r}\right)e^{jn\phi_{l'r}} = \sum_{m=-\infty}^{\infty} J_m\left(k\rho_{lr}\right)e^{jm\phi_{lr}}H_{m-n}^{(2)}\left(k\rho_{l'l}\right)e^{-j(m-n)\phi_{ll'}}, \tag{A.2.3}$$

Substituting (A.2.3) into (A.2.1) leads to the following double sum formula,

$$H_0^{(2)}\left(k\left|\boldsymbol{r}-\boldsymbol{r}'\right|\right) = \sum_{m=-\infty}^{\infty}\sum_{n=-\infty}^{\infty} J_n\left(k\rho_{l'r'}\right)e^{-jn\phi_{l'r'}}J_m\left(k\rho_{lr}\right)e^{jm\phi_{lr}}H_{m-n}^{(2)}\left(k\rho_{ll'}\right)e^{-j(m-n)\phi_{ll'}}, \tag{A.2.4}$$

which is useful to solving scattering problems of two groups.

A.3. Gaussian Quadrature

An *n*-point Gaussian quadrature rule is stated as [104]

$$\int_{-1}^{1} f\left(x\right)dx \approx \sum_{i=1}^{n} w_i f\left(x_i\right). \tag{A.3.1}$$

The quadrature rule can produce accurate results if the function $f\left(x\right)$ is well approximated by a polynomial of degree 2*n*-1 within the range [-1, 1]. For basic non-singular integrations, Legendre polynomials $P_n\left(x\right)$ are commonly used. The *i*th Gauss node x_i is the *i*th root of $P_n\left(x\right)$ and its associated weight w_i is given by [119]

$$w_i = \frac{2}{\left(1-x_i^2\right)P_n'^2\left(x_i\right)}. \tag{A.3.2}$$

For integration intervals other than [-1, 1], the interval must be changed and the quadrature rule becomes

$$\int_a^b f\left(x\right)dx \approx \frac{b-a}{2}\sum_{i=1}^{n} w_i f\left(\frac{b-a}{2}x_i + \frac{b+a}{2}\right). \tag{A.3.3}$$

A.4 Derivation of Equation (4.11)

Refer to vector notations in Fig. A.2 and using the addition theorem for Hankel functions (A.2.1) in the local cylindrical coordinate of the source port. The integral β_{ij} becomes

$$\beta_{ij} = a_i a_j \int_0^{2\pi} \underbrace{\int_0^{2\pi} H_0^{(2)}\left(k\left|\vec{\rho}_{l'r} - \vec{\rho}_{l'r'}\right|\right) d\phi_{l'r'}}_{\beta_j} d\phi_{lr}, \tag{A.4.1}$$

where

$$\beta_j = \sum_{n=-\infty}^{\infty}\left[J_n\left(ka_j\right)e^{jn\phi_{l'r}} H_n^{(2)}\left(k\left|\vec{\rho}_{l'r}\right|\right)\right]\int_0^{2\pi} e^{jn\phi_{l'r'}} d\phi_{l'r'}, \tag{A.4.2}$$

J_n and $H_n^{(2)}$ are the n-th order Bessel functions and Hankel functions of the second kind, respectively. Due to the orthogonality of exponential harmonics, the summation in (A.4.2) collapses to the term of $n = 0$. Thus, $\beta_j = 2\pi J_0\left(ka_j\right)H_0^{(2)}\left(k\left|\vec{\rho}_{l'r}\right|\right)$ and

$$\beta_{ij} = 2\pi a_i a_j J_0\left(ka_j\right)\int_0^{2\pi} H_0^{(2)}\left(k\left|\vec{\rho}_{l'r}\right|\right) d\phi_{lr}, \tag{A.4.3}$$

for $i = j$, $\left|\vec{\rho}_{l'r}\right| = a_j$ and

$$\beta_{ij} = \left(2\pi a_j\right)^2 J_0\left(ka_j\right)H_0^{(2)}\left(ka_j\right) \qquad \left(i = j\right). \tag{A.4.4}$$

For $i \neq j$, the vector $\vec{\rho}_{l'r}$ can be expressed as $\vec{\rho}_{l'r} = \vec{\rho}_{lr} - \vec{\rho}_{ll'}$, as shown in Fig. 4.2. Using again the addition theorem (A.2.1), we obtain

$$\begin{aligned}\beta_{ij} &= 2\pi a_i a_j J_0\left(ka_j\right)\sum_{n=-\infty}^{\infty}\left[J_n\left(ka_i\right)H_n^{(2)}\left(k\left|\vec{\rho}_{ll'}\right|\right)\int_0^{2\pi} e^{-jn\phi_{lr}} d\phi_{lr}\right] \\ &= \left(2\pi\right)^2 a_i a_j J_0\left(ka_i\right)J_0\left(ka_j\right)H_0^{(2)}\left(k\left|\rho_{ij}\right|\right) \qquad \left(i \neq j\right),\end{aligned} \tag{A.4.5}$$

where $\rho_{ij} = \left|\vec{\rho}_{ll'}\right|$, is the distance between centers of source and observation ports. Combing (A.4.4) and (A.4.5) under the consideration of (4.6), one can find the elements of matrix $\overline{\overline{H}}^{pp}$ in (4.10).

A.5. Derivation of Equation (4.12)

For solving the matrix $\overline{\overline{U}}^{pp}$, since it is always valid for a circular port that the normal direction $\hat{n}' = -\vec{\rho}_{l'r'}$, the integral α_{ij} can be expressed as

$$\alpha_{ij} = a_i \int_0^{2\pi} \left(-a_j\right) \underbrace{\int_0^{2\pi} \frac{\partial H_0^{(2)}\left(k\left|\vec{\rho}_{l'r} - \vec{\rho}_{l'r'}\right|\right)}{\partial \rho_{l'r'}} d\phi_{l'r'}}_{\alpha_j} d\phi_{lr}. \tag{A.5.1}$$

The integrand in (A.5.1) contains a first-order singularity for diagonal terms of $\overline{\overline{U}}^{pp}$, for which $\vec{\rho}_{l'r} = \vec{\rho}_{l'r'}$ is possible. The off-diagonal terms are solved first and the singularity for the diagonal terms will be evaluated later. Taking again the addition theorem for Hankel functions (A.2.1), the integral α_j in (A.5.1) is transformed to

$$\alpha_j = \sum_{n=-\infty}^{n=\infty} \left[\frac{\partial J_n\left(k\rho_{l'r'}\right)}{\partial \rho_{l'r'}} H_n^{(2)}\left(k\left|\vec{\rho}_{l'r}\right|\right) e^{jn\phi_{l'r}} \int_0^{2\pi} e^{jn\phi_{l'r'}} d\phi_{l'r'} \right]. \tag{A.5.2}$$

The summation is again only finite when n=0,

$$\alpha_j = 2\pi \frac{\partial J_0\left(k\rho_{l'r'}\right)}{\partial \rho_{l'r'}} H_0^{(2)}\left(k\left|\vec{\rho}_{l'r}\right|\right). \tag{A.5.3}$$

Referring to the recurrence relation for derivatives of Bessel functions (A.1.14), the following expression is found,

$$\alpha_j = -2\pi k J_1\left(ka_j\right) H_0^{(2)}\left(k\left|\vec{\rho}_{l'r}\right|\right). \tag{A.5.4}$$

The integral α_{ij} becomes

$$\alpha_{ij} = 2\pi k a_i a_j J_1\left(ka_j\right) \int_0^{2\pi} H_0^{(2)}\left(k\left|\vec{\rho}_{l'r}\right|\right) d\phi_{lr} \qquad (i \neq j). \tag{A.5.5}$$

Expression (A.5.5) can be solved in a similar way as for (A.4.3),

$$\alpha_{ij} = (2\pi)^2 k a_i a_j J_0\left(ka_i\right) J_1\left(ka_j\right) H_0^{(2)}\left(k\rho_{ij}\right) \quad (i \neq j). \tag{A.5.6}$$

For evaluation of the singularity for the diagonal terms, we rewrite α_j as

$$\begin{aligned} \alpha_j &= \lim_{\varepsilon \to 0} \left[\int_{\varepsilon}^{2\pi-\varepsilon} H_0^{(2)}\left(k\left|\vec{\rho}_{l'r} - \vec{\rho}_{l'r'}\right|\right) d\phi_{l'r'} + \int_{-\varepsilon}^{\varepsilon} H_0^{(2)}\left(k\left|\vec{\rho}_{l'r} - \vec{\rho}_{l'r'}\right|\right) d\phi_{l'r'} \right] \\ &= -2\pi k J_1\left(ka_j\right) H_0^{(2)}\left(ka_j\right) + \underbrace{\lim_{\varepsilon \to 0} \int_{-\varepsilon}^{\varepsilon} k \cdot H_1^{(2)}\left(k\rho_{rr'}\right) \frac{\rho_{l'r} \cos\phi_{l'r'} - \rho_{l'r'}}{\rho_{rr'}} d\phi_{l'r'}}_{\chi}. \end{aligned} \tag{A.5.7}$$

To find χ, let's select an observation point just outside the source port, so that the small argument approximation for Hankel function, $H_1^{(2)}(z) = -2j/\pi z$, can be used. This leads to a simplification of χ as follows

$$\chi = -\frac{2j}{\pi} \int_{-\varepsilon}^{\varepsilon} \frac{\rho_{l'r} \cos \phi_{l'r'} - \rho_{l'r'}}{\rho_{rr'}{}^2} d\phi_{l'r'} = -\frac{4j}{\pi} \int_{0}^{\varepsilon} \frac{\rho_{l'r} \cos \phi_{l'r'} - \rho_{l'r'}}{\rho_{l'r}{}^2 + \rho_{l'r'}{}^2 - 2\rho_{l'r}\rho_{l'r'} \cos \phi_{l'r'}} \cos \phi_{l'r'}. \tag{A.5.8}$$

With the help of an integral table [112],

$$\chi = -\frac{4j}{\pi} \left[-\frac{1}{2\rho_{l'r'}} \varepsilon + \frac{1}{\rho_{l'r'}} \arctan\left(\frac{\rho_{l'r} + \rho_{l'r'}}{\rho_{l'r} - \rho_{l'r'}} \tan \frac{\varepsilon}{2} \right) \right]. \tag{A.5.9}$$

Next, let the observation point approach the source port,

$$\lim_{\rho_{l'r} \to \rho_{l'r'}{}^+} \chi = \frac{2j}{\pi \rho_{l'r'}} [\varepsilon - \pi]. \tag{A.5.10}$$

Substituting (A.5.10) into (A.5.7) leads to

$$\alpha_j = -2\pi k J_1(ka_j) H_0^{(2)}(ka_j) - \frac{2j}{a_j}. \tag{A.5.11}$$

Inserting (A.5.11) into (A.5.7), we obtain

$$\alpha_{ij} = (2\pi a_j)^2 k \left[J_1(ka_j) H_0^{(2)}(ka_j) + \frac{j}{\pi k a_j} \right] \qquad (i = j). \tag{A.5.12}$$

With the Wronskian of Bessel functions (A.1.15), one may write (A.5.12) as

$$\alpha_{ij} = (2\pi a_j)^2 k \left[J_0(ka_j) H_1^{(2)}(ka_j) - \frac{j}{\pi k a_j} \right] \qquad (i = j). \tag{A.5.13}$$

Based on the solutions of the integral α_{ij} in (A.5.6) and (A.5.13), the elements of matrix $\overline{\overline{U}}^{pp}$ in (4.10) can be found.

A.6. Derivation of Equations (4.19)-(4.22)

The simplification from (4.15)-(4.16) to (4.19)-(4.20) relies on solving the following two integrals,

$$\oint_{c_j} \frac{\partial H_0^{(2)}\left(k\left|\boldsymbol{r}-\boldsymbol{r}'\right|\right)}{\partial n} ds', \tag{A.6.1}$$

$$\oint_{c_j} H_0^{(2)}\left(k\left|\boldsymbol{r}-\boldsymbol{r}'\right|\right) ds'. \tag{A.6.2}$$

The two integrals are mathematically identical to the integral α_j in (A.5.1) and β_j in (A.5.1), respectively. The solutions of them are written as, respectively,

$$2\pi J_0\left(ka_j\right) H_0^{(2)}\left(k\rho_{ij}\right), \tag{A.6.3}$$

$$2\pi k a_j J_1\left(ka_j\right) H_0^{(2)}\left(k\rho_{ij}\right), \tag{A.6.4}$$

where ρ_{ij} corresponds to the distance between the center of circular source point and a point on the observation boundary line port. Substituting (A.6.3) and (A.6.4) into (4.15) and (4.16), respectively, leads to the expressions (4.19) and (4.20). With the same procedures, equations (4.21) and (4.22) can also be derived.

A.7. Derivation of Equations (4.44)-(4.45)

To relate to cylindrical wave modes, one may resort to the Graf's addition formulas (A.2.4) to decompose the Hankel function and its normal derivative with respect to the port centers $\boldsymbol{l}$ and $\boldsymbol{l}'$, as shown in Fig. A.2,

$$H_0^{(2)}\left(k\left|\boldsymbol{r}-\boldsymbol{r}'\right|\right) = \begin{cases} \sum\limits_{m=-\infty}^{\infty} J_m\left(k\rho_{lr}\right) e^{jm\phi_{lr}} \sum\limits_{n=-\infty}^{\infty} T_{mn} J_n\left(k\rho_{l'r'}\right) e^{-jn\phi_{l'r'}} & \boldsymbol{l} \neq \boldsymbol{l}' \\ \sum\limits_{m=-\infty}^{\infty} H_m^{(2)}\left(k\rho_{l'r}\right) e^{jm\phi_{l'r}} J_m\left(k\rho_{l'r'}\right) e^{-jm\phi_{l'r'}} & \boldsymbol{l} = \boldsymbol{l}', \quad \boldsymbol{r} \neq \boldsymbol{r}', \end{cases} \tag{A.7.1}$$

and

$$\frac{\partial H_0^{(2)}\left(k\left|\boldsymbol{r}-\boldsymbol{r}'\right|\right)}{\partial n}=\begin{cases}-\sum\limits_{m=-\infty}^{\infty} J_m\left(k\rho_{lr}\right)e^{jm\phi_{lr}}\sum\limits_{n=-\infty}^{\infty} T_{mn}J_n'\left(k\rho_{l'r'}\right)e^{-jn\phi_{l'r'}} & \boldsymbol{l}\neq\boldsymbol{l}' \\ -\sum\limits_{m=-\infty}^{\infty} H_m^{(2)}\left(k\rho_{l'r}\right)e^{jm\phi_{l'r}}J_m'\left(k\rho_{l'r'}\right)e^{-jm\phi_{l'r'}} & \boldsymbol{l}=\boldsymbol{l}',\quad \boldsymbol{r}\neq\boldsymbol{r}',\end{cases} \tag{A.7.2}$$

respectively, where

$$T_{mn}=H_{m-n}^{(2)}\left(k\rho_{ll'}\right)e^{-j(m-n)\phi_{ll'}}. \tag{A.7.3}$$

The prime denotes differentiation of the Bessel function with respect to its argument. The purpose of the decomposition is to decouple the source and observation coordinates in order to perform integrals over each port circumference independently. Substituting (A.7.1) and (A.7.2) into the integrals in (4.37) leads to

$$\beta_j=\begin{cases}\sum\limits_{m=-\infty}^{\infty} J_m\left(k\rho_{lr}\right)e^{jm\phi_{lr}}\sum\limits_{n=-\infty}^{\infty} T_{mn}J_n\left(k\rho_{l'r'}\right)\oint_{c_j}\mathcal{H}_{\phi}\left(\boldsymbol{r}'\right)e^{-jn\phi_{l'r'}}ds' & \boldsymbol{l}\neq\boldsymbol{l}' \\ \sum\limits_{m=-\infty}^{\infty} H_m^{(2)}\left(k\rho_{l'r}\right)e^{jm\phi_{l'r}}J_m\left(k\rho_{l'r'}\right)\oint_{c_j}\mathcal{H}_{\phi}\left(\boldsymbol{r}'\right)e^{-jm\phi_{l'r'}}ds' & \boldsymbol{l}=\boldsymbol{l}',\quad \boldsymbol{r}\neq\boldsymbol{r}',\end{cases} \tag{A.7.4}$$

$$\alpha_j=\begin{cases}-\sum\limits_{m=-\infty}^{\infty} J_m\left(k\rho_{lr}\right)e^{jm\phi_{lr}}\sum\limits_{n=-\infty}^{\infty} T_{mn}J_n'\left(k\rho_{l'r'}\right)\oint_{c_j}E_z\left(\boldsymbol{r}'\right)e^{-jn\phi_{l'r'}}ds' & \boldsymbol{l}\neq\boldsymbol{l}' \\ -\sum\limits_{m=-\infty}^{\infty} H_m^{(2)}\left(k\rho_{l'r}\right)e^{jm\phi_{l'r}}J_m'\left(k\rho_{l'r'}\right)\oint_{c_j}E_z\left(\boldsymbol{r}'\right)e^{-jm\phi_{l'r'}}ds' & \boldsymbol{l}=\boldsymbol{l}',\quad \boldsymbol{r}\neq\boldsymbol{r}'.\end{cases} \tag{A.7.5}$$

The integrals in (A.7.4) and (A.7.5) can be evaluated with the help of the modal voltage and current definition in (4.26),

$$\oint_{c_j}\mathcal{H}_{\phi}\left(\boldsymbol{r}'\right)e^{-jn\phi_{l'r'}}ds'=a_j\cdot\int_0^{2\pi}\mathcal{H}_{\phi}\left(\boldsymbol{r}'\right)e^{-jn\phi_{l'r'}}d\phi_{l'r'}=I_{jn}, \tag{A.7.6}$$

$$\oint_{c_j}\mathcal{E}_z\left(\boldsymbol{r}'\right)e^{-jn\phi_{l'r'}}ds'=a_j\cdot\int_0^{2\pi}\mathcal{E}_z\left(\boldsymbol{r}'\right)e^{-jn\phi_{l'r'}}d\phi_{l'r'}=\frac{2\pi a_j}{d}V_{jn}. \tag{A.7.7}$$

By substituting (A.7.4) and (A.7.5) into (4.37) with the consideration of (A.7.6) and(A.7.7), one can rewrite (4.6) as

$$
\begin{aligned}
2E_z(\boldsymbol{r}_i) = {} & \frac{k\pi a_j}{jd}\cdot \sum_{j=1;j\neq i}^{N} \sum_{m=-\infty}^{\infty} J_m(ka_i) e^{jm\phi_{lr}} \sum_{n=-\infty}^{\infty} T_{mn} J_n(ka_j) V_{jn} \\
& + \frac{k\eta}{2}\cdot \sum_{j=1;j\neq i}^{N} \sum_{m=-\infty}^{\infty} J_m(ka_i) e^{jm\phi_{lr}} \sum_{n=-\infty}^{\infty} T_{mn} J_n(ka_j) I_{jn} \\
& + \frac{k\pi a_i}{jd}\cdot \sum_{j=i;m=-\infty}^{\infty} H_m^{(2)}(ka_i) e^{jm\phi_{l'r}} J'_m(ka_i) V_{im} \\
& + \frac{k\eta}{2}\cdot \sum_{j=i;m=-\infty}^{\infty} H_m^{(2)}(ka_i) e^{jm\phi_{l'r}} J_m(ka_i) I_{im},
\end{aligned}
\tag{A.7.8}
$$

where $a_i = \rho_{lr}$ and $a_j = \rho_{l'r'}$ are the radii of the observation and source ports, respectively. The factor 2 in the left side of (A.7.8) emerges due to a singularity in the integral when $\boldsymbol{r} = \boldsymbol{r}'$, whose extraction has been discussed in the previous section. The electric field on the observation port is next projected into azimuthal modes, as defined in (4.23) and expressed in the form of modal voltages (4.24) as

$$
V_{im} = \tilde{E}_m d = \frac{d}{2\pi} \int_0^{2\pi} E_z(\boldsymbol{r}_i) e^{-jm\phi_{lr}} d\phi_{lr}. \tag{A.7.9}
$$

Substituting (A.7.8) into (A.7.9) and evaluating the integral lead to the following system of equations,

$$
\begin{aligned}
& V_{im} - \frac{k\pi a_i}{2j}\left[H_m^{(2)}(ka_i) J'_m(ka_i) V_{im} + \sum_{j=1;j\neq i}^{N} J_m(ka_i) \sum_{n=-\infty}^{\infty} T_{mn} J_n(ka_j) V_{jn} \right] \\
& = \frac{k\eta d}{4}\left[H_m^{(2)}(ka_i) J_m(ka_i) I_{im} + \sum_{j=1;j\neq i}^{N} J_m(ka_i) \sum_{n=-\infty}^{\infty} T_{mn} J_n(ka_j) I_{jn} \right], \\
& \qquad i = 1,2,\ldots,N, \quad m = -\infty,\ldots,-1,0,1,\ldots,\infty.
\end{aligned}
\tag{A.7.10}
$$

Here, the orthogonality of exponential harmonics has been applied. By using the Wronskian of Bessel functions, (A.1.15), one can further simplify (A.7.10) to

$$
\begin{aligned}
& -\frac{k\pi a_i}{j}\left[H_m'^{(2)}(ka_i) J_m(ka_i) V_{im} + \sum_{j=1;j\neq i}^{N} J_m(ka_i) \sum_{n=-\infty}^{\infty} T_{mn} J_n(ka_j) V_{jn} \right] \\
& = \frac{k\eta d}{2}\left[H_m^{(2)}(ka_i) J_m(ka_i) I_{im} + \sum_{j=1;j\neq i}^{N} J_m(ka_i) \sum_{n=-\infty}^{\infty} T_{mn} J_n(ka_j) I_{jn} \right], \\
& \qquad i = 1,2,\ldots,N, \quad m = -\infty,\ldots,-1,0,1,\ldots,\infty,
\end{aligned}
\tag{A.7.11}
$$

which can be written in to matrix form (4.41) whose elements in (4.44) and (4.45) can be read from (A.7.11).

A.8. Derivation of Equations (4.48)-(4.51)

One may resort to the integrals in (4.37) to find interactions between the circular port and a point on the line port,

$$\beta_j = \sum_{n=-\infty}^{\infty} H_n^{(2)}\left(k\rho_{ll'}\right) e^{jn\left(\phi_{ll'}+\pi\right)} J_n\left(k\rho_{l'r'}\right) \oint_{c_j} \mathcal{H}_\phi\left(\boldsymbol{r}'\right) e^{-jn\phi_{l'r'}} ds', \tag{A.8.1}$$

$$\alpha_j = \sum_{n=-\infty}^{\infty} H_n^{(2)}\left(k\rho_{ll'}\right) e^{jn\left(\phi_{ll'}+\pi\right)} J'_n\left(k\rho_{l'r'}\right) \oint_{c_j} \mathcal{E}_z\left(\boldsymbol{r}'\right) e^{-jn\phi_{l'r'}} ds', \tag{A.8.2}$$

for the case that the source point $\boldsymbol{r}'$ lies on a circular port and

$$\beta_j = \sum_{m=-\infty}^{\infty} H_m^{(2)}\left(k\rho_{ll'}\right) e^{-jm\phi_{ll'}} J_m\left(k\rho_{lr}\right) e^{jm\phi_{lr}} \mathcal{H}_\phi\left(\boldsymbol{r}'\right), \tag{A.8.3}$$

$$\alpha_j = \sum_{m=-\infty}^{\infty} H_m^{(2)}\left(k\rho_{ll'}\right) e^{-jm\phi_{ll'}} J_m\left(k\rho_{lr}\right) e^{jm\phi_{lr}} \mathcal{E}_z\left(\boldsymbol{r}'\right), \tag{A.8.4}$$

for the case that the source point $\boldsymbol{r}'$ lies on a boundary line port. The vector notations are referred to Fig. A.2, for which the circle c_j collapses to a point if the source $\boldsymbol{r}'$ is on boundary line ports, whereas c_i collapses to a point if the observation $\boldsymbol{r}$ is lies on a line port. Substituting (A.8.1)-(A.8.4) into (4.37) and following the same procedure as (A.7.8)-(A.7.11), the off-diagonal matrices in (4.48)-(4.51) can be obtained.

Appendix B: Extension of Cavity Resonator Model for Circular Ports

---

In the cavity resonator model (CRM), due to the specific geometry of the power plane structure, the impedance can be calculated by integrating the Green's function and taking an average over a rectangular port area, as described in [64],[65]. However, very often the physical geometry of the ports is circular, especially for applications involving vias. Under the assumption of isotropic ports, the tangential magnetic field on the area of source port j is considered constant and an equivalent sheet current in z-direction can be defined as $J_z = \mathcal{H}_\phi$. The electric field along the circumference of port i can then be described by the electric field integral equation,

$$\mathcal{E}_z\left(\boldsymbol{r}\right) = \oint_{s'} \mathcal{H}_\phi \cdot G\left(\boldsymbol{r}, \boldsymbol{r}'\right) ds', \tag{B.1}$$

where $G\left(\boldsymbol{r}, \boldsymbol{r}'\right)$ is the Green's function of the 2-D Helmholz equation [64]. For a rectangular cavity with a perfect magnetic conductor (PMC) boundary,

$$\begin{gathered} G\left(\boldsymbol{r}, \boldsymbol{r}'\right) = G\left(x, y, x', y'\right) = \\ \frac{j\mu\omega}{P_x P_y} \cdot \sum_{m=0}^{\infty} \sum_{n=0}^{\infty} \frac{C_m^2 C_n^2}{k_{xm}^2 + k_{yn}^2 - k^2} \cos\left(k_{xm} x'\right) \cos\left(k_{yn} y'\right) \cos\left(k_{xm} x\right) \cos\left(k_{yn} y\right), \end{gathered} \tag{B.2}$$

where P_x and P_y are the plane widths in the x- and y-direction, respectively, as shown in Fig. B.1. μ denotes the permeability and ω is the angular frequency. m and n represent the m-th and n-th eigenmode in the x- and y-direction respectively, whereas $C_{m,n} = 1$ if $m,n = 0$ and $C_{m,n} = 1$ if $m,n \neq 0$. $k_{xm} = m\pi/P_x$ and $k_{yn} = n\pi/P_y$. Substituting (B.2) into the isotropic parallel-plate impedance (*Zpp*) definition (4.3), *Zpp* can be expressed as

$$Z_{ij} = \frac{d}{2\pi a_i \cdot 2\pi a_j} \cdot \oint_{c_i} ds \cdot \oint_{c_j} ds' \cdot G\left(\boldsymbol{r}, \boldsymbol{r}'\right), \tag{B.3}$$

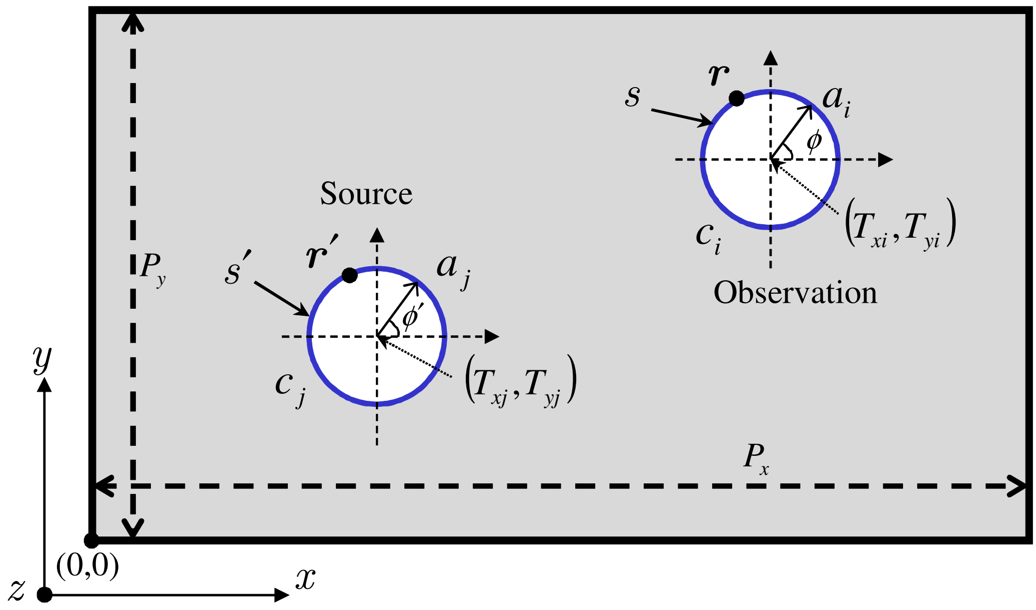

Figure B.1 Top view of a rectangular power plane structure with two ports and parameter definition for circular ports in the cavity model.

where c_j and c_i are the circumferences of the source and observation ports, respectively, as shown in Fig. B.1. Equation (B.3) can be explicitly written as

$$
\begin{aligned}
Z_{ij} = \frac{j\mu\omega d}{P_x P_y} \cdot \sum_{n=0}^{\infty} \sum_{m=0}^{\infty} \frac{C_n^2 C_m^2}{k_{xm}^2 + k_{yn}^2 - k^2} \\
\cdot \underbrace{\frac{1}{2\pi} \int_0^{2\pi} \cos\left(k_{yn} T_{yi} + a_i \cos\phi\right) \cos\left(k_{xm} T_{xi} + a_i \sin\phi\right) d\phi}_{\alpha_1} \\
\cdot \underbrace{\frac{1}{2\pi} \int_0^{2\pi} \cos\left(k_{yn} T_{yj} + a_j \cos\phi'\right) \cos\left(k_{xm} T_{xj} + a_j \cos\phi'\right) d\phi'}_{\alpha_2},
\end{aligned}
\tag{B.4}
$$

where $(T_{xj},\ T_{yj})$ and $(T_{xi},\ T_{yi})$ are the coordinates of the centers of the source and observation ports, respectively. ϕ and ϕ' are azimuthal angles in the local coordinates of observation and source circles, as shown in Fig. B.1. The two integrals in (B.4) are of the same form and can be solved similarly. Applying the addition formula for cosine functions, α_1 can be decomposed into

$$
\alpha_1 = K_1 + K_2 + K_3 + K_4, \tag{B.5}
$$

where

$$K_1 = \cos\left(k_{xm}T_{xi}\right)\cos\left(k_{yn}T_{yi}\right)\int_0^{2\pi}\cos\left(k_{xm}a_i\cos\phi\right)\cos\left(k_{yn}a_i\sin\phi\right)d\phi,$$

$$K_2 = \sin\left(k_{xm}T_{xi}\right)\sin\left(k_{yn}T_{yi}\right)\int_0^{2\pi}\sin\left(k_{xm}a_i\cos\phi\right)\sin\left(k_{yn}a_i\sin\phi\right)d\phi,$$

$$K_3 = \cos\left(k_{xm}T_{xi}\right)\sin\left(k_{yn}T_{yi}\right)\int_0^{2\pi}\cos\left(k_{xm}a_i\cos\phi\right)\sin\left(k_{yn}a_i\sin\phi\right)d\phi,$$

$$K_4 = \sin\left(k_{xm}T_{xi}\right)\cos\left(k_{yn}T_{yi}\right)\int_0^{2\pi}\sin\left(k_{xm}a_i\cos\phi\right)\cos\left(k_{yn}a_i\sin\phi\right)d\phi.$$

The above integrals in $K_1 - K_4$ can be solved with the assistance of the following generating functions [119]:

$$\cos\left(z\cdot\cos\theta\right) = \sum_{k=-\infty}^{\infty}\left(-1\right)^k J_{2k}\left(z\right)\cos\left(2k\theta\right), \tag{B.6}$$

$$\cos\left(z\cdot\sin\theta\right) = \sum_{k=-\infty}^{\infty} J_{2k}\left(z\right)\cos\left(2k\theta\right), \tag{B.7}$$

$$\sin\left(z\cdot\cos\theta\right) = 2\sum_{k=-\infty}^{\infty}\left(-1\right)^k J_{2k+1}\left(z\right)\cos\left[\left(2k+1\right)\theta\right], \tag{B.8}$$

$$\sin\left(z\cdot\sin\theta\right) = 2\sum_{k=-\infty}^{\infty} J_{2k+1}\left(z\right)\sin\left[\left(2k+1\right)\theta\right]. \tag{B.9}$$

Substituting (B.6) and (B.7) into the integral for K_1 yields

$$\begin{aligned}K_1 &= \cos\left(k_{xm}T_{xi}\right)\cos\left(k_{yn}T_{yi}\right)\cdot\\ &\sum_{p=-\infty}^{\infty}\sum_{q=-\infty}^{\infty}\left(-1\right)^p J_{2p}\left(k_{xm}a_i\right)J_{2q}\left(k_{yn}a_i\right)\int_0^{2\pi}\cos\left(2p\phi\right)\cos\left(2q\phi\right)d\phi.\end{aligned} \tag{B.10}$$

The integral in (B.10) is only non-zero when $\left|p\right| = \left|q\right|$, leading to

$$\begin{aligned}K_1 &= 2\pi\cos\left(k_{xm}T_{xi}\right)\cos\left(k_{yn}T_{yi}\right)\cdot\\ &\left[J_0\left(k_{xm}a_i\right)J_0\left(k_{yn}a_i\right) + 2\cdot\sum_{p=1}^{\infty}\left(-1\right)^p J_{2p}\left(k_{xm}a_i\right)J_{2p}\left(k_{yn}a_i\right)\right].\end{aligned} \tag{B.11}$$

Applying the addition theorem for Bessel functions [36],

$$J_0\left(\sqrt{\alpha^2+\beta^2}\right)=J_0(\alpha)\cdot J_0(\beta)+2\cdot\sum_{k=1}^{\infty}(-1)^k J_{2k}(\alpha)J_{2k}(\beta), \tag{B.12}$$

K_1 can be simplified as

$$K_1=2\pi\cdot\cos\left(k_{xm}T_{xi}\right)\cos\left(k_{yn}T_{yi}\right)\cdot J_0\left(\sqrt{k_{xm}^2+k_{yn}^2}\cdot a_i\right). \tag{B.13}$$

Similarly, using (B.6)–(B.9) to solve for K_2–K_4, we obtain

$$K_2=K_3=K_4=0, \tag{B.14}$$

since the integrands are combinations of orthogonal sinusoidal basis functions. We can solve α_2 in the same manner and by substituting the solutions of α_1 and α_2 into (B.4), the following expression is derived

$$Z_{ij}=\frac{j\mu\omega d}{P_xP_y}\cdot\sum_{m=0}^{\infty}\sum_{n=0}^{\infty}\frac{C_m^2C_n^2f_{cp}}{k_{mn}^2-k^2}\cos\left(k_{xm}T_{xi}\right)\cos\left(k_{yn}T_{yi}\right)\cos\left(k_{xm}T_{xj}\right)\cos\left(k_{yn}T_{yj}\right), \tag{B.15}$$

where

$$k_{mn}=\sqrt{k_{xm}^2+k_{yn}^2}, \qquad f_{cp}=J_0\left(k_{mn}\,a_i\right)\cdot J_0\left(k_{mn}\,a_j\right).$$

Equation (B.15) can be considered as the Green's function (B.2) modulated with the function f_{cp}, that results from the finite size of the circular port. In the formulation for square ports [65], this port modulation function is

$$f_{sp}=\sin c\left(\frac{k_{xm}W_i}{2}\right)\cdot\sin c\left(\frac{k_{yn}W_i}{2}\right)\cdot\sin c\left(\frac{k_{xm}W_j}{2}\right)\cdot\sin c\left(\frac{k_{yn}W_j}{2}\right),$$

where W_i, W_j are widths of port i and j, respectively, which usually corresponds to the equivalent circular port diameter. Instead of *sinc* functions, the circular port expression (B.15) contains Bessel functions.

To give a first impression of the difference between the two functions, we consider the input impedance of a square power plane pair with a port in the center. Suppose that

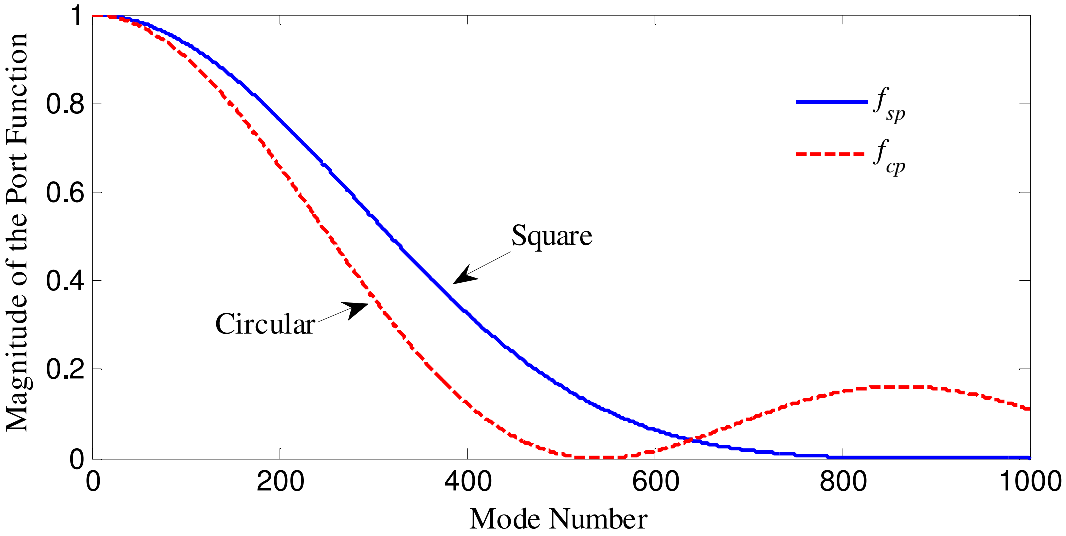

Figure B.2 Comparison of the port modulation function between circular port f_{cp} and square port fsp of a square power plane pair for mode number $m = n$. The ratio of the port radius to the plane width is 0.001.

the port radius is 1/1000 of the plane width and the square port width equals the circular port diameter ($W = 2a$). Fig. B.2 plots the two port modulation functions when $m = n$ and $k_{xm} = k_{yn}$. It can be observed that both functions converge to 1 for small arguments. However, the square port approximation overestimates the contribution of the first hundreds of modes and diminishes the higher order modes beyond that. Therefore, the square port model is only accurate in the low frequency range, where the impedance values are mainly determined by lower order modes.

It should be noted that the Green's function represents modes in a PMC bounded rectangular cavity, sandwiched by two solid planes. However, impedance is defined by assuming that a current is impressed on one port and all other ports remain open. This means that *Zpp* should be calculated in presence of open circular ports, i.e., PMC holes in the solid plane, whose Green's function is in general not known. The effect of these PMC holes should be included for an exact calculation of *Zpp*. The impedance calculated by (B.15) can be considered as *Zpp* in parallel connection to many small circular plane pairs, whose impedances Z^h can be found in e.g. [64] as

$$Z_{ii}^h = \frac{\omega\mu d}{2\pi k a_i} \frac{J_0\left(k a_i\right)}{J_1\left(k a_i\right)}. \tag{B.16}$$

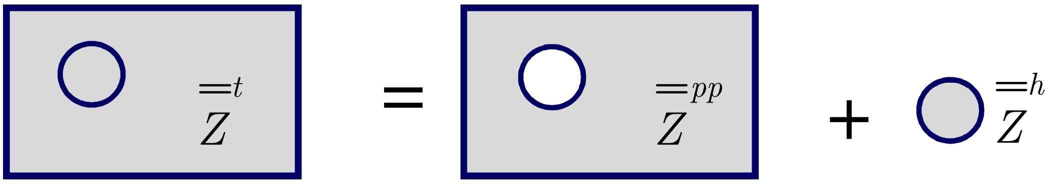

Figure B.3 Illustration of the desegmentation procedure. The impedances of the PMC holes $\bar{\bar{Z}}^{h}$ are extracted from impedance matrix of a solid plane $\bar{\bar{Z}}^{t}$ to yield the parallel-plate impedance $\bar{\bar{Z}}^{pp}$.

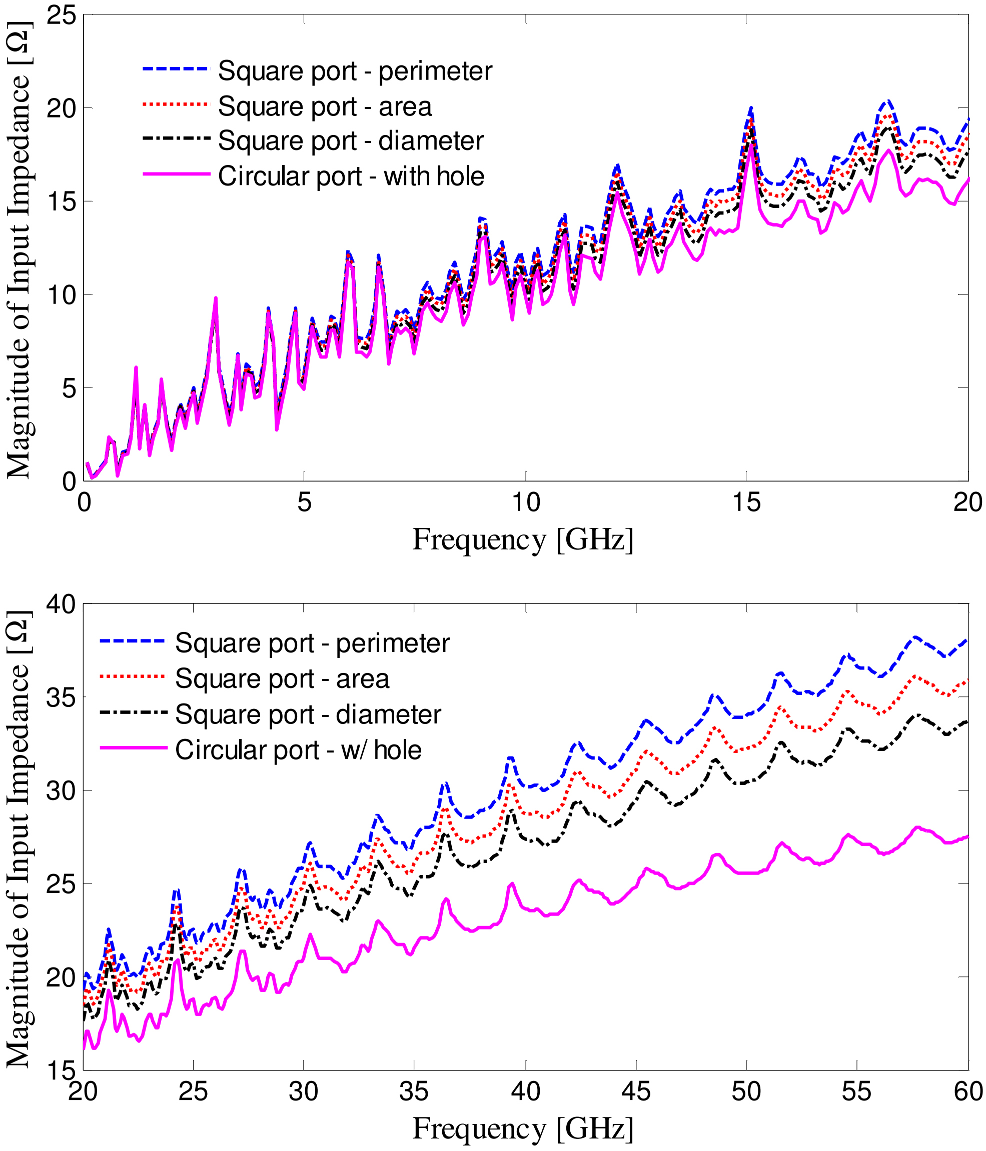

Figure B.4 Input impedance computed for the case in Fig. 4.6, obtained by the cavity model for circular port with the PMC hole and square port with equivalent perimeter, equivalent area, and equivalent diameter at frequencies (upper) up to 20 GHz and (lower) 20 – 60 GHz.

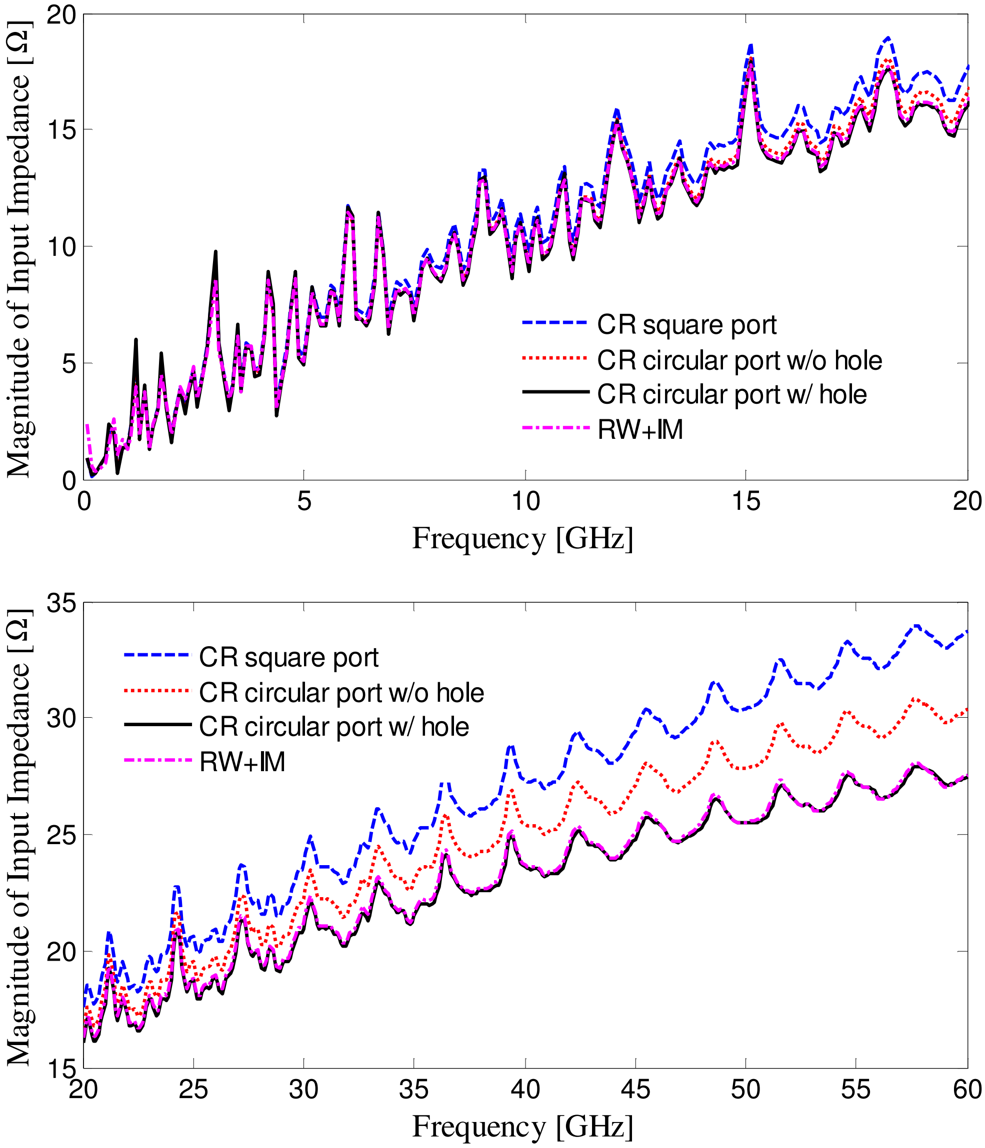

Figure B.5 Input impedance computed for the case in Fig. 4.6, obtained by the cavity model for square port, circular port with and without the PMC hole, as well as radial waveguide method plus image theory at frequencies (upper) up to 20 GHz and (lower) 20 – 60 GHz.

The contribution of these small plane pairs can be excluded using the desegmentation technique [85],[168]. As illustrated in Fig. B.3, The parallel-plate impedance $\overline{\overline{Z}}^{pp}$ can be viewed as the impedance matrix of a solid plane $\overline{\overline{Z}}^{t}$ subtracts the impedance of the PMC holes $\overline{\overline{Z}}^{h}$, where $\overline{\overline{Z}}^{h}$ is a diagonal matrix with its entries defined in (B.16). By observing the voltage and current relations, the following expression can be found

$$\overline{\overline{Z}}^{pp} = \overline{\overline{Z}}^{t}\left(\overline{\overline{Z}}^{h} - \overline{\overline{Z}}^{t}\right)^{-1}\overline{\overline{Z}}^{h}. \tag{B.17}$$

As an example, the single-port rectangular power plane pair structure shown in Fig. 4.6 is analyzed. The effect of port shape approximations on *Zpp* is first evaluated. Fig. B.4 plots the input impedance results calculated by the new expression for circular ports, compared to three approximated square port cases, namely, equivalent perimeter ($W = \pi a/2$), equivalent area ($W = \sqrt{\pi} \cdot a$), and equivalent diameter ($W = 2a$). 1500*1500 modes are used for all the calculations. It is observed that the impedance is almost not affected by the port shape at the frequencies below 10 GHz and mainly determined by the board resonances. However, at higher frequencies, where the board resonances are significantly damped by the loss, the square port approximations overestimate the input impedance of the power planes, whereas the equivalent diameter approximation predicts the closest value to the circular port.

To demonstrate the effect of the PMC holes, the same configuration in Fig. 4.6 is computed with and without the PMC holes. The results are compared with the impedance obtained by the radial waveguide formula combined with image theory, which is an efficient approach for modeling of lossy rectangular power planes with circular ports [73]. The number of image layers is 10. As shown in Fig. B.5, the result of circular port with the PMC hole overlaps with that calculated by the RW method, whereas higher impedance is predicted without extracting the small circular plates at frequencies higher than 20 GHz.

References

---

[1] International Technology Roadmap for Semiconductors, Executive summary 2010 edition, 2010 [Online]. Information available: http://www.itrs.net (August 2011).

[2] R. R. Tummala, M. Swaminathan, *Introduction to System-on-package (SOP) Miniaturization of the Entire System*, New York, USA: McGraw-Hill, 2008.

[3] U. Knickerbocker, P. S. Andry, L. P. Buchwalter, A. Deutsch, R. R. Horton, K. A. Jenkins, Y. H. Kwark, G. McVicker, C. S. Patel, R. J. Polastre, C. Schuster, A. Sharma, S. M. Sri-Jayantha, C. W. Surovic, C. K. Tsang, B. C. Webb, S. L. Wright, S. R. McKnight, E. J. Sprogis, and B. Dang, "Development of the next-generation system-on-package (SOP) technology based on silicon carriers with fine-pitch chip interconnection," *IBM Journal of Research and Development*, vol. 49, no. 4/5, pp. 725-754, July/September, 2005.

[4] S. F. Al-sarawi, D. Abbott, and P. D. Franzon, "A Review of 3-D Packaging Technology," *IEEE Transaction on Components, Packaging, and Manufacturing Technologies—Part B.*, vol. 21, no. 1, pp. 2-14, February 1998.

[5] D. Derickson and M. Müller, *Digital Communications Test and Measurement: High-speed Physical Layer Characterization*, Upper Saddle River, NJ, USA: Prentice Hall, 2007.

[6] D. G. Kam, M. B. Ritter, T. J. Beukema, J. F. Bulzacchelli, P. K. Pepeljugoski, Y. H. Kwark, L. Shan, X. Gu, C. W. Baks, R. A. John, G. Hougham, C. Schuster, R. Rimolo-Donadio, and B. Wu, "Is 25 Gb/s on-board signaling viable?," *IEEE Transactions on Advanced Packaging*, vol. 32, no. 2, pp. 328-344, May 2009.

[7] C. R. Paul, *Introduction to Electromagnetic Compatibility*, New York, USA: Wiley, 1992.

[8] E.-P. Li, X.-C. Wei, A. C. Cangellaris, E.-X. Liu, Y.-J. Zhang, M. D'Amore, J. Kim, T. Sudo, "Progress review of electromagnetic compatibility analysis technologies for packaging, printed circuit boards, and novel interconnects," *IEEE Transactions on Electromagnetic Compatibility*, vol. 52, no. 2, pp. 248-265, May 2010.

[9] T. Okoshi, *Planar Circuits for Microwaves and Lightwaves*, Chapter 3, Berlin, Germany: Springer-Verlag, 1985.

[10] X. Duan, R. Rimolo-Donadio, S. Müller, K. J. Han, X. Gu, Y. H. Kwark, H.-D. Brüns, and C. Schuster, "Impact of multiple scattering on passivity of equivalent-circuit via models," *IEEE Electrical Design of Advanced Package & Systems Symposium EDAPS*, Hangzhou, China, December 12-14, 2011.

[11] X. Duan, R. Rimolo-Donadio, H.-D. Brüns, and C. Schuster, “A hybrid CIM/MoM approach for power plane analysis including radiation loss,” in Proc. *Asia-Pacific Symposium on Electromagnetic Compatibility APEMC*, Jeju Island, South Korea, May 16-19, 2011.

[12] S. Müller, X. Duan, R. Rimolo-Donadio, H.-D. Brüns, and C. Schuster, “Non-uniform currents on vias and their effects in a parallel-plate environment,” in Proc. *IEEE Electrical Design of Advanced Package & Systems Symposium EDAPS*, Singapore, December 7-9, 2010.

[13] X. Duan, R. Rimolo-Donadio, H.-D. Brüns, and C. Schuster, “Fast and concurrent simulations for SI, PI, and EMI analysis of multilayer printed circuit boards,” in Proc. *Asia-Pacific Symposium on Electromagnetic Compatibility APEMC*, invited paper, Beijing, China, April 12-16, 2010.

[14] X. Duan, R. Rimolo-Donadio, H.-D. Brüns, B. Archambeault, and C. Schuster, “Special session on power integrity techniques: contour integral method for rapid computation of power/ground plane impedance,” in Proc. *IEC DesignCon Conference*, Santa Clara, USA, February 1-4, 2010.

[15] X. Duan, R. Rimolo-Donadio, H.-D. Brüns, and C. Schuster, “A combined method for fast analysis of signal propagation, ground noise, and radiated emission of multilayer printed circuit boards,” *IEEE Transactions on Electromagnetic Compatibility*, vol. 52, no. 2, pp. 487-495, May 2010.

[16] X. Duan, R. Rimolo-Donadio, H.-D. Brüns, and C. Schuster, “Extension of the contour integral method to anisotropic modes on circular ports,” *IEEE Transactions on Component, Packaging, and Manufacturing Technology*, vol. 2, no. 2, pp. 321-331, February 2012.

[17] X. Duan, R. Rimolo-Donadio, H.-D. Brüns, and C. Schuster, “Circular ports in parallel-plate waveguide analysis with isotropic excitations,” accepted for publication at *IEEE Transactions on Electromagnetic Compatibility*, 2011.

[18] M. Swaminathan and A. Ege Engin, *Power Integrity Modeling and Design for Semiconductors and Systems*, Upper Saddle River, NJ, USA: Prentice Hall, 2008.

[19] I. Novak and J. R. Miller, *Frequency-Domain Characterization of Power Distribution Networks*, Boston, MA, USA: Artech House, 2007.

[20] P. Larsson, “di/dt noise in CMOS integrated circuits,” *Analog Integrated Circuits and Signal Processing*, vol. 14, pp. 113-129, September 1997.

[21] M. Swaminathan, D. Chung, S. Grivet-Talocia, K. Bharath, V. Laddha, and J. Xie, “Designing and modeling for power integrity,” *IEEE Transactions on Electromagnetic Compatibility*, vol. 52, no. 2, pp. 288-310, May 2010.

[22] T. H. Hubing, J. L. Drewniak, T. P. Van Doren, and D. M. Hockanson, “Power bus decoupling on multilayer printed circuit boards,” *IEEE Transactions on Electromagnetic Compatibility*, vol. 37, no. 2, pp. 155-166, May 1995.

[23] J. L. Knighten, B. Archambeault, J. Fan, G. Selli, S. Connor, and J. L. Drewniak, "PDN Design Strategies: I. Ceramic SMT decoupling capacitors – what values should I choose?," *IEEE EMC Society Newsletter*, issue no. 207, pp. 54-64, Fall 2005.

[24] L. D. Smith, R. E. Anderson, D. W. Forehand, T. J. Pelc, and T. Roy, "Power distribution system design methodology and capacitor selection for modern CMOS technology," *IEEE Transactions on Advanced Packaging*, vol. 22, no. 3, pp. 284-291, August 1999.

[25] M. Zhao, R. V. Panda, S. Sachin, S. Sapatnekar, and D. Blaauw, "Hierarchical analysis of power distribution networks," *IEEE Transactions on Computer Aided Design*, vol. 21, no. 2, pp. 159-168, February 2002.

[26] J. Fan, X. Ye, J. Kim, B. Archambeault, and A. Orlandi, "Signal integrity design for high-speed digital circuits: progress and directions," *IEEE Transactions on Electromagnetic Compatibility*, vol. 52, issue 2, pp. 392-400, May 2010.

[27] H. W. Johnson and M. Graham, *High-Speed Digital Design: A handbook of black magic*, New Jersey, USA: Prentice Hall, 1993.

[28] H. W. Johnson and M. Graham, *High-speed signal propagation: advanced black magic*, New Jersey, USA: Prentice Hall, 2003.

[29] P. Triverio, S. Grivet-Talocia, M. S. Nakhla, F. G. Canavero, and R. Achar, "Stability, causality, and passivity in electrical interconnect models," *IEEE Transactions on Advanced Packaging,* vol.30, no.4, pp.795-808, November 2007.

[30] B. Archambeault, *PCB Design for Real-World EMI Control*, Novato, CA, USA: Riverdeep Interactive Learning, 2002.

[31] B. Archambeault, C. Brench, and S. Connor "Review of printed-circuit-board level EMI/EMC issues and tools," *IEEE Transactions on Electromagnetic Compatibility*, vol. 52, issue 2, pp. 455-461, May 2010.

[32] M. Mondal, B. Mutnury, P. Patel, S. Connor, B. Archambeault, and M. Cases, "Electrical analysis of multi-board PCB systems with differential signaling considering non-ideal common ground connection," in *Proc. Electrical Performance of Electronic Packaging Conference EPEP*, Atlanta, Georgia, USA, October 29-31, 2007, pp. 37 - 40.

[33] B. Archambeault, J. C. Diepenbrock, and S. Connor, "EMI emissions from mismatches in high speed differential signal traces and cables," in *Proc. IEEE Int. Symposium on Electromagnetic Compatibility*, Honolulu, Hawaii, July 8-13, 2007, pp. 1-6.

[34] J. L. Knighten, B. Archambeault, J. Fan, G. Selli, A. Rajagopal, S. Connor, and J. L. Drewniak, "PDN design strategies: IV. Sources of PDN noise," *IEEE EMC Society Newsletter*, issue no. 212, pp. 54-64, Winter 2007.

[35] F. De Paulis, B. Archambeault, A. Orlandi, L. Raimondo, and S. Connor, "Common mode filtering performances of planar EBG structures," in *Proc. IEEE Symposium Electromagnetic Compatibility*, Austin, TX, USA, August 2009.

[36] C. A. Balanis, *Advanced Engineering Electromagnetics*, New York, USA: John Wiley and Sons, 1989.

[37] S. Müller, X. Duan, M. Kotzev, Y. J. Zhang, J. Fan, X. Gu Y. Kwark, R. Rimolo-Donadio, H.-D. Brüns, and C. Schuster, "Accuracy of physics-based via models for simulation of dense via arrays," accepted for publication on *IEEE Transactions on Electromagnetic Compatibility*, 2012.

[38] R. F. Harrington, *Time-harmonic Electromagnetic Fields*, New York, USA: McGraw-Hill, 1961.

[39] D. G. Dudley, *Mathematical Foundations for Electromagnetic Theory*, New York, USA: IEEE Press, 1994.

[40] C. C. Mei, *The Applied Dynamics of Ocean Surface Waves*, New York, USA: John Wiley and Sons, 1983.

[41] J. L. Knighten, B. Archambeault, J. Fan, G. Selli, L. Xue, S. Connor, and J. L. Drewniak, "PDN Design Strategies: III. Planes and materials – are they important factors in power bus design?," *IEEE EMC Society Newsletter*, issue no. 210, pp. 58-69, Summer 2006.

[42] S. Van den Berghe, F. Olyslager, D. De Zutter, J. De Moerloose, and W. Temmerman, "Study of the ground bounce caused by power planes resonance," *IEEE Transactions Electromagnetic Compatibility*, vol. 40, no. 2, pp. 111-119, May 1998.

[43] Institut für Theoretische Elektrotechnik, TUHH, CONCEPT-II [Online], Hamburg, Germany. Information available: http://www.tet.tu-harburg.de (September 2011).

[44] H. Kim, B. K. Sun, and J. Kim, "Suppression of GHz range power/ground inductive impedance and simultaneous switching noise using embedded film capacitors in multilayer packages and PCBs," *IEEE Microwave and Wireless Components Letters*, vol. 14, no. 2, pp. 71-73, February 2004.

[45] M. Swaminathan, J. Kim, I. Novak, and J. Libous, "Power distribution networks for system-on-package: status and challenges," *IEEE Transactions on Advanced Packaging*, vol. 27, no. 2, pp. 286-300, May 2004.

[46] T. L. Wu, Y. H. Lin, T. K. Wang, C. C. Wang, and S. T. Chen, "Electromagnetic bandgap power/ground planes for wideband suppression of ground bounce noise and radiated emission in high-speed circuits," *IEEE Transactions on Microwave Theory and Techniques,* vol. 53, no. 9, pp. 2935-2942, September 2005.

[47] T. Wang, R. F. Harrington, and J .R. Mautz, "Quasi-static analysis of a microstrip via through a hole in a ground plane," IEEE *Transactions on Microwave Theory and Techniques*, vol. 36, no. 6, pp. 1008-1013, June 1988.

[48] C. Schuster and W. Fichtner, "Parasitic modes on printed circuit boards and their effects on EMC and signal integrity," *IEEE Transactions Electromagnetic Compatibility*, vol. 43, no. 4, pp. 416-425, November 2000.

[49] A. Taflove, S. C. Hagness, *Computational Electrodynamics – the Finite-Difference Time-Domain Method*, Boston, MA, USA: Artech House, 2000.

[50] J. Yook, N. I. Dibb, and L. P. B. Katehi, "Characterization of high frequency interconnects using the finite difference time domain and finite element methods", *IEEE Transactions on Microwave Theory and Techniques*, vol. 42, no. 9, pp. 1727-1735, September 1994.

[51] H. Gajan, L. Pichon, and C. Marchand, "Finite element method for radiated emissions in EMC analysis", *IEEE Transactions on Magnetics*, vol. 36, no. 4, pp. 964-967, July 2000.

[52] R. F. Harrington, *Field Computation by Moment Methods*, Florida, USA: Krieger, 1968.

[53] A. E. Engin, K. Bharath, M. Swaminathan, M. Cases, B. Mutnury, N. Pham, D. N. de Araujo, and E. Matoglu, "Finite-difference modeling of noise coupling between power/ground planes in multilayered packages and boards," in *Proc. 56th Electronic Components Technology Conference ECTC*, San Diego, California, USA, May 30-June 2, 2006, pp. 1262–1267.

[54] A. Ege Engin, K. Bharath, and M. Swaminathan, "Multilayered finite-difference method (MFDM) for modeling of package and printed circuit board planes*,"* *IEEE Transactions on Electromagnetic Compatibility*, vol. 49, no. 2, pp. 441-447, May 2007.

[55] M. Stumpf and M. Leone, "Efficient 2-D integral equation approach for the analysis of power bus structures with arbitrary shape," *IEEE Transactions Electromagnetic on Compatibility*, vol. 51, no. 1, pp. 38-45, February 2009.

[56] X. Wei, E. Li, E. Liu, and X. Cui, "Efficient modeling of rerouted return currents in multilayered power-ground planes by using integral equation," *IEEE Transactions on Electromagnetic Compatibility*, vol. 50, No. 3, pp.740-743, August 2008.

[57] J. H. Kim and M. Swaminathan, "Modeling of irregular shaped power distribution planes using transmission matrix method," *IEEE Transactions on Advanced Packaging*, vol. 25, no. 2, pp. 189-199, May 2002.

[58] J. Park, H. Kim, Y. Jeong, J. Kim, J. S. Pak, D. G. Kam, and J. Kim, "Modeling and measurement of simultaneous switching noise coupling through signal via transition," *IEEE Transactions on Advanced Packaging*, vol. 29, no. 3, pp. 548-559, August 2006.

[59] S. Ramo, J. R. Whinnery, and T. Van Duzer, *Fields and waves in communications electronics*, 3rd Ed., New York, USA: John Wiley & Sons, 1993.

[60] R. Ito, R. W. Jackson, and T. Hongsmatip, "Modelling of interconnections and isolation within a multilayered ball grid array package," *IEEE Transactions on Microwave Theory and Techniques*, vol. 47, no. 9, pp. 1819-1825, September 1999.

[61] R. Abhari, G. V. Eleftheriades, and E. van Deventer-Perkins, "Physics-based CAD models for the analysis of vias in parallel-plate environments," *IEEE Transactions on Microwave Theory and Techniques*, vol. 49, no. 10, pp. 1697-1707, October 2001.

[62] M. Xu, Y. Ji, T. H. Hubing, T. Van Doren, and J. L. Drewniak, "Development of a closed-form expression for the input impedance of power-ground plane structures," in Proc. *IEEE International Symposium on Electromagnetic Compatibility*, Washington D.C., USA, August 21-25, 2000, pp. 77-82.

[63] J. C. Parker, “Via coupling within parallel rectangular planes,” *IEEE Transactions on Electromagnetic Compatibility*, vol. 39, no. 1, pp. 17-23, February 1997.

[64] T. Okoshi, *Planar Circuits for Microwaves and Lightwaves*, Chapter 2, Berlin, Germany: Springer-Verlag, 1985.

[65] G. T. Lei, R. W. Techentin, P. R. Hayes, D. J. Schwab, and B. K. Gilbert, “Wave model solution to the ground/power plane noise problem,” *IEEE Transactions on Instrumentation and Measurement*, vol. 44, no. 2, pp. 300-303, April 1995.

[66] G. T. Lei, R. W. Techentin, and B. K. Gilbert, “High-frequency characterization of power/ground plane structures,” *IEEE Transactions on Microwave Theory and Techniques*, vol. 47, no. 5, pp. 562-569, April 1999.

[67] A. Benalla and K. C. Gupta, “Faster computation of Z/matrices for rectangular segments in planar microstrip circuits,” *IEEE Transactions on Microwave Theory and Techniques*, vol. 34, pp. 733-736, June 1986.

[68] G. Antonini, “A low-frequency accurate cavity model for transient analysis of power-ground structures,” *IEEE Transactions on Electromagnetic Compatibility*, vol. 50, no. 1, pp. 138-148, February 2008.

[69] Z. L. Wang, O. Wada, Y. Toyota, and R. Koga, “Convergence acceleration and accuracy improvement in power bus impedance calculation with a fast algorithm using cavity modes,” *IEEE Transactions on Electromagnetic Compatibility*, vol. 47, no. 1, pp. 2-8, February 2005.

[70] J. Trinkle and A. Cantoni, “Single summation expression for the rectangular power ground plane cavity,” in Proc. *16th Int. Zurich Symposium on Electromagnetic Compatibility*, Zurich, Switzerland, February 16-20, 2005, pp. 247-250.

[71] M. Hampe, V. Palanisamy, and S. Dickmann, “Single summation expression for the impedance of rectangular PCB power-bus structures loaded with multiple lumped elements,” *IEEE Transactions on Electromagnetic Compatibility*, vol. 49, no. 1, pp. 58-67, February 2007.

[72] A. R. Chada, Y. Zhang, G. Feng, J. L. Drewniak, and J. Fan, “Impedance of an infinitely large parallel-plane pair and its applications in engineering modeling,” in Proc. *IEEE International Symposium on Electromagnetic Compatibility*, Austin, Texas, USA, August 17-21, 2009, pp. 78-82.

[73] R. Rimolo-Donadio, H.-D. Brüns, and C. Schuster, “Hybrid approach for efficient calculation of the parallel-plate impedance of lossy power/ground planes,” *Microwave and Optical Technology Letters*, vol. 51, no. 9, pp. 2051-2056, September 2009.

[74] J. Trinkle and A. Cantoni, “Impedance expressions for unloaded and loaded power ground planes,” *IEEE Transactions on Electromagnetic Compatibility*, vol. 50, no. 2, pp. 390-398, May 2008.

[75] R. Chadha and K. C. Gupta, “Green’s functions for triangular segments in planar microwave circuits,” *IEEE Transactions on microwave theory and techniques*, vol. 28, no. 10, pp. 1139-1143, October 1980.

[76] R. Chadha and K. C. Gupta, “Green’s functions for circular sectors, annular rings, and annular sectors in planar microwave circuits,” *IEEE Transactions on Microwave Theory and Techniques*, vol. 29, no. 1, pp.68-71, January 1981.

[77] B. Archambeault and A. E. Ruehli, “Analysis of power/ground-plane EMI decoupling performance using the partial-element equivalent circuit technique*,” IEEE Transactions Electromagnetic Compatibility*, vol. 43, no. 4, pp. 437-445, November 2001.

[78] J. Kim, K Shringarpure, J. Fan, J. Kim, and J. L. Drewniak, “Equivalent circuit model for power bus design in multi-layer PCBs with via arrays,” *IEEE Microwave and Wireless Components Letters*, vol. 21, no. 2, pp. 62-64, May 2011.

[79] N. Na, J. Jinseong, S. Chun, M. Swaminathan, and J. Srinivasan, “Modeling and transient simulation of planes in electronic packages,” *IEEE Transactions on Advanced Packaging*, vol. 23, no. 3, pp. 340-352, August 2000.

[80] S. N. Lalgudi, E. Engin, G. Casinovi, and M. swaminathan, “Accurate transient simulation of interconnects characterized by band-limited data with propagation delay enforcement in a modified nodal analysis framework*,” IEEE Transactions Electromagnetic Compatibility*, vol. 50, no. 3, pp. 715-729, August 2008.

[81] L. Tsang, H. Chen, C. C. Huang, and V. Jandhyala, “Modeling of multiple scattering among vias in planar waveguides using foldy-lax equations,” *Microwave Optical Technology Letters*, vol. 31, no. 4, pp. 375-384, Nov. 2004.

[82] H. Chen, Q. Li, L. Tsang, C. C. Huang, and V. Jandhyala, “Analysis of a large number of vias and differential signaling in multilayered structures,” *IEEE Transactions on Microwave Theory and Techniques*, vol. 51, no. 3, pp. 818-829, March 2003.

[83] Z. Z. Oo, E. X. Liu, E. P. Li, X. Wei, Y. Zhang, M. Tan, L. W. J. Li, and R. Vahldieck, “A semi-analytical approach for system-level electrical modeling of electronic packages with large number of vias,” *IEEE Transactions on Advanced Packaging*, vol. 31, no. 2, pp. 267-274, May 2008.

[84] E. X. Liu, E. P. Li, Z. Z. Oo, X. C. Wei, Y. J. Zhang, and R. Vahldieck, “Novel methods for modelling of multiple vias in multilayered parallel-plate structures,” *IEEE Transactions on Microwave Theory and Techniques*, vol. 57, no. 7, pp. 1724-1733, July 2009.

[85] K. C. Gupta M. D. Abouzahra, Ed., *Analysis and Design of Planar Microwave Components*, New Jersey, USA: IEEE Press, Chapter 3, pp. 75-86, 2004.

[86] R. Sorrentino, “Planar circuits, waveguide methods, and segmentation method,” *IEEE Transactions on Microwave Theory and Techniques,* vol. 33, no. 10, pp. 1057-1066, October 1985.

[87] R. Chadha and K. C. Gupta, “Segmentation method using impedance matrices for analysis of planar microwave circuits,” *IEEE Transactions on Microwave Theory and Techniques*, vol. 29, no. 1, pp. 71-74, January 1981.

[88] R. Rimolo-Donadio, X. Gu, Y. H. Kwark, M. B. Ritter, B. Archambeault, F. D. Paulis, Y. Zhang, J. Fan, H.-D. Brüns, and C. Schuster, “Physics-based via and trace models for

efficient link simulation on multilayer structures up to 40 GHz," *IEEE Transactions on Microwave Theory and Techniques*, vol. 57, no. 8, pp. 2072-2083, August 2009.

[89] R. Rimolo-Donadio, X. Duan, H.-D. Brüns, and C. Schuster, "Comprehensive multilayer substrate models for co-simulation of power and signal integrity," in Proc. *42th International Symposium on Microelectronics IMAPS*, San Jose, California, USA, November 1-5, 2009.

[90] R. Rimolo-Donadio, X. Duan, H.-D. Brüns, and C. Schuster, "Differential to common mode conversion due to asymmetric ground via configurations," in *Proc. 13th IEEE Workshop on Signal Propagation on Interconnects SPI*, Strasbourg, France, May 12-15, 2009, pp. 1-4.

[91] J. Kim, Y. Joeng, J. Kim, J. Lee, C. Ryu, J. Shim, M. Shin, and J. Kim, "Modeling and measurement of interlevel electromagnetic coupling and fringing effect in a hierarchical power distribution network using segmentation method with resonant cavity model," *IEEE Transactions on Advanced Packaging*, vol. 31, no. 3, pp. 544–557, August 2008.

[92] X. C. Wei, E. P. Li, E. X. Liu, and R. Vahldieck, "Efficient simulation of power distribution network by using integral-equation and modal-decoupling technology," *IEEE Transactions on Microwave Theory and Techniques*, vol. 56, no. 10, pp. 2277- 2285, October 2008.

[93] T. Okoshi and T. Miyoshi, "The planar circuit – an approach to microwave integrated circuitry," *IEEE Transactions on Microwave Theory and Techniques*, vol. 20, no. 4, pp. 245-252, April 1972.

[94] R. Garg, *Microstrip Antenna Design Handbook,* Boston, USA: Artech House, 2001.

[95] T. Anada, J.-P. Hsu, and T. Okoshi, "New synthesis method for a branch-line 2 dB hybrid: a hybrid approach comprising planar and transmission line circuit concepts," *IEEE Transactions on Microwave Theory and Techniques*, vol. 39, no. 6, pp. 969- 979, June 1991.

[96] C. M. Krowne and R. E. Neidert, "Theory and numerical calculations for radially inhomogeneous circular ferrite circulators," *IEEE Transactions on Microwave Theory and Techniques*, vol. 44, no. 2, pp. 419-431, March 1996.

[97] B. Young, *Digital signal integrity: modeling and simulation with interconnect and packages,* London, U.K.: Prentice Hall Modern Semiconductors Design Series, 2000.

[98] J. Fan, M. Cocchini, B. Archambeault, J. L. Knighten, J. L. Drewniak, and S. Connor, "Noise coupling between signal and power/ground nets due to signal vias transitioning through power/ground plane pair," *IEEE Symposium on Electromagnetic Compatibility*, Detroit, USA, August 18-22, 2008.

[99] J. A. Stratton, *Electromagnetic Theory,* New York, USA: McGraw-Hill 1941.

[100] M. Stumpf, O. Kröning and M. Leone, "Power-bus modeling using 2D-integral-equation formulation," in Proc. *20th International Zurich Symposium on Electromagnetic Compatibility*, Zurich, Switzerland, January 12-16, 2009, pp.189-192.

[101] G. Lehner, *Elektromagnetische Feldtheorie,* Chapter 8, Berlin, Germany: Springer-Verlag, 1996.

[102] D. M. Pozar, *Microwave Engineering*, 3rd Ed., New York, USA: John Wiley & Sons, 2005.

[103] W. L. Stutzman and G. A. Thiele, *Anatenna Theory and Design*, New York, USA: John Wiley & Sons, 1981.

[104] P. J. Davis and P. Rabinowitz, *Methods of Numerical Integration*, Chapter 2, Florida, USA: Academic Press, 1984.

[105] A. Jennings and J. J. McKeown*, Matrix Computation*, United Kingdom: John Wiley & Sons, 1992.

[106] C. Schuster, Y. H. Kwark, G. Selli, and P. Muthana, "Developing a "physical" model for vias", in Proc. *IEC DesignCon 2006*, Santa Clara, California, USA, February 6-9, 2006.

[107] C. A. Balanis, *Antenna Theory*, 2nd ed., New York, USA: John Wiley & Sons, 1997.

[108] M. Leone, "The radiation of a rectangular power-bus structure at multiple cavity-mode resonances," *IEEE Transactions on Electromagnetic Compatibility*, vol. 45, no. 3, pp. 486-492, August 2003.

[109] J. S. Pak, H. Kim, J. Lee, and J. Kim, "Modeling and measurement of radiated field emission from a power/ground plane cavity edge excited by a through-hole signal via based on a balanced TLM and via coupling model," *IEEE Transactions on Advanced Packaging*, vol. 30, no. 1, pp. 73-85, Februrary 2007.

[110] Y. Zhang and J. Fan, "An intrinsic circuit model for multiple vias in an irregular plate pair through rigorous electromagnetic analysis," *IEEE Transactions on Microwave Theory and Techniques*, vol. 58, no. 8, pp. 2251-2265, August 2010.

[111] Y. Zhang, G. Feng and J. Fan "A novel impedance definition of a parallel-plate pair for an intrinsic via circuit model," *IEEE Transactions on Microwave Theory and Techniques*, vol. 58, no. 12, pp. 3780-3789, August 2010.

[112] I. S. Gradshteyn, and I. M. Ryzhik, *Table of Integrals, Series, and Products*, London: Academic Press, 1980, pp. 148.

[113] CST Corporation, CST Microwave Studio (MWS) Ver. 2008/2009 [Online], Darmstadt, Germany, Information available: http://www.cst.com (September 2011).

[114] S. Maeda, T. Kashiwa, and I. Fukai, "Full wave analysis of propagation characteristic of a through hole using the finite-difference time domain method," *IEEE Transactions on Microwave Theory and Techniques*, vol. 39, no. 12, pp, 2154-2159, December 1991.

[115] H.-I. Liaw and H. Merkelo, "Simulation and modeling of mode conversion at vias in multilayer interconnections," in Proc. *Electronic Components and Technology Conference ECTC*, pp.361-367, May 1995.

[116] B. Archambeault, S. Connor, D. N. de Araujo, M. R. Hashemi, R. Mittra, C. Schuster, and A. Ruehli, "Full Wave Simulation and Validation of a Simple Via Structure," *IEC DesignCon 2006,* Santa Clara, CA, USA, 2006.

[117] Ansoft Corporation, High Frequency Structure Simulator (HFSS) Ver. 12 [Online], Pittsburgh, USA. Information available: http://www.ansoft.com (September. 2011).

[118] R. E. Collin, *Foundations for Microwave Engineering*, Singapore: McGraw-Hill, 1992, chapter 4.

[119] M. Abramowitz and I. A. Stegun, *Handbook of Mathematical Functions with Formulas, Graphs, and Mathematical Tables*, New York: Dover, 1965, pp. 363.

[120] W. C. Chew, J.-M. Jin, E. Michielssen, and J. M. Song *Fast and Efficient Algorithm in Computational Electromagnetics*, Boston, MA, USA: Artech House, 2001.

[121] H. Wu and C. Cangellaris, “A finite-element domain-decomposition methodology for electromagnetic modeling of multilayer high-speed interconnects” *IEEE Transactions on Advanced Packaging*, vol. 31, no. 2, pp. 339-350, May 2008.

[122] X. C. Wei, E. P. Li, E. X. Liu, E. K. Chua, Z. Z. Oo, and R. Vahldieck, “Emission and susceptibility modeling of finite-size power-ground planes using a hybrid integral equation method” *IEEE Transactions on Advanced Packaging*, vol. 31, no. 3, pp. 536-543, August 2008.

[123] S. Wu, X. Chang, C. Schuster, X. Gu, and J. Fan, “Eliminating via-plane coupling using ground vias for high-speed signal transitions,” in *Proc. IEEE Electrical Performance of Electronic Package Conference EPEP*, San Jose, California, USA, October 27-29, 2008, pp. 247-250.

[124] E. R. Pillai, “Coax via— A technique to reduce crosstalk and enhance impedance match at vias in high-frequency multilayer packages verified by FDTD and MoM modeling,” *IEEE Transactions on Microwave Theory and Techniques*, vol. 45, no. 10, pp. 1981-1985, October 1997.

[125] X. Gu, A. E. Ruehli, and M. B. Ritter, “Impedance design for multi-layered vias,” in Proc. *IEEE Electrical Performance of Electronic Package Conference EPEP*, San Jose, California, USA, October 27-29, 2008, pp. 317-320.

[126] M. P. Goetz “Time and frequency domain analysis of integral decoupling capacitors,” *IEEE Transactions on Components, Packaging, and Manufacturing Technology – Part B*, vol. 19, no. 3, pp. 518-522, August 1996.

[127] J. L. Knighten, B. Archambeault, J. Fan, G. Selli, S. Connor, and J. L. Drewniak, “PDN Design Strategies: II. Ceramic SMT decoupling capacitors – does location matters?,” *IEEE EMC Society Newsletter*, issue no. 208, pp. 56-67, Winter 2006.

[128] A. Madou and L. Martens, “Electrical behavior of decoupling capacitors embedded in multilayered PCBs,” *IEEE Transactions on Electromagnetic Compatibility*, vol. 43, no. 4, pp. 549-556, November 2001.

[129] P. Muthana, K. Srinivasan, A. E. Engin, M. Swaminathan, R. Tummala, V. Sundaram, B. Wiedenman, D. I. Amey, K. H. Dietz, and S. Banerji, “Improvements in noise suppression for I/O circuits using embedded planar capacitors,” *IEEE Transactions on Advanced Packaging*, vol. 31, no. 2, pp. 234–245, May 2008.

[130] R. L. Chen, J. Chen, T. H. Hubing, and W. Shi, "Analytical model for the rectangular power-ground structure including radiation loss," *IEEE Transactions on Electromagnetic Compatibility*, vol. 47, no. 1, pp. 10-16, February 2005.

[131] H. W. Shim and T. H. Hubing, "A closed-form expression for estimating radiated emissions from the power planes in a populated printed circuit board," *IEEE Transactions on Electromagnetic Compatibility*, vol. 48, no. 1, pp. 74-81, February 2006.

[132] T. Mader, *Berechnung elektromagnetischer Felderscheinungen in abschnittsweise homogenen Medien mit Oberflächenstromsimulation,* Technische Universität Hamburg-Harburg, Dissertation, 1992.

[133] Q. Gu, Y. E. Yang, and M. A. Tassoudji, "Modeling and analysis of vias in multilayered integrated circuits," *IEEE Transactions on Microwave Theory and Techniques*, vol. 41, no. 2, pp. 206-214, February 1993.

[134] A. G. Williamson, "Radial-line/coaxial-line junctions: analysis and equivalent circuits," *International Journal of Electronics*, vol. 58, no. 1, pp. 91-104, January 1985.

[135] X. Gu, R. Rimolo-Donadio, Z. Yu, F. de Paulis, Y. H. Kwark, M. Cocchini, M.B. Ritter, B. Archambeault, A. Ruehli, J. Fan, and C. Schuster, "Fast-physics-based via and trace models for signal and power integrity co-analysis," in *Proc. IEC DesignCon Conference*, Santa Clara, USA, February 1-4, 2010.

[136] X. Gu, F. De Paulis, R. Rimolo-Donadio, K. Shringarpure, Y. Zhang, B. Archambeault, S. Connor, Y. H. Kwark, M. B. Ritter, J. Fan, and C. Schuster, "Fully analytical methodology for fast end-to-end link analysis on complex printed circuit boards including signal and power integrity effects," in *Proc. IEC DesignCon Conference*, Santa Clara, USA, February 2-5, 2009.

[137] R. Rimolo-Donadio, A. J. Stepan, H.-D. Brüns, J. L. Drewniak, and C. Schuster, "Simulation of via interconnects using physics-based models and microwave network parameters," in *Proc. 12th IEEE Workshop on Signal Propagation on Interconnects SPI*, Avignon, France, May 12-15, 2008.

[138] G. Selli, C. Schuster, Y. Kwark, M. Ritter, and J. L. Drewniak, "Model-to-hardware correlation of physics based via models with the parallel plate impedance included," in *Proc. IEEE Symposium Electromagnetic Compatibility*, Portland, Oregon, USA, August 2006, pp. 781-785.

[139] C. Schuster, G. Selli, Y. H. Kwark, M. B. Ritter, J. L. Drewniak, "Progress in representation and validation of physics-based via models", in *Proc. 11th IEEE Workshop Signal Propagation on Interconnects*, Genova, Italy, May 13-16, 2007, pp. 145-148.

[140] C. Schuster, G. Selli, Y. H. Kwark, M. B. Ritter, and J. L. Drewniak, "Accuracy and application of physics-based circuit models for vias," in *Proc. IMAPS 39th International Symposium on Microelectronics*, San Diego, California, USA, October 8-12, 2006.

[141] G. Selli, C. Schuster, Y. H. Kwark, M. B. Ritter, and J. L. Drewniak, "Developing a "physical" model for vias - part II: coupled and ground return vias," in *Proc. IEC DesignCon*, Santa Clara, California, USA, 2007.

[142] R. Rimolo-Donadio, *Development, Validation, and Application of Semi-Analytical Interconnect Models for Efficient Simulation of Multilayer Substrates,* Technische Universität Hamburg-Harburg, Dissertation, 2011.

[143] H. Marko, *Theorie linearer Zweipole, Vierpole und Mehrtore*, Stuttgart, Germany: S. Hirzel Verlag Stuttgart, 1971.

[144] Y. Zhang, R. Rimolo-Donadio, C. Schuster, E. Li, and J. Fan, "Extraction of via-plate capacitance of an eccentric via by an integral approximation method," *IEEE Microwave and Wireless Components Letters*, vol. 19, no. 5, pp. 275-277, May 2009.

[145] Y. Zhang, J. Fan, G. Selli, M. Cocchini, and D. P. Francesco, "Analytical evaluation of via-plate capacitance for multilayer printed circuit boards and packages," *IEEE Transactions on Microwave Theory and Techniques*, vol. 56, no. 9, pp. 2118–2128, September 2008.

[146] R. Rimolo-Donadio, H.-D. Brüns, and C. Schuster, "Including stripline connections into network parameter based via models for fast simulation of interconnects," in *Proc. 20th International Zurich Symposium on Electromagnetic Compatibility*, Zurich, Switzerland, January 12-16, 2009, pp. 345-348.

[147] A. Ege Engin, W. John, G. Sommer, W. Mathis, and H. Reichl, "Modeling of striplines between a power and a ground plane," *IEEE Transactions on Advanced Packaging*, vol. 29, no. 3, pp. 415–426, August 2006.

[148] C. R. Paul, "Analysis of multiconductor transmission lines," New York, USA: Wiley Series in Microwave and Optical Engineering, 1994.

[149] X. C. Wei, E. P. Li, E. X. Liu, and R. Vahldieck, "Efficient simulation of power distribution network by using integral-equation and modal-decoupling technology," *IEEE Trans. Microwave Theory and Techniques*, vol. 56, no. 10, pp. 2277- 2285, October 2008.

[150] Z. Z. Oo, E. X. Liu, E. P. Li, X. Wei, E. X. Liu, Y. J. Zhang, and L. W. J. Li, "Hybridization of the scattering matrix method and modal decomposition for analysis of signal traces in a power distribution network," *IEEE Transactions on Electromagnetic Compatibility*, vol. 51, no. 3, pp. 784-791, August 2009.

[151] Y. Chen, Z. Chen, Y. Wu, D. Xue, and J. Fang, "A new approach to signal integrity analysis of high-speed packaging," in *Proc. IEEE 4th Topical Meeting on Electrical Performance of Electronic Packaging EPEP*, Portland, USA, October 2-4, 1995, pp. 235-238.

[152] D. A. Frickey, "Conversions between S, Z, Y, h, ABCD, and T parameters which are valid for complex source and load impedance," *IEEE Transactions on Microwave Theory and Techniques*, vol. 42, no. 2, pp. 205-211, February 1994.

[153] N. Marcuvitz, *Waveguide handbook*, in IEE Electromagnetic Waves Series 21, London, United Kingdom: Peter Peregrinus Ltd., 1986.

[154] J. Kim, "EZPP Test Board Measurement," Missouri University of Science and Technology, personal communication, 2009.

[155] Z. L. Wang, O. Wada, Y. Toyota, and R. Koga, “Modeling of gapped power bus structures for isolation using cavity modes and segmentation,” *IEEE Transactions on Electromagnetic Compatibility*, vol. 47, no. 2, pp. 210-218, May 2005.

[156] Y. Jeong, A. C. Lu, L. L. Wai, W. Fan, B. K. Lok, H. Park, and J. Kim, “Hybrid analytical modeling method for split power bus in multilayered package,” *IEEE Transactions on Electromagnetic Compatibility*, vol. 48, no. 1, pp. 82-94, February 2006.

[157] Z. L. Wang, O. Wada, Y. Toyota, and R. Koga, “Application of segmentation method to analysis of power/ground plane resonance in multilayer PCBs,” in *Proc. IEEE 3rd International Symposium on Electromagnetic Compatibility*, Beijing, China, May 21-24, 2002, pp. 775-778.

[158] Z. L. Wang, O. Wada, Y. Toyota, and R. Koga, “Analysis of resonance characteristics of a power bus with rectangle and triangle elements in multilayer PCBs,” in *Proc. Asia-Pacific Conference on Environmental Electromagnetics CEEM*, November 4-7, 2003, pp.73-76.

[159] C. Wang, J. Mao, G. Selli, S. Luan, L. Zhang, J. Fan, D. J. Pommerenke, R. E. DuBroff, and J. L. Drewniak, “An efficient approach for power delivery network design with closed-form expressions for parasitic interconnect inductances,” *IEEE Transactions on Advanced Packaging*, vol. 29, no. 2, pp. 320-334, May 2006.

[160] B. Gustavsen, “Fast passivity enforcement for S-parameter models by perturbation of residue matrix eigenvalues,” *IEEE Transactions on Advanced Packaging*, vol. 33, no. 1, pp. 257-265, July 2010.

[161] S. Grivet-Talocia and A. Ubolli, “Passivity enforcement with relative error control,” *IEEE Transactions on Microwave Theory and Techniques*, vol. 55, no. 11, pp. 2384-2383, November 2007.

[162] T. Kushta, K. Narita, T. Kaneko, T. Saeki, and H. Tohya, “Resonance stub effect in a transition from a through via hole to a stripline in multilayer PCBs,” *IEEE Microwave Wireless Component Letters*, vol. 13, no. 5, pp. 169-171, May 2003.

[163] X. Duan , B. Archambeault, H.-D Bruens, and C. Schuster, “EM emissions of differential signals across connected printed circuit boards,” in *Proc. IEEE Symposium Electromagnetic Compatibility*, Austin, TX, USA, August 2009.

[164] J. Zhao and R. Chen, “A review of PCB level power delivery system,” in *EE Times Asia*, China/Korea, May/June 2006.

[165] J.U. Knickerbocker, C. S. Patel, P. S. Andy, C. K. Tsang, L. P. Buchwalter, E. J. Sprogis, H. Gan, R. R. Horton, R. J. Polastre, S. L. Wright, and J. M. Cotte, “3-D silicon integration and silicon packaging technology using silicon through-via,” *IEEE Journal of Solid-State Circuits*, vol. 41, no. 8, pp. 1718-1725, August 2006.

[166] V. Kripesh, S. W. Yoon, V. P. Ganesh, N. Khan, M. D. Rotaru W. Fang, and K. Iyer, “Three-dimensional system-in-package using stacked silicon platform technology,” *IEEE Transaction on Advanced Packaging*, vol. 28, no. 3, pp. 377-386, August 2005.

[167] M. Wax and T. Kailath, "Efficient inversion of Toeplitz-block Toeplitz matrix," *IEEE Transaction on Acoustics, Speech and Signal Processing*, vol. 31, no. 5, pp. 1218-1221, August 1983.

[168] P. C. Sharma and K. C. Gupta, "Desegmentation method for analysis of two-dimensional microwave circuit," *IEEE Transactions on Microwave Theory and Techniques*, vol. 29, no. 10, pp. 1094-1098, October 1981.

Curriculum Vitae

Xiaomin Duan

Born on October 19, 1980,

in Jiangsu, China.

Education

09/2007 – 04/2012

Technische Universität Hamburg-Harburg, Hamburg (TUHH), Germany.

Doctoral studies on “Extension of the Contour Integral Method for the Electrical Design of Planar Structures in Digital Systems”.

10/2004 – 05/2007

Technische Universität Hamburg-Harburg, Hamburg (TUHH), Germany.

Master of Science in Microelectronics and Microsystems.

09/1998 – 06/2002

Zhejiang University, Hangzhou, China.

Bachelor of Science in Electrical Engineering.

Professional Experience

07/2010 – 10/2010

IBM T. J. Watson Research Center, Yorktown Heights, New York, USA.

Intern at the Optical Communication and High-Speed Test Department.

05/2006 – 08/2006

Silicon Image GmbH (former Sci-worx GmbH), Hamburg, Germany.

Intern at the Research and Development Department.

10/2002 – 05/2004

Ciat Thermal Equipment Corporation, Hangzhou, China.

Electronic Engineer.

07/2002 – 09/2002

Coet Optical Electronics Corporation, Hangzhou, China.

Printed Circuit Board Layout Designer.

Hamburg, 03.04.2011